Unravelling the formation of Hells Bells: underwater speleothems from the Yucatán Peninsula in Mexico

---

Dissertation

Submitted to the

Combined Faculty of Natural Sciences and Mathematics

Heidelberg University, Germany

for the Degree of

Doctor of Natural Sciences (Dr. rer. nat.)

Presented by

M.Sc. Simon Michael Ritter

Oral examination: January 31st, 2020

1. Referee: Prof. Dr. Margot Isenbeck-Schröter
2. Referee: Prof. Dr. Wolfgang Stinnesbeck

Abstract

Hells Bells are unique bell-shaped underwater speleothems recently discovered in deep meromictic sinkholes (cenotes) on the Yucatán Peninsula, Mexico. In order to unravel the underwater growth of Hells Bells and identify the mechanism of subaqueous calcite precipitation, several deep meromictic cenotes with and without Hells Bells were investigated. Comprehensive hydro-, bio- and geochemical analyses of the water bodies and Hells Bells specimens including stable carbon isotope analyses, petrographic examination, U-series age-dating, aquifer monitoring and microbiological investigations, resulted in a consistent hypothesis on Hells Bells formation. The subaqueous authigenic calcite precipitation in cenotes with Hells Bells is most likely promoted by biogeochemical processes within the narrow 1–2 m thick pelagic redoxcline immediately above the halocline. Chemolithoautotrophy and incomplete microbial oxidation of sulfide to zero-valent sulfur via proton-consuming sulfide oxidation were identified as dominant biogeochemical processes within the redoxcline. Both processes favor authigenic calcite precipitation by increasing the pH of the surrounding water. A low degree of convection within the water body is identified as crucial hydrogeological prerequisite for the development of pelagic redoxclines, in which biogeochemical conditions favoring calcite precipitation prevail. Furthermore, in order to preserve the authigenic calcite formed in the redoxcline and build Hells Bells, a dynamic elevation of the halocline is hypothesized. Suitable conditions for Hells Bells formation are likely to be encountered in other deep stratified cenotes on the Yucatán Peninsula that are so far unexplored or unrecognized. Age-dating indicates that Hells Bells growth is an ongoing process covering the present to previous interglacial phases from ~0.1-12.5 and ~90–120 ka BP, respectively, outlasting aerial exposure during glacial sea level low stands. Eventually, isotope-geochemical and age-dating analyses reveal a great potential of Hells Bells as a geoarchive for reconstructing minimum sea level elevations, the development of the Yucatán Karst Aquifer and vegetation changes on the Yucatán Peninsula.

Zusammenfassung

Einzigartige glockenförmige Unterwasser-Speläotheme, die sogenannten Hells Bells, wurden jüngst in wenigen tiefen wassergefüllten Einsturzdolinen (Cenote) auf der Yucatán Halbinsel, Mexiko, entdeckt. Um die Bildungsweise dieser ungewöhnlichen Strukturen zu verstehen und insbesondere dem Mechanismus einer subaquatischen Kalzitfällung auf den Grund zu gehen, wurden im Rahmen dieser Arbeit mehrere Cenote mit und ohne Hells Bells untersucht. Auf Grundlage von umfassenden hydro-, bio- und geochemischen Analysen der Wasserkörper der Cenote sowie von Hells Bells Proben, konnte, ergänzt durch weitere Untersuchungen von stabilen Kohlenstoffisotopen, Uran-Thorium Datierungen, sowie der Petrografie und Mikrobiologie, eine konsistente Hypothese für die Bildung der Hells Bells Speläotheme erarbeitet werden. Demnach führen biogeochemische Prozesse in der pelagischen Redoxkline, einer 1–2 m mächtigen Wasserschicht direkt über der Halokline, zu einer subaquatischen authigenen Kalzitfällung. Dabei sind die Chemolithoautotrophie und eine unvollständige Oxidation von Sulfid zu null-wertigem Schwefel die dominanten biogeochemischen Prozesse. Beide Prozesse führen zu einer Erhöhung des pH–Werts im Umgebungswasser und damit zu einer authigenen Kalzitfällung innerhalb der Redoxkline. Ein geringer Grad an Konvektion wurde dabei als hydrogeologische Voraussetzung ausgemacht, um die biogeochemischen Bedingungen in Redoxklinen auszubilden, die eine Kalzitfällung begünstigen. Um die in der Wassersäule gebildeten Kalzite zu erhalten und damit die Hells Bells Speläotheme aufzubauen, wird eine dynamische Änderung der Höhenlage der Halokline vorgeschlagen und diskutiert. Altersbestimmungen deuten darauf hin, dass das Hells Bells Wachstum ein bis heute andauernder Prozess ist und dabei die Zeiträume des jetzigen und vorigen Interglazials von ~0.1–12.5 und ~90–120 ka vor heute abdeckt. Die Kombination von Isotopen-und geochemischen Untersuchungen mit Altersbestimmungen zeigen großes Potenzial von Hells Bells als Geoarchiv für die Rekonstruktion von Minimum-Meeresspiegelhöhen, der Entwicklung des Yucatán Karst Aquifers und des Vegetationswechsels auf der Yucatán Halbinsel auf.

Author statement

Part of this thesis is already published in Ritter et al. (2019a). This publication is distributed under the Creative Commons Attribution 4.0 License and the individual author contributions are annexed in the article. The publication, Ritter et al. (2019a), resulted from this PhD project and was prepared and written by the first author. Therefore, results, text and figures of the publication Ritter et al. (2019a) are integrated into this thesis, partially updated but mostly unmodified. In order to maintain readability of this thesis and avoid constant self-citing, the respective individual text passages, results and figures of this publication were not strictly cited nor quoted. In addition, several publications and manuscripts in preparation are related to this PhD project, which are properly credited and cited accordingly in this thesis.

Related publications and manuscripts in preparation:

Leberecht, K., Ritter, S. M., Isenbeck-Schröter, M., Klose, L., Stinnesbeck, W., Gescher, J.: Microbially promoted growth of subaqueous calcite formations called Hells Bells in an oxidant-deficient pelagic redoxcline, in preparation.

Ritter, S. M., Isenbeck-Schröter, M., Scholz, C., Keppler, F., Gescher, J., Klose, L., Schorndorf, N., Avilés Olguín, J., González-González, A. and Stinnesbeck, W.: Subaqueous speleothems (Hells Bells) formed by the interplay of pelagic redoxcline biogeochemistry and specific hydraulic conditions in the El Zapote sinkhole, Yucatán Peninsula, Mexico, Biogeosciences, 16(11), 2285–2305, 2019a.

Ritter, S. M., Isenbeck-Schröter, M., Scholz, C., Klose, L., Schorndorf, N. and Stinnesbeck, W.: Hells Bells - underwater speleothems, in Goldschmidt Abstracts, p. 2836., 2019b.

Schorndorf, N., Ritter, S. M., Frank, N., Klose, L. and Stinnesbeck, W.: Hells Bells–underwater speleothems: A novel paleohydrological archive for the Yucatán Peninsula, Mexico, in Goldschmidt Abstracts 3015., 2019.

Schorndorf, N., Ritter, S. M., Frank, N., Warken, S. and Stinnesbeck, W.: U-series dating of subaqueous speleothems (Hells Bells) from the Yucatán Peninsula in Mexico and their usability as a paleohydrological archive, in preparation.

Stinnesbeck, W., Frey, E., Zell, P., Avilés, J., Hering, F., Frank, N., Arps, J., Geenen, A., Gescher, J., Isenbeck-Schröter, M., Ritter, S., Stinnesbeck, S., Núñez, E. A., Dahne, V. F., González, A. G. and Deininger, M.: Hells Bells – unique speleothems from the Yucatán Peninsula, Mexico, generated under highly specific subaquatic conditions, Palaeogeography Palaeoclimatology Palaeoecology, 489, 209–229, 2017.

Content

1. Introduction

In 2009, local cave diver Vicente Fito Dahne explored the small sinkhole "cenote El Zapote" on the Yucatán Peninsula west of Puerto Morelos in Mexico. He discovered unusual bell-shaped speleothems growing from the cavern ceiling and the surrounding walls in 30–40 m water depth. Encouraged by the strong belief of exploring something unique and novel to the underwater world of the Yucatán Peninsula, cenote El Zapote was intensively explored and surveyed by a group of befriended local divers in close cooperation with the owners of the land around the cenote. These "pioneer-divers" named the unusual speleothems "Hells Bells" or "Campanas" (Spanish for bell) because of their bell-like shape and their occurrence in a "hellish" ambience of low-light conditions in great water depths close to a sulfidic turbid halocline with a characteristic rotten-egg odor.

Apart from Hells Bells, skeletal remains of a novel genus and species of giant ground sloth were found at the bottom of the cenote in 50–55 m water depth. This discovery was subsequently investigated by Stinnesbeck et al. (2017a). Shortly after, Hells Bells speleothems were scientifically investigated for the first time by an international team of divers and researchers from Mexico and Germany under the lead of Prof. Dr. Wolfgang Stinnesbeck, Institute of Earth Sciences, Heidelberg University. In this context, water samples of cenote El Zapote were brought for analysis to the research group of Hydrogeochemistry and Hydrogeology of Prof. Dr. Margot Isenbeck-Schröter at the Institute of Earth Sciences, Heidelberg University. As part of this group I was involved into investigating Hells Bells by examining and evaluating the results of these water samples with regard to the preparation of a manuscript on Hells Bells (Stinnesbeck et al., 2017b). This fundamental publication by Stinnesbeck et al. (2017b) provides detailed analyses on the morphology and structure of Hells Bells and states that Hells Bells speleothems are so far known in only a few cenotes of a restricted area in the North-Eastern Yucatán Peninsula. The major finding of this study is that Hells Bells grow underwater. However, the mechanism leading to

Hells Bells growth, i.e. the subaqueous precipitation of calcite in an otherwise carbonate dissolving karstic aquifer environment, remained unresolved. Fascinated by the topic from the beginning and financially supported by the research group "Hydrogeochemistry and Hydrogeology" of Prof. Dr. Margot Isenbeck-Schröter and by the Deutsche Forschungsgemeinschaft projects No. STI128/28 and STI128/36 of Prof. Dr. Wolfgang Stinnnesbeck, I initiated my PhD project intending to unravel the mystery of Hells Bells growth.

This project aspired to resolve the major question of underwater growth of Hells Bells addressing their bell-shaped morphology and their rareness in terms of known occurrences in only a few cenotes. For this purpose, water and Hells Bells samples were gathered in two field trips to the Yucatán Peninsula in Mexico in December 2017 and May/June 2018.

The first field trip was performed together with Christian Scholz in collaboration with W. Stinnesbeck. Detailed water analyses and sampling were conducted at cenote El Zapote with the aid of the technical divers Jerónimo Avilés Olguín, Eugenio Aceves Núñez, Christine Loew, Dirk Penzel and Thomas Vogt. The results of this sampling campaign resulted in the hypothesis on Hells Bells formation by an interplay of pelagic redoxcline biogeochemistry and specific hydraulic conditions in cenote El Zapote reported in Ritter et al. (2019).

In order to infer factors controlling Hells Bells formation and elucidate their restricted occurrence in a certain area on the Yucatán Peninsula, a second field trip was performed together with Master Student Lukas Klose, in collaboration with Kerstin Leberecht, who is a PhD Student of Prof. Dr. Johannes Gescher, Institute for Applied Biosciences, Karlsruhe Institute of Technology. Several cenotes with and without Hells Bells were investigated (Klose, 2018, unpub.) with the aid of the technical divers Christine Loew and Dirk Penzel. Microbiological analyses of water and Hells Bells samples were conducted by Kerstin Leberecht at cenote El Zapote (Leberecht et al., in prep.).

Aside from understanding Hells Bells growth, the PhD project aimed to evaluate the potential of Hells Bells as a geoarchive for the Yucatán Peninsula. For this purpose, Master Student Tianxiao Sun investigated an elongated Hells Bells specimen for its petrographic characteristics (Sun, 2018,

unpub.) and Nils Schorndorf carried out geochemical analyses including stable carbon and oxygen isotope analyses and U-series age-dating in collaboration with the research group "Biogeochemistry" of Prof. Dr. Frank Keppler, Institute of Earth Sciences, Heidelberg University and the research group of "Physics of environmental Archives" of Prof. Dr. Norbert Frank, Institute of Environmental Physics and Institute of Earth Sciences, Heidelberg University (Schorndorf, 2018, unpub.). Additionally, U-series age dating of laminated Hells Bells from different cenotes where carried out in collaboration with the "Speleothem Research" group of Prof. Dr. Denis Scholz, Institute for Geosciences, Mainz University.

This thesis intends to combine the different research approaches in studying Hells Bells and aims to integrate the numerous results to resolve the major question of an underwater growth of Hells Bells. At first, the mechanism for a subaqueous precipitation of calcite in the pelagic redoxcline of cenote El Zapote is developed by elaborated investigation of the biogeochemical and hydrological processes of the water body, in combination with geochemical and petrographic analyses of Hells Bells specimens. The factors controlling calcite precipitation in redoxclines of deep stratified cenotes of the Yucatán Peninsula is then further assessed by comparing the biogeochemistry and hydrology of cenotes with and without Hells Bells. Since a dynamic halocline elevation is recognized to be crucial for Hells Bells formation, evaluation of data loggers installed at different cenotes offers insights into the dynamics of the Yucatán Karst Aquifer. Eventually, once Hells Bells growth is deciphered, their potential as geoarchive for reconstructing paleo environmental conditions on the Yucatán Peninsula will be assessed.

2. Scientific Background

2.1 Underwater speleothems

Speleothems, such as stalactites or dripstones, result from physicochemical processes under subaerial conditions in a cave atmosphere. Calcite usually precipitates due to CO_2-degassing and evaporation of water enriched in dissolved carbonate dripping into the cave. In recent years, however, researchers have identified a small group of speleothems that appear to have calcified underwater. For these formations, interactions between physicochemical and biological calcite

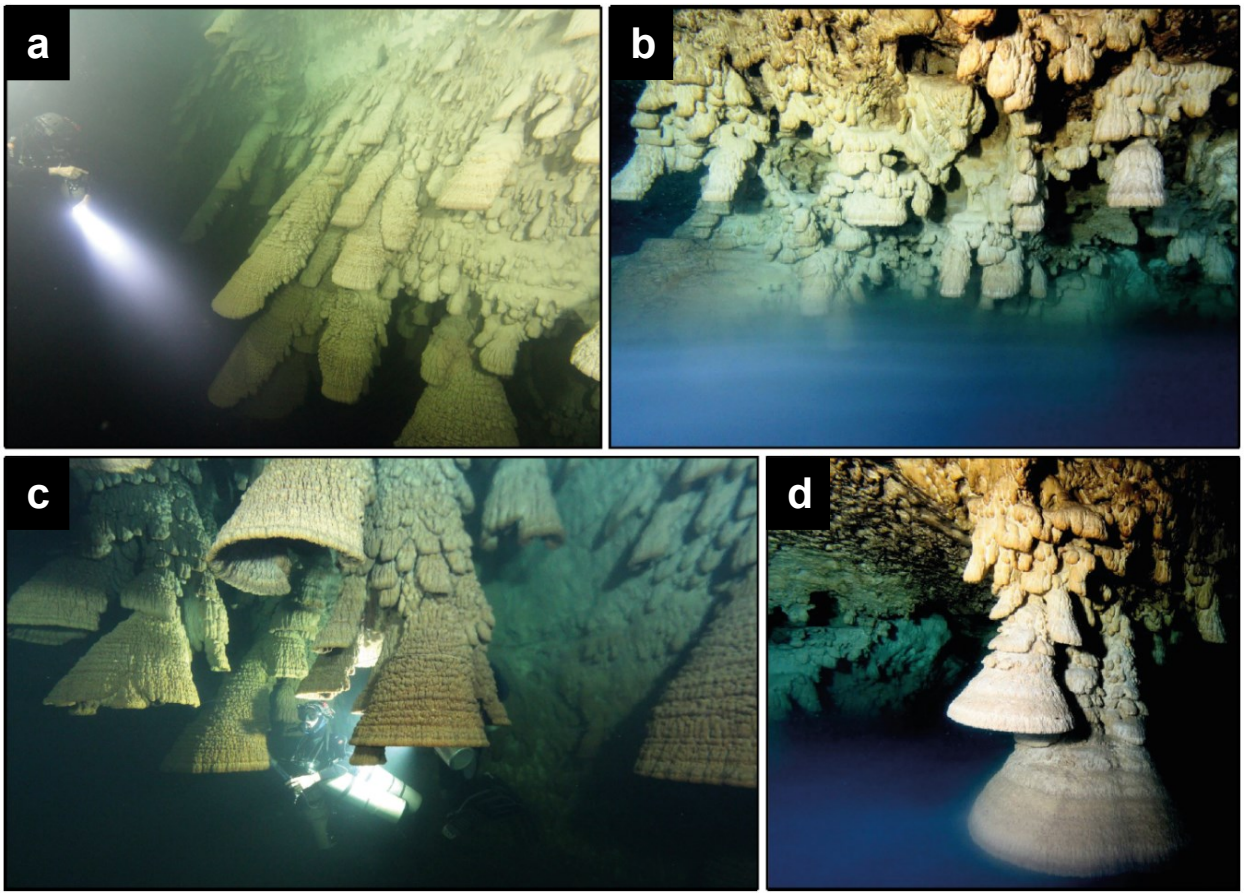

Fig. 1: Underwater photographs of Hells Bells speleothems from El Zapote between 30 and 35 m water depth. Note the white cloudy turbid layer in 2 and 4. A technical diver serves as scale in 1 and 3 (taken from Stinnesbeck et al., 2017b).

precipitation processes are interpreted (Barton and Northup, 2007; Bontognali et al., 2016; Gradzinski et al., 2012; Guido et al., 2013; Holmes et al., 2001; Jones et al., 2008, 2012; Macalady et al., 2007; Macintyre, 1984; Melim et al., 2001; Queen and Melim, 2006; Tredici et al., 2018). Furthermore, sea level controlled phreatic subaqueous calcite overgrowths were observed for

stalagmites (Harmon et al., 1978) and stalactites (Tuccimei et al., 2010; Vesica et al., 2000) in littoral endokarst caves.

Stinnesbeck et al., (2017b) recently presented a spectacular example for subaqueous speleothems termed Hells Bells from El Zapote sinkhole about 26 km west of Puerto Morelos on the Yucatán Peninsula of southern Mexico (Fig. 1 and Fig. 2). The occurrence of Hells Bells speleothems is so far only reported for six deep stratified cenotes restricted to a small area west of Puerto Morelos on the North-Eastern YP (cenotes Siete Bocas, Holbox, Maravilla, Tortugas, Kin-Ha and El Zapote). These bell-shaped structures consist of calcite and reach lengths of up to four meters. Hells Bells conically expand downward with strictly horizontal ring-like concentric swellings and neckings on the surface (Fig. 1c). A detailed description and analyses of the habitus and shape of Hells Bells is presented by Stinnesbeck et al., (2017b). Apparently, Hells Bells form in a lightless environment in freshwater above the anoxic and sulfidic halocline (Stinnesbeck et al., 2017b). Because of these environmental conditions in complete darkness, the local diving community has termed the El Zapote speleothem formations as Hells Bells.

Hells Bells grow from the cavern ceiling and the surrounding walls (Fig. 1a and c). Additionally, small individuals also cover a tree that has fallen into the sinkhole around ~3.5 cal kyr BP, which indicates that Hells Bells must have formed during the Holocene until at least historical times, and thus at periods when the deep sections of the cenote had already been submerged for thousands of years (Stinnesbeck et al., 2017b). Thus, the conditions for the formation of the biggest underwater speleothems worldwide must have existed consistently throughout the past thousands of years at cenote El Zapote. The internal structure of Hells Bells is characterized by laminar fabrics of alternating units of elongated dogtooth spar calcite and microcrystalline spar calcite (Fig. 2e). Microspar layers and corroded lobes of dogtooth spar crystals indicate either discontinuous growth of Hells Bells and/or intermittent dissolution (Stinnesbeck et al., 2017b). Phylogenetic analyses of Hells Bells speleothem surfaces from specimens of 33 and 34 m water

depth indicate that microorganisms inhabiting the Hells Bells potentially support a full nitrogen-

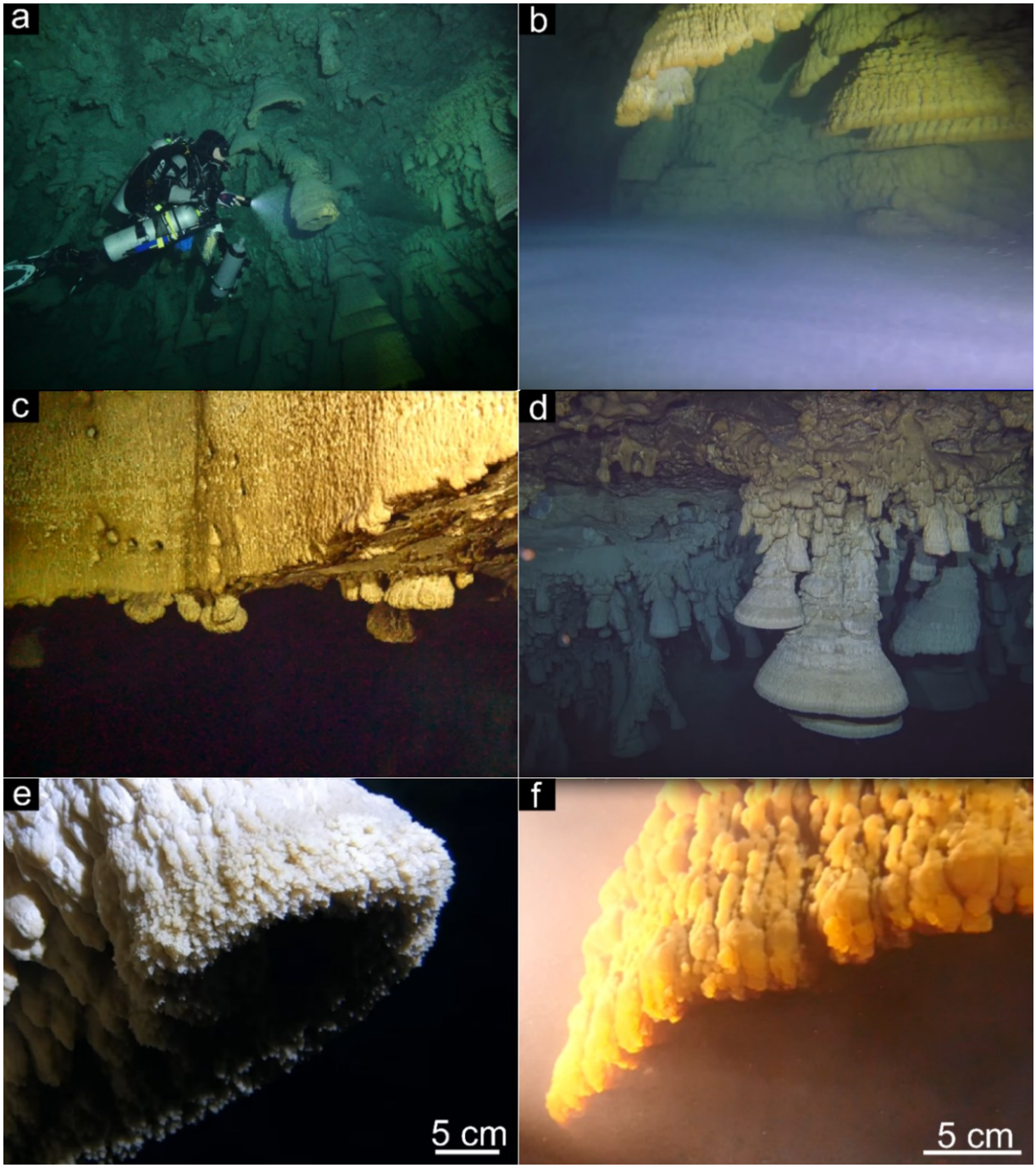

Fig. 2: Hells Bells of cenote El Zapote. Technical diver in cenote El Zapote during a sample collecting dive carrying the Niskin bottle, sample containers and the multiparameter sonde attached to the sidemount gas bottle (a). Turbid layer immediately above the halocline forming a distinct horizontal white cloud at around 36 m water depth (b). Transition of cenote shaft to the open dome-shaped cavern at 28 m water depth (c), where the vertical wall of the cenote shaft is devoid of Hells Bells speleothems (upper part of picture c), whereas small specimens of Hells Bells grow down from the horizontal ceiling below (lower part of c). Brown-colored Mn-oxide coatings on host rock carbonates and Hells Bells speleothems reach down from 28 m water depth to around 30 m water depth at the transition of the cenote shaft to the wide dome-like cavern (c and d). Below around 30 m water depth, Hells Bells speleothem and host rock carbonate surfaces are devoid of brownish Mn-oxide coatings. They are white to light-grey colored revealing a distinct horizontal boundary (d). Close-up shot of the lowermost calcite rim of a Hells Bell speleothem at around 32–35 m water depth showing mm-sized calcite crystals (e).

circle and autotrophic growth.

The growth of Hells Bells may thus be mediated by specific physical and biogeochemical conditions above and in the halocline, while formation of Hells Bells was likely restricted to the lowermost part of the freshwater body (Stinnesbeck et al., 2017b). However, due to the limited available data including geochemical parameters, the suggested processes for Hells Bells formation in Stinnesbeck et al. (2017b) were regarded as highly speculative.

Therefore, detailed geochemical analysis including stable carbon isotopes and U-series age-dating of the water body and Hells Bells speleothems of cenote El Zapote as well as further cenotes with and without Hells Bells were conducted in this PhD project. The cumulative results of these investigations are presented and discussed in this thesis.

2.2 Yucatán Peninsula

The Yucatán Peninsula (YP) consists of horizontally layered shallow-water carbonates of Mio-, Plio- and Pleistocene ages, dolomites and evaporites reaching a thickness of more than 1500 m (Lefticariu et al., 2006; Weidie, 1985). The Yucatán Karst Aquifer probably hosts the largest network of underwater caves in the world (Fig. 3). The Mexican state of Quintana Roo alone counts more than 370 underwater caves with a confirmed total length of ~1460 km and individual cave systems reaching up to >350 km in length (QRSS, 2018). These cave systems developed predominantly by the interaction of glacioeustacy, littoral processes and mixing-zone hydrology during glacial periods of the Pleistocene (Smart et al., 2006; Weidie, 1985). Flooding of these cave systems is indicated for the early to middle Holocene followed by an apparently dry deglacial episode (e.g. Collins et al., 2015 and Hodell et al., 1995). Pollen records indicate the establishment of tropical forest around 8600 cal yrs BP (Islebe et al., 1996) and warm and humid conditions most likely prevailed throughout the middle Holocene (e.g. Carrillo-Bastos et al., 2010 and references therein). Modern water levels were reached at around 4500 a BP (Grant et al., 2012; Hengstum et al., 2010) and variations in the water levels of up to a few meters are reported during Maya times (Curtis et al., 1996; Kennett et al., 2012; Medina-Elizalde et al., 2016).

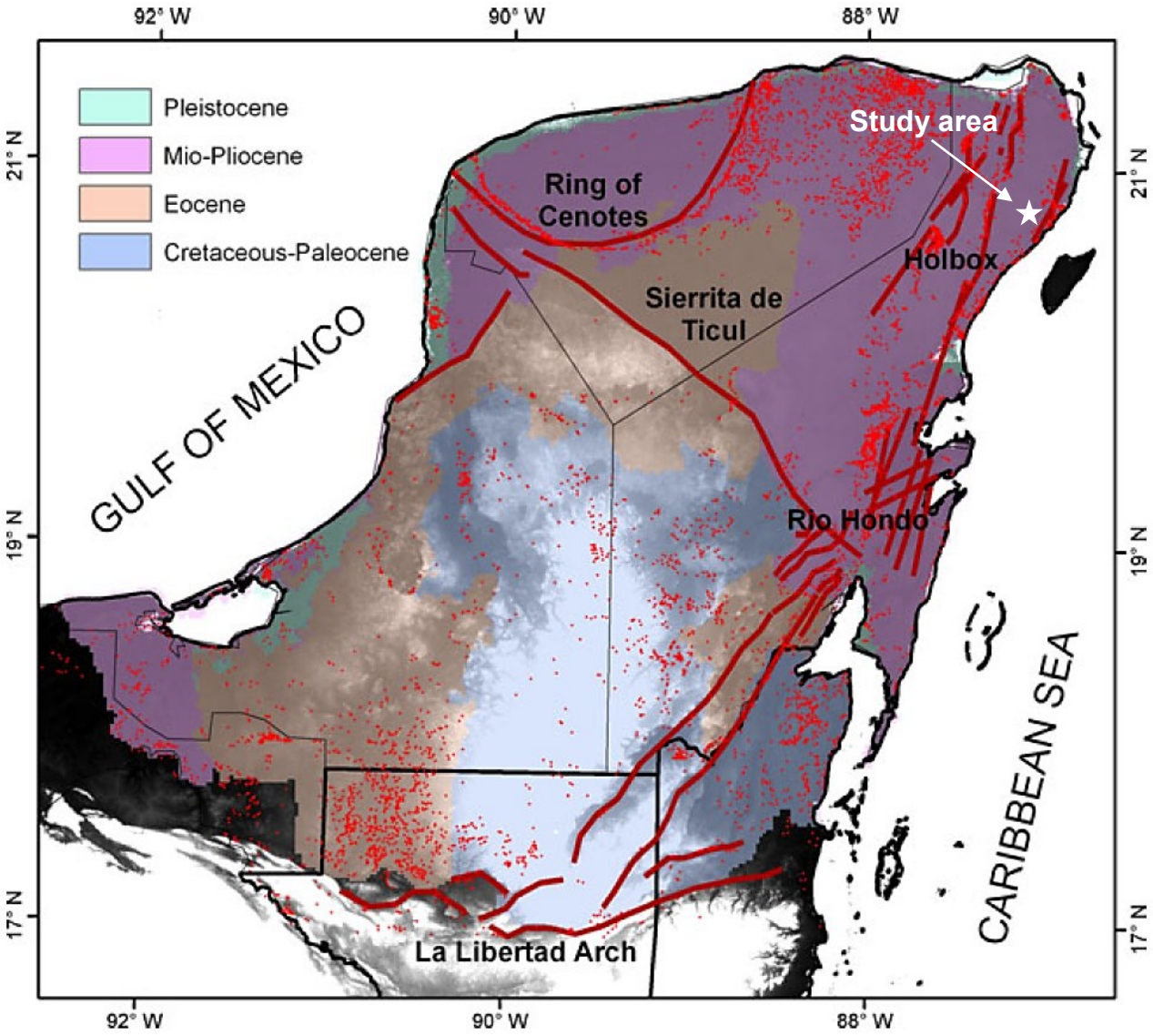

Fig. 3: Regional-scale map of the Yucatán Peninsula showing the preferential flow paths (red lines) and cenote locations (red dots). The area of cenotes with Hells Bells occurrences is indicated by the white star. Cenotes (red dots) were identified visually on high-resolution satellite imagery and background colors indicate ages of surface geology (modified from Bauer-Gottwein et al., 2011).

The YP has a tropical climate with mean air temperatures between 23–27 ° C and annual rainfalls range from 800 mm a^{-1} in the drier North-Western part of the YP to up to 1800 m a^{-1} on the east coast of the YP (Villasuso and Méndez Ramos, 2000). Approximately 90 % of the rainfall occurs between June to September within the rainy season from May and October. However, precipitation levels are highly spatially variable and vary within and between years (Villasuso and Méndez Ramos, 2000). Estimations of the evapotranspiration range from 40–85 % of the total annual rainfall (Gondwe et al., 2010 and references therein). Precipitation rapidly infiltrates through the

porous limestone into the underlying coastal groundwater consisting of a meteoric water mass, the freshwater lens above a saline water mass intruding from the coast (e.g. Kovacs et al., 2017a) (Fig. 4). Due to the karstic nature of the aquifer, rivers or surface run-offs are absent at the YP and drainage occurs solely subterranean via caves and conduits. The thickness of the freshwater lens varies between ~10–100 m and is generally thinner towards the coast (Beddows et al., 2002), while seawater intrudes up to 100 km inland (Beddows et al., 2007). The halocline separates the meteoric and marine water bodies and is usually characterized by undersaturation with respect to $CaCO_3$, leading to cave formation and conduit enlargement in the coastal carbonate aquifer (Back et al., 1986; Gulley et al., 2016; Mylroie and Carew, 1990; Smart et al., 2006).

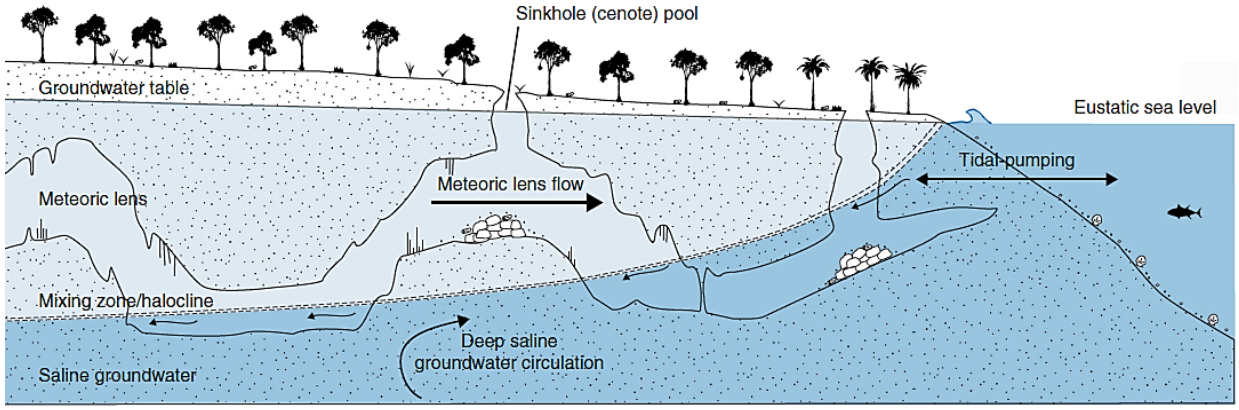

Fig. 4: Schematic cross-section showing important features of the Yucatán Karst Aquifer. The two groundwater masses, freshwater and saline groundwater, are separated by a mixing zone or halocline. The Yucatán Karst Aquifer is characterized by cenotes (sinkholes) and interconnected cave conduits resulting in high permeability (taken from Brankovits et al., 2017).

The depth of the halocline increases with distance from the coast (Bauer-Gottwein et al., 2011) and areas closer to the coast show a higher salinity of the freshwater lens than inland areas (Kovacs et al., 2017b). The position of the halocline is also dependent on global sea level and the thickness of the freshwater lens. Hydraulic gradients are generally very low with values of 1–10 cm km^{-1} (Bauer-Gottwein et al., 2011 and references therein). Whereas Moore et al. (1992) and Stoessell et al. (1993) report that the thickness of the freshwater lens does not vary significantly between seasons or on a yearly basis, local and short-termed variations are reported depending on recharge events and periodic variations of sea level elevation (Vera et al., 2012). Strong halocline elevations in response to heavy recharge events were reported by Escolero et al.

(2007), who documented a significant halocline elevation of up to 17.5 m in between two measurements in the years 2000 and 2003. The influence of tropical storms and hurricanes on the costal aquifer of the YP was studied by Coutino et al., (2017) and Kovacs et al. (2017b) who found a significant influence of such events on the salinity of the freshwater lens.

Sinkholes are formed by dissolution and collapse of the carbonate rock (Fig. 4). These structures are locally called *cenotes*, which is derived from the Maya word *ts´onot*. Cenotes are common throughout the YP representing the only natural access to freshwater by connecting the subterranean cave system with the surface (Bauer-Gottwein et al., 2011). There is a variety of cenote shapes on the YP. One group of cenotes is associated with conduits such as cenotes with large elongated open water pools that represent collapsed cave ceilings over conduits within the host rock and cave entrances that lead to the groundwater (Torres-Talamente et al., 2011). Circular pit-shaped cenotes are apparently not associated to conduits, though. These cenotes reach water depths of up to 150 m and show a notable concentration in the North-Western YP forming the so called “ring of cenotes” (Fig. 3) (Torres-Talamente et al., 2011). Their formation is presumably connected to basement faults, which were generated in relation to the Chicxulub impact at the K-T boundary in some distance off the northern coast of the YP (Hildebrand et al., 1995; Perry et al., 1995). The water bodies of such deep cenotes is often density stratified into a freshwater body overlying a saltwater body, separated by the halocline (e.g. Moore et al., 1992; Stoessell, 1995; Stoessell et al., 1993, 2002). Detailed information about the hydrogeology, the formation and occurrence of cenotes on the YP is given by Bauer-Gottwein et al., (2011) Schmitter-Soto et al. (2002) and Torres-Talamente et al. (2011). Good reviews on the hydrogeochemistry of the YP aquifer are given by Perry et al. (2002 and 2009) and Schmitter-Soto et al. (2002).

3. Methods

3.1 Study sites

3.1.1 Cenote El Zapote

The cenote El Zapote (Fig. 2 and Fig. 7a) is located 26 km west of the coast of Puerto Morelos (20°51´27.78" N 87°07´35.93" W; Fig. 5). In cross-section the cenote is bottle-shaped with a deep vertical water-filled shaft that opens at 28 m water depth to a wide cavern of 60 to >100 m in diameter that reaches to about 54 m water depth with a 20 m high debris mound in the center (Fig. 6a). A fallen tree stands on top of the debris mound and small Hells Bells cover the stem (Fig. 6a). There are no apparent passages or conduits that connect cenote El Zapote to a cave system. Additional details on cenote El Zapote are given in Stinnesbeck et al. (2017b) and Stinnesbeck et al. (2017a) who described the new genus and species of a giant ground sloth, *Xibalbaonyx oviceps,* from skeletal remains of an individual, which was found on the floor of cenote El Zapote. The cenote is part of an Eco Park and the spectacular Hells Bells speleothems attract many tourist diving groups performing several dives each day throughout the year.

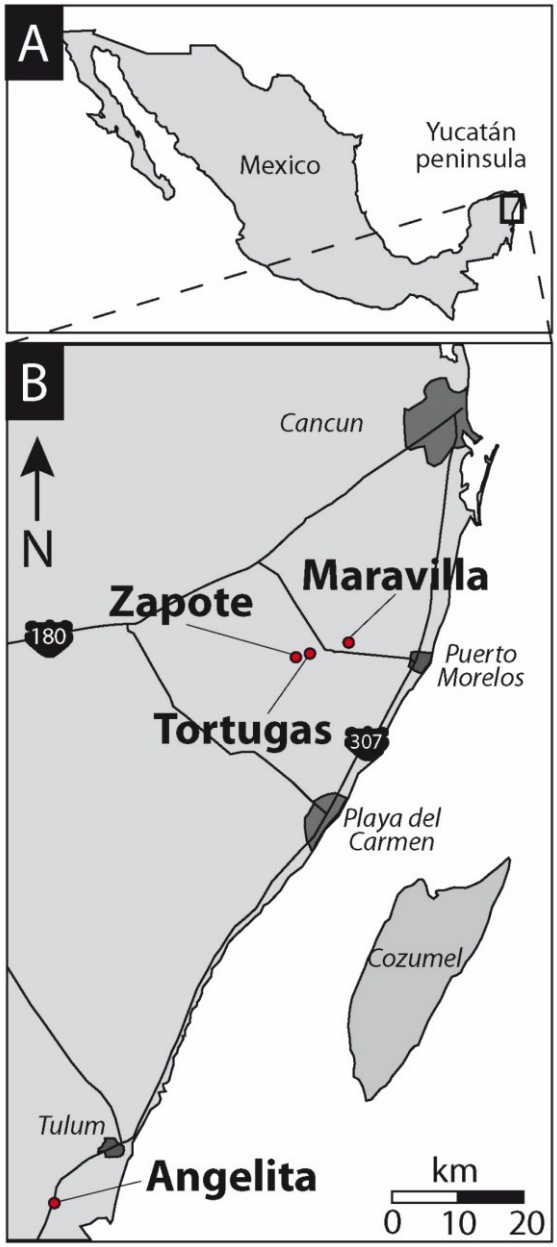

Fig. 5: The study area relative to Mexico (A) and the locations of the studied cenotes on the North-Eastern Yucatán Peninsula (B). Modified from Ritter et al., (2019) and Stinnesbeck et al., (2017b)

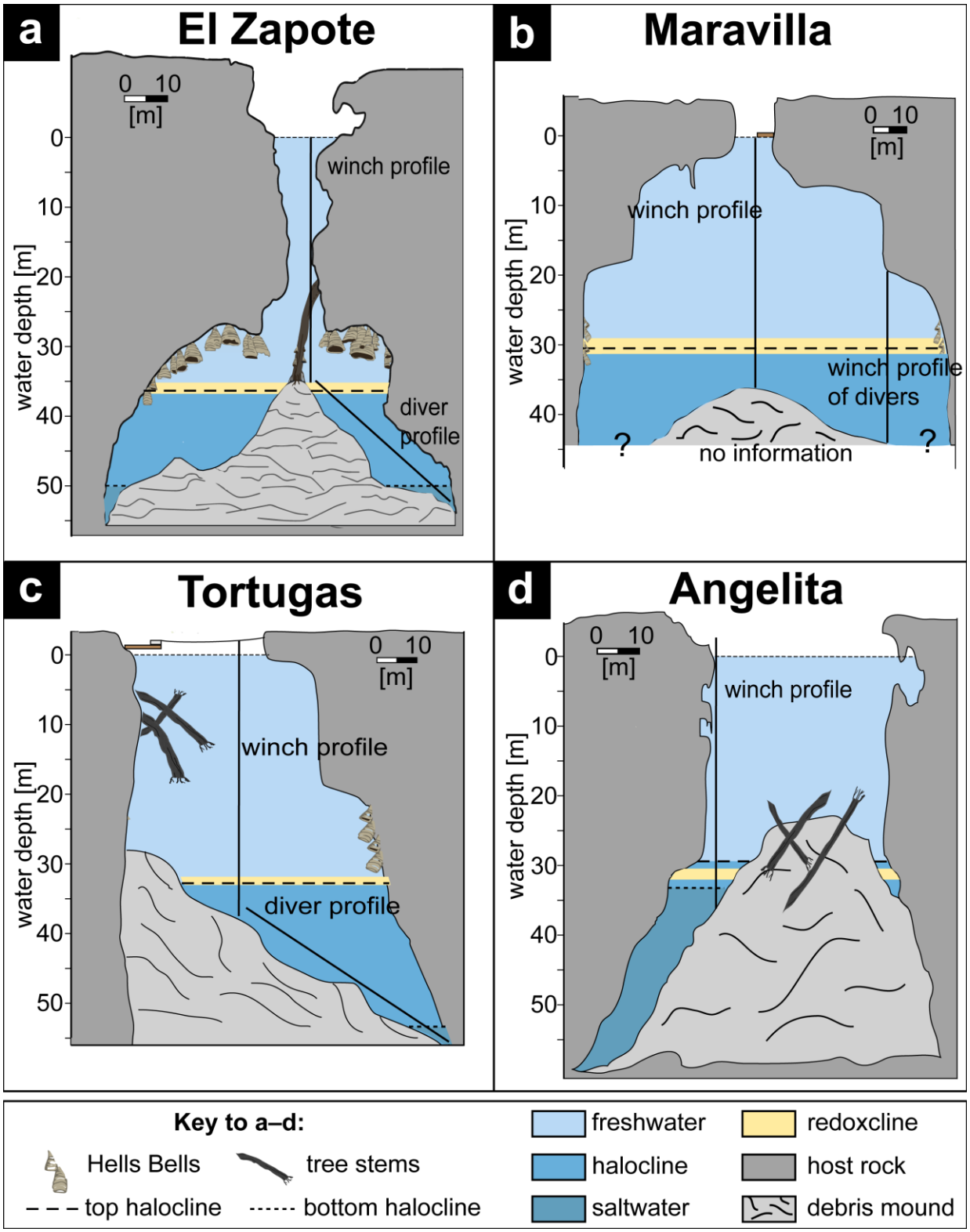

Fig. 6: Schematic cross-sections of the studied cenotes with morphological and hydrological characteristics (A–D). Sketches of cenotes El Zapote and Angelita were taken and modified from Stinnesbeck et al. (2017a) and from the sketch at cenote Angelita produced by Octavio del Rio (undated), respectively. Sketches of Tortugas and Maravilla were produced on the basis of drawings of technical diver Dirk Penzel. Winch profiles and diver profiles indicate the sampling and measuring method for the respective water depths. The hydrological features were determined from the in-situ measurements (section 4.1.2.1, p.45).

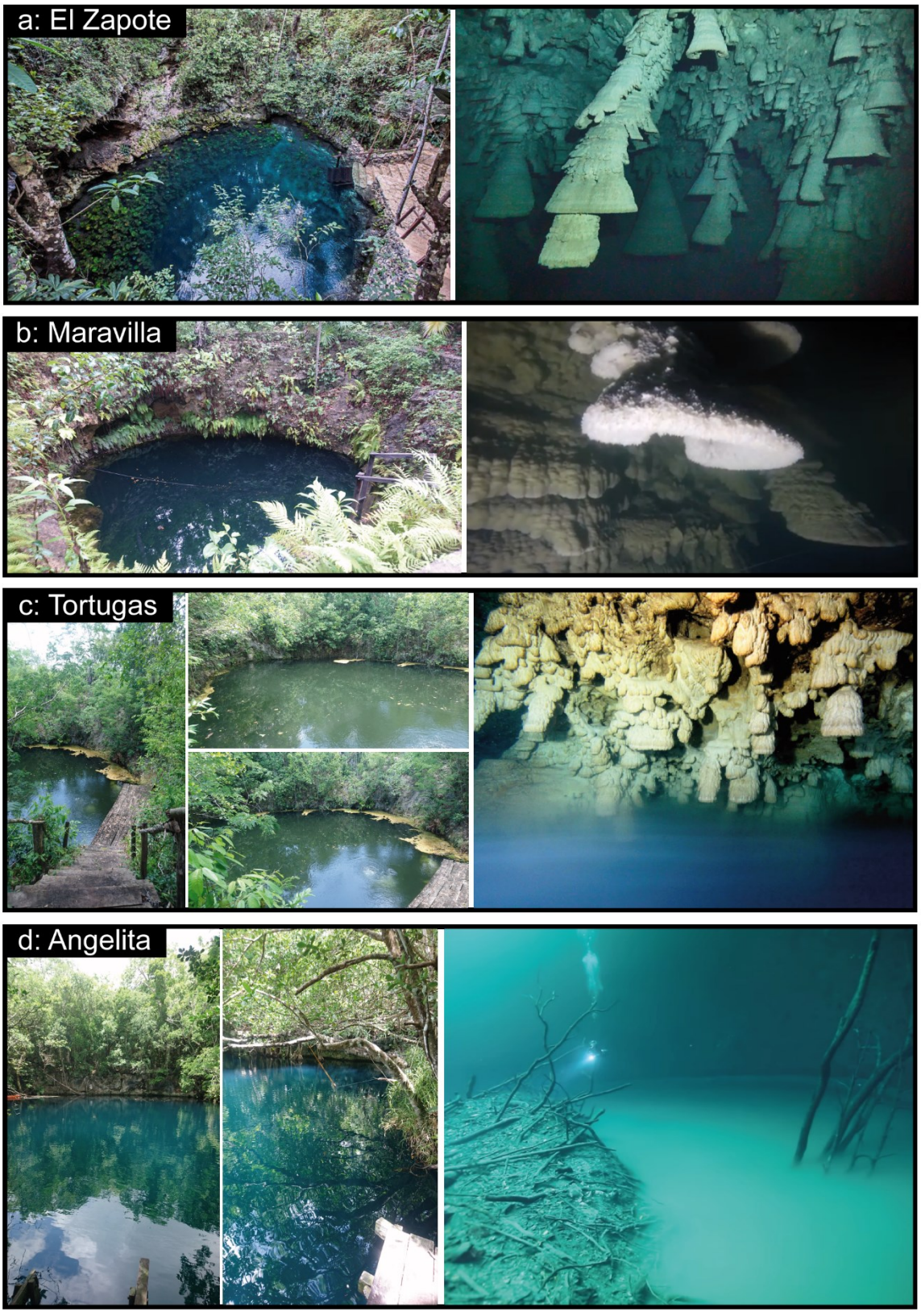

Fig. 7: Pictures of the water surfaces and subaquatic pictures of the studied cenotes in water depths immediately above the halocline. Hells Bells are present in cenotes El Zapote (a), Maravilla (b) and Tortugas (c) while cenote Angelita (d) is devoid of Hells Bells. Underwater imagery: Thomas Vogt (a), Dirk Penzel (b), Jerónimo Avilés Olguín (c) and Anatoly Beloshchin (d).

3.1.2 Cenote Maravilla

The cenote Maravilla (Fig. 7b) is located about 16 km west of the coast of Puerto Morelos (20°52'18.9"N 87°01'24.5"W; Fig. 5). In cross-section, cenote Maravilla is similar to cenote El Zapote, as it is also bottle-shaped with a central debris mound (Fig. 6b). Although cenote Maravilla has not been surveyed in detail yet, it can be shown that some features of cenote Maravilla clearly differ from those of cenote El Zapote. According to reports of the technical divers the narrow ~8 m wide shaft opens already in ~5 m water depth to a ~100 m wide circular cavern, which appears to be much larger than that of cenote El Zapote. They also reported two steps in the cavern opening, one in about 5 m water depth and one in around between 19–22 m water depth (Fig. 6b). The top of the debris mound was reached at ~38 m depth with the winch profile in the center of the cenote and in around 44 m water depth by the winch profile of the divers at the flank of the cenote (Fig. 6b). There is no further information about the total depth of cenote Maravilla. Hells Bells appear in water depths from ~29 m to at least 32 m (Fig. 6b). The cenote is not publicly accessible but open for pre-announced tourist diving groups. Thus, the diving activity in this cenote is likely less than in cenote El Zapote.

3.1.3. Cenote Tortugas

Cenote Tortugas (Fig. 7c) is located 24 km west of Puerto Morelos coast and about 2 km east of cenote El Zapote (20°51'11.7"N 87°06'30.1"W; Fig. 5). So far, the cenote is not surveyed in detail and the features described here are based on the observations of the cooperating technical divers. The cenote shows a large cenote circular opening of about 25–35 m diameter and is slightly asymmetric in cross-section (Fig. 6c). The debris mound lies against the wall of one side of the cenote, the top of the debris mound is at around 25 m water depth and dips towards the opposite cenote wall to a maximum water depth of around 60 m (Fig. 6c). Divers reported various tree trunks on the side and the debris mound of the cenote. The cenote shows a step-like widening in 15–20 m water depth (Fig. 6c). Hells Bells appear in water depths from 25–35 m (see also Stinnesbeck et

al., 2017b). The cenote is neither publicly accessible nor used by tourist diving groups and therefore, diving activities at this cenote are rare.

3.1.4 Cenote Angelita

Cenote Angelita (Fig. 7d) is located approximately 12 km off the coast south-west of Tulum (20°08'15.2"N 87°34'41.1"W; Fig. 5). The morphology of the cenote is well surveyed and the its hydrogeochemistry was studied before (Gulley et al., 2016; Stoessell, 1995; Stoessell et al., 1993, 2002). In cross-section the cenote also reveals a bottle-like shape with a very wide "bottle-neck" or opening of the cenote of around 30 m in diameter (Fig. 6d). In around 30 m water depth (depth of the halocline) the cenote slightly opens up indicated by inclined cenote walls to a maximum water depth of around 60 m (Fig. 6d). The large debris mound is almost at the center of the cenote and covered by several tree trunks. The cenote is publicly accessible and, due to the spectacular turbid layer, highly frequented by many tourist diving groups. No Hells Bells or other unusual formations have been reported to occur in this cenote. Therefore, this deep stratified cenote was chosen to study the conditions for cenotes devoid of Hells Bells in order to infer the conditions for Hells Bells formation.

3.2 Sampling Techniques

3.2.1 Water sampling

Sampling at cenote El Zapote was first carried out between December 10th and 15th 2017. A short video giving impressions of this sampling campaign can be accessed via the TIB AV-Portal (Ritter, 2018: "Hells Bells – Underwater speleothems from the Yucatán Peninsula"). Cenote El Zapote was sampled again in 2018 together with cenotes Tortugas, Maravilla and Angelita between May 29th and June 12th. With exception of cenote Angelita, all samples were taken in the morning prior to any diving activity. Water sample recovery and the recording of the in-situ parameters were carried out with a winch (Fig. 8g) from the surface down to the cenote floor or the debris mound of the cenotes. At cenotes El Zapote and Tortugas the water sampling and in-situ parameter profiles were then completed by technical divers from the top of the debris mound down to

the cenote floor following the slope of the debris mound (Fig. 8a). The performed profiles at each cenote are specified in Figure 21 and section 4.1.2.1 (p.45).

3.2.2 In-Situ Parameters (EXO-1 Probe)

In-situ parameters pH (± 0.1), EH (± 20 mV), dissolved oxygen (± 0.1 mg l^{-1}, detection limit 0.1 mg/l), electrical conductivity (± 0.05 % of value), temperature (± 0.01 °C) and turbidity (± 2 % of value) were determined with a multiparameter water sonde EXO-1 (Xylem Analytics, Norway) (Table A1). All parameters, including water depth via pressure measurement were internally logged by the sonde (± 0.04 m). Water depths were corrected to the ambient air pressure of the respective day of sampling and the increasing salinity. Detailed information on the correction of water depth with respect to increasing salinity in the halocline is given in the Appendix section 8.2 (p. 147). The measured redox potentials (Ag/Ag^+ electrode) were corrected to EH values by adding +210 mV to the measured values.

At all cenotes multiple winch-operated profiles of in-situ parameters were conducted from the surface to the top of the debris mound. At cenote Maravilla an underwater vertical winch-operated profile of in-situ parameters was conducted by technical divers at water depths between ca. 25–43 m (Fig. 8f). The measurement of the water column of the cenotes were completed by technical divers, who carried the EXO-1 sonde with them during sampling at cenotes Zapote and Tortugas (Fig. 8a). The EXO-1 sonde was attached to a side mounted compressed air bottle pointing towards the front of the technical diver in order to record the in-situ parameters of each water sample (Fig. 8a). In the sampling campaign 2017, a shift of pH of up to 0.2 pH units towards higher values was observed when comparing the pH logs of the way down with the pH logs of the way up (Fig. 9). This was due to interaction of sulfide with the Ag/Ag^+ pH electrode and increasing sulfide concentrations in water depths below the turbid layer. This shift is dependent on the exposure time of the electrode and the respective sulfide concentrations and could neither be quantified nor corrected. However, the sensor recovers to initial pH values after a certain time in non- sulfidic water (Fig. 9).

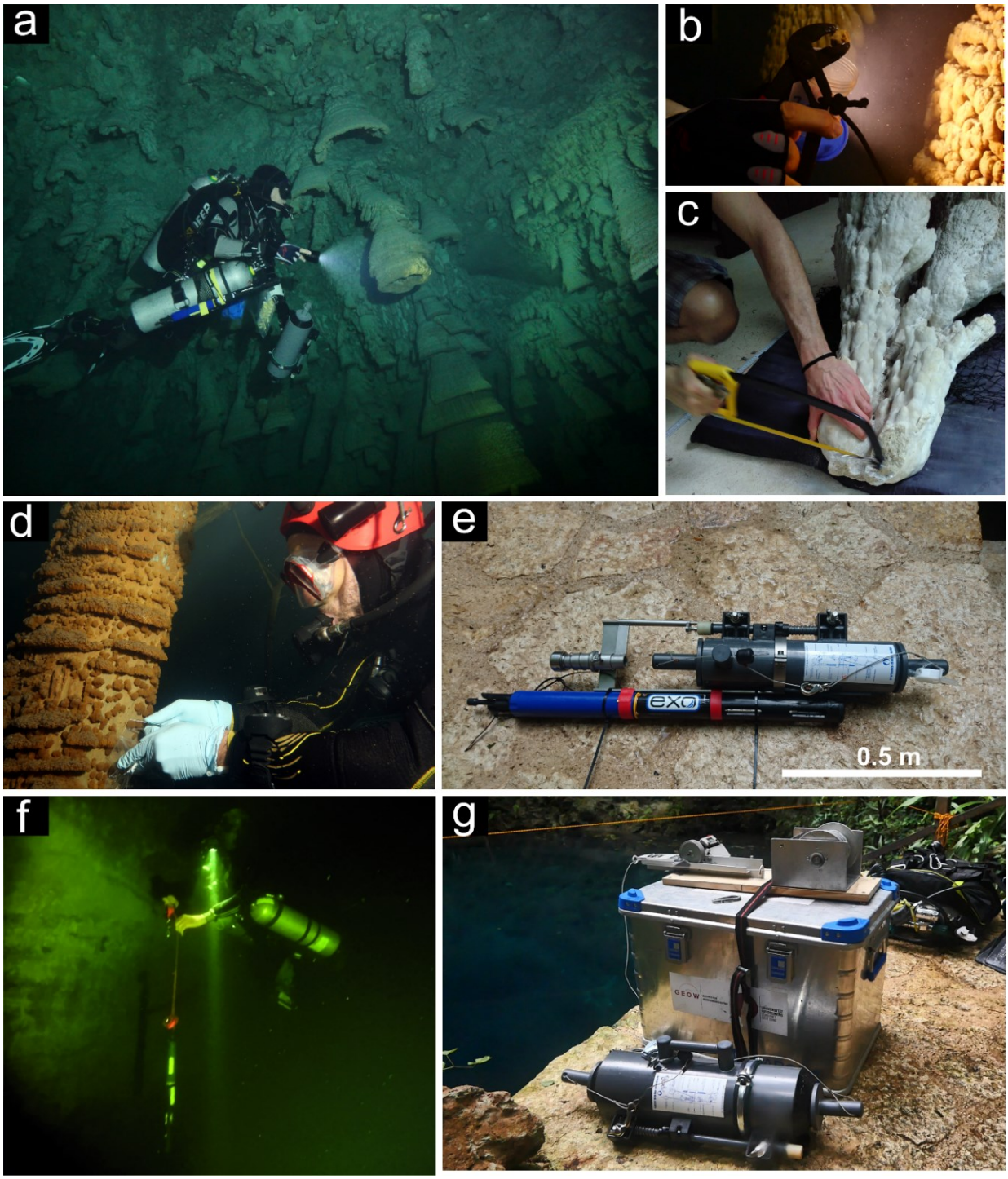

Fig. 8: Different sampling techniques used at cenote El Zapote. (a): Technical diver carries the EXO-1 probe attached to side-mounted gas tank, the 5 l Niskin bottle and further sampling equipment. (b): Close-up of underwater Hells Bells sampling with a plyer. (c) Sampling the "root" of the ~2m long Hells Bells specimen "Big Bell" at the visitor's center of El Zapote ecopark. (d) Technical diver samples the "baby bells" that grew on the tree stem. (e) Water sampling device, FreeFlow bottle (1 L), with EXO-1 Sonde attached for determination of in-situ parameters and exact water depth of each water sample. (f) Technical diver conducting an underwater EXO-1 profile from ~40 m down to ~54 m water depth at cenote El Zapote. (g) Winch mounted on top of a transport box with Niskin bottle attached on the 0.6 mm steel wire.

Therefore, the pH values presented in this study are representative for the water column from 0 to 37 m water depth and are overestimated in water depths from 37–50 m where the actual absolute pH values are most likely lower than those measured by the sonde, i.e. more acidic. Re-

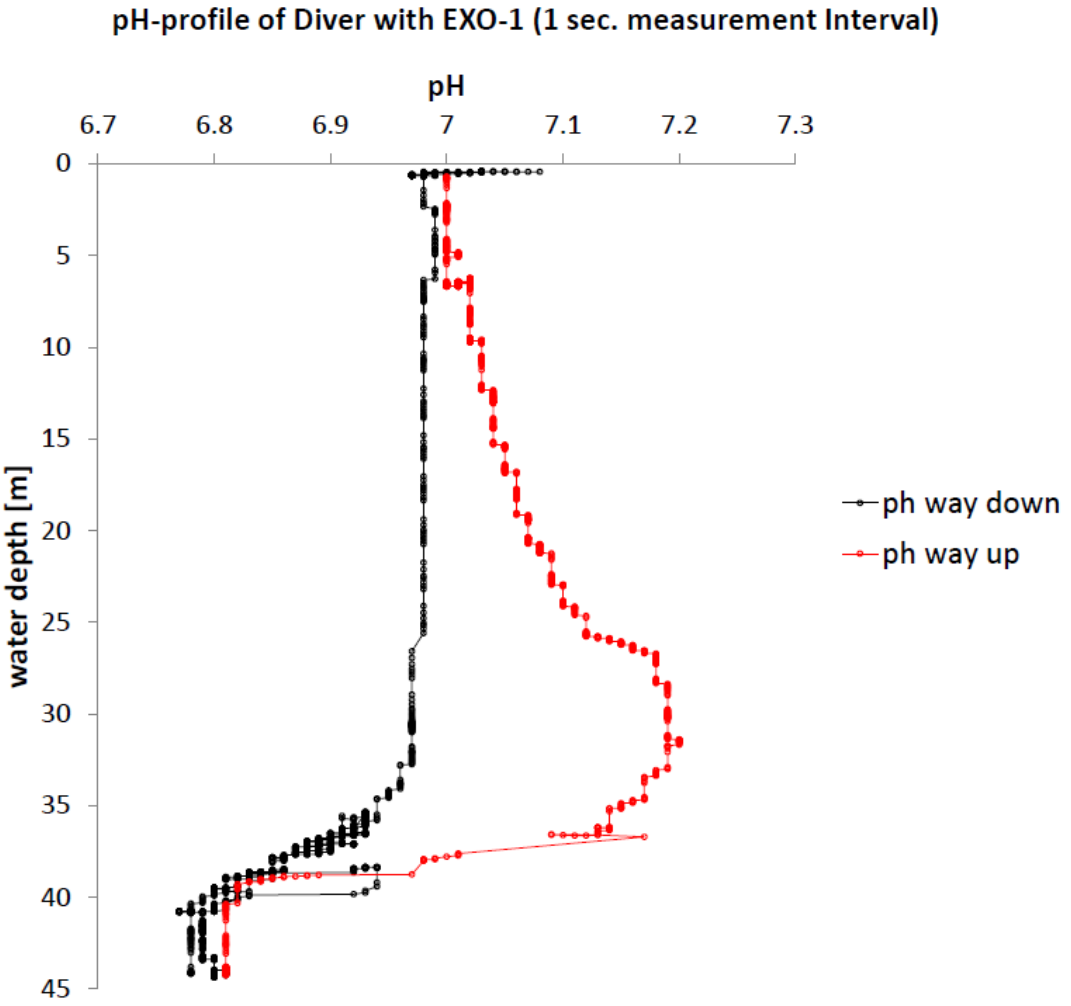

Fig. 9: pH-logs of EXO-1 probe deployed at a dive down to 45 m water depth. The probe was attached to the gas bottle of a technical diver and pH was logged every second. The pH-electrode reacted on elevated sulfide concentrations below 36 m water depth resulting in higher pH readings. This is evident in the pH readings on the way up that are elevated compared the readings on the way down. The probe seems to regenerate itself in some time after the exposure to sulfidic waters.

peated measurement with a new sonde of the same type during the sampling campaign in June 2018 confirmed this assumption and showed lower pH values below 37 m water depth (Fig. 21 and section 4.1.2.2, p. 50). In the sampling campaign 2018 the pH sensor was regularly calibrated and regenerated in dilute ~1 M HCl to avoid alteration due to exposure to sulfidic waters in the cenotes.

3.2.3 Water sampling and sample treatment in the sampling campaign 2017

The water sample collection and water sample treatment slightly differed in sampling campaigns 2017 and 2018. In 2017, winch-operated water samples were retrieved with a 5 l and 0.6 m high Polyethylene (PE) Niskin bottle (HydroBios Kiel) from 0–36 m water depth (Fig. 8g). The sampling depths of samples taken with the sampling bottle represent the center of the sampling bottle and were determined by the cable length with a depth counter attached to the winch. Water samples from 35.2–45 m water depth were retrieved by technical divers and were collected with 120 ml PE-containers. The containers were carried open and water-filled by the divers. At the desired sample depth, the water in the containers was exchanged by surrounding water via shaky motions, sealed underwater and the water depth was noted for each sample. Water samples for the analysis of dissolved gases (CO_2, CH_4) were taken in 24 ml glass vials and sealed underwater at the respective depth (four samples at each depth level). Water samples were treated on-site immediately after the water samples were retrieved. Samples for determination of dissolved ions were taken with 20 ml sterile polypropylene (PP) syringes and then filtered through a cellulose acetate filter (0.45 µm). Samples for cation determination were acidified with 50 µl of 65 % analytical grade HNO_3 (A.G.) to adjust a pH <2. They were stored in 15 ml Falcon PP-centrifuge tubes. Samples for anion determination were taken equivalent, but not acidified, and stored cool in 15 ml Falcon PP-centrifuge tubes. Samples for the determination of dissolved inorganic carbon (DIC) and dissolved organic carbon (DOC) were filtered through a cellulose acetate filter (0.45 µm), stored in 24 ml glass vials and sealed gas-tight. Samples for the determination of content and isotopic ratios of the dissolved gases CH_4 and CO_2 were filled in 24 ml glass vials. Subsequently, 100 µl 60 % $HgCl_2$ solution was added via a syringe pierced through the septum to sterilize the samples.

Additionally, in 2017, a large volume sample (5 l) of the turbid layer water at around 36 m water depth was taken with a Niskin bottle by technical divers and subsequently filtered through a 0.45 µm cellulose acetate filter with a vacuum pump. The filter was air-dried; back in the laboratory a

small piece of the filter was coated with carbon for subsequent secondary electron (SE) imaging and analyses.

3.2.4 Water sampling and sample treatment in the sampling campaign 2018

At cenote Zapote water samples between 0–36 m were taken with the 0.5 m high Polyetehylene FreeFlow bottle (HydroBios Kiel) and samples between 36–52 m were taken by technical divers. At cenotes Maravilla (0–38 m) and Angelita (27–36 m) all samples were taken using the FreeFlow bottle. The EXO-1 sonde was attached to the FreeFlow bottle to obtain the related in-situ parameters and the exact depth of each water sample (Fig. 8e).

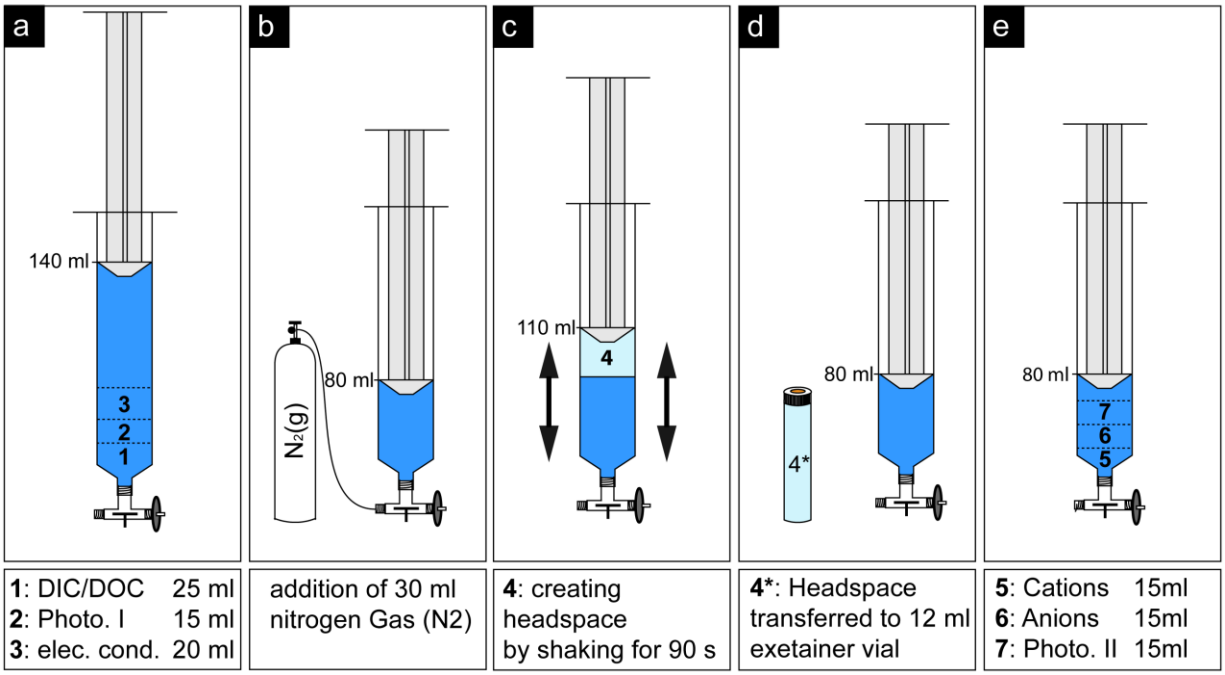

Fig. 10: Scheme showing the procedure of taking subsamples from the 140 ml samples syringes (modified from Klose, 2018, unpub.).

Water samples taken by technical divers were collected by drawing up the water of the desired sampling depth into 140 ml sterile PE-luer-lock syringes with an attached three-way valve (Fig. 10). The water depth and in-situ parameters of samples taken by technical divers were determined with the EXO-1 sonde, which was attached to a side mounted gas bottle and pointed towards the front (Fig. 8 and Fig. 10a).

Additionally, technical divers collected water samples in cenotes Zapote and Tortugas in water depths that could not be reached with the winch-operated sampling bottles from the surface (Fig.

6a and d, p. 14). At cenote Tortugas (5–55 m) all water samples were taken by technical divers. The depth of the water samples taken by technical divers was corrected to the depth of the attached logging device (EXO-1). For samples between 35 and 38 m at cenote El Zapote, the exact water depth of the sample was interpreted from the increase of sodium and chloride contents correlated to the electrical conductivity in this interval.

All water samples were treated on-site immediately after retrieval. Water samples taken with the FreeFlow bottle were transferred into 140 ml sterile PE-luer-lok syringes with an attached three-way valve. From the sampling volume of 140 ml, subsamples for the determination of dissolved organic carbon (DOC) and dissolved inorganic carbon (DIC), cations, anions, on-site photometric analyses and dissolved gases were taken. Samples of dissolved gases were taken according to the headspace method (Hartmann et al., 2018 and Kampbell et al., 1989). This holistic sampling approach should ensure that all subsamples and respective parameters represent the same water depth. The procedure and the sequence of sampling are shown in Figure 10. First, 25 ml for determination of DIC and DOC and 15 ml for subsequent photometric analysis of sulfide were filtered through a cellulose acetate filter (0.22 µm mesh size) into a 24 ml glass vial and sealed gas-tight and into a 15 ml Falcon PP-centrifuge tube, respectively. Subsequently, ~20 ml of sample was transferred into a 50 ml Falcon PP-centrifuge tube used to determine electrical conductivity on-site via a WTW LF330 and 15 ml were filtered and filled into centrifuge tubes for subsequent photometric determination of sulfide (Fig. 10a). Then, 30 ml of N_2-Gas (99.999 %) was added into the sample syringe to the remaining 80 ml of water sample via the three-way valve, using a 50 ml sterile PP-luer-lok syringe (Fig. 10b). This water-gas mixture was then shaken vigorously for 90 seconds (Fig. 10c). After that, the gas phase in the sample syringe was transferred into an evacuated 12 ml exetainer vial through the septum using a sterile PP-luer-lock syringe with an attached cannula (Fig. 10d). After this, samples for the determination of dissolved ions and for subsequent photometric analyses of ammonium and nitrite were filtered through a cellulose acetate filter (0.22 µm) and transferred

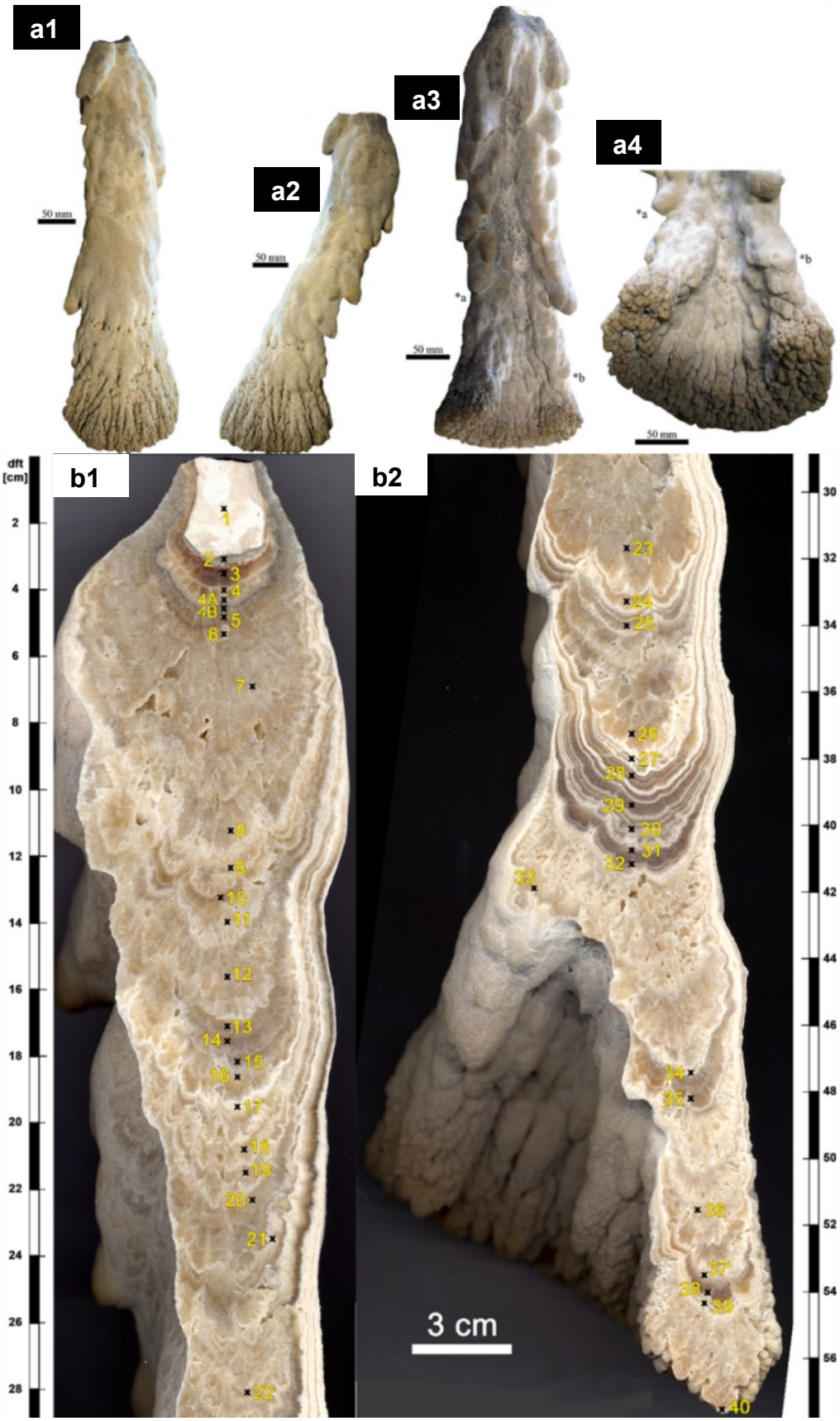

Fig. 11: Different views of the 57 cm long Hells Bell specimen "Long Bell" (named ZPT-7 by Stinnesbeck et al., 2017b). a1: frontal view, a2: lateral view, a3: interior view, a4: diagonal view from below (Stinnesbeck et al., 2017b). Scan of the polished half of the vertically cut "Long Bell" showing 42 sample spots of the upper (b1) and lower (b2) part of which an approximate amount of 100 mg each were drilled for subsequent analysis.

into 15 ml Falcon PP-centrifuge tubes (Fig. 10e). Samples for cation determination were acidified with 150 µl HNO_3 (32 %) to adjust a pH < 2.

3.2.5 Hells Bells samples

Several Hells Bells samples from cenote El Zapote were collected by local divers during field campaigns in November 2015 and May 2016, some of which were already presented and analyzed by Stinnesbeck et al. (2017b). An elongated ~60 cm long specimen called "Long Bell" was also taken during these early campaigns and was intensively studied by master students Tianxiao Sun and Nils Schorndorf who investigated its petrography and (isotope-) geochemistry including U-series age-dating, respectively (Schorndorf, 2018, unpub. and Sun, 2018, unpub.) (Fig. 11).

In the sampling campaign 2017, technical divers collected several Hells Bells that grew on the tree trunk from seven water depth levels between 32.7 and 37.3 m (Fig. 8d and Fig. 12). To obtain the youngest part of individual Hells Bells growth, samples were first studied under the microscope. Only samples with apparently fresh, well accentuated crystal tips were chosen for geochemical analysis and stable isotope analysis (Fig. 12d1). Additionally, several Hells Bells samples of different water depths from Hells Bells

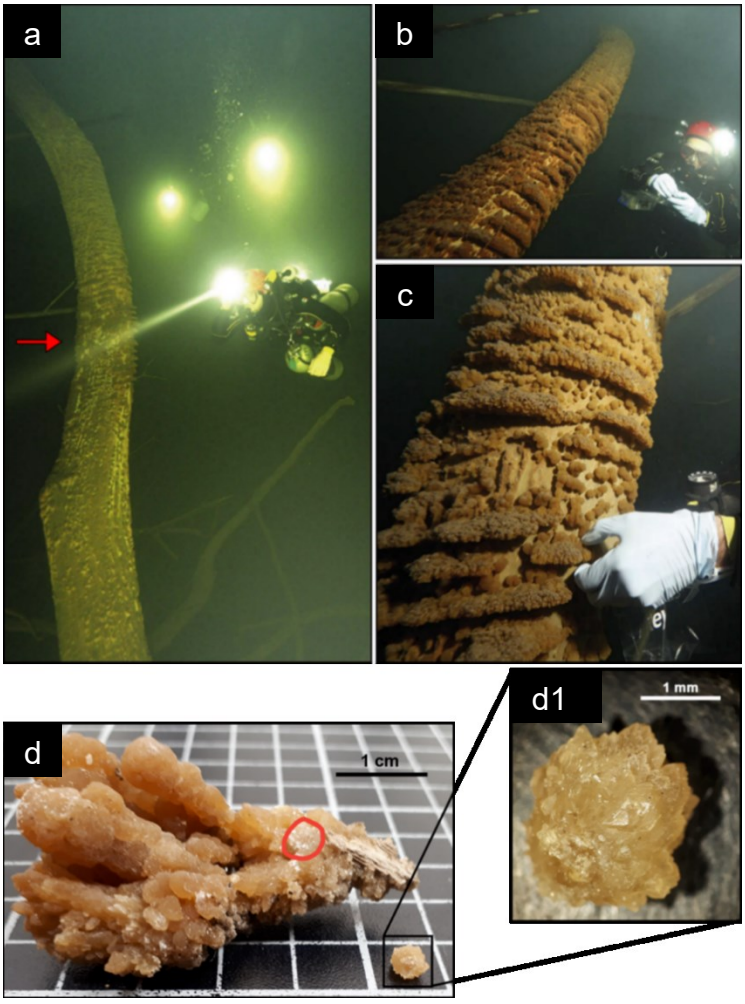

Fig. 12: Sub-fossil stem of a drowned Ceiba tree (Ceiba pentandra) from El Zapote (a); underwater photograph. Red arrow points to an interval on the stem with dense coverage of small lime nodules and horizontal lime protrusions at a water depth of about 32 to 33 m. Details of these Hells Bells are given in (b) and (c). Well-accentuated crystal tips of Tree Bells chosen for analysis (d and d1). Image a, b and c are taken from (Stinnesbeck et al., 2018) and images d and d1 are taken from Schorndorf (2018, unpub.).

hanging from the ceiling and the walls of cenote El Zapote were taken by technical divers (Fig. 8b). A large Hells Bells specimen of ~1.8 m length was recovered by a group of divers around Vincente Fito in 2017 (Fig. 13a).

The recovery was documented by Armando Gasse and is accessible via YouTube (Gasse, 2017:

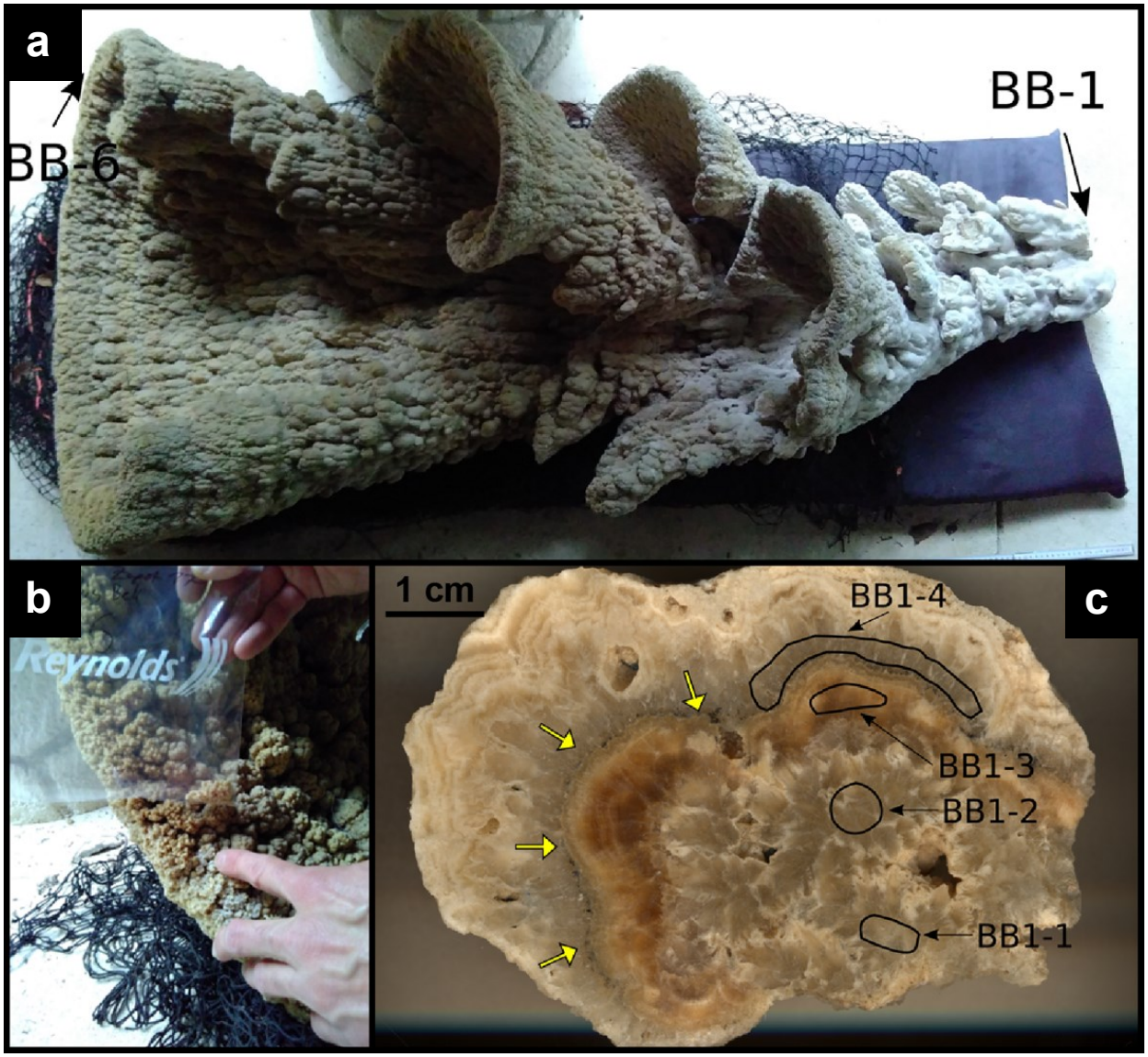

Fig. 13: Large Hells Bell specimen (Big Bell) exhibited in the El Zapote visitors center next to the cenote. a: ~1.8 m long Hells Bells specimen, arrows point to the samples; b: Probably the youngest part of BB; c: Cross-section of the root of BB showing the drilling spots of the sampling. Yellow arrows point to a layer of a FeS_x-phase.

"Extracción campana cenote el Zapote"). This specimen is referred to as “Big Bell”. Samples were taken from the root and from the bottom of this specimen during the sampling campaign in 2017 (Fig. 8c and Fig. 13b and c).

During the sampling campaign 2018 the technical divers collected several small hand-specimen sized Hells Bells samples from the cenotes Tortugas (T6, T7 and T12) and Maravilla (MI, MII and MII).

3.2.6 Hells Bells sample preparation

For geochemical analyses an amount of ~100 mg each was drilled from one half of the vertically cut Hells Bells specimens "Long Bell", TL4, T7, T12, MII and MIII. Drilling was performed with a high speed rotary drilling tool using a stainless steel diamond coated drill bit. The samples of the lowermost well accentuated crystal tips were manually removed and homogenized by grinding in an agate mortar. All samples were stored in 5 ml PE beakers. Subsamples were taken for the subsequent different geochemical analyses.

3.3 Analytical techniques

3.3.1 Water analysis

3.3.1.1 Major and trace element analysis

Cation concentrations (Ca, Mg, Na, K, Ba, Sr, Si, Fe, Mn) of water samples were determined by optical emission spectroscopy with an Agilent 720 (ICP-OES). Quality control was performed by using the reference materials SPS-SW1, SPS-SW2 and TMDA-70.2. Recovery rates were in the range of 94.5 % and 102.4 % for the analyzed elements.

Concentrations of anions Cl^-, SO_4^{2-} and NO_3^- were determined with ion-chromatography (Dionex ICS-1100) with a recovery rate between 95 % and 98 % and a RSD of <3 % derived from long-term repeated analysis of reference material SPS-WW1 NUTR.

The concentrations of DIC and DOC were determined with a Total Carbon Analyzer (Shimadzu TOC-CPH) with a RSD of <2 % derived from repeated analysis of an in-house standard water.

Orthophosphate was determined by the photometric molybdenium phenyl blue method on 880 nm light extinction with an UV/VIS photometer (Specord 50, Analytic Jena).

Sulfide, ammonium (only in sampling campaign 2018) and nitrite were determined on-site within 8 hours after sample collection by photometric analysis using Merck Spectroquant spectrometric methods and a Hach Lange DR200 photometer. For quality control, charge balances of all water samples were calculated. The charge balance errors were below 5 % in all analyzed samples, usually around 1 % in freshwater samples and 1–5 % in saline water samples (Table A2).

3.3.1.2 Analysis of dissolved gases

For the determination of dissolved gases CH_4 and CO_2, the gas samples extracted via the Headspace-Method were analyzed by a gas chromatograph (GC-2010 Plus, Shimadzu Corporation, Kyoto, Japan) coupled to a Barrier Ionization Discharge (BID) detector (BID-2010 Plus, Shimadzu Corporation, Kyoto, Japan). Gas samples were measured as follows: 50 µl of sample was injected in a flow of a 1mL min^{-1} of helium (ALPHAGATM 2) with a split ratio of 5:1 to a Shin Carbon ST column (80/100 mesh, 2m x 0.53mm i.d., Restek Corporation). The GC oven was held at 30 °C for 6.5 minutes and then ramped at 10°C/min to 200°C. Quantification of CH_4 and CO_2 was carried out by comparison of the integrals of the peaks eluting at the same retention time as that of the authentic standard with calibration curves. The dissolved concentrations of CH_4 in the water samples were then calculated from the measured mixing ratio using Henry's law (Wiesenburg and Guinasso, 1979) and solubility coefficients for CH_4 according to Weiss (1974).

3.3.1.3 Stable carbon isotope analysis

Stable carbon isotope ratios of CO_2 ($\delta^{13}C$-CO_2 values) were analyzed by gas chromatography stable isotope ratio mass spectrometry (GC-IRMS) by a HP 6890N gas chromatograph, coupled to a 253 Plus™ isotope ratio mass spectrometer (ThermoQuest Finnigan, Bremen, Germany) with average analytical uncertainties of 0.2‰ for $\delta^{13}C$-CO_2 values. 2 σ uncertainties were derived from five replicates. All $^{13}C/^{12}C$ isotope ratios are expressed in the conventional δ-notation in per mil versus VPDB, defined in equation (1):

$$\delta^{13}C_{V-PDB} = \left[\frac{^{13}C/^{12}C_{sample}}{^{13}C/^{12}C_{standard}} - 1\right] * 1000 \qquad (1)$$

For details of the $\delta^{13}C\text{-}CO_2$ measurements by GC-IRMS the reader is referred to previous studies by Keppler et al. (2010) and Laukenmann et al. (2010). Stable carbon isotope ratios of CH_4 ($\delta^{13}C\text{-}CH_4$ values) were determined (GC-IRMS). In brief, CH_4 of the sample was trapped on Hayesep D and then transferred to the IRMS system (ThermoFinnigan Delta^{plus} XL, Thermo Finnigan, Bremen, Germany). The working reference gas was carbon dioxide of high purity (carbon dioxide 4.5, Messer Griesheim, Frankfurt, Germany) with a known $\delta^{13}C\text{-}CH_4$ value of –23.634 ‰ ± 0.006 ‰ versus V-PDB. All $\delta^{13}C\text{-}CH_4$ values were corrected using two CH_4 working standards (isometric instruments, Victoria, Canada) and normalized by two-scale anchor calibration according to Paul et al. (2007). The average standard deviation of the analytical measurements was in the range of 0.1 to 0.3 ‰.

The $\delta^{13}C\text{-}HCO_3^-$ values were calculated from the measured $\delta^{13}C\text{-}CO_2$ of the headspace of the water samples that was generated in the laboratory as equilibrium fractionation at 23° C ($\delta^{13}C\text{-}CO_2$ + 8.16 ‰ = $\delta^{13}C\text{- }HCO_3^-$) after Mook (2000).

3.3.2 Hells Bells geochemical analysis

3.3.2.1 Element geochemistry

Around 3 mg of the powdered speleothem samples were digested in 2ml 10% HNO_3 for major and trace cation analyses. Subsequently, concentrations of Ca, Mg, Sr, Ba, P, S, Fe and Mn of the aliquots were determined by ICP-OES. Quality control of the measurements was performed using reference materials SPS-SW1 and SPS-SW2 with recovery rates ranging from 99–111 % for the analyzed elements. Quality control for digestion of the carbonate material was performed with limestone reference material ECRM 752-1 with recovery rates between 106–110 % for the elements Ca, Mg, Ba, Sr and Mn and 82 % for the element Fe.

3.3.2.2 U-series dating

Selected powdered samples prepared for geochemical analyses were also used for age-dating. The samples of counter-slabs form thin section preparation of laminated Hells Bells from different cenotes were analyzed at the Institute of Earth Sciences, Mainz University by the Speleothem

Research Group of Prof. Denis Scholz using reported methods for age-dating (e.g. Obert et al., 2018).

3.3.2.3 Stable carbon and oxygen isotopes

For stable carbon and oxygen isotope analyses of carbonates, approximately 50 µg of powdered speleothem subsamples were analyzed using a ThermoFinnigan MAT253Plus gas source mass spectrometer equipped with a Thermo Fisher Scientific Kiel IV Carbonate Device at Heidelberg University. The $\delta^{13}C$ and $\delta^{18}O$ values are reported relative to VPDB (Eq. 1) through the analysis of an in-house standard (Solnhofen limestone) calibrated to IAEA-603. The precision of the $\delta^{13}C$ analyses is better than 0.08 ‰ and 0.06 ‰ (at 1σ level), respectively.

3.3.3 Hells Bells optical analysis

Hells Bells specimen "Long Bell" or ZPT 7, described in Stinnesbeck et al. (2017b) was vertically cut in half and thin sections were prepared from one half of the specimen. The other half was polished and subsequently scanned in order to get a high-resolution image of the structures of this specimen. Additionally, Hells Bells specimens TL4, T7 and T12, as well as MII and MIII from cenotes Zapote, Tortugas and Maravilla, respectively, were cut in half along their presumed growth axis. Subsequently, thin sections were prepared from one half of the samples. The other half of the samples was polished and scanned. Thin section examination and photography of the thin sections were taken with a Keyence VHX-6000.

Polished counterparts of the thin sections and small pieces of the lowermost parts of Hells Bells were coated with carbon for secondary electron (SE) imaging and energy dispersive X-ray (EDX) analyses. SE-imaging and element mapping was performed with a Leo 440 at 20 kV with a X-Max 80 mm^2 detector.

3.4 Aquifer monitoring

3.4.1 Logger installation and data collection

Data loggers were installed at the studied cenotes with Hells Bells El Zapote, Maravilla and Tortugas to monitor the water level and the halocline elevation over a large time period. During the sampling campaign 2017 a suite of 3 data loggers, Baro-Diver, Mini-Diver (TD) and CTD-Diver all by VanEssen Instruments was installed on 17 December 2017 at cenote El Zapote (Table A4). The Baro-Diver logs barometric pressure and temperature and was installed at the El Zapote visitor center (Table A3). The Mini-Diver (VanEssen Instruments) logs temperature and water depth (TD) and was installed by technical divers in the freshwater layer at ~6 m water depth (Fig. 14a). The CTD-Diver (100m) logs conductivity, temperature and depth (CTD) and was installed by technical divers in the halocline at around ~39 m water depth (Fig. 14b). Logging of all data at

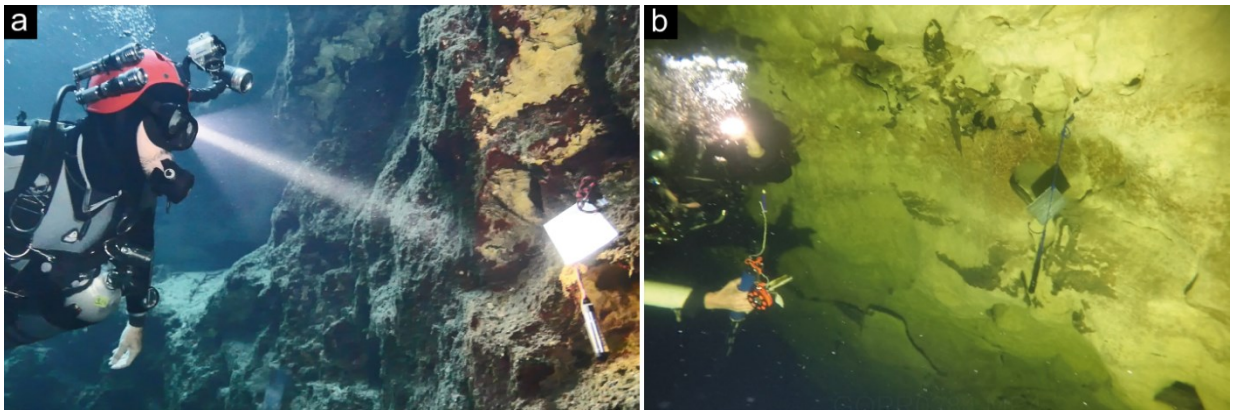

Fig. 14: Underwater pictures of the Mini (TD)-Diver (a) and CTD-Diver (b) loggers installed in the freshwater layer and the halocline at cenote El Zapote on 15 December 2017.

El Zapote loggers started on 15 December 2017 on 11:00 (UTC -5) with a logging interval of 15 min. For data download and functional checks, all loggers were retrieved by technical divers on 20 April, 1 June, 17 December 2018 and on 19 September 2019 (Fig. 15). After data download, the loggers were immediately reinstalled by the technical divers on approximately the same positions as before. Logger recovery, data collection and reinstallation were always conducted within one day. Unfortunately, the CTD-logger failed logging since 29 April 2019 due to full memory (Fig. 15b).

Additional pairs of data loggers (TD and CTD-Diver) were installed by technical divers in the freshwater layer (TD-Diver) in ~6 m water depth and the haloclines (CTD-Diver) in ~35 m water

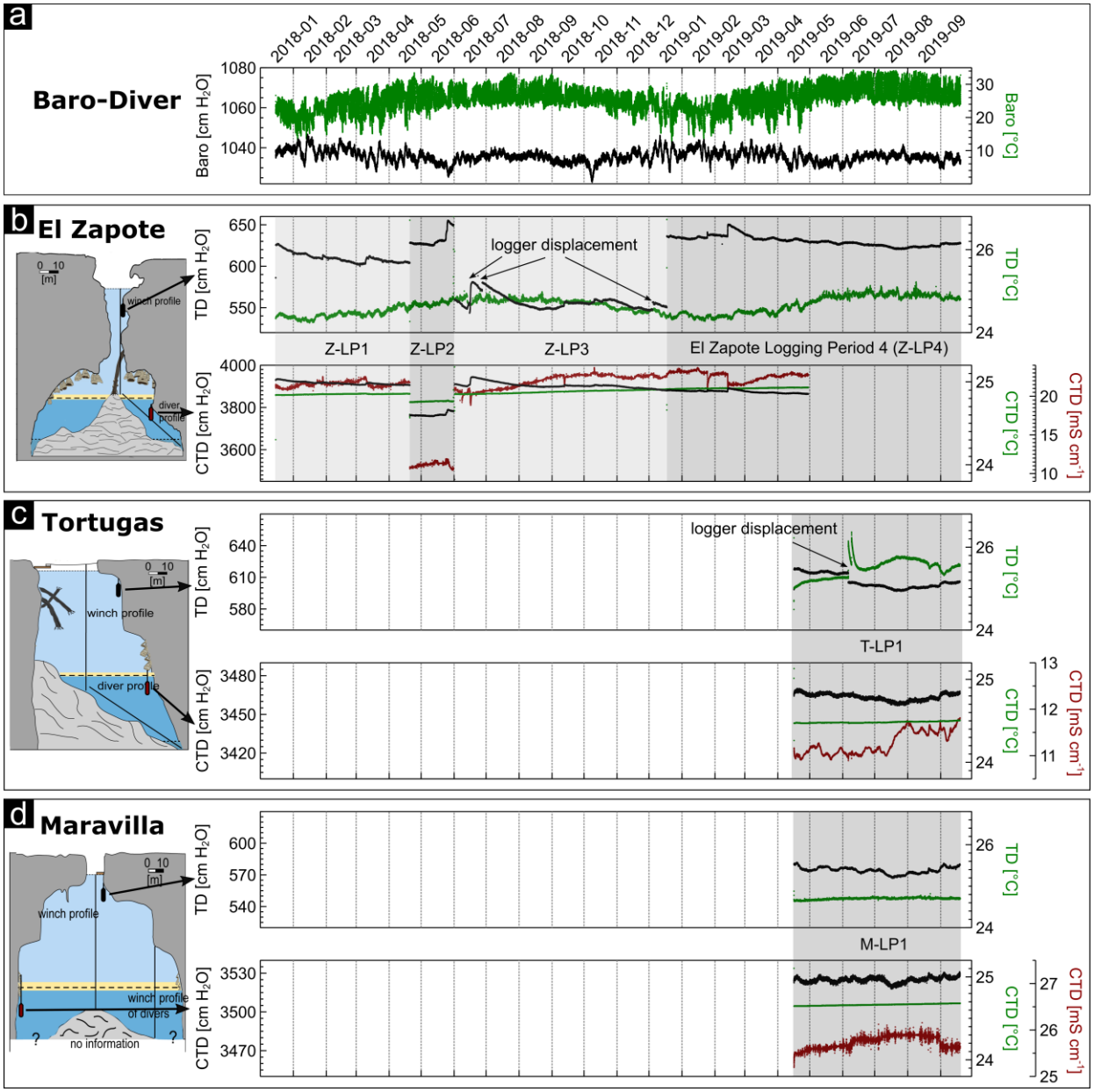

Fig. 15: Time series of raw data of the Baro-Diver installed at the visitor center at cenote El Zapote showing ambient air temperature and pressure (a), TD-Diver and CTD data loggers showing water depth levels, temperatures and electrical conductivities (b, c and d). The relative positions of TD and CTD loggers is indicated in cenotes El Zapote (b), Tortugas (c) and Maravilla (d). Recovery, data collection and re-installation by the technical divers is indicated by grey-underlined logging periods (e.g. Z-LP1 meaning "Zapote logging period one"). The logging periods are usually marked by an abrupt change in the data series, because the loggers were not re-installed at the exact same position, e.g. water depth as before. Additionally, several data leaps appear within the time series of cenote El Zapote that result from random displacements of the shallow data loggers at ~6 m water depth by unknown divers and the subsequent re-mounting of the data loggers by the cooperating technical divers during check-dives. The logger displacement at cenote Tortugas was due to fixing the mounting of the data logger by the cooperating technical divers.

depth at cenotes Tortugas and Maravilla both on 16 April 2019 (Fig. 15 and Tables A5 and A6). The loggers and data were recovered once in both cenotes on 24 September 2019 at Tortugas and on 19 September 2019 at Maravilla (Fig. 15). After data download, the loggers were immediately reinstalled by technical divers on the same days of recovery.

The preliminary results of the logging period from 15 December 2017 until the date of the last logger recovery on 24 September 2019 will be evaluated in this thesis (Fig. 15).

3.4.2 Logger data preparation and evaluation

The collected data of the data loggers installed at the cenotes had to be properly prepared in order to evaluate the data for an interpretation of the aquifer dynamics. First, to gain water depth level changes from the TD and CTD data loggers, the pressure data of these loggers was compensated for changes of the barometric pressure by subtraction of the barometric pressure data (Baro-Diver) from the water depth pressure data of the TD and CTD loggers. In order to create a coherent and comparable time series of all depth level logger data, the deviation of all the depth level data with respect to 17 April 2019 at 0:00 h (UTC -5). Several data leaps occur in the time series due to the regular recovery, data collection and re-installation of the data loggers during the logging periods as well as random logger displacements of the shallow data loggers (Fig. 15b and c). These data leaps were leveled by adding up the difference of the water level depth before and after the short-termed displacement, which had short durations of <1 d for the data collection related data leaps and <0.5 h for the random displacement related data leaps (Fig. 15b and c). The relative deviation of the water level was always calculated from the pressure values of the shallow Mini (TD)-divers. Depth level changes of the halocline were approached by translating the conductivity values of the CTD data loggers installed in the halocline into relative depth deviations assuming linear increasing conductivity with water depth. Linear fit values of 6.40, 2.73 and 5.49 mS cm^{-1} m^{-1} (Fig. 25, p. 55 and Table 2, p.54) were used for the translation of conductivity values into relative deviations of the halocline depth level. The relative deviation of the freshwater layer was calculated by subtraction of the water level deviation from the halocline depth level.

Maximum and Minimum tide elevations at Puerto Morelos were predicted with the program "Programa MAR V1.0" provided by CICESE, the "Centro de Investigación Científica y de Educación Superior de Ensenada, Baja California", Mexico.

3.5 Evaluation methods

3.5.1 Definition of halocline and redoxcline

Within the physically and chemically stratified water column of the cenotes. the electrical conductivity increases in distinct parts of the water column, the halocline. In order compare the haloclines of different cenotes efficiently, a uniform definition of halocline boundaries (top and basis of the halocline) has to be obtained. The top of the halocline is defined at the water depth where EC ≥3.5 mS cm^{-1} and the basis of the halocline at the water depth, where EC ≥50 mS cm^{-1}. The top of the redoxcline is clearly defined in all cenotes at the depth, where EH values show an abrupt shift to lower values. The lower boundary of the redoxcline is visually identified at the depth, where EH values stabilized at low values with only small changes in consecutive values (<20 mV).

3.5.2 Correction of water depths

The multiparameter water sonde EXO-1 (Xylem Analytics, Norway) has an integrated pressure sensor, which expresses the water depth according to Pascal's law and calculates water density from the measured electrical conductivity and temperature. Due to the density stratification of the cenotes, water depths of samples below the top of the halocline had to be corrected via a numerical approach. Sample depth had to be corrected by up to 1–2 m for the deepest samples taken. Details of the method used for correcting the water depth are given in the Appendix section 8.2 (p. 147). Note that this correction of water depth was only conducted for the sampling campaign 2018. The exact depth of the water samples taken by technical divers was determined by comparison of the EXO-1 electrical conductivity profile with the measured electrical conductivities of the samples.

3.5.3 Hydrogeochemical calculations

Calcite saturation as well as HS^- and HCO_3^- activities were calculated with PhreeqC version 3.5.0 (Parkhurst and Appelo, 1999) using phreeqc.dat.

Diffusive ion fluxes within the water column (J) were calculated with the first Fick´s law with diffusion coefficients of D_{O2}, D_{NO3-}, D_{HCO3-} and D_{HS-} of 2.1, 1.9, 1.2 and 1.8 10^{-9} m^{-2} s^{-1}, respectively taken from phreeqc.dat (Parkhurst and Appelo, 1999).

3.6 Data storage and availability

The data for geochemical and age-dating analyses of Hells Bells are tabulated within this thesis (section 4.3, p. 64). The in-situ parameters (EXO-1), the hydrogeochemical data and the stable carbon isotope analyses of dissolved CO_2 and CH_4 of the sampling campaign at cenote El Zapote in December 2017 is tabulated in Tables S1, S2 and S3, respectively, in the supplement of Ritter et al. (2019). The data of the hydrogeochemical analyses and the in-situ (EXO-1) parameters of the sampling campaign in May/June 2018, as well as the data of the aquifer monitoring of the cenotes is tabulated in Tables A1–A6 and stored in HeiDATA, an institutional repository for research data of the Heidelberg University (Ritter, 2019, "Unravelling the formation of Hells Bells: underwater speleothems from the Yucatán Peninsula [Data]") The data is available online under the persistent digital object identifier https://doi.org/10.11588/data/TMYLWS.

4. Results

This chapter comprises the results obtained with the different research approaches of studying Hells Bells. The water analyses of the two sampling campaigns in December 2017 at cenote El Zapote and in May/June 2018 at cenotes El Zapote, Maravilla, Tortugas and Angelita are presented at first. This is followed by elaborating petrographic characteristics and presenting the geochemical and age-dating analyses of several Hells Bells species of the different cenotes. This chapter is then concluded with the results of the aquifer monitoring at the different cenotes.

4.1 Water analyses

4.1.1 Water sampling in December 2017

4.1.1.1 Hydrogeochemistry

The water column of the cenote El Zapote is stratified into an oxygenated freshwater body overlying an anoxic transition zone of increasing electrical conductivity (EC), the halocline, and an anoxic saltwater body below (Fig. 16a). Water temperatures vary little between 0 to 30 m water depth (24.37–24.42 °C); a steep increase is identified in a narrow zone from 30–32 m water depth (24.42–24.55 °C), followed by constantly increasing temperatures from 32 m water depth (24.55 °C) down to the bottom of the cenote (25.22°C) (Fig. 16a and b). A distinct density boundary, the top of the halocline, is identified at 36.6 m water depth by a steep increase in EC. Seawater-like salinity is reached at around 46 m water depth indicating a thick halocline layer of around 10 m thickness (Fig. 16a and b). Low turbidity readings indicate clear water throughout the water column, except for a ~1.6 m thick layer of increased turbidity immediately above the halocline from 35.0–36.6 m water depth, with a peak of 8.0 FNU detected at 35.8 m water depth (Fig. 16a and b; Table S1 in Ritter et al., 2019). This turbid layer is also easily detected macroscopically in the water column as a white cloudy layer (Fig. 2b, p. 7) and coincides with a distinct redoxcline from ~35–37 m water depth, in which the redox potential (EH) decreases from ~250 to ~140 mV (Fig. 16a and b).

Dissolved oxygen (DO) decreases nearly linear from around 125 µmol l^{-1} at 30 m to concentrations below detection limit (<0.03 µmol l^{-1}) at ~35 m water depth just above the turbid layer. Below, DO was below detection limit (Fig. 16a and b). The pH shows neutral values from 0–30 m

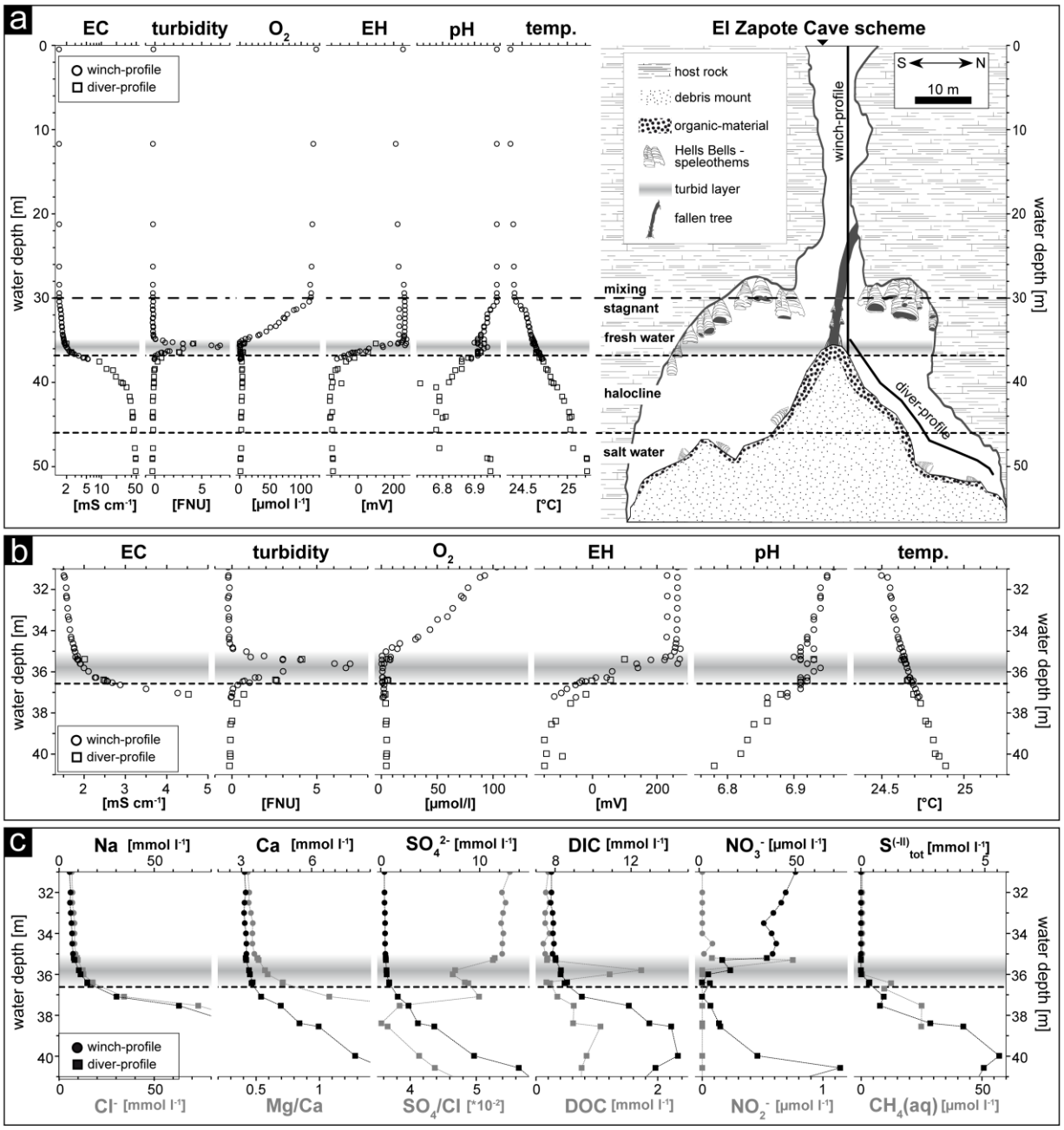

Fig. 16: Hydrogeochemistry of the water column of cenote El Zapote (December 2017). The horizontal grey band indicates the depth position of the turbid layer, while the dashed line indicates the top of the halocline at 36.6 m water depth. a: Water in-situ parameters versus water depth (left) in relation to the cenote El Zapote cross-section (right). In-situ parameters and samples were taken along a winch profile and a diver profile as shown in the cenote cross-section. Note the logarithmic scale of the electrical conductivity (EC). b: Close-up of the water in-situ parameters in 31–41 m water depth. Note that the scale of EC is non-logarithmic and is only shown for the range between 1–5 mS cm^{-1}, in order to point out the increase in salinity at the beginning of the halocline. c: Water chemical parameters determined in the water column between 31–41 m water depth. Na^+ and Cl^- concentrations are only shown in the range of 0–80 mmol l^{-1} to highlight the concentration pattern above and within the halocline.

water depth and slightly decreases to 6.90 at the top of the turbid layer (Fig. 16a). Within the turbid layer pH values increase to more alkaline values of around 6.94 at 35.8 m water depth. The pH values decrease again below the turbid layer to 6.73 at 40 m and invariably remain at about this value down to 48 m. From there, values increase to about neutral (6.95) close to the cenote bottom at 49 m water depth (Fig. 16a and b).

Concentrations of the major dissolved ions Na, Cl^-, Ca, Mg and SO_4^{2-} reflect the stratification of the water column in the cenote, with generally low concentrations in the freshwater body from 0–30 m water depth and slightly increasing concentrations from 30 m water depth to the top of the turbid layer at 35 m water depth, a stronger increase within the turbid layer from 35–36.6 m water depth, and an even stronger increase from the top of the halocline at 36.6 m water depth down to the cenote bottom (Fig. 16c and Table S2 in Ritter et al., 2019). Mg/Ca ratios strongly increase from the top of the turbid layer at 35 m water downwards, due to higher Mg concentrations in the saltwater body (Fig. 16c). Although sulfate concentrations increase downwards from the top of the halocline, a relative decrease of SO_4^{2-} ions is detected, compared to the chemically conservative ion Cl^-, by a decrease in SO_4^{2-}/Cl^- within the turbid layer and below in the halocline (Fig. 16c).

Concentrations of DIC are about 7.8 mmol l^{-1} in the freshwater body. They increase in the turbid layer and show a peak at 40 m water depth with concentrations increasing to 14.5 mmol l^{-1}; below, DIC decreases towards the cenote bottom (Fig. 16c and Table S2 in Ritter et al., 2019). The dissolved organic carbon (DOC) concentrations are low in the freshwater body and show a distinct peak within the turbid layer, coinciding with the peak in turbidity at 35.7 m water depth (Fig. 16c). Below the turbid layer, DOC concentrations slightly increase and peak at 39–40 m water depth, decreasing from there towards the cenote bottom (Fig. 16c and able S2 in Ritter et al., 2019). Nitrate concentrations are ~50 µmol l^{-1} in the freshwater unit of the cenote shaft (Table S2 in Ritter et al., 2019). They decrease from 30 m water depth towards the top of the turbid layer and rapidly fall below detectable concentrations within this layer (Fig. 16c). Nitrite peaks in a narrow zone at the top of the turbid layer with concentrations of up to 0.8 µmol l^{-1} (Fig. 16c).

High total sulfide (S^{-II}) concentrations of up to 5.6 mmol l^{-1} are detected in 40 m water depth. Concentrations decrease upwards, fading in the lower part of the turbid layer at 36 m water depth (Fig. 16c). Below the 40 m depth level, sulfide concentrations decrease to values around 3 mmol l^{-1} down to 45 m water depth (Fig. 16c). Concentrations of dissolved CH_4 (CH_4(aq)) are low in the freshwater body with values of about 0.09 µmol l^{-1}. Methane concentrations increase from the turbid layer at 36 m water depth downwards to values of 25 µmol l^{-1} at 39 m water depth (Fig. 16c).

4.1.1.2 Calcite Saturation

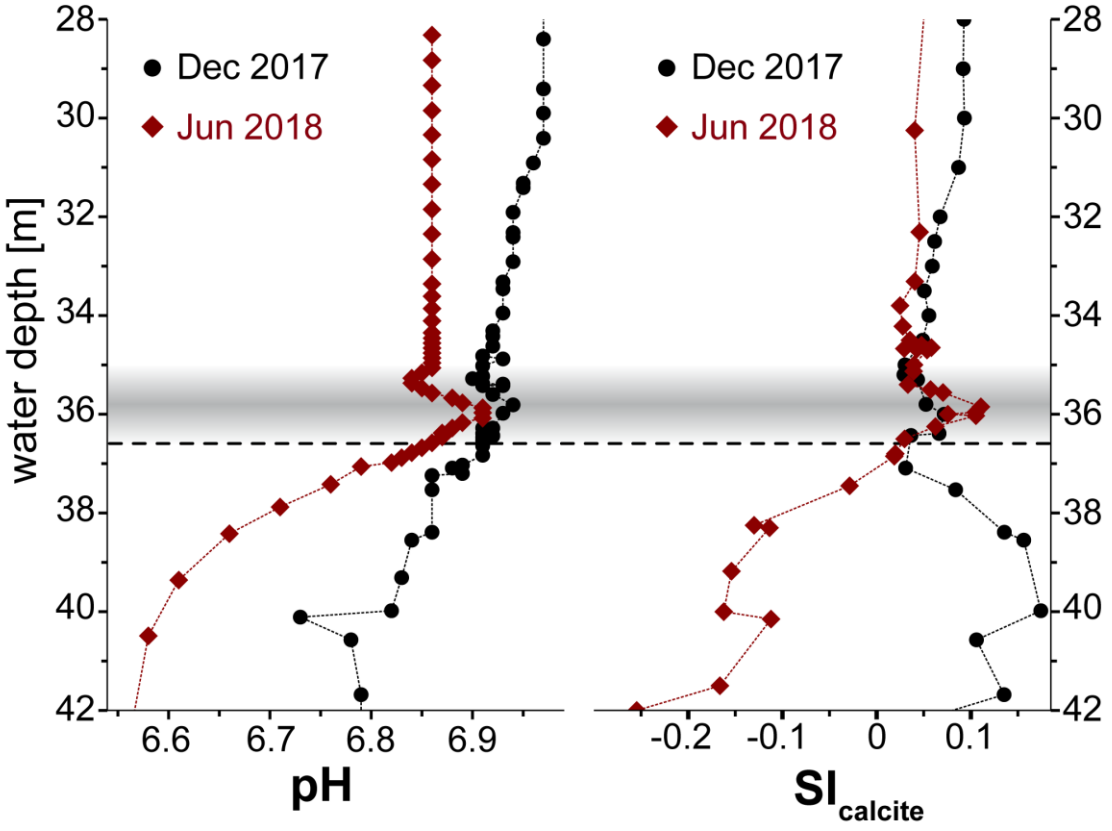

Fig. 17: The pH values and calculated saturation indices for calcite at different water depths of the two sampling campaigns in December 2017 and June 2018. Note the distinct peak of calcite oversaturation at ~35.8 m water depth and the difference of pH and SI values below the turbid layer (grey band), which is due to a non-quantifiable positive pH shift in the measurement of December 2017 (described in section 3.2.2, p.18 and shown in Fig. 9, p. 20).

The calculated saturation index (SI) of calcite in the water column of cenote El Zapote shows calcite saturation in the freshwater body and the uppermost part of the halocline with values from 0.03–0.07 (Fig. 16b and Fig. 17). The SI closely follows the pH in the freshwater body revealing a

distinct peak of slightly higher values of SI = 0.1 in the turbid layer at ~36 m water depth. The water body below the redoxcline is undersaturated with respect to calcite indicating calcite dissolution in the halocline (Fig. 17).

4.1.1.1 Trace elements

Dissolved iron and manganese concentrations are very low in the freshwater body with concentrations of 0.1 and 0.01 µmol l^{-1}, respectively, and slightly increase within the turbid layer towards the saltwater body, to concentrations of up to 0.47 (Fe) and 0.06 (Mn) µmol l^{-1} (Fig. 18). Phosphate and silica concentrations are invariably low in the freshwater body (P_{ortho} of ~0.25 and Si of~63 µmol l^{-1}) and increase in the saltwater body peaking at 40 m water depth with concentrations up to 10.3 (P_{ortho}) and 275 (Si) µmol l^{-1} (Fig. 18). Uranium content correlates to the redox potential of the water as indicated by uniform contents of ~0.012 µmol l^{-1} in the freshwater column and rapidly decreasing values in one order of magnitude in the turbid layer, to 0.0012 µmol l^{-1} at 40 m water depth (Table S2 in Ritter et al., 2019).

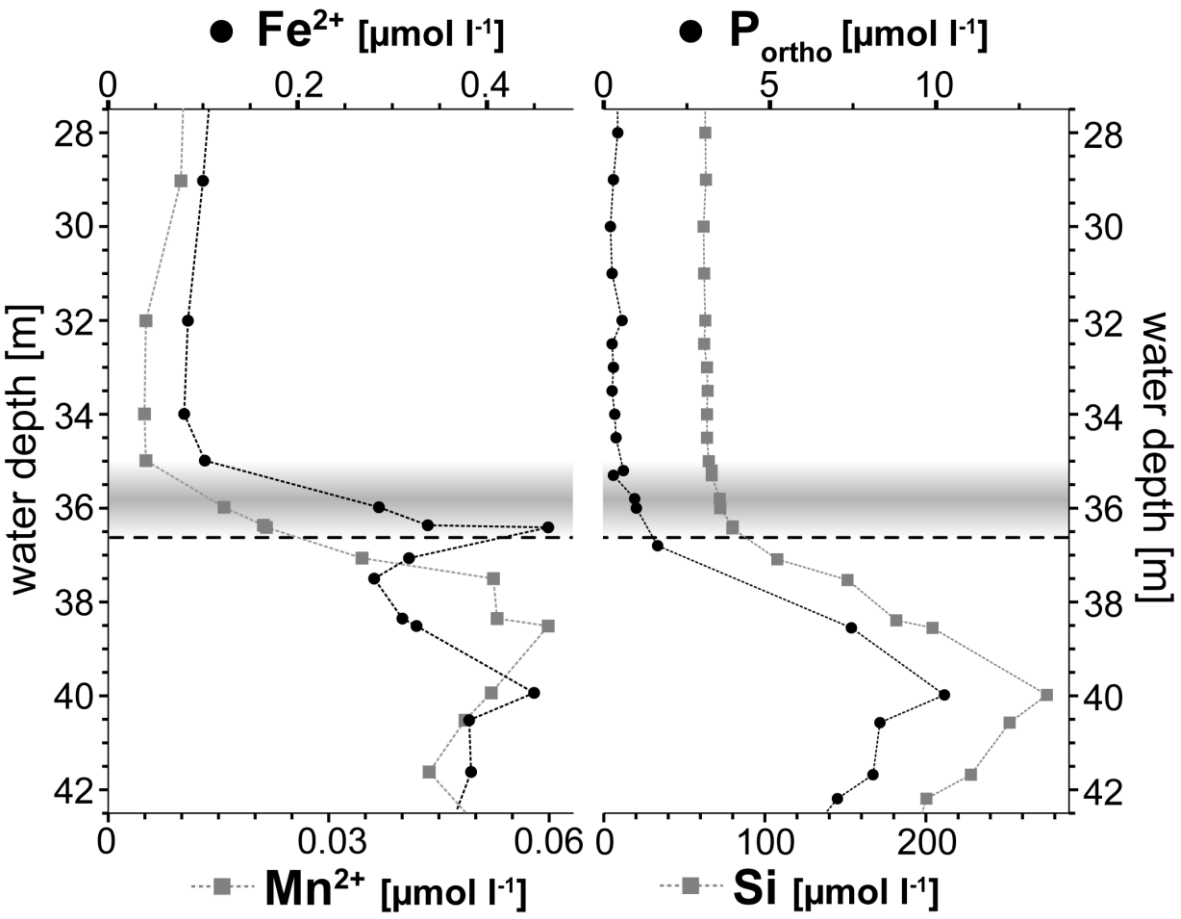

Fig. 18: Concentrations of dissolved iron and manganese (left) as well as orthophosphate and silica (right) in 28–42 m water depth. The grey band represents the turbid layer in 35–36.6 m water depth and the dashed line indicates the top of the halocline at 36.6 m water depth.

4.1.1.3 Stable carbon isotopes of DIC and CH_4

The $\delta^{13}C$-HCO_3^- values at water depth from 28 to 42 are shown in Figure 19. The average $\delta^{13}C$-HCO_3^- value is −9.8 ‰ in the freshwater body, where DIC content is about 8 mmol l^{-1}. In the turbid layer, $\delta^{13}C$-HCO_3^- values show a distinct peak towards less negative values of up to −7.9 ‰ at slightly increasing DIC concentrations. Below the turbid layer $\delta^{13}C$-HCO_3^- values rapidly decrease towards more negative values of −12.4 ‰ between 39 and 42 m water depth at increasing DIC concentrations (Fig. 19). A rather slight increase of $\delta^{13}C$-HCO_3^- values (-11.6 ± 0.7 ‰) is observed towards the cenote bottom at 44 m water depth (Table S3).

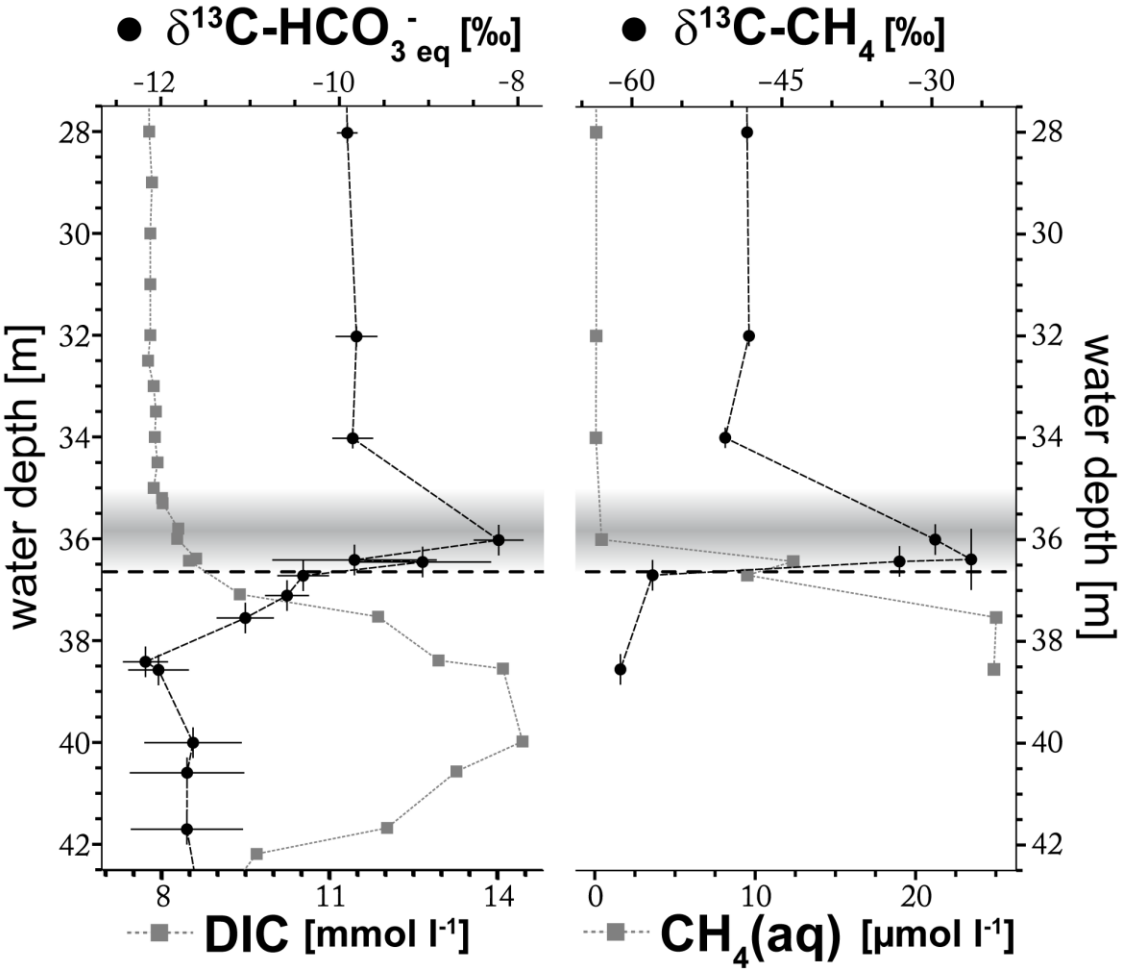

Fig. 19: Stable carbon isotope values $\delta^{13}C\text{-}HCO_{3\,eq}^{-}$ of the dissolved HCO_3^- in equilibrium with $\delta^{13}C\text{-}CO_2$ values measured in headspace and $\delta^{13}C\text{-}CH_4$ values of water samples alongside the concentrations of DIC and CH_4 of water samples. The grey band represents the turbid layer in 35–36.6 m water depth and the horizontal dashed line indicates the top of the halocline at 36.6 m water depth. Horizontal error bars represent 2σ uncertainties and vertical error bars indicate up to 0.6 m uncertainty of the gas samples that where not taken from the same sample used to determine chemical parameters (section 3.2.3, p. 21).

The $\delta^{13}C\text{-}CH_4$ values are shown alongside with the CH_4 concentrations in Figure 19. The pattern of $\delta^{13}C\text{-}CH_4$ within the water column is similar to that of $\delta^{13}C\text{-}HCO_3^-$. In the freshwater body values of $\delta^{13}C\text{-}CH_4$ are approximately constant at about –49 ‰ and CH_4 concentrations are very low, roughly corresponding to that of atmospheric equilibrium (0.04–0.09 µmol l^{-1}). $\delta^{13}C\text{-}CH_4$ increases to –28 ‰ within the turbid layer and again decreases to –61 ‰ below the turbid layer, while CH_4 concentrations increase within and below the turbid layer (Fig. 19).

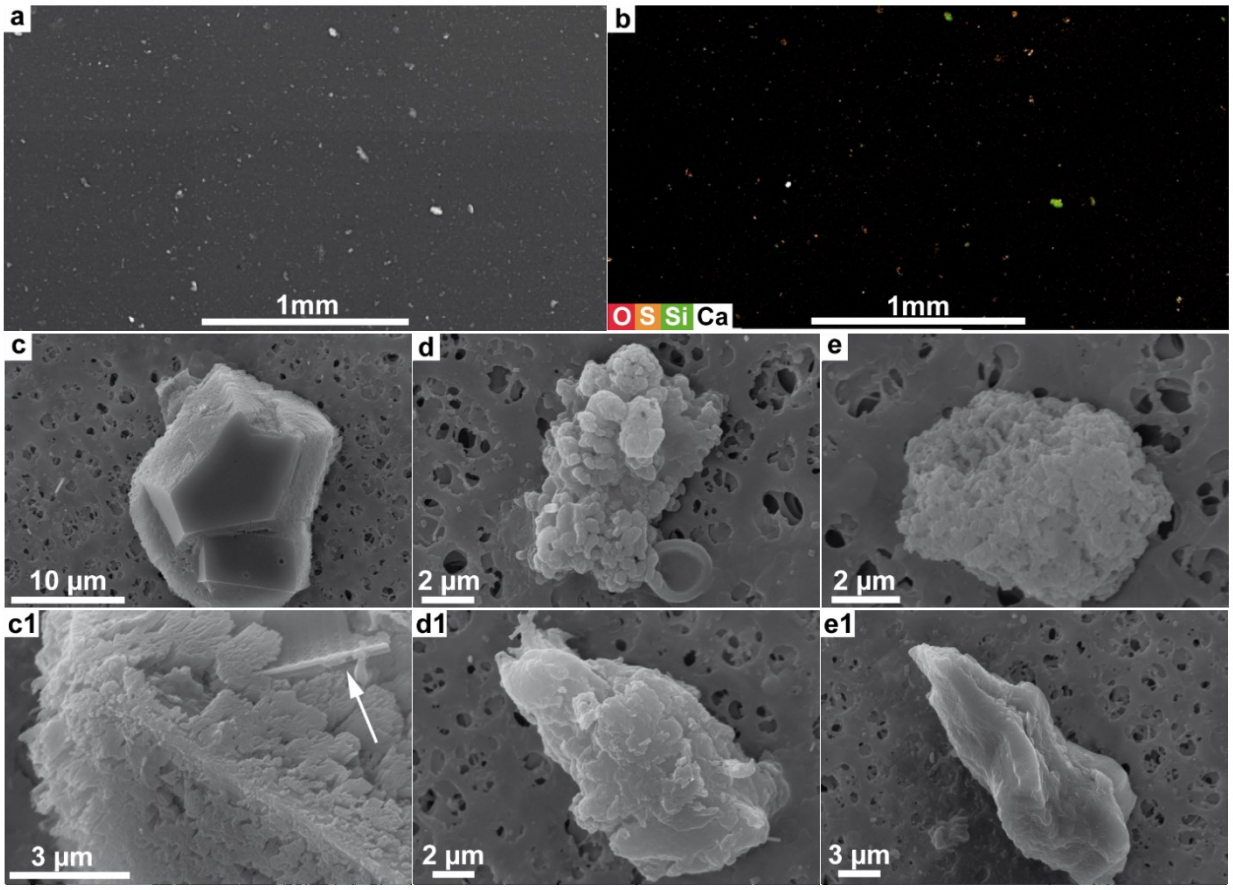

Fig. 20: SEM-analysis of turbid layer filtrate. Various particles on the filter are visible on the SEM picture of a larger area of the filter (a). An element map for O, S, Si and Ca of the same filter area of (a) is shown in (b) revealing that most particles consist of elemental sulfur, Ca-rich particles and silica particles. EDX analysis of individual particles on the filter verified the particles as Ca-carbonates (c, c1), elemental sulfur (d, d1) and silicate phases (e, e1). The white arrow in c1 points to a fragmentary silica shell.

4.1.1.4 Turbid layer filtrate

Although the turbid layer appears dense in photographs taken during dives, the water sampled from the turbid layer was clear, with no visible turbidity during sample handling. Electron microscopy of the filter, however, reveals that abundant particles were extracted from the turbid layer (Fig. 20a). Particle sizes range between 1–100 µm, but most are in the range of 1–10 µm. They consist of Ca-carbonate crystals (Fig. 20c and c1), globular particles consisting of elemental sulfur (Fig. 20d and d1) and silicate particles of different compositions (Fig. 20e and e1). In addition, numerous intact and broken shells of siliceous diatoms were found on the filter. Some calcite crystals incorporated broken parts of silica shells (Fig. 20c1).

4.1.2 Water sampling of cenotes El Zapote, Tortugas and Maravilla with Hells Bells and cenote Angelita devoid of Hells Bells in May/June 2018

The results of the water analysis for cenote El Zapote of the sampling campaign in 2018 presented in this chapter generally confirm the published results, which are also presented above, for the water body of El Zapote of the sampling campaign in 2017. The hydrogeochemical results of the other cenotes with Hells Bells, cenotes Maravilla and Tortugas, are similar to that of cenote El Zapote revealing several common features. In cenote Angelita, a deep stratified cenote devoid of Hells Bells, several features of the water body could be identified that differ from the water bodies of the cenotes with Hells Bells. The following presentation of the hydrogeochemical results thus focusses on highlighting the common features of the cenotes with Hells Bells contrasting to the features of the deep stratified cenote Angelita.

4.1.2.1 Characteristics of the water columns of the different cenotes

The results of the in-situ parameters specific electrical conductance, turbidity, dissolved oxygen (O_2), redox potential (EH), pH and water temperature of the water columns of the four studied cenotes are given in Figure 21 and were used to describe the typical characteristics of the water bodies. In total, three different characteristic features can be distinguished in the water body: the halocline, the redoxcline and the turbid layer. These features are specified in Table 1 for the studied cenotes. The halocline of cenotes with Hells Bells is typically between 10–20 m thick and therefore significantly thicker than the halocline of cenote Angelita with around 2 m thickness (Fig. 21 and Table 1). All cenotes reveal a distinct redoxcline, a 1.6–2.4 m thick zone showing steep gradients in the redox potential (Fig. 21 and Table 1). The redoxclines of the cenotes with Hells Bells are located around the top of the halocline (Fig. 21a–c), whereas the redoxcline of cenote Angelita is located within the halocline (Fig. 21d). The redoxclines of cenotes with Hells Bells typically correspond to a zone of increased turbidity, the so called “turbid layer” (Fig. 21a and c, Fig. 21a and c). This turbid layer is well pronounced in cenotes El Zapote and Maravilla while cenote Tortugas shows only a minor increase in turbidity within the redoxcline (Fig. 21c and Fig. 21c). At cenote Angelita, which is devoid of Hells Bells, the turbid layer is most

pronounced and already starts above the redoxcline at the top of the halocline peaking at the top of the redoxcline (Fig. 21d and Fig. 21d and Table 1).

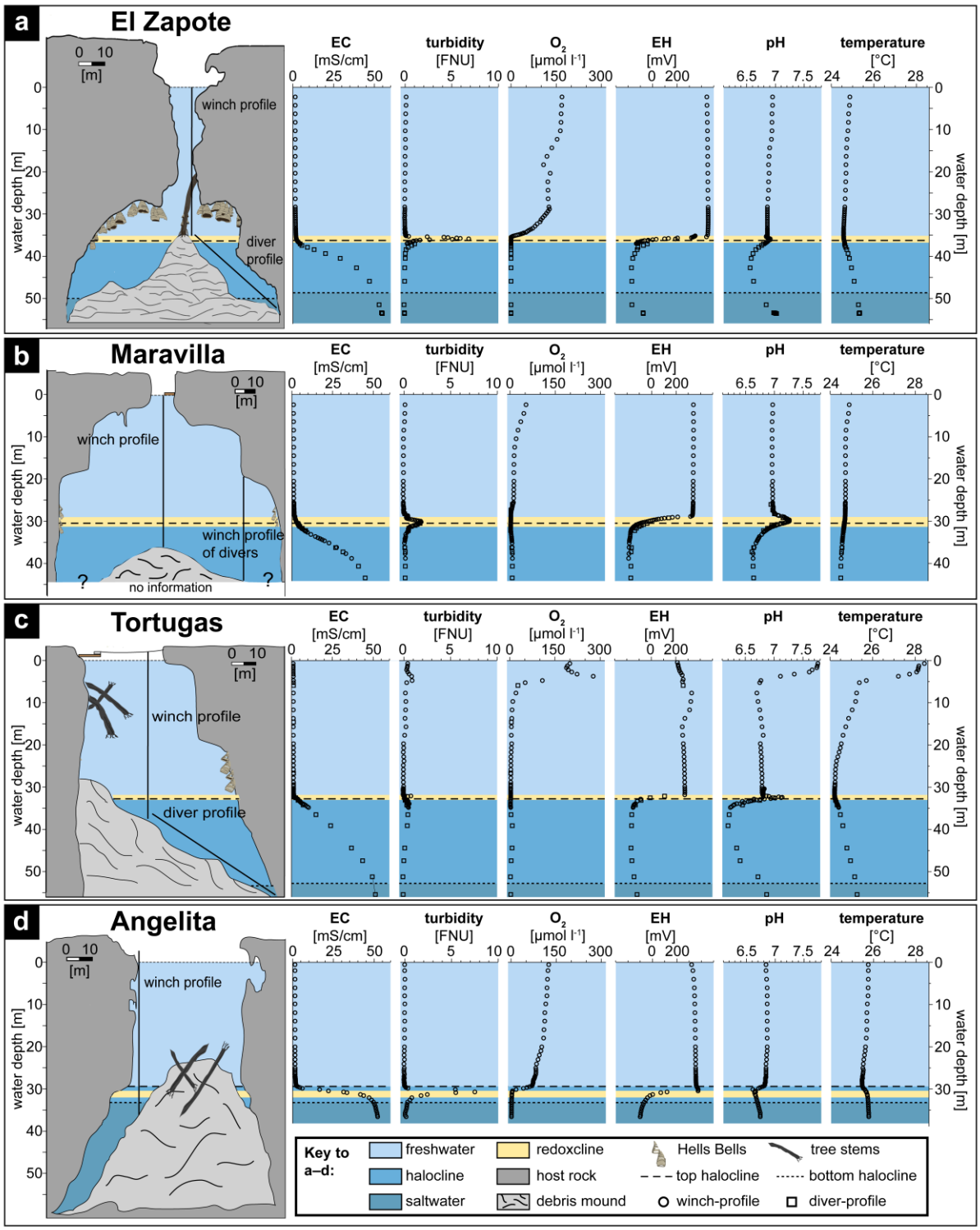

Fig. 21: Morphological and hydrological characteristics of the studied cenotes (A–D). Sketches of cenotes El Zapote and Angelita were taken and modified from Stinnesbeck et al. (2017a) and the info board at the cenote, respectively. Sketches of Tortugas and Maravilla were produced on the basis of drawings of technical diver Dirk Penzel.

Table 1: Hydrologic characteristics of the studied cenotes with Hells Bells El Zapote, Maravilla, Tortugas and cenote Angelita devoid of Hells Bells.

	Top halo-cline [w.d. in m]	Basis halo-cline [w.d. in m]	Halocline thickness [m]	Top redox-cline [w.d. in m]	Basis re-doxcline [w.d. in m]	Redoxcline thickness [m]	Peak turbid layer water [w. d. in m]	Turbid layer thickness [m]
El Zapote	36.7	47.0	10.3	35.5	37.1	1.6	35.9	~1.2
Maravilla	30.6	>43.4	>12.8	28.3	30.7	2.4	30.2	~1.6
Tortugas	32.9	52.2	19.3	31.7	33.3	1.6	32.1	~0.2
Angelita	29.5	33.5	4.0	30.4	32.6	2.2	30.4	~2

In all studied cenotes, high EH values indicate oxidizing conditions in the freshwater bodies (Fig. 21). At the top of the redoxclines Oxygen concentrations then drop to undetectable levels (<0.03 µmol l^{-1}) and stay at undetectable levels below (Fig. 21). While the freshwater bodies of cenotes Zapote and Angelita are well-oxygenated, cenotes Tortugas and Maravilla show low concentrations of dissolved oxygen in the freshwater body (Fig. 21b and c). The uppermost part in cenote Tortugas shows a peak of dissolved oxygen concentrations in ~4 m water depth (Fig. 21c). The water temperatures of all studied cenotes decrease within the freshwater body towards the halocline and increase within the halocline towards the saltwater body (Fig. 21a, c and d), except in cenote Maravilla where temperatures further decrease within the halocline (Fig. 21b). At cenote Tortugas, a thermocline developed in the uppermost freshwater body, with significantly elevated water temperatures of up to 29°C in water depths of 0–3 m (Fig. 21c). Except for the thermocline in the uppermost freshwater body of cenote Tortugas, the pH values of the studied cenotes are generally circumneutral and invariable in the freshwater bodies (Fig. 21). Cenotes with Hells Bells show distinct peaks of alkaline pH values of up to ~7.3 within the redoxcline. Below the redoxcline the pH values decease to values of up to ~6.2 at around 40 m water, followed by an increase towards the saltwater body at the cenote bottoms (Fig. 21a, b and c, Fig. 24a, b and c,). Cenote Angelita, which is devoid of Hells Bells shows a peak of acidic pH values of ~6.6 just above the redoxcline at 30 m water depth, followed by slightly increasing pH values towards 6.7 at the cenote floor (Fig. 21 d and Fig. 24d).

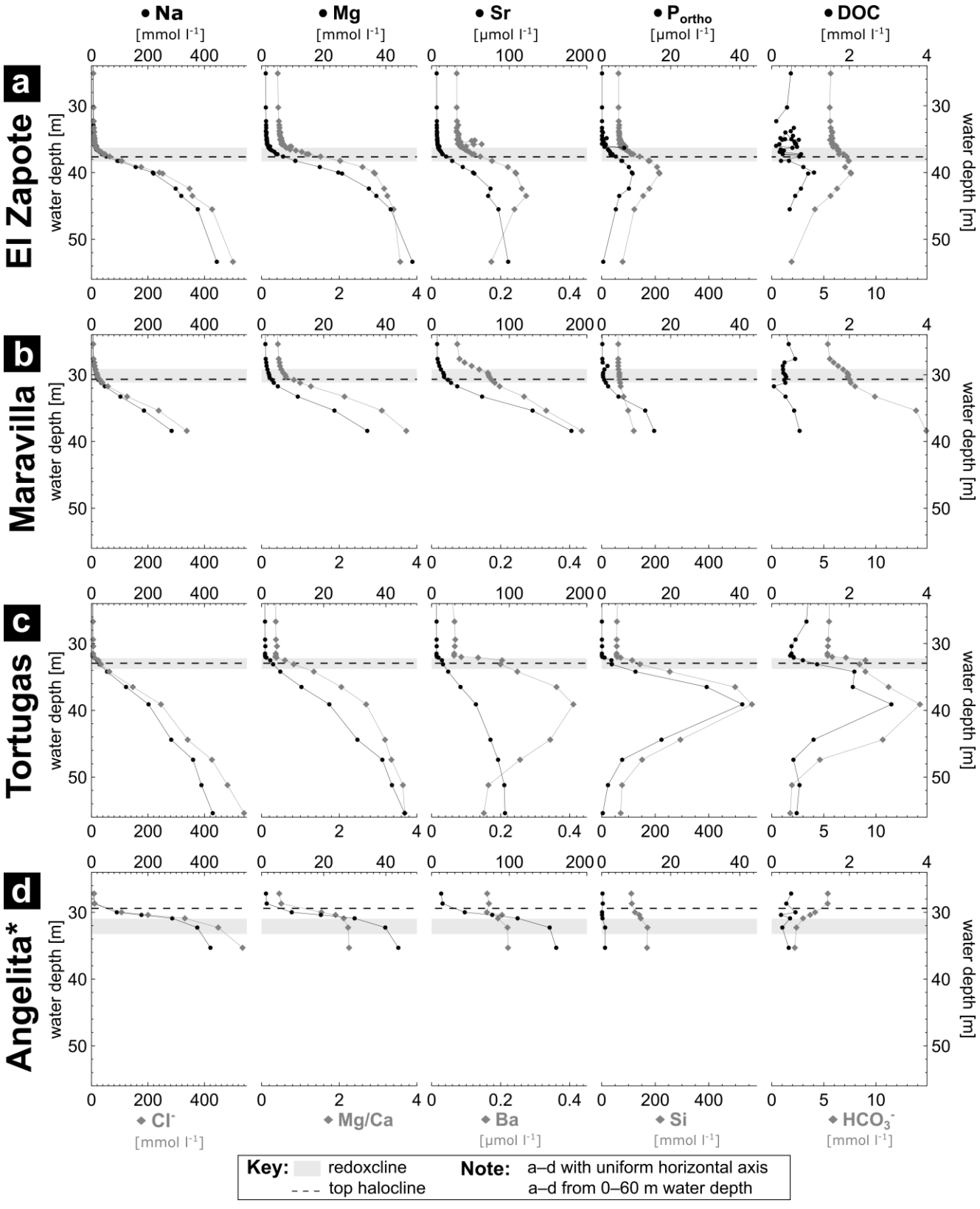

Fig. 22: Hydrogeochemistry (part I) of the studied cenotes with Hells Bells El Zapote (a), Maravilla (b) and Tortugas (c) and cenote Angelita devoid of Hells Bells (d). The data is given in Table A2.

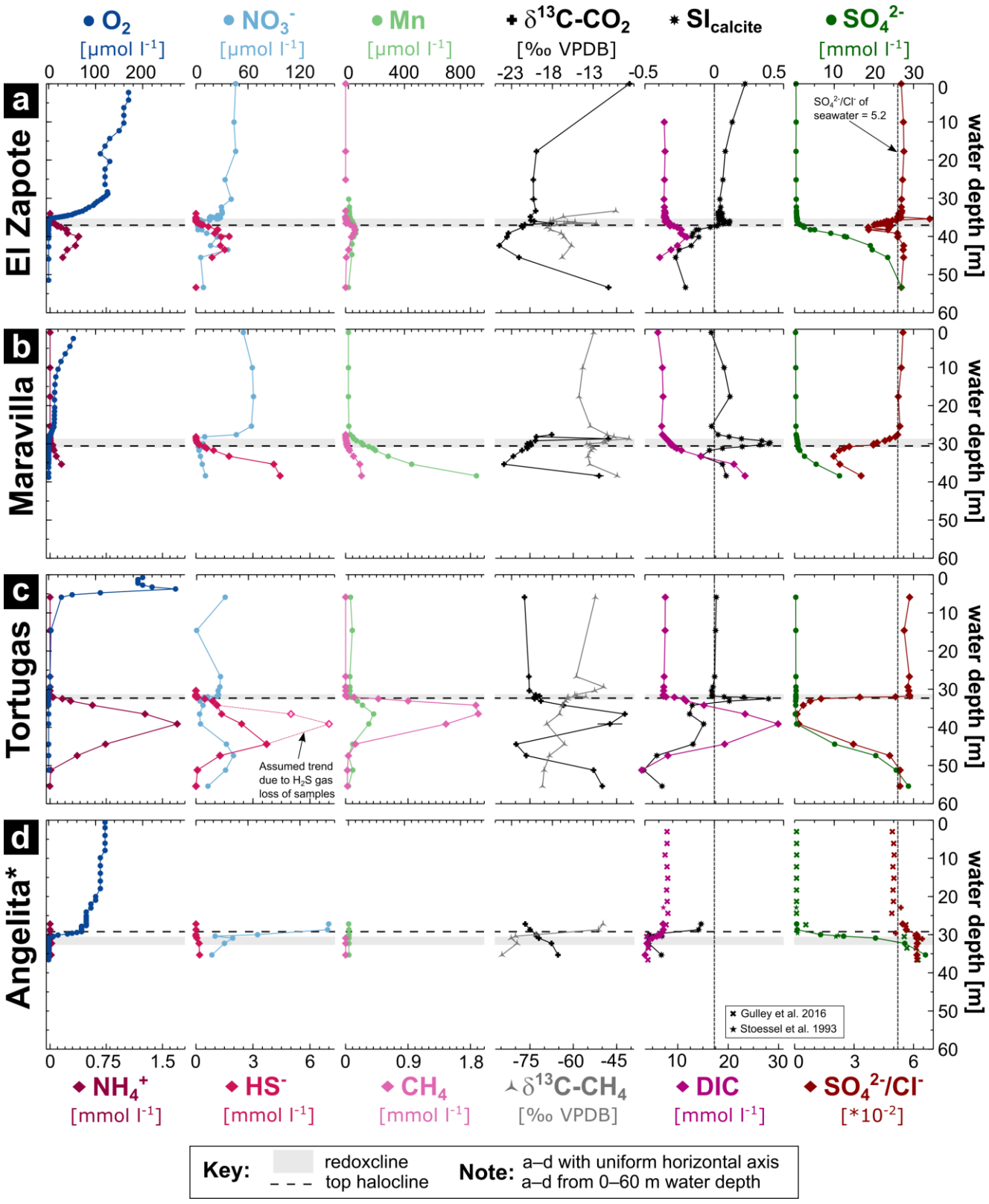

Fig. 23: Hydrogeochemistry (part II) of the studied cenotes with Hells Bells El Zapote (a), Maravilla (b) and Tortugas (c) and cenote Angelita devoid of Hells Bells (d). The data is given in Table A2 and taken from Gulley et al. (2016) and Stoessel (1993, unpub.). The seawater SO_4^{2-}/Cl^- is taken from Stoessel et al. (1993).

4.1.2.2 Hydrogeochemistry

The hydrogeochemical results relevant for biogeochemical processes and calcite precipitation in the water column of the studied cenotes are given in Figures 22 and 23 over the full range of the water bodies. The results relevant with regard to biochemical redox processes in the redoxcline are presented in Figure 24 for water depths around the redoxclines of the respective cenotes. The stratification of all studied cenotes is reflected by constant concentrations of dissolved Ca, Mg, Sr, Na, Cl^- within the freshwater bodies and a strong increase of concentrations within the haloclines towards the saltwater bodies (Fig. 22, Fig. 23 and Table A2). As contents of Mg increase more within the halocline relative to Ca contents, the Mg/Ca ratios increase within the haloclines of all cenotes (Fig. 22). All studied cenotes show elevated concentrations of reduced species of sulfur (HS^-), nitrogen (NH_4^+) and carbon (CH_4(aq)) within the haloclines and fading concentrations within the redoxclines (Fig. 23 and Fig. 24). These species are much more abundant in cenotes with Hells Bells compared to cenote Angelita, where the concentrations are 10–100 fold lower (Fig. 23 and Fig. 24). The concentration patterns of orthophosphate (P_{ortho}), silica (Si), barium (Ba) as well as dissolved organic carbon (DOC) are similar to that of the reduced species HS^-, NH_4^+ and CH_4(aq)) showing low values in the freshwater bodies and increasing values in the haloclines (Figs. 4, Fig. 23). Concentrations of dissolved inorganic carbon (DIC) in cenotes with Hells Bells follow the same pattern with increasing concentrations within the haloclines (Fig. 23a, b, c and Fig. 24a, b, c), while DIC concentrations in cenote Angelita decrease below the halocline (Fig. 23d and Fig. 24d). Interestingly, concentrations of ions linked to biogeochemical redox processes (HS^-, NH_4^+, CH_4(aq), P_{ortho}, Si, Ba, DIC and DOC) peak at around 40 m water depth in cenotes Zapote and Tortugas coinciding with a peak of the lowest pH values within the redoxclines (Fig. 21 and Fig. 23a and c). Although no water samples were taken below 38 m water depth in cenote Maravilla, the slight increase of pH values below ~40 m water depth in Maravilla indicates a maximum of these species around this water depth (Fig. 21b). Sulfate (SO_4^{2-}) concentrations increase within the halocline in all cenotes beginning from the top of the halocline (Fig. 23a, b, d) except cenote Tortugas were the increase of sulfate starts well

beneath the top of the halocline at ~40 m water depth (Fig. 23c). The ratios of SO_4^{2-}/Cl^- of all cenotes are close to the SO_4^{2-}/Cl^- ratio of seawater in the freshwater bodies.

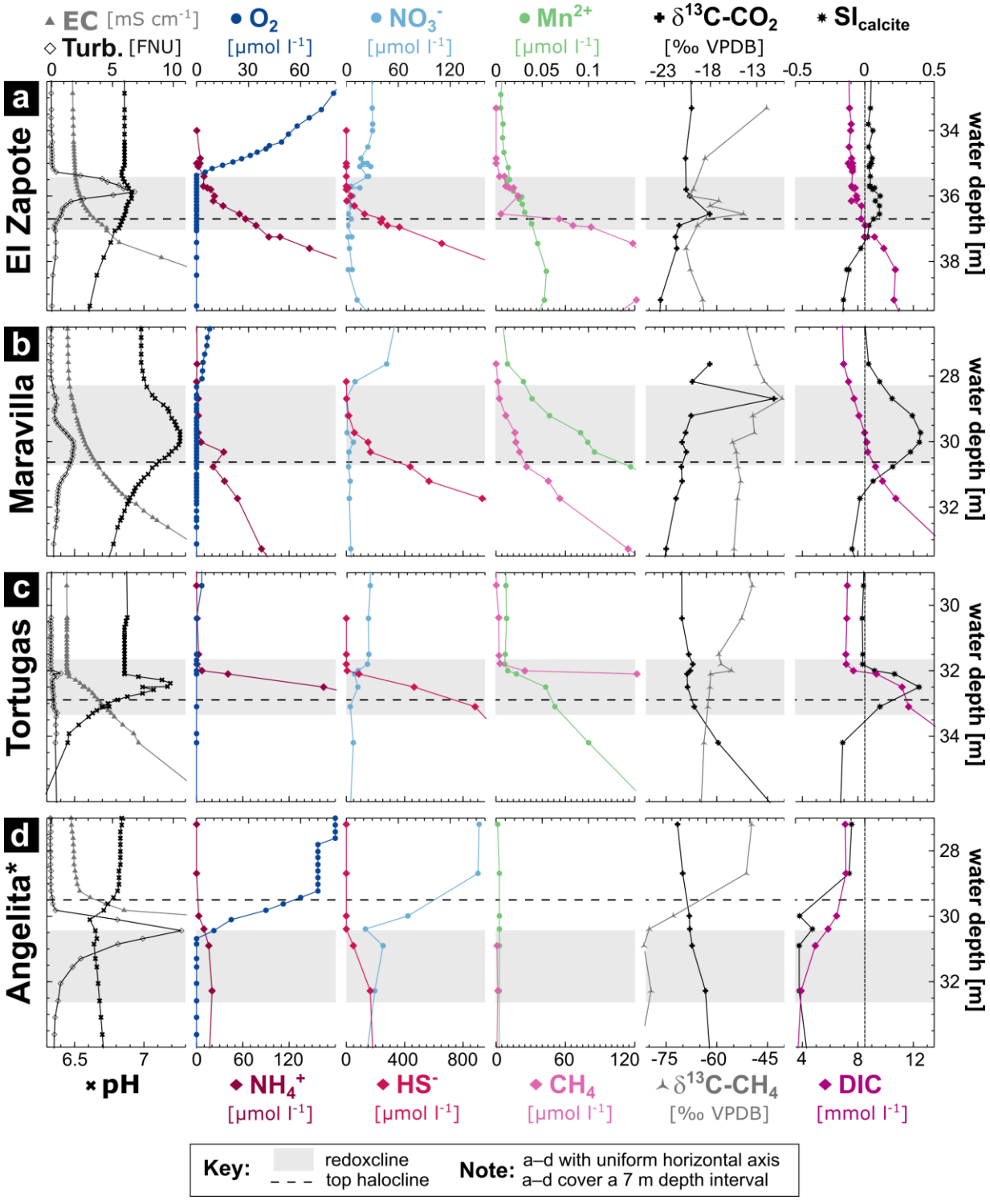

Fig. 24: Hydrogeochemistry around the redoxclines of the studied cenotes with Hells Bells El Zapote (a), Maravilla (b) and Tortugas (c) and cenote Angelita devoid of Hells Bells (d). The data is given in Table A2.

While the SO_4^{2-}/Cl^- ratios shows a slight increase within the halocline of cenote Angelita, SO_4^{2-}/Cl^- ratios of cenotes with Hells Bells decrease within the haloclines showing minimum values in water depths a few meters beneath the top of the haloclines and increasing values towards the saltwater bodies below (Fig. 23a, b, c). Nitrate is present in the freshwater bodies (30–150 µmol l^{-1}) of all studied cenotes, rapidly decreases towards the redoxclines at the lowermost part of the freshwater bodies and stays at low levels below (Fig. 23 and Fig. 24). The cenotes with Hells Bells show elevated concentrations of dissolved manganese within the haloclines with maximum values of 0.05–0.09 µmol l^{-1} (Fig. 24a, b, c and Fig. 23a, b, c). Manganese concentrations decrease towards the upper part of the redoxclines and show constantly low values within the freshwater bodies of the cenotes with Hells Bells. In cenote Angelita, which is devoid of Hells Bells, Mn concentrations were below the detection limit (<0.018 µmol l^{-1}) throughout the sampled water column (Fig. 24d and Fig. 23d).

4.1.2.3 Stable carbon isotopes of dissolved inorganic carbon species and methane (CH_4)

The stable carbon isotope ratios of dissolved inorganic carbon species and methane, the $\delta^{13}C\text{-}CO_2$ and $\delta^{13}C\text{-}CH_4$ values, measured in the headspace of water samples of the studied cenotes are shown in Figure 24 for water depth around the redoxcline and displayed in Figure 23 over the full range of the water columns.

The $\delta^{13}C\text{-}CO_2$ values in the freshwater bodies of all studied cenotes are generally low around –20 ‰ except for the surface water value of cenote El Zapote, which is higher and close to the atmospheric value of around –9 ‰ (Fig. 24 and Fig. 23). In cenotes with Hells Bells, the $\delta^{13}C\text{-}CO_2$ increase within the redoxclines showing peaks towards values which are 2, 4 and 10 ‰ higher than in the freshwater bodies of cenotes Tortugas, El Zapote and Maravilla, respectively (Fig. 24, b, c). The $\delta^{13}C\text{-}CO_2$ values decrease in the upper part of the haloclines immediately below the redoxclines of cenotes El Zapote and Maravilla towards minimum values of about –24 ‰. The values then increase to values of up to -13 ‰ in the lower part of the haloclines towards the saltwater layer (Fig. 24a, b and Fig. 23a, b). The other cenote with Hells Bells, cenote Tortugas,

shows strongly increasing $\delta^{13}C\text{-}CO_2$ values immediately below the redoxclines with maximum values of –9 ‰ peaking between 36–39 m water depth. Below, the values decrease again to about –22 ‰ in 44 m water depth and increase from there to values of up to –12 ‰ towards the salt-water layer (Fig. 24c and Fig. 23c). The $\delta^{13}C\text{-}CO_2$ values of cenote Angelita without Hells Bells are rather invariant showing only a slight increase of the values in the halocline from -21 ‰in the freshwater body to around –18 ‰ in the lower part of the halocline (Fig. 24d and Fig. 23d).

The $\delta^{13}C\text{-}CH_4$ values of the cenotes with Hells Bells show generally similar patterns of lower and rather constant values in the freshwater bodies and haloclines with values ranging from –65 to –50 ‰. They show distinct positive peaks of around –6, –14 and –18 ‰ higher values within the redoxclines of cenotes Tortugas, Maravilla and El Zapote, respectively (Fig. 24a, b, c and Fig. 23a, b, c). In cenote Angelita, the $\delta^{13}C\text{-}CH_4$ are higher in the freshwater body with values of around –50 ‰ and immediately decrease from the top of the halocline to minimum values of around –80 ‰ at the top of the redoxcline (Fig. 24d and Fig. 23d). *4.1.2.4 Fluxes of dissolved species in the water column*

The fluxes of several dissolved species towards the redoxcline and the gradient of the increase of electrical conductivity are given in Table 2. The fluxes were calculated using linear best fits considering the data points that yield the largest possible fluxes illustrated in Figure 25.

The gradients in electrical conductivity (Grad EC) and the upward fluxes of the chemically conservative ion chloride (J Cl^-) reflect the differences in the halocline thicknesses of the cenotes (Table 1 and section 4.1.2.1, p.45). The increase of electrical conductivity is 4–10 fold and the chloride flux is 5–8 fold lower in cenotes with Hells Bells compared to cenote Angelita devoid of Hells Bells (Table 2). Considering only cenotes with Hells Bells, the gradients of EC and the chloride flux J Cl^- decrease in the order of El Zapote > Maravilla > Tortugas.

The upward fluxes of Ca^{2+} ions are similar in all cenotes within a range of 4.9-9.3 10^{-4} µmol m^{-2} s^{-1}. The fluxes of HCO_3^-, however, reveal a distinct difference in the cenotes with Hells Bells and cenote Angelita. While the flux of HCO_3^- is directed towards the redoxcline in cenotes with Hells

Bells, it is directed downwards from the redoxcline and the freshwater layer towards the halocline in cenote Angelita (Fig. 24, Fig. 25 and Table 2).

Generally, oxidized species reveal a downward diffuse flux towards the redoxcline from above and reduced species show an upward diffusive flux towards the redoxcline from below in all cenotes. The upward fluxes of the reduced species (HS^-, NH_4^+, CH_4) is 5–10 fold higher and the downward fluxes of oxygenized species (O_2 and NO_3^-) is 2–14 fold lower in cenotes with Hells Bells compared to cenote Angelita (Table 2). In cenotes with Hells Bells the upward fluxes of the reduced species are around an order of magnitude higher compared to the downward fluxes of the oxidized species dissolved oxygen and nitrate (Table 2). In contrast, in cenote Angelita the fluxes of the reduced species are similar to the fluxes of the oxidized species dissolved oxygen and nitrate (Table 2).

Upward fluxes of Mn^{2+} could only be determined for cenotes with Hells Bells due to very low concentrations and range from 1.2–3.9 10^{-8} µmol m^{-2} s^{-1} (Table 2).

Table 2: Fluxes (J) of dissolved species towards the redoxcline and gradient of increase of electrical conductivity (Grad EC) of the respective cenotes. Upward fluxes from below the redoxcline are denoted as positive values and downward fluxes from above the redoxcline as negative values. Fluxes were calculated from the liner best fit of the respective dissolved species illustrated in Figure 25.

	J Cl^-	Grad EC	J Ca^{2+}	J HCO_3^-	J HS^-	J O_2	J NO_3^-	J NH_4^+	J CH_4	J Mn^{2+}
	µmol m^{-2} s^{-1}	mS cm^{-1} m^{-1}	µmol m^{-2} s^{-1}	µmol m^{-2} s^{-1}	µmol m^{-2} s^{-1}	µmol m^{-2} s^{-1}	µmol m^{-2} s^{-1}	µmol m^{-2} s^{-1}	µmol m^{-2} s^{-1}	µmol m^{-2} s^{-1}
Zapote 17	1.14E-01	6.4	1.01E-03	2.51E-03	6.01E-04	-6.71E-05	-5.68E-05	n.a.	3.04E-05	1.2E-08
Zapote 18	9.23E-02	6.5	9.32E-04	7.75E-04	7.90E-04	-9.12E-05	-3.01E-05	1.55E-04	9.33E-05	1.2E-08
Tortugas	6.09E-02	2.7	4.88E-04	1.43E-03	1.40E-03	-6.37E-06	-9.65E-05	5.47E-04	1.54E-03	2.5E-08
Maravilla	8.27E-02	5.5	7.54E-04	1.93E-03	1.24E-03	-7.27E-06	-6.66E-05	5.91E-05	7.06E-05	3.9E-08
Angelita	5.01E-01	26.9	4.88E-04	-1.50E-03	1.49E-04	-1.05E-04	-1.41E-04	2.83E-05	1.59E-06	n.a.

Notably, in the cenotes with Hells Bells the upward fluxes of NH_4^+ intersect with the downward fluxes of O_2 at the top of the redoxclines, while the upward fluxes of HS^- intersect with the downward fluxes of NO_3^- in the lower part of the redoxclines (Fig. 24a, b, c and Fig. 23a, b, c). In cenote Angelita, both upward fluxes of HS^- and NH_4^+ intersect with the downward fluxes of O_2 and NO_3^- at the top of the redoxcline (Fig. 24d and Fig. 23d).

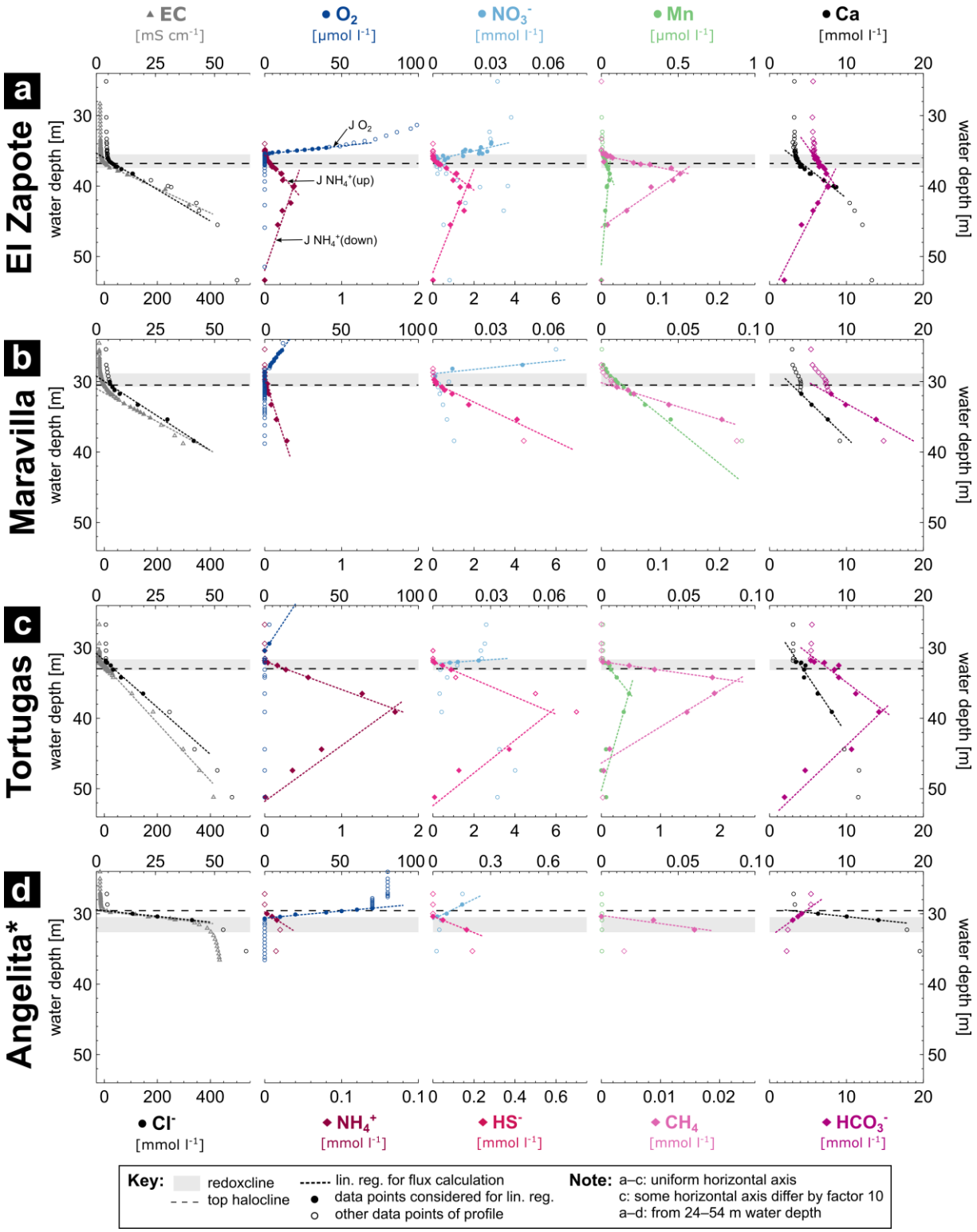

Fig. 25: Linear best fits for the calculation of ion fluxes in the water column of cenotes with Hells Bells El Zapote (a), Maravilla (b) and Tortugas (c), as well as cenote Angelita devoid of Hells Bells (d). The data is given in Table A2.

4.1.2.5 Calcite saturation

The calcite saturation is shown in Figures 24 and 23 for water depths around the halocline and the whole water columns of the studied cenotes, respectively. All studied cenotes show constant $SI_{calcite}$ close to equilibrium in the freshwater bodies and negative $SI_{calcite}$ values in the haloclines indicating calcite under saturation (Fig. 24 and Fig. 23). Notably, the cenotes with Hells Bells all show a more or less pronounced peak towards positive $SI_{calcite}$ values within the redoxclines indicating calcite oversaturation in a narrow 1–2 m wide water layer (Fig. 24a, b, c). The $SI_{calcite}$ of cenote Angelita show slightly undersaturated values of the freshwater body and further decrease within the halocline and the redoxcline (Fig. 24d).

4.2 Petrography of Hells Bells

4.2.1 General petrographic characteristics of Hells Bells from cenote El Zapote

The size of individual crystals of Hells Bells is varying from µm scale to several mm-sized crystals that are easily identified macroscopically (Fig. 26). Large crystals are frequently dominant in the youngest calcite rims at the bottom or lowermost part of Hells Bells from water depths reaching from ~28 to ~35 m (Fig. 2e, p. 7 and Fig. 26a). Hells Bells from greater water depths show rounded or globular calcite surfaces at the lowermost margin of the speleothems indicating dissolution (Fig. 2f, p 7). The calcite crystals appear as clear white (Fig. 2e and Fig. 26a) to a yellowish color (Fig. 2f, p. 7). In lower water depth from ~28–30 m, they additionally show brown-colored coatings (Fig. 2d p. 7 and Fig. 26b), which were identified as Mn-oxides in EDX measurements.

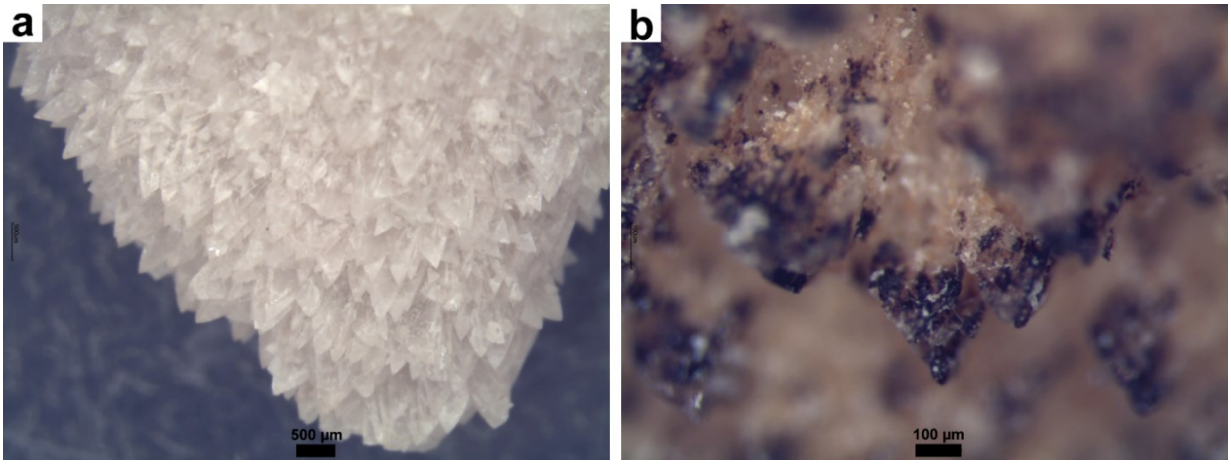

Fig. 26: Light microscopic images of Hells Bells calcite needles of clear white Hells Bells found below ~30 m water depth and with brownish Mn-oxide coatings on Hells Bells from 28–30 m water from cenote El Zapote.

High-resolution petrographic characteristics of Hells Bells are shown in Figures 27 and 28. SEM-images of the lowermost part of Hells Bell surfaces are shown in Figure 27a, b and c and in Figure 28. The calcite morphology varies from bladed or book-like calcite crystals (Fig. 27a), dogtooth-like calcite crystals (Fig. 27b and Fig. 26a) and blocky calcite rhombs (Fig. 27c). In thin sections of the specimen "Long Bell" (Fig. 27d1) (ZPT-7 in Stinnesbeck et al., 2017b), these crystal morphologies are expressed as rather botryoidal (dog-tooth-like and bladed-shaped) and mosaic calcite phases (blocky calcite rhombs) (Fig. 27d1). Electron images of the polished counter-slabs of the thin sections are shown in Figure 27d2.

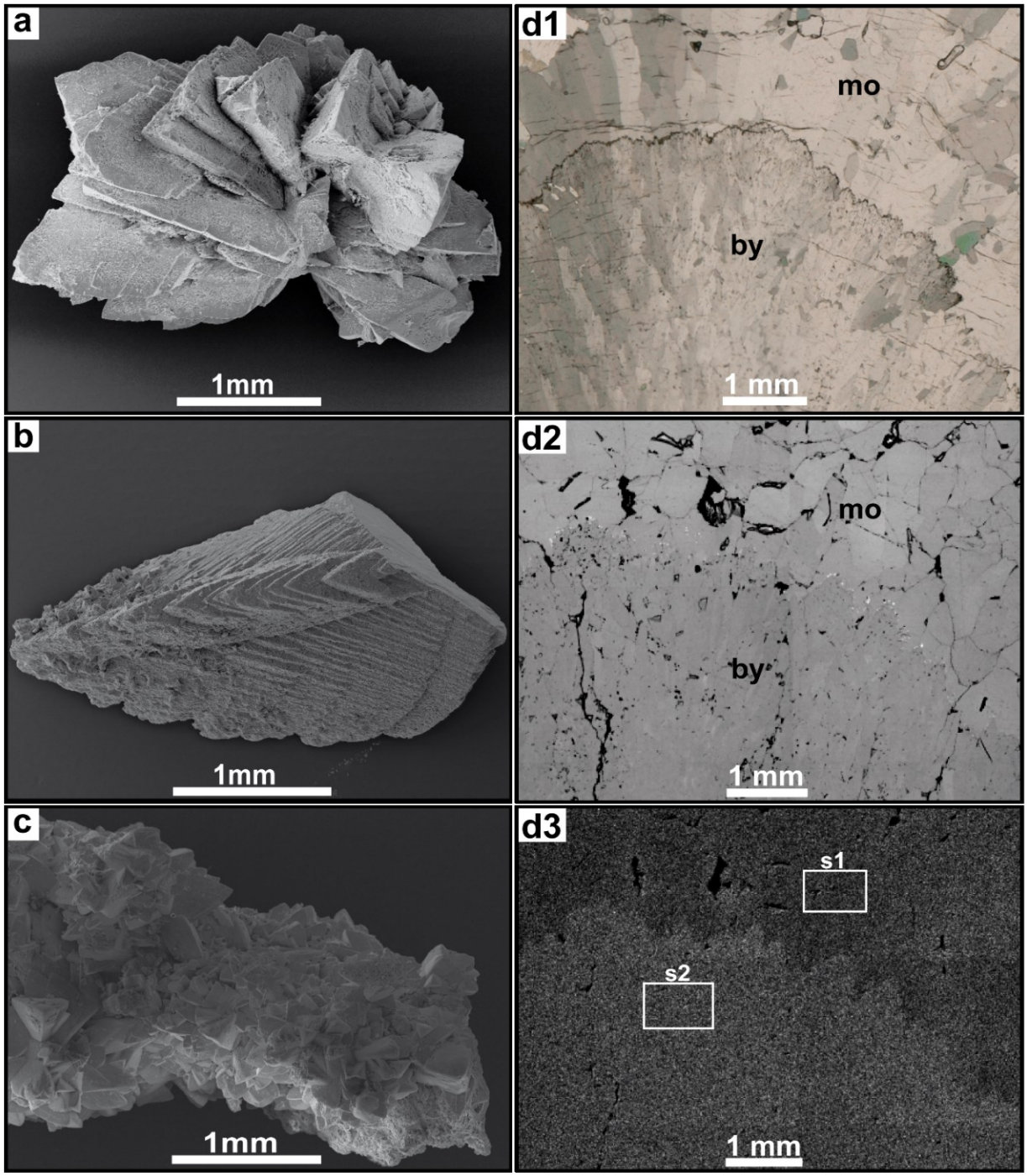

Fig. 27: Petrographic characteristics of Hells Bells speleothems. SE-images of Hells Bell samples Z17-8DC (a), Z17-18J (b), Z17-9J (c) of cenote El Zapote showing bladed (a), dogtooth-like (b) and blocky (c) calcite rhombs. Polarized transmitted light-microscopic images of a thin section from ZPT-7 (d1) (shown in Stinnesbeck et al., 2017b) showing different calcite fabrics of angular coarse-grained mosaic calcite (mo) and fine grained elongated botryoidal calcite (by). The same detail is shown in the BSE-image of the polished counter slab that corresponds to the thin section (d2). The Mg-element map (d3), where higher abundances of Mg appear brighter, indicates a difference in Mg content between the botryoidal and mosaic calcite phases. The white rectangles represent areas of measured integrated element spectra.

An element map of Mg of this part indicates that botryoidal calcite phases incorporated more Mg (appearing brighter in Fig. 27d3) than the mosaic calcite phases (appearing darker in Figure

27d3). The SEM-images of the surfaces of Hells Bells samples show that the sizes of Hells Bells calcites vary significantly from a few micrometers to several millimeters or even cm-seized individual crystals (Fig. 26, Fig. 27 and Fig. 28). Furthermore, SEM-images Hells Bells surfaces reveal dissolution features on the calcite crystal surfaces (Fig. 28b).

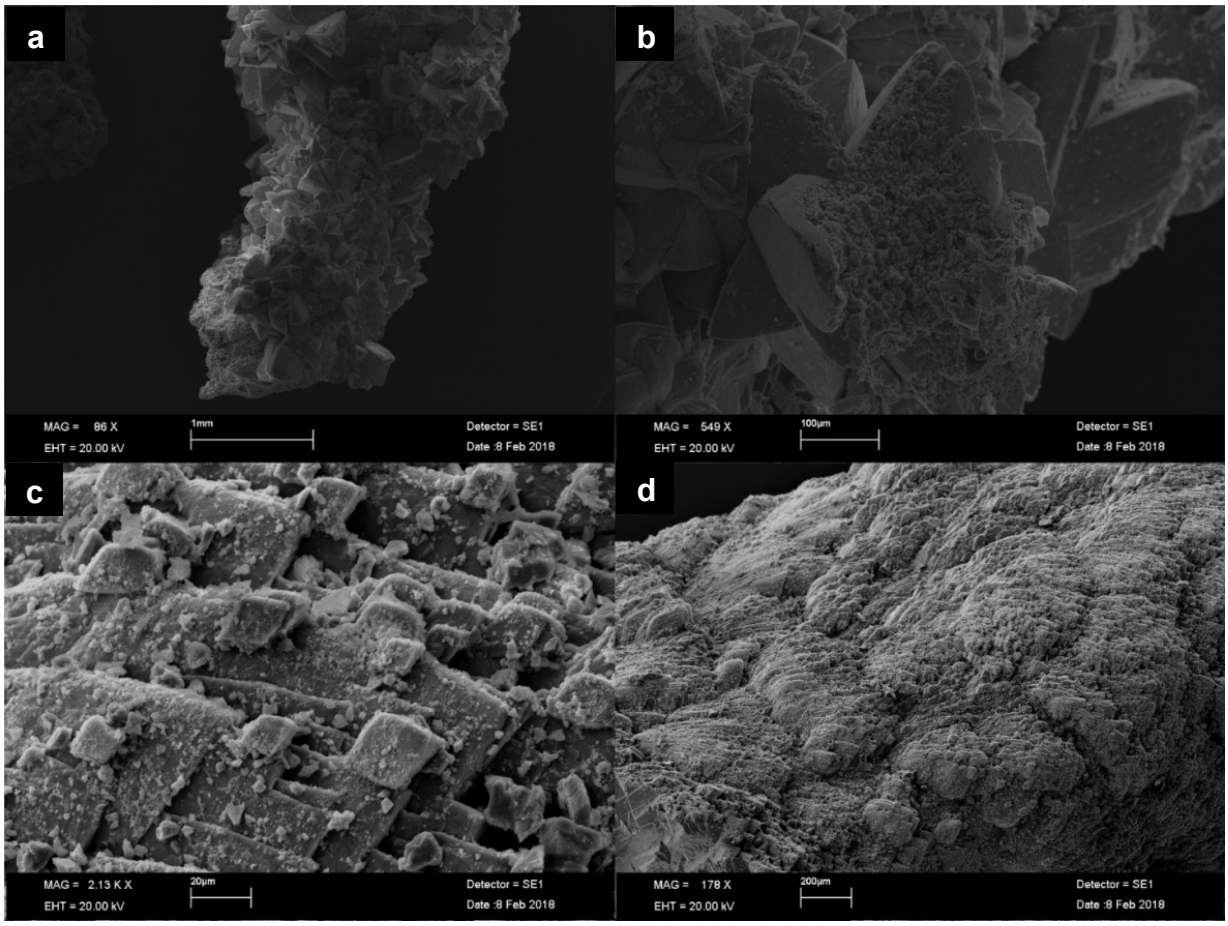

Fig. 28: SEM-images of Hells Bells surfaces. a: Blocky calcites; b: Dissolutions features on the surface of blocky crystals; c: Small calcite rhombs on surface (detail of D); d: Multiphase of spherulitic crystals (Fascicular Optic Calcite) with new crystallization on the surface.

4.2.2 Laminated Hells Bells

The common lamination of Hells Bells is revealed in specimens that were cut more or less parallel to the c-axis of the calcite crystals, which represents the presumed growth axis. Examples for laminated Hells Bells from cenotes El Zapote, Maravilla and Tortugas are shown in Fig. 29. The specimen of El Zapote and Tortugas show a fine relatively regular lamination (Fig. 29a1 and c1). The laminae of these specimens seem to join towards the outer parts giving an impression of the direction of growth. The specimen of cenote El Zapote reveals increasingly irregular lamination with increasing distance to the top showing numerous small parallel laminated lobes in the lower part of the specimen (Fig. 29a1). The specimen of cenote Maravilla shows different phases with a fine lamination in the upper part and coarser calcite grains at the lower part of the specimen (Fig. 29b1).

In thin sections, the lamination of Hells Bells is reflected by linearly interconnected opaque dotty structures (Fig. 29a2, b2 and c2). These opaque dots most likely represent dissolution features of the former surfaces of Hells Bells that were also observed in calcites of the lowermost part of Hells Bells (Fig. 28b). High-resolution images of the thin sections reveal that the contours of calcite crystals are preserved more or less by the opaque phases (Fig. 29a3 and c3). The preserved calcite surfaces range from a non-existent horizontal opaque line, a lobe-like structures to slightly rounded tips of dog tooth-like calcite crystals (Fig. 29a3 and c3).

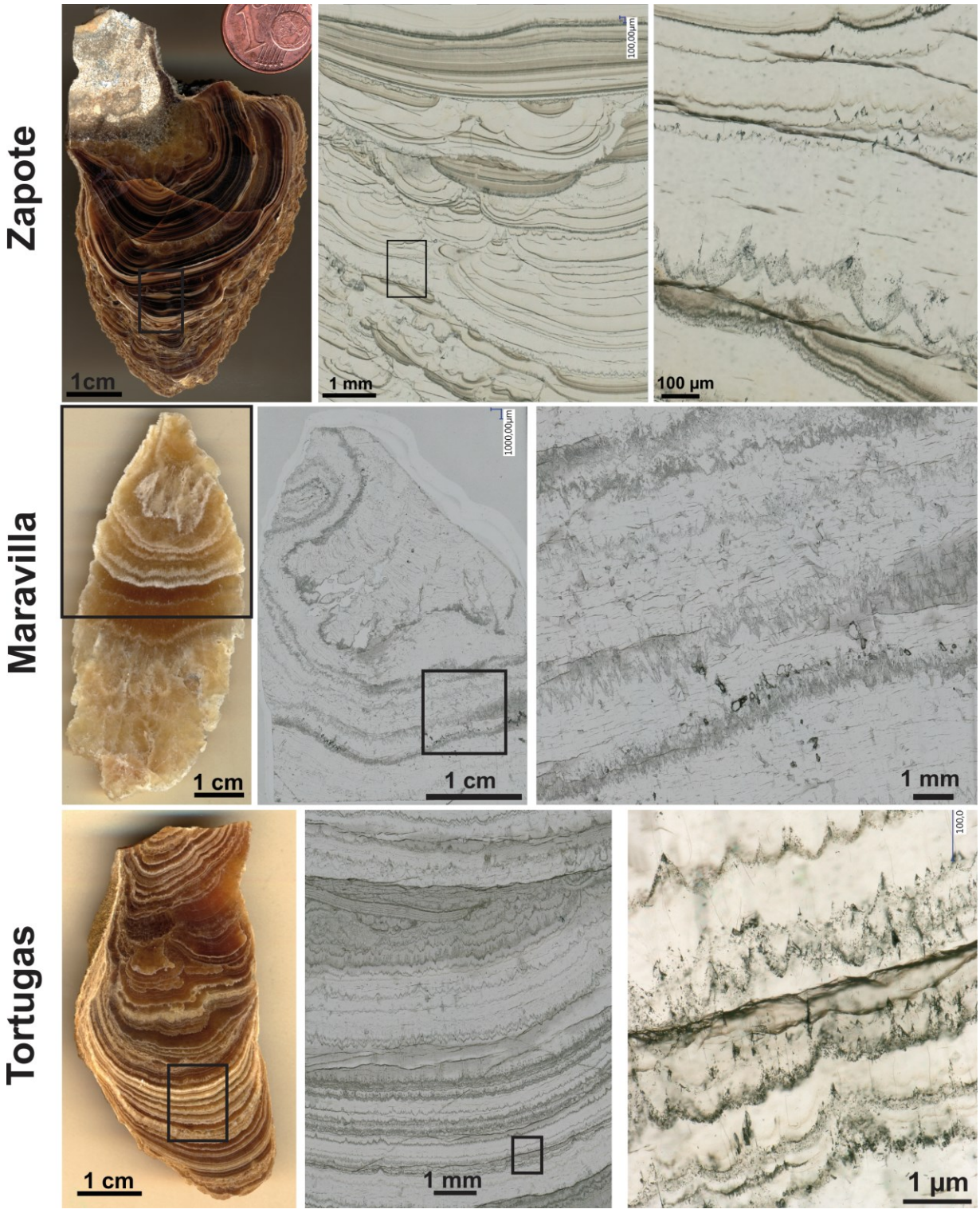

Fig. 29: Laminated Hells Bells specimen of cenotes El Zapote (TL4), Maravilla (MIII) and Tortugas (T_7). The specimens were vertically cut in half, while one half was polished (a1, b1, c1). Thin sections were prepared from the other half revealing details of the macroscopic lamination (a2, b2, c2). The terminations of each layer appear as an aggregation of tiny opaque spots along calcite crystal surfaces (a3, b3, c3).

4.2.3 Petrography of "Long Bell"

Petrographic characteristics of the elongated Hells Bells specimen "Long Bell" (ZPT-7 in Stinnesbeck et al., 2017b) are shown in Figure 30. The uppermost part of the specimen reveals that the Hells Bells specimen grew on top of a knobby piece of host rock (Fig. 30a). This marine carbonatic host rock is easily distinguishable from Hells Bells by its bright color compared to that of Hells Bells calcite (Fig. 30a and d). Furthermore, thin sections reveal that the host rock is composed of numerous marine fossils (Fig. 30b and c).

Three different phases of growth of "Long Bell" can be summarized (Sun, 2018, unpub.) indicated by black lines in Figure 30d. Phase 1 represents the initial growth phase on the host rock. At first, a thin seam of clear fibrous isopachous crystal phases formed around the host rock (F in Figure 30c). Then, a botryoidal fan-like calcite grew further from this (B in Figure 30c), which reveals brownish colors in the polished half of the specimen (Fig. 30a and d). Interestingly, a layer of a FeS-phase was identified with SEM-imaging and EDX at the outer margin of Phase 1 (bright spots in Figure 27d1) marking the boundary of Phase 1 to Phase 2 (Fig. 27d2 and Fig. 30a). Phase 2 represents rather steady growth conditions and its fabric consists of long spherulitic and blocky mosaic calcites (Fig. 30f). Phase 3 displays rather unsteady growth conditions or repeated phases of dissolution indicated by lamination in the polished surface and by increasingly micritic fabric (Fig. 30e). Phase 1 is restricted to the uppermost part of the specimen while phases 2 and 3 occur recurrently in the Hells Bells specimen "Long Bell" (Fig. 30d).

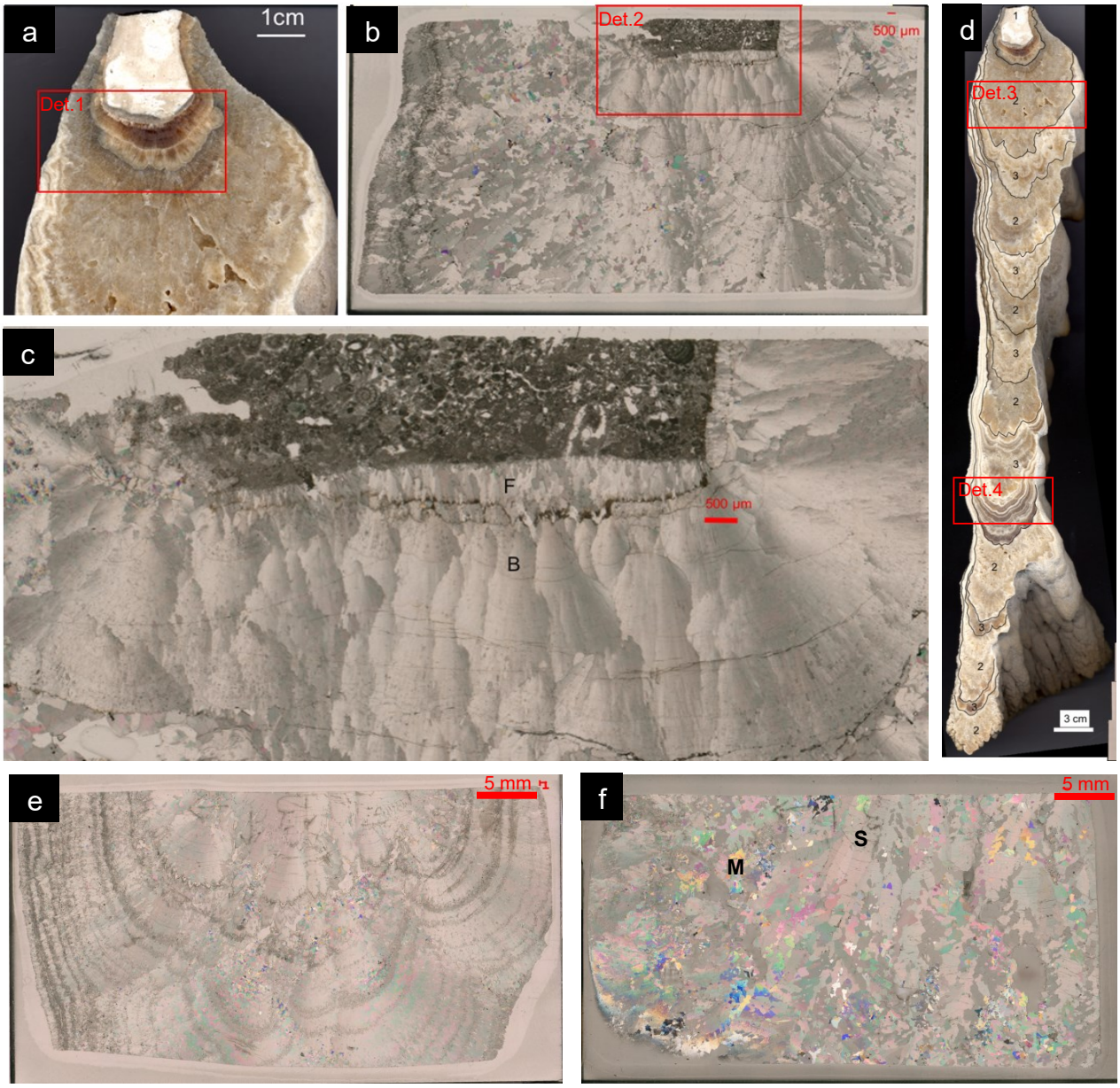

Fig. 30: Petrographic analyses of "Long Bell". a: Location of thin section shown in B in the upper part, the "root" of the specimen; b: Transmitted light microscopic polarized image of thin section (Det. 1 in a); c: Detail of thin section shown in b (Det. 2), note the different lithologies of marine carbonate host rock in the upper part appearing dark with various fossils and Hells Bells calcites appearing bright and massive surrounding the host rock fragment. F represents fibrous, isopachous phases and B represents botryoidal crystal phases. d: Scan of "Long Bell", vertically cut in half and polished. Different growth phases are tentatively distinguished by black lines indicating the initial growth phase on the carbonate host rock (1), periods of rather steady growth conditions (2) and periods of rather frequently interrupted growth conditions indicated by increased lamination (3). e: Landscape image of thin section No. 13 from "Long Bell" (Det. 4 in d) showing repeated phases of dissolution indicated by lamination and the predominantly micritic calcite fabric. f: Landscape image of thin section No. 3 from "Long Bell" (Det. 3 in d) showing rather steady growth conditions indicated by long spherulitic (S) and blocky mosaic calcite (M). Images modified from Sun (2018, unpub.)

4.3 Geochemistry of Hells Bells

In all geochemical analyses, the calcite of Hells Bell speleothems revealed no residues after digesting ~3 mg sample in 12 ml dilute 1 M Nitric indicating that Hells Bells calcite is devoid of acid insoluble impurities. Generally, the geochemistry of Hells Bells is fairly constant over the range of analyzed samples from different cenotes and varying from age-dependent samples taken along the presumed growth axis of several Hells Bells specimen (Table 3 and Table 4) to the "youngest" samples of the lowermost tips of Hells Bells from different water depth (Table 5). The carbonates originating from the host rock can be easily distinguished from Hells Bells carbonate by stable

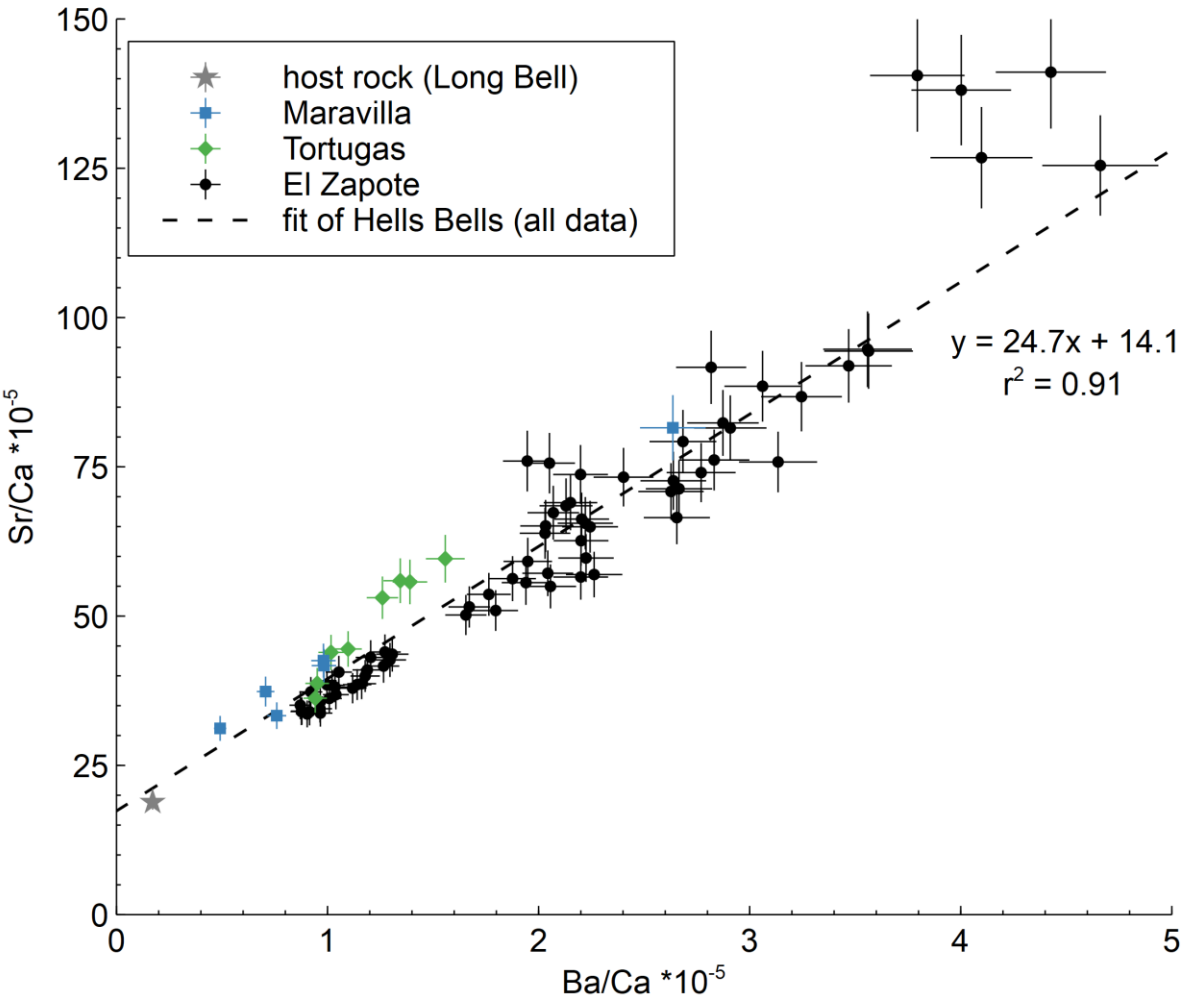

Fig. 31: Ba/Ca against Sr/Ca ratios of all analyzed Hells Bells samples including those of cenotes Maravilla and Tortugas and the host rock sample from the root of "Long Bell". Ba and Sr incorporated into Hells Bells calcite are linearly correlated and indicate that the initial Sr/Ba ratios of the host rock are preserved in Hells Bells carbonates. The data is tabulated in Table 4 (p. 71) and Table 5 p. (72).

carbon isotope values. The host rock shows a $\delta^{13}C$ value of —4.9 ‰ (Table 4) and Hells Bells

samples show a range of $\delta^{13}C$ values of —7.6 to —14.0 ‰ (Table 4and Table 5). Regarding the element chemistry, Hells Bells carbonates differ only slightly from the host rock carbonate by showing generally slightly higher concentrations of Sr, Ba and S (Table 4). The Ba/Ca and Sr/Ca ratios are linearly correlated in all analyzed Hells Bells samples from all cenotes and the linear fit intersects with the Ba/Ca and Sr/Ca ratio of the host rock (Fig. 31). This indicates that the initial Sr/Ba ratio of the host rock is preserved in the Hells Bells carbonates, e.g. via host rock dissolution and re-precipitation.

Details of the respective sample sets of Hells Bells from cenotes El Zapote, Tortugas and Maravilla are presented in the following with regard to their relation of geochemistry to time and water depth.

4.3.1 Time-related variation of Hells Bells geochemistry

4.3.1.1 U-series dating of laminated Hells Bells from cenotes El Zapote, Tortugas and Maravilla

The counter-slabs of the thin sections of the laminated Hells Bells specimens presented before in Figure 29 (p. 61) were sampled and age-dated with U-series age-dating. The sample locations of the specimen are shown together with the respective ages in Figure 32 and the age-dating results are tabulated in Table 3. The age-dating results show that the samples were generally taken along the growth axis of each specimen, except for specimen of cenote Maravilla, which shows a minor age inversion in the middle part of the specimen (Fig. 32). This might indicate that the intersecting plane of specimen MIII from cenote Maravilla is not parallel to the growth axis (Fig. 32). The comparatively small laminated Hells Bells specimen from cenotes El Zapote, Maravilla and Tortugas all reveal relatively high maximum ages of up to 8.58, 6.39 and 4.59 ka BP, respectively (Fig. 32 and Table 3). Minimum ages from the lowermost tips of Hells Bells from cenotes Maravilla and Tortugas show ages of 2.30 to 0.92 ka BP, respectively (Fig. 32). This either indicates that the growth of this specimens has already stopped or that it reflects very slow net growth rates of Hells Bells, which is more likely considering that several 100 µm from the lowermost parts of specimen MIII, T7 and T12 were sampled for analyses. The net growth rates of the Hells Bells specimen are

approximated considering the distances between each sample point, measured as distance from the top (Table 3). The net growth rates of the laminated specimen all show low values ranging from 4–18 µm a^{-1} (Fig. 32). Notably, the specimen of different water depths from cenote Tortugas show opposed trends of net growth rates. Specimen T12 from 30.5 m water depth shows a trend of decreasing growth rates with decreasing age, while this trend is vice versa for specimen T7 from 32.9 m water depth (Table 3 and Fig. 32).

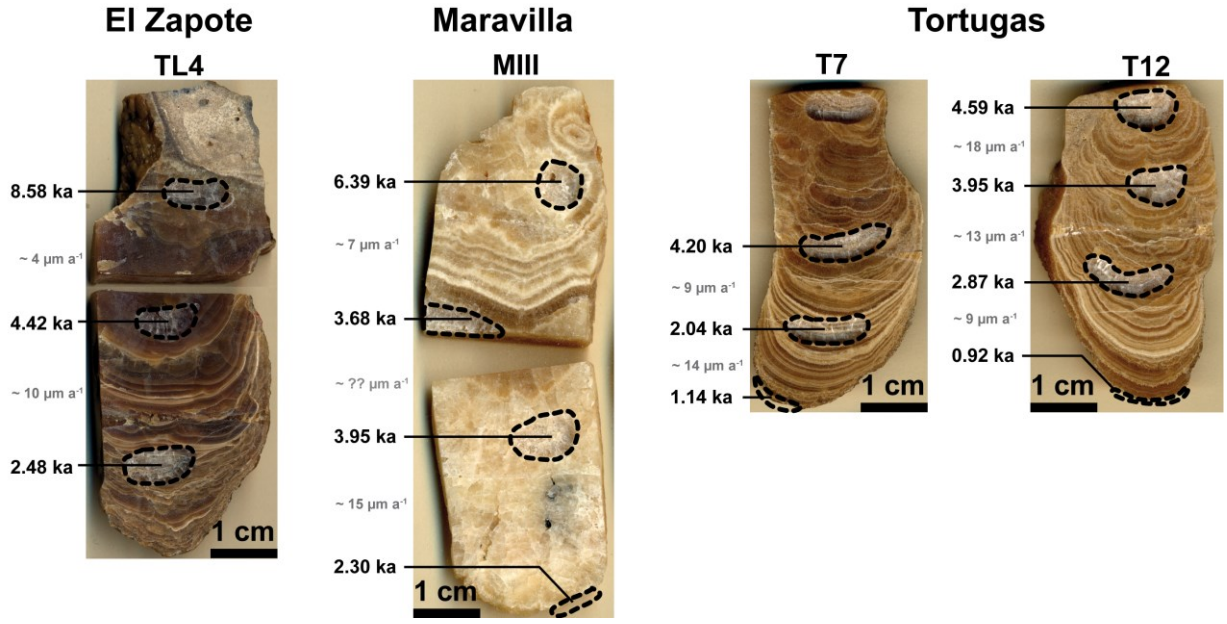

Fig. 32: U-series ages of the respective sampling spots of Hells Bells specimen from cenotes El Zapote (TL4), Maravilla (MIII) and Tortugas (T7 and T12) that were vertically cut along their presumed growth axis. Samples were taken from counter-slabs corresponding to thin sections and polished halves shown in Figure 29 (p.61). U-series ages are tabulated in Table 3. Net growth rates (in grey) are approximated between sampling points taking the ages and distance to the top (dft) given in Table 3 into account. Note: image seizes reflect the original sample proportions to each other.

The geochemical results of the samples from the laminated Hells Bells specimen are tabulated in Table 4 and selected geochemical parameters are plotted against the sample ages in Figure 33. Several similar trends in element an isotope geochemistry are observed in the samples of the laminated Hells Bells specimen from different cenotes (Fig. 33). The Sr/Ca and Ba/Caratios show a decreasing trend from ~4 ka BP towards younger ages in all specimens, while for Mg/Ca ratios this trend is not as clear as for Sr/Ca and Ba/Ca (Fig. 33 and Table 4). The S/Ca ratios gradually increase towards younger ages in the samples of cenotes El Zapote and Tortugas, while the samples of cenote Maravilla show an opposed trend (Fig. 33).

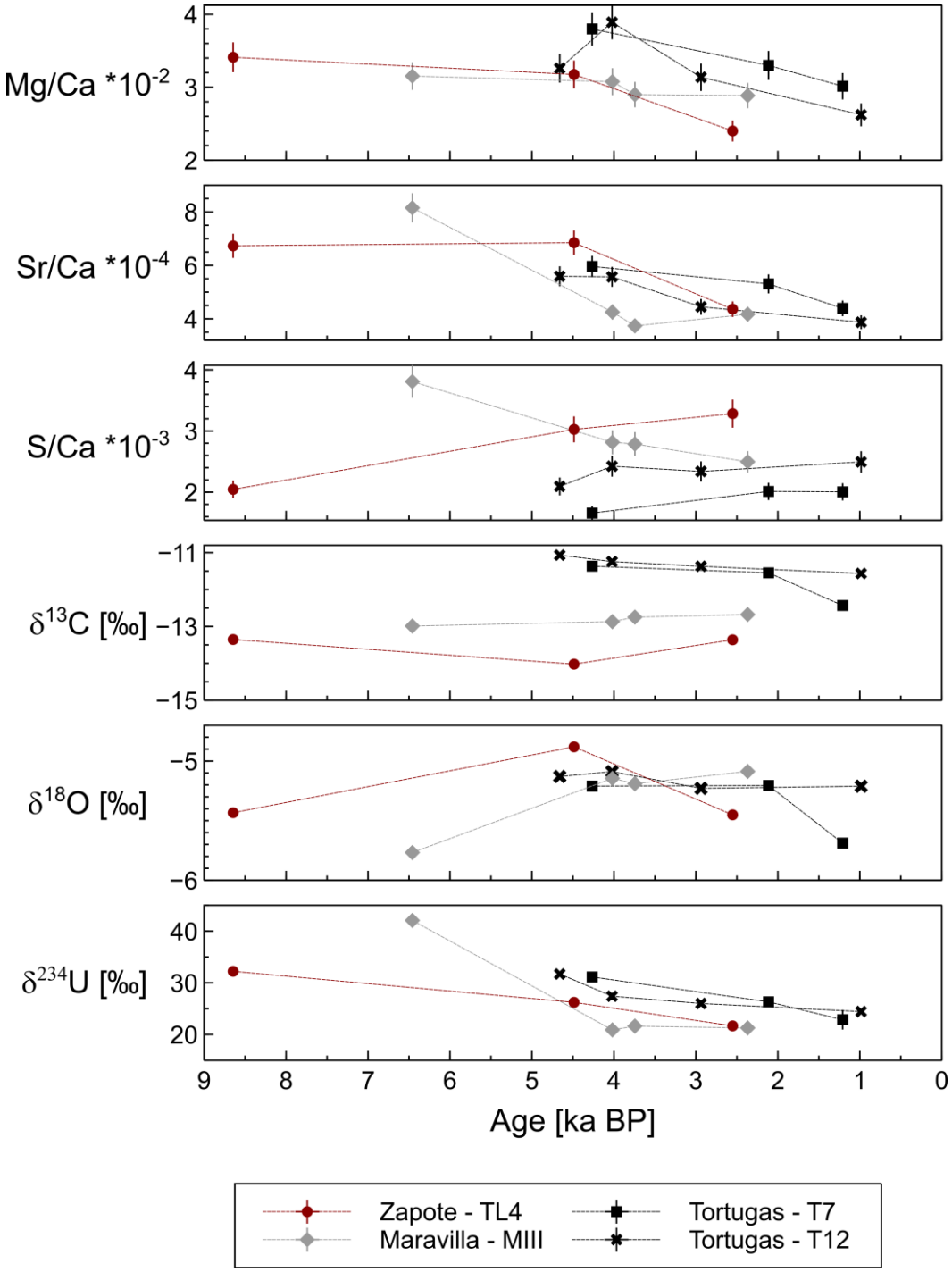

Fig. 33: Element- and isotope-geochemistry of the laminated Hells Bells specimens from cenotes El Zapote (TL4), Maravilla (MIII) and Tortugas (T7 and T12) over time. The data is tabulated in Table 3 and Table 4 (p.71).

The values of $\delta^{234}U_{initial}$, a "byproduct" of U-series age dating, show a trend of decreasing values from up to 32–42 ‰ towards values of ~21 ‰ for the youngest measured sample ages (Table 3). Stable oxygen isotope values of all samples from the different cenotes fall in a narrow range of

$\delta^{18}O$ values of –5.1 to –5.8 ‰ revealing no clear trends (Fig. 33). The patterns of stable carbon isotope values show no clear trends within each specimen but the patterns show a clear differentiation between the cenotes El Zapote, Maravilla and Tortugas with $\delta^{13}C$ values of –13.6 ± 0.3, –12.8 ± 0.1 and –11.4 ± 0.1, respectively (Fig. 33 and Table 3).

Table 3: Results of U-series dating of Hells Bells specimen from cenotes El Zapote, Maravilla and Tortugas along their presumed growth axis. dft = depth from top.

Sample No./ID	Sample location	water depth [m]	dft [m]	^{238}U [µg/g]	^{232}Th [ng/g]	2σ	$^{230}Th/^{238}U$	2σ	Age_{corr} [ka BP]	2σ	$\delta^{234}U_{initial}$	2σ
TL4_1	Zapote	35.8	1.6	0.67	0.53	0.00	78.5	0.23	8.58	0.03	32.2	0.5
TL4_3	Zapote	35.8	3.6	0.47	0.26	0.00	41.3	0.21	4.42	0.02	26.2	0.3
TL4_2	Zapote	35.8	5.8	0.95	3.12	0.02	23.6	0.43	2.48	0.05	21.7	0.4
MIII_1	Maravilla	29.4	1.4	1.51	0.32	0.00	59.8	0.14	6.39	0.02	42.1	0.4
MIII_2	Maravilla	29.4	4.5	1.83	0.28	0.00	34.4	0.09	3.68	0.01	21.6	0.4
MIII_3	Maravilla	29.3	3.5	1.72	0.30	0.00	36.9	0.10	3.95	0.01	20.9	0.3
MIII_4	Maravilla	29.3	7.0	3.10	0.91	0.01	21.9	0.07	2.30	0.01	21.3	0.3
T7_2	Tortugas	32.9	2.3	1.01	0.44	0.00	39.5	0.15	4.20	0.02	31.1	0.4
T7_3	Tortugas	32.9	3.6	1.15	0.82	0.01	19.7	0.11	2.04	0.01	26.3	0.3
T7_4	Tortugas	32.9	4.6	1.31	1.82	0.01	11.3	0.20	1.14	0.02	22.8	1.9
T12_1	Tortugas	30.5	0.4	0.93	0.34	0.00	43.1	0.13	4.59	0.01	31.7	0.4
T12_2	Tortugas	30.5	1.6	0.70	0.98	0.01	37.2	0.22	3.95	0.02	27.4	0.7
T12_3	Tortugas	30.5	3.0	0.85	0.49	0.00	27.2	0.12	2.87	0.01	26.0	0.6
T12_4	Tortugas	30.5	4.8	0.90	1.07	0.01	9.2	0.16	0.92	0.02	24.4	0.5

4.3.1.2 Geochemistry of "Long Bell" and "Big Bell" from cenote El Zapote

The elongated specimen "Long Bell" (ZPT 7 in Stinnesbeck et al., 2017b) was sampled and analyzed in with a high resolution along its presumed growth axis (Schorndorf, 2018, unpub.). The results are tabulated in Table 4 and selected geochemical parameters are presented in Figure 34 with respect to the sample location and the distance from the top. The consecutive age of "Long Bell" can be approximated by the distance from the top, since its growth direction is indicated by petrographic analyses (section 4.2.3, p.62).

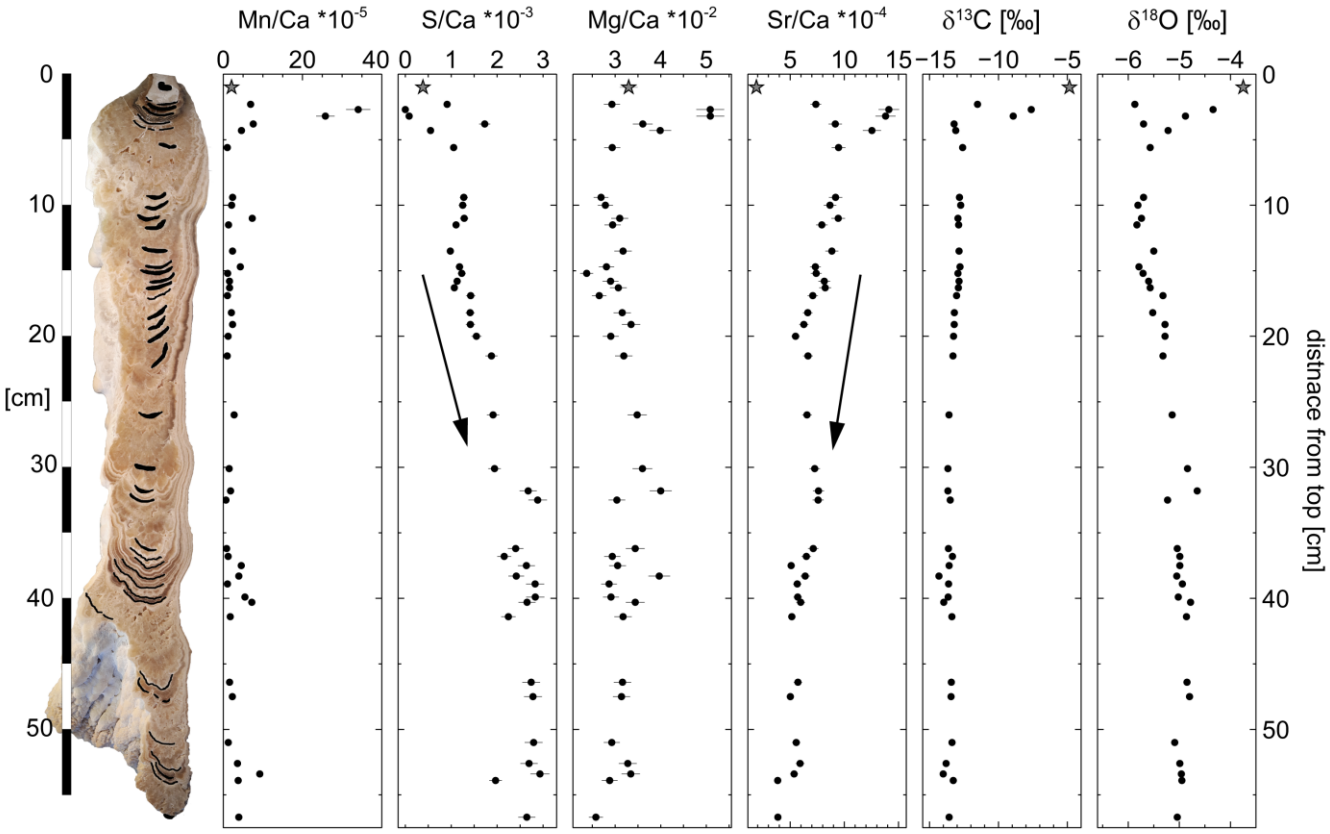

Fig. 34: Geochemistry of "Long Bell" along the presumed growth axis. Sample spots on the specimen are indicated by blackened areas in the image on the left and the uppermost sample represents carbonate host rock as indicated by petrographic analyses (section 4.2.3, p. 62). Note the increasing and decreasing trends of S/Ca and Sr/Ca ratios between ~15–40 cm from top, respectively.

Dark, brownish-colored layers identified on the polished half of "Long Bell" correspond to elevated Mn/Ca and Fe/Ca values (Fig. 34). The Sr/Ca and Ba/Ca ratios show trends of decreasing values with increasing distance from the top (Fig. 34) similar to those observed in the laminated Hells Bells samples (Fig. 33). Also, likewise to the trend observed for the laminated specimen of cenotes El Zapote and Maravilla (Fig. 33), the S/Ca ratios of "Long Bell" reveal an increasing trend with increasing distance to the top (Fig. 34). The Mg/Ca ratios show elevated values of 0.051 in the uppermost, probably the oldest, part of "Long Bell". Subsequently, Mg/Ca ratios show variable values within a relatively wide range from 0.024–0.040 (Fig. 34 and Table 4). In the uppermost part of "Long Bell", stable carbon isotopes show high $\delta^{13}C$ values of up to -7.6 ‰. The $\delta^{13}C$ values then abruptly drop at ~3.8 cm distance from the top. From there $\delta^{13}C$ values slightly decrease from -12.7 to -14.0 ‰ with increasing distance from the top (Fig. 34 and Table 4). The stable oxygen isotopes show high $\delta^{18}O$ values of up to -4.3 ‰ in the uppermost part of the

specimen with an abrupt drop to $\delta^{18}O$ values of –5.7‰ at ~3.8 cm distance from the top. From there, opposed to the trend of stable carbon isotope, the $\delta^{18}O$ values slightly increase with increasing distance to the top to values of up to –5.0 ‰ in the lowermost part of "Long Bell" (Fig. 34 and Table 4).

The Hells Bells specimen "Big Bell" from cenote El Zapote was sampled for geochemical analyses at the lowermost part (samples BB6) and at a slab that was cut off from the "root" of "Big Bell" perpendicular to its growth axis (Fig. 13, p.26). The data is tabulated in Table 4. The innermost samples of the slab from the root (BB1-1 and BB1-2) show similar values of the element ratios Mg/Ca, Sr/Ca, Ba/Ca, S/Ca and Mn/Ca to the majority of the other Hells Bells samples of cenote El Zapote (Table 4). The stable carbon and oxygen isotopes, however, differ with higher $\delta^{13}C$ of –12.0 ‰ and lower $\delta^{18}O$ values of around –6.3 ‰ compared to the rest of the values of cenote El Zapote (Table 4). The two outermost samples of the "root" of "Big Bell" show the highest measured Mg/Ca ratios of all samples of up to 0.061 (Table 4). The other element ratios of these samples resemble those of the uppermost part of "Long Bell" with elevated ratios of Sr/Ca, Ba/Ca and Mn/Ca (Table 4). The samples BB6-1 and BB6-2, taken from the lowermost part of "Big Bell", show values similar to the other analyses of Hells Bells specimen from El Zapote, except for the uppermost and innermost parts of "Long Bell" and "Big Bell" (Table 4).

Table 4: Geochemical data of different Hells Bells specimen of samples taken along their presumed growth axis. Uncertainties of stable isotope analyses $\delta^{13}C$ and $\delta^{18}O$ are <0.02 ‰. dft = depth from top.

Sample No./ID	Sample location	Sample type	Water depth [m]	dft [cm]	Mg/Ca [10^{-2}]	Sr/Ca [10^{-4}]	Ba/Ca [10^{-5}]	Fe/Ca [10^{-5}]	Mn/Ca [10^{-5}]	S/Ca [10^{-3}]	$\delta^{13}C$ [‰VPDB]	$\delta^{18}O$ [‰VPDB]
TL4_1	Zapote	-	35.8	1.6	3.41	6.7	2.07	4.1	3.0	2.0	-13.35	-5.43
TL4_3	Zapote	-	35.8	3.6	3.18	6.8	2.13	1.8	2.1	3.0	-14.02	-4.88
TL4_2	Zapote	-	35.8	5.8	2.40	4.4	1.31	9.0	8.1	3.3	-13.36	-5.45
MII_1	Maravilla	-	29.4	-	3.17	3.1	0.49	7.9	2.3	1.5	-	-
MII_2	Maravilla	-	29.4	-	2.50	3.3	0.76	1.6	1.2	1.8	-	-
MIII_1	Maravilla	-	29.3	1.4	3.15	8.2	2.64	1.7	1.9	3.8	-12.99	-5.77
MIII_2	Maravilla	-	29.3	3.5	2.90	3.7	0.71	2.3	5.8	2.8	-12.75	-5.19
MIII_3	Maravilla	-	29.3	4.5	3.08	4.3	0.98	1.9	3.2	2.8	-12.87	-5.15
MIII_4	Maravilla	-	29.3	7.0	2.89	4.2	0.98	0.8	2.1	2.5	-12.68	-5.09
T7_1	Tortugas	-	32.9	0.2	3.80	6.0	1.56	5.5	2.4	1.7	-	-
T7_2	Tortugas	-	32.9	2.3	3.30	5.3	1.26	6.6	1.7	2.0	-11.37	-5.21
T7_3	Tortugas	-	32.9	3.6	3.01	4.4	1.02	9.1	4.0	2.0	-11.55	-5.21
T7_4	Tortugas	-	32.9	4.6	2.17	3.6	0.94	5.4	1.8	2.3	-12.43	-5.69
T12_1	Tortugas	-	30.5	0.4	3.26	5.6	1.34	4.7	1.1	2.1	-11.07	-5.13
T12_2	Tortugas	-	30.5	1.6	3.89	5.6	1.39	4.0	1.5	2.4	-11.24	-5.09
T12_3	Tortugas	-	30.5	3.0	3.14	4.4	1.10	10.4	2.5	2.3	-11.37	-5.23
T12_4	Tortugas	-	30.5	4.8	2.62	3.9	0.95	5.0	1.8	2.5	-11.56	-5.21
LB-1	Zapote	Host rock	-	1.0	3.30	1.9	0.17	5.1	2.1	0.4	-4.85	-3.75
LB-2	Zapote	Long Bell	-	2.3	2.93	7.4	2.20	31.3	6.9	0.9	-11.52	-5.87
LB-3	Zapote	Long Bell	-	2.7	5.09	14.1	4.43	4.1	34.1	0.0	-7.62	-4.34
LB-4	Zapote	Long Bell	-	3.2	5.09	13.8	4.00	4.4	25.8	0.1	-8.93	-4.88
LB-5	Zapote	Long Bell	-	3.8	3.61	9.2	2.82	7.1	7.6	1.7	-13.22	-5.70
LB-6	Zapote	Long Bell	-	4.3	3.99	12.5	4.66	3.5	4.6	0.5	-13.10	-5.22
LB-7	Zapote	Long Bell	-	5.6	2.94	9.5	3.56	5.6	1.0	1.1	-12.60	-5.57
LB-8	Zapote	Long Bell	-	9.4	2.69	9.2	3.47	4.2	2.4	1.3	-12.83	-5.70
LB-9	Zapote	Long Bell	-	10.0	2.79	8.7	3.25	3.4	2.1	1.2	-12.74	-5.81
LB-10	Zapote	Long Bell	-	11.0	3.10	9.4	3.56	6.3	7.3	1.3	-12.94	-5.74
LB-11	Zapote	Long Bell	-	11.5	2.94	7.9	2.68	2.4	1.3	1.1	-12.89	-5.83
LB-12	Zapote	Long Bell	-	13.5	3.17	8.9	3.06	1.7	2.3	1.0	-12.86	-5.50
LB-13	Zapote	Long Bell	-	14.7	2.81	7.3	2.40	11.2	4.3	1.2	-12.79	-5.79
LB-14	Zapote	Long Bell	-	15.2	2.38	7.4	2.77	1.6	1.1	1.2	-12.94	-5.71
LB-15	Zapote	Long Bell	-	15.8	2.90	8.2	2.91	2.6	1.6	1.1	-12.86	-5.60
LB-16	Zapote	Long Bell	-	16.3	3.07	8.2	2.87	2.9	1.6	1.1	-12.91	-5.57
LB-17	Zapote	Long Bell	-	16.9	2.65	7.1	2.63	4.0	1.1	1.4	-13.04	-5.32
LB-18	Zapote	Long Bell	-	18.2	3.16	6.6	2.20	2.2	2.1	1.4	-13.20	-5.52
LB-19	Zapote	Long Bell	-	19.1	3.35	6.3	2.20	2.2	2.3	1.4	-13.21	-5.28
LB-20	Zapote	Long Bell	-	20.0	2.90	5.5	2.06	6.0	1.2	1.5	-13.26	-5.28
LB-21	Zapote	Long Bell	-	21.5	3.19	6.6	2.65	0.8	1.0	1.9	-13.30	-5.32
LB-22	Zapote	Long Bell	-	26.0	3.48	6.6	2.22	12.3	2.7	1.9	-13.59	-5.14
LB-23	Zapote	Long Bell	-	30.1	3.60	7.3	2.64	2.1	1.5	1.9	-13.67	-4.84
LB-24	Zapote	Long Bell	-	31.8	4.00	7.6	2.83	2.0	1.8	2.7	-13.67	-4.65
LB-25	Zapote	Long Bell	-	32.5	3.04	7.6	3.13	0.9	0.7	2.9	-13.50	-5.23
LB-26	Zapote	Long Bell	-	36.2	3.44	7.1	2.67	0.5	0.8	2.4	-13.63	-5.04
LB-27	Zapote	Long Bell	-	36.8	2.94	6.5	2.24	11.3	1.2	2.2	-13.34	-4.99
LB-28	Zapote	Long Bell	-	37.5	3.05	5.1	1.80	5.6	4.5	2.6	-13.58	-4.99
LB-29	Zapote	Long Bell	-	38.3	3.97	6.4	2.03	0.7	3.9	2.4	-14.32	-5.05
LB-30	Zapote	Long Bell	-	38.9	2.87	5.7	2.20	0.5	1.1	2.8	-13.62	-4.94
LB-31	Zapote	Long Bell	-	39.9	2.91	5.7	2.26	4.4	5.5	2.8	-13.65	-5.02
LB-32	Zapote	Long Bell	-	40.3	3.44	6.0	2.22	3.7	7.2	2.7	-13.97	-4.78
LB-33	Zapote	Long Bell	-	41.4	3.17	5.2	1.67	2.0	1.8	2.2	-13.38	-4.86
LB-34	Zapote	Long Bell	-	46.4	3.16	5.7	2.04	2.3	1.6	2.7	-13.42	-4.85
LB-35	Zapote	Long Bell	-	47.5	3.14	5.0	1.66	2.0	2.3	2.8	-13.44	-4.80
LB-36	Zapote	Long Bell	-	51.0	2.93	5.6	1.94	6.3	1.3	2.8	-13.37	-5.09
LB-37	Zapote	Long Bell	-	52.6	3.28	5.9	1.95	4.4	3.6	2.7	-13.80	-4.99
LB-38	Zapote	Long Bell	-	53.4	3.34	5.4	1.76	7.6	9.2	2.9	-14.01	-4.96
LB-39	Zapote	Long Bell	-	53.9	2.88	3.9	1.00	7.1	3.8	2.0	-13.28	-4.95
LB-40	Zapote	Long Bell	-	56.7	2.58	3.9	1.16	6.0	3.9	2.6	-13.58	-5.04
BB 1 - 1	Zapote	Big Bell	-	0	2.57	7.6	1.95	46.4	2.5	1.8	-11.99	-6.39
BB 1 - 2	Zapote	Big Bell	-	0	2.83	7.6	2.05	22.6	1.4	1.6	-12.03	-6.10
BB 1 - 3	Zapote	Big Bell	-	0	6.10	14.1	3.79	5.1	23.8	-	-8.15	-4.19
BB 1 - 4	Zapote	Big Bell	-	0	4.80	12.7	4.10	11.3	2.4	-	-12.67	-5.40
BB 6 - 1	Zapote	Big Bell	-	~180	3.58	6.9	2.15	3.9	10.9	3.4	-	-
BB 6 - 2	Zapote	Big Bell	-	~180	3.46	6.5	2.03	4.2	10.3	3.1	-14.27	-4.90

4.3.1 Water depth-related variation of Hells Bells geochemistry

Samples were taken from the lowermost and presumably youngest part of several Hells Bells specimens of different water depths that grew on the cavern ceiling and walls and on a ceiba tree fallen into the cenote El Zapote at about 3.5 cal kyr BP (Stinnesbeck et al., 2017b). The lack of samples in water depths from 34.3 to 36.8 m water depth is due to poor visibility in the turbid layer above the halocline. The samples were analyzed for major and trace elements as well as stable carbon isotopes. The results are given in Table 5 and selected parameters are plotted in Figure 35. Schorndorf et al. (in prep.) analyzed the samples of the lowermost tips from the Tree Bells and found similar ages of 100–200 years BP in all samples with no age-dependency on water depth. This indicates that the dependency of the geochemistry of Hells Bells on water depth can be evaluated with the data obtained from the lowermost tips of Hells Bells since it can be assumed that the environmental conditions on the YP have not changed significantly within the last 200 years.

Table 5: Geochemistry of "youngest" lowermost tips of Hells Bells growing on a subfossil ceiba tree (Tree Bells) that fell into the cenote El Zapote about 3.5 cal ka BP and from other Hells Bells of different water depths. Individual Hells Bells samples were sampled at water depths from 30 to 37.3 m. Uncertainties of element chemistry are given in the method section 3.3.2.1 (p. 29) and given uncertainties of $\delta^{13}C$ and $\delta^{18}O$ represent 2σ standard deviations.

Sample No.	Sample type	water depth [m]	Mg/Ca [10^{-2}]	Sr/Ca [10^{-4}]	Ba/Ca [10^{-5}]	Fe/Ca [10^{-5}]	Mn/Ca [10^{-5}]	S/Ca [10^{-3}]	$\delta^{13}C$ [‰$_{VPDB}$]	$\delta^{18}O$ [‰$_{VPDB}$]
1	Tre Bell	31.3	2.14	4.16	1.27	4.3	2.1	2.78	-13.47 ±	-4.34 ±
2	Tre Bell	32.8	2.56	4.10	1.19	5.2	2.6	2.69	-13.69 ±	-4.83 ±
3	Tre Bell	33.3	2.20	4.27	1.30	3.8	2.4	3.05	-13.82 ±	-4.92 ±
4	Tre Bell	33.3	2.23	3.85	1.14	3.0	1.6	2.54	-13.43 ±	-4.92 ±
5	Tre Bell	33.8	2.08	3.79	1.12	3.5	2.4	2.72	-13.52 ±	-4.96 ±
6	Tre Bell	33.9	2.32	4.00	1.18	3.9	2.2	2.76	-13.68 ±	-4.84 ±
7	Tre Bell	36.8	2.23	3.40	0.88	11.3	3.9	3.14	-12.87 ±	-5.40 ±
8	Tre Bell	36.8	2.11	3.41	0.88	10.6	2.8	3.02	-12.85 ±	-5.35 ±
9	Tre Bell	37.3	2.40	3.73	0.92	6.2	3.2	3.17	-12.99 ±	-5.13 ±
10	Other	30.0	3.00	5.63	1.88	13.1	14.4	3.12	-12.96 ±	-4.60 ±
11	Other	32.9	2.33	3.40	0.92	8.5	3.13	2.4	-13.72 ±	-5.10 ±
12	Other	34.0	2.62	3.68	1.04	5.4	1.55	2.6	-13.75 ±	-4.90 ±
13	Other	34.3	2.79	4.40	1.27	2.9	2.63	2.9	-13.33 ±	-4.82 ±
14	Other	36.8	2.54	3.51	0.87	9.0	2.58	2.9	-13.32 ±	-5.22 ±
		Mean	2.40	3.95	1.13	6.49	3.39	2.84	-13.38	-4.95
	2σ	0.53	1.13	0.51	6.50	6.21	0.47	0.66	0.55	2σ

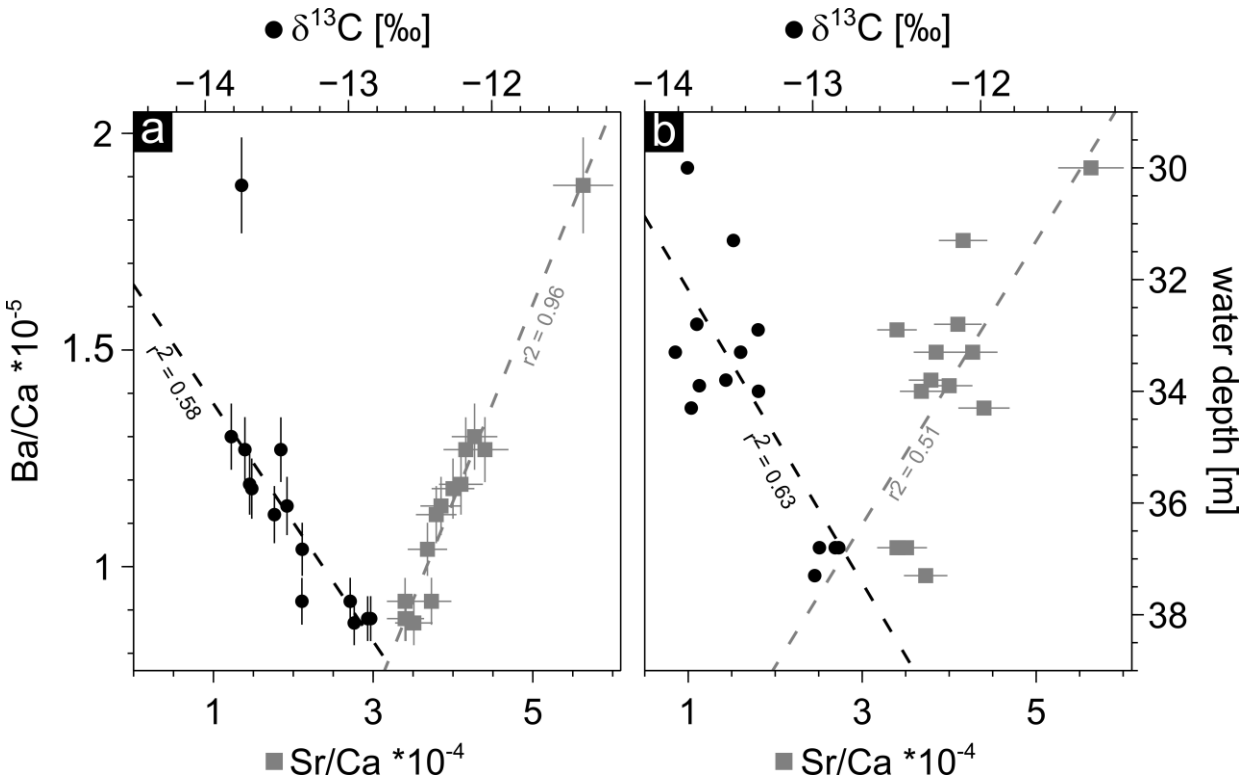

Fig. 35: Geochemical data of lowermost "youngest" part of Hells Bells speleothems showing correlations between Sr/Ca and Ba/Ca ratios and between Ba/Ca and $\delta^{13}C_{calcite}$ (a) and a trend of increasing $\delta^{13}C$ and decreasing Sr/Ca with increasing water depth of the samples (b). Given uncertainties represent 2σ standard deviations and ± 0.25 m is assumed as uncertainty for the water depth of the Hells Bell samples.

The Mg/Ca, Sr/Ca and Ba/Ca ratios show narrow ranges with mean values of 2.40 ± 0.53 10^{-2}, 3.95 ± 1.13 10^{-4} and 1.13 ± 0.51 10^{-4}, respectively. They are closely related and positively correlate in each sample (Fig. 35a). There is also a trend towards decreasing ratios with increasing water depth of the respective sample (Fig. 35b). Iron and manganese show more variable concentrations with ratios of Fe/Ca and Mn/Ca between 3.0–13.1 10^{-5} and 1.6–14.4 10^{-5}, respectively. Iron and manganese show a weak positive correlation but no dependency on water depth. The content of sulfur in Hells Bells carbonate is constantly high with mean S/Ca ratios of 2.84 ± 0.47 10^{-3}, showing no dependency on water depth of the sample (Table 5).

Stable carbon isotope values of "youngest" Hells Bells calcite samples ($\delta^{13}C$) from different water depth range from –12.85 to –13.82 ‰ with a mean value of -13.38 ± 0.66 ‰ (Table 5). There is a

weak correlation of increasing $\delta^{13}C$ values with water depth of the samples (Fig. 35b). Furthermore, $\delta^{13}C$ values show a negative correlation with Sr/Ca and Ba/Ca with r^2 of 0.58 and 0.63, respectively (Fig. 35a).

The stable carbon isotope ratio of the HCO_3^-, which is in equilibrium with the Hells Bells calcite ($\delta^{13}C\text{-}_{eq}HCO_3^-$) at 25 °C water temperature ($\delta^{13}C_{Calcite}$ – 0.91 ‰ = $\delta^{13}C\text{-}_{eq}HCO_3^-$), was calculated after Mook (2000). The calculated $\delta^{13}C\text{-}_{eq}HCO_3^-$ is –14.29 ± 0.66 ‰, which is lower than the $\delta^{13}C\text{-}HCO_3^-$ determined for the water column with a range of -9.1 to –12.3 ‰ (section 4.1.1.3, p. 42).

4.4 Observation of aquifer dynamics with data of loggers

Data loggers were installed in the freshwater bodies and the haloclines of cenotes with Hells Bells El Zapote, Maravilla and Tortugas for a continuous monitoring of the water level and the halocline elevation (for details see section 3.4, p. 31). The longest time series data was obtained for cenote El Zapote with ~22 months while the period for cenotes Maravilla and Tortugas comprise ~5 months each. Yet, the results on aquifer dynamics presented in the following are preliminary as the recorded period is too short to cover all relevant processes with respect to the aquifer dynamics of the Yucatán Karst Aquifer.

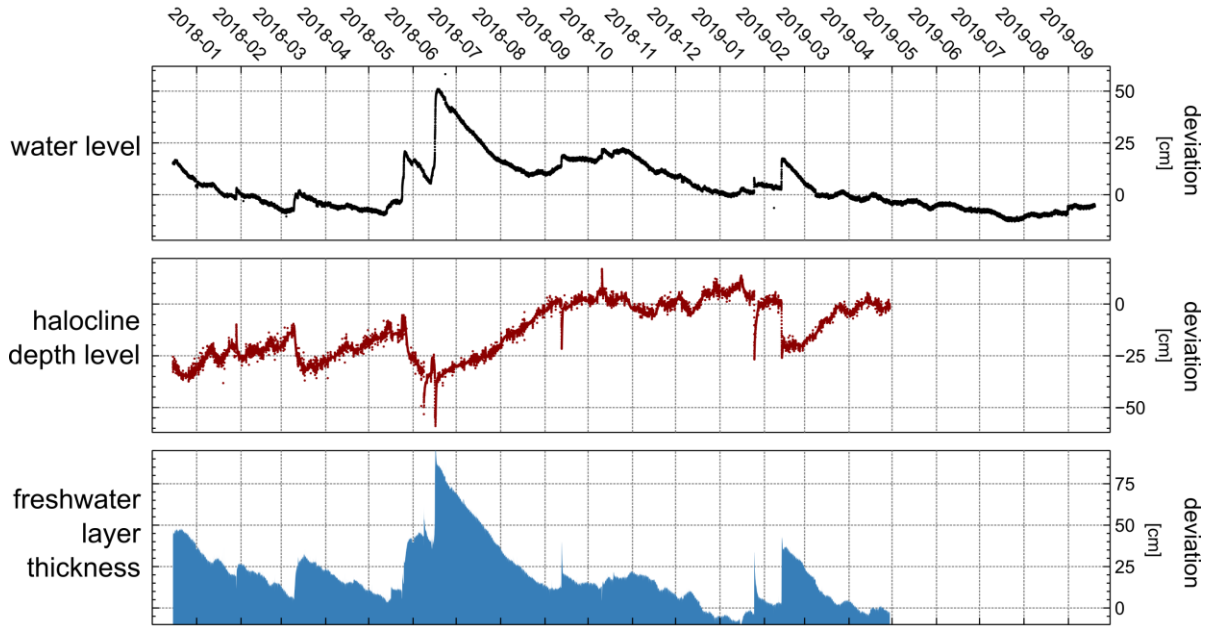

Fig. 36: Time series of deviations of the water level, halocline depth level and freshwater layer thickness at cenote El Zapote. Note that the missing data from end of April 2019 and forth is due to recording failure of the CTD logger placed in the halocline. The data is given in Table A3.

The complete time series for El Zapote regarding relative changes in water level, halocline elevation and thickness of the freshwater lens is presented in Figure 36. Generally, the water level and the halocline depth level is controlled by several factors, which are in order of increasing frequency, glacial sea-level fluctuations, dry/wet periods, annual sea-level fluctuations, tidal and subtidal effects and recharge/precipitation including heavy precipitation events like hurricanes. Only the latter three can be assessed with the preliminary data set presented here.

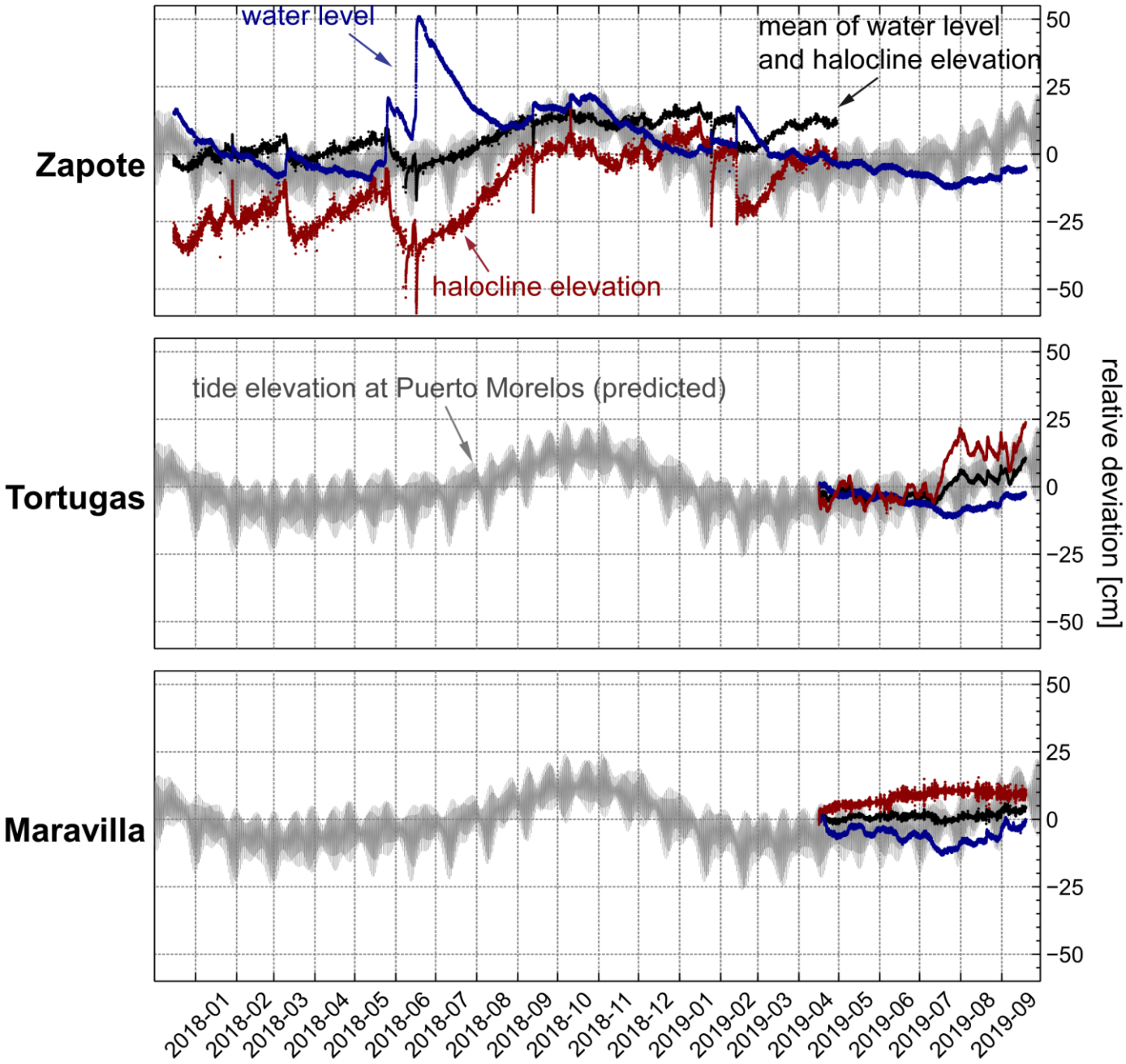

Fig. 37: Timeseries of the deviation of water level (blue) and halocline elevation (red) in context of the predicted maximum and minimum tide elevation at Puerto Morelos (grey). The mean values of the water level and the halocline deviations (black) roughly follow the annual tidal variation. The water level and the halocline elevation show a general negative correlation. Tide elevations at Puerto Morelos were calculated with "Programa MAR V1.0" provided by CICESE, the "*Centro* de Investigación Científica y de Educación Superior de Ensenada, Baja California", Mexico. The data is given in Tables A4–A6.

The data shows that the water level and the halocline elevation are generally anti-correlated, indicated by an increasing halocline elevation with decreasing water levels and vice versa (Fig. 36). This reflects the variation of the thickness of the freshwater layer (Fig. 36). This variation mainly results from both, variable groundwater recharge due to seasonal precipitation patterns, which is

preferentially wet in summer and autumn (May–October) and dry in winter and spring (November–April) as well as from annual sea level fluctuations with autumn highs and spring lows (Fig. 37). The annual sea level is given in Figure 37 together with the halocline elevation and the water level. The mean of halocline elevation and of the water level can be explained by a first order control of the annual sea level changes as they closely follow the annual sea level fluctuation calculated for Puerto Morelos (Fig. 37). For the limited period of data available for cenotes Tortugas and Maravilla this seems to be equally valid (Fig. 37). The sea level varies within ~0.4 m in height coinciding with the variations of the halocline elevation (Fig. 36 and Fig. 37). A fortnight periodicity of tidal effects (spring/neap tides) is present but has only marginal amplitudes of <5 cm of variation in height (Fig. 36 and Fig. 37). Such low frequent effects on water levels were also reported for measurements at a borehole 10 km inland (Vera et al., 2012).

A longer-term influence of droughts or a sequence of drier/wetter years resulting in a thinning of the freshwater lens is indicated by the steady increase of the mean values of halocline elevation and water level (Fig. 36, Fig. 37). However, the logging period is too short for definitive conclusions regarding long-term developments.

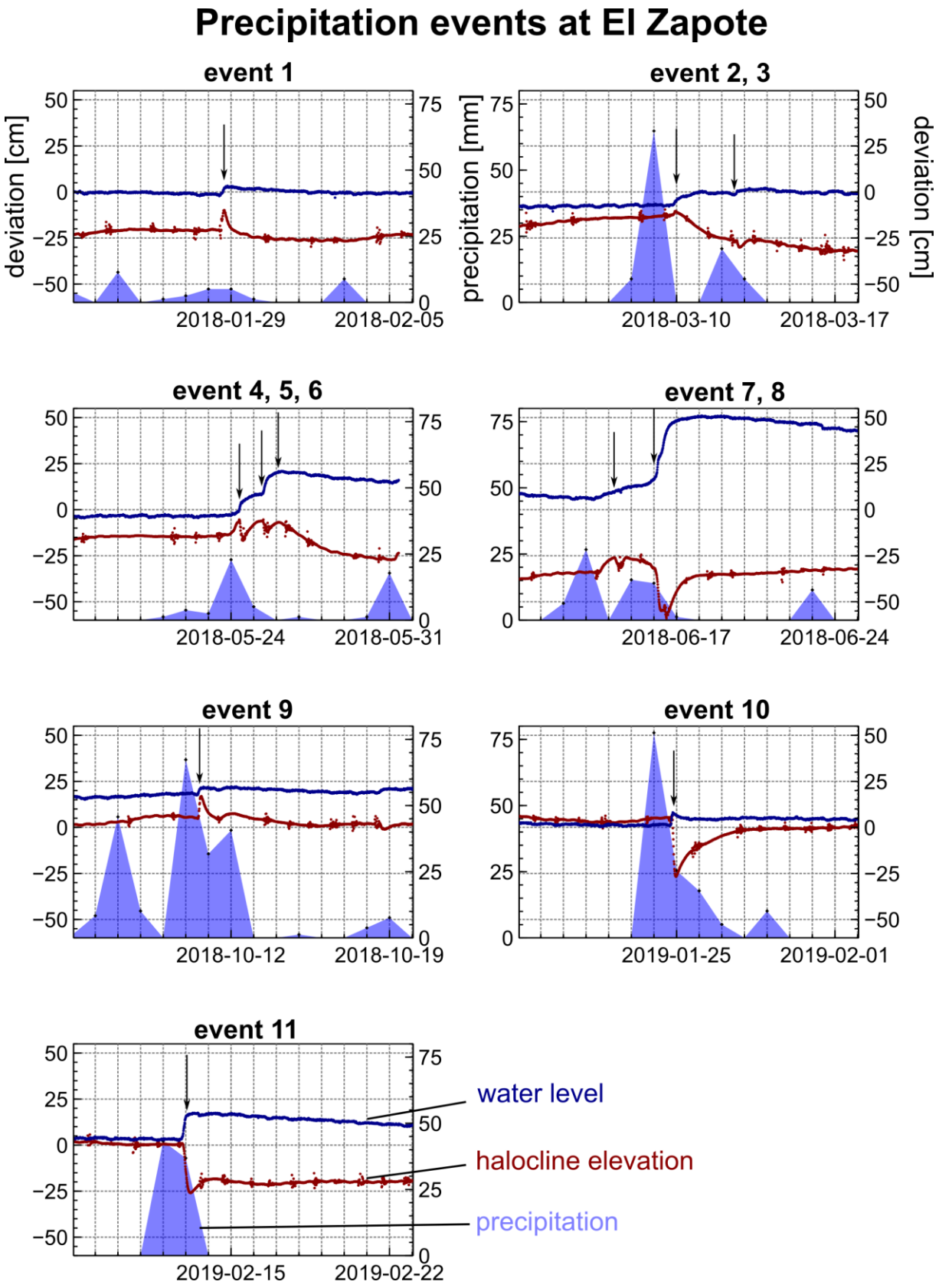

Fig. 38: Precipitation events detected in cenote El Zapote during the whole logging period. The logger data is given in Table A4 and the precipitation record is taken from weather station at Cancun International (Elevation: 7m 21.03 °N, -86.87 °W, data source: wundergroud.com).

For the period of logging in El Zapote, 11 precipitation events were identified revealing that short-termed precipitation events appear to result in different aquifer responses (Fig. 38). The responses can be separated into two groups. One group shows the expected hydraulic aquifer reaction in response to precipitation expressed by a decreasing halocline elevation coinciding with an increase of the water level indicated by events 3, 8, 10 and 11 in Figure 38. The other group is comprised of events that show a counter-intuitive aquifer response to precipitation. The precipitation signal for events 1, 2, 4, 5, 6, 7 and 9 shows an initial abrupt increase of both, halocline elevation and water level, followed by a slower decrease of the halocline elevation while the water level stays at the elevated level (Fig. 38). Although the amplitudes of the halocline elevation related to these events of a counter-intuitive aquifer behavior are low with <10 cm, it proves the principle of the mechanism of a recharge-driven halocline elevation suggested by Ritter et al., (2019) and discussed later on in section 5.3 (p. 121). Furthermore, heavy precipitation events such as tropical cyclones and major hurricanes that occur with every ~2–10 years less frequent in the area (Farfán et al., 2014), must have a much greater influence on the aquifer responses and would most certainly result in higher amplitudes of halocline elevations. However, no major precipitation events occurred during the logging period so far.

In conclusion, the results of the logger data show that the first order control of the halocline elevation with regard to short-term variations is the annual sea level fluctuation leading to variations in height of the halocline of ~0.4 m. This may be combined with long-term (intra-decadal and decadal) changes of the freshwater layer thickness in response to fluctuations in precipitation.

5. Discussion

The processes leading to Hells Bells growth, their characteristic morphology and distribution in cenotes of the Yucatán Peninsula (YP) are discussed in the following. First of all, biogeochemical mechanisms for a subaqueous authigenic calcite precipitation within the narrow water layer of the redoxcline are elaborated on the basis of the data set from cenote El Zapote. This is followed by elucidating the hydrologic controls on the biogeochemistry and authigenic calcite precipitation in the redoxclines of deep stratified cenotes. Furthermore, the essential role of a dynamic halocline elevation in Hells Bells formation is discussed. Based on this, the characteristic shape of Hells Bells and the spatial distribution of cenotes with Hells Bells are examined. Finally, their potential as geoarchive for reconstructing paleo environmental conditions on the YP is assessed.

5.1 Unravelling the mechanism for subaqueous calcite precipitation

This chapter is comprised of the major findings of Ritter et al. (2019). In order to understand the processes leading to subaqueous calcite precipitation in cenotes with Hells Bells, the limnological and hydrological conditions at cenote El Zapote are assessed at first, followed by the identification of the zone of subaqueous calcite precipitation within the water body. By focusing on a detailed discussion of the biogeochemical and hydrological conditions in cenote El Zapote, a hypothesis on biochemically induced authigenic calcite precipitation in the pelagic redoxcline is established. The proposed hypothesis is substantiated by results of the microbiologic investigations of Leberecht et al. (in prep.) and an evaluation of calcite precipitation rates within the pelagic redoxcline.

5.1.1 Limnological and hydrological conditions in cenote El Zapote

The water temperature profile (Fig. 16a, p. 38) offers valuable clues on the hydrological conditions in the cenote El Zapote. Mixing of the water in the narrow cenote shaft from 0–30 m water depth is indicated by constant temperatures and oxygenation, whereas linearly increasing temperatures in the wide dome-shaped cenote from 30–55 m water depth and linearly decreasing

dissolved oxygen concentrations indicate conductive heat transport and oxygen diffusion, respectively (Fig. 16a, p. 38). This suggests that the water body from 0–30 m water depth is mixing-dominated and diffusion-dominated from 30 to >50 m water depth. This interpretation is also supported by constant EC values in the cenote shaft and constantly increasing EC values from 30 m water depth down to the top of the halocline at 36.8 m water depth (Fig. 16a, p. 38). Another indication for stagnant conditions of the water body is the shape of the halocline itself. Compared to other cenotes of the YP that are deep enough to reach the halocline, cenote El Zapote particularly differs in the extent of the halocline, which is the transition zone from fresh- to saltwater. At cenote El Zapote, the halocline is about 10 m thick (Table 1, p. 47 and Fig. 16a, p. 38), as compared to a transition zone thickness of 1–5 m of other cenotes of Quintana Roo (Kovacs et al., 2017b; Stoessell et al., 1993).

The constant decrease of DIC, sulfide and orthophosphate below ~40 m water depth indicates a sink of these chemical species into depths greater than the cenote (>54 m water depth). This sink may result from advection of flowing water masses in conduits or zones of intensified hydraulic conductivity in a deeper cave system at around 60 m below the present sea level. Such deep cave systems could have developed during glacial sea level low stands (e.g. Smart et al., 2006).

In general, the water body of cenote El Zapote is stagnant from 30 m water depth down to the bottom of the cave, where mass transfer is predominantly due to chemical diffusion. This is essential for the understanding of the hydrogeochemistry and the ongoing biogeochemical processes in cenote El Zapote, which will be discussed later on.

5.1.2 Subaqueous calcite precipitation in the pelagic redoxcline

It was suspected before that Hells Bells form within the freshwater body of cenote El Zapote (Stinnesbeck et al., 2017b). The depth zone of Hells Bells formation within the freshwater layer can now be narrowed down by a more detailed investigation of the water body presented here. The peak towards alkaline pH values together with oversaturation with respect to calcite indicated

by a peak of $SI_{calcite}$ (Fig. 16b, p. 38) points towards the redoxcline as the most probable horizon of subaqueous calcite precipitation.

The calcite crystals found in the turbid layer filtrate give further hints on calcite precipitation in the redoxcline (Fig. 20c, p.44). It is not yet known, whether these particles represent autochthonous matter of the turbid layer. Nevertheless, formation of calcite crystals at the density boundary is likely, as fine particulate matter is accumulated there and may act as crystallization seeds. Thus, calcite may crystalize at lower calcite saturation states. The process of heterogeneous crystallization of calcite is indicated by calcite crystal formation around silica shells (Fig. 20c1, p.44). The high sulfur contents found in Hells Bells calcite also supports this assumption, as small sulfur particles are abundant in this water layer and are easily enclosed in calcite crystals growing there (Table 4, p. 71 and Table 5, p. 72).

Additionally, the temperature-dependent partitioning of magnesium into calcite is suitable to locate the water depth of calcite precipitation by application of equation (2) with given distribution coefficients D(Mg).

$$(Mg/Ca)_{solution} = \frac{(Mg/Ca)_{solid}}{D(Mg)} \qquad (2)$$

Using the mean value of Mg/Ca_{solid} determined for "youngest" Hells Bells calcites (Table 5, p. 72) and D(Mg) at 25°C given by Huang and Fairchild (2001) and Rimstidt et al. (1998), the calculation of Mg/Ca of the solution from which the Hells Bells calcite precipitated yields a $Mg/Ca_{solution}$ of 0.73 and 1.06, respectively. $Mg/Ca_{solution}$ ratios in this range are found in water depths around the redoxcline and the uppermost top of the halocline in 36–37 m water depth, thus supporting the interpretation that Hells Bells formation takes place in the redoxcline (Fig. 16c, p. 38).

Redoxclines with steep counter gradients of oxidized and reduced species are highly attractive milieus for a variety of microbes (e.g. Glaubitz et al., 2009; Grote et al., 2008; Noguerola et al., 2015). Therefore, biogeochemical processes are likely to be involved in the subaqueous calcite precipitation within the redoxcline of cenote El Zapote.

5.1.3 Biogeochemical processes in cenote El Zapote related to calcite precipitation

There are two main biogeochemical domains regulating the redox conditions of the meromictic cenote El Zapote, namely the organic matter-rich sediments of the debris mound and the pelagic redoxcline. The biogeochemical processes occurring in the sediment and in the redoxcline of the water body are discussed in detail in the following.

5.1.3.1 Sedimentary biogeochemical processes

The anaerobic conditions and high concentrations of metabolites such as sulfide (S^{-II}) and CH_4 in the halocline can be attributed to anaerobic heterotrophic organic matter decay in the debris mound sediments. According to the descriptions of the technical divers and sediment samples, both, the debris mound and the cenote floor are covered with a relatively thick layer (~1 m) of organic matter consisting of leaves and other plant remains. As a consequence of stagnancy in the meromictic water body and oxygen deficiency, this organic matter is respired by heterotrophic microorganisms in the sediment via anaerobic fermentative and respiratory pathways.

Anaerobic organic matter degradation in the sediment of the debris mound by fermentation and sulfate reducing bacteria produce hydrogen and hydrogen sulfide (S^{-II}), CO_2 (DIC) and acidity, thus lowering the pH. Elevated concentrations of DIC and sulfide are found in the halocline (Fig. 16c, p. 38), and low $\delta^{13}C\text{-}HCO_3^-$ within the halocline indicate a microbial origin of the DIC (e.g. Mook, 2000) (Fig. 19, p. 43). Additionally, pH values are more acidic in the halocline (Fig. 16a and b, p. 38) and sulfate reduction is further supported by decreasing SO_4^{2-}/Cl^- ratios in the halocline of up to 32% compared to the seawater ratio of 5.2 (Fig. 16c, p. 38) (Stoessell et al., 1993).

Methane-producing archaea (methanogens) metabolize degraded organic matter releasing CH_4 and DIC. Although this pathway is less energy efficient than sulfate reduction, methanogens may dominate in deeper parts of the sediments, where sulfate is already consumed (e.g. Whiticar, 1999). Diffusion of CH_4 from the sediment into the water column leads to CH_4 concentrations of up to 25 µmol l^{-1} identified in the halocline of El Zapote.

Ammonium is released from organic matter degradation in the organic rich sediments and diffuses upwards towards the redoxcline (Fig. 24, p. 51 and Fig. 25, p. 55). Its upward flux intersects with the downward flux of oxygen indicating an aerobe oxidation of ammonium as discussed later on in section 5.2.2.2 (p. 98).

Other common anaerobic heterotrophic metabolic pathways in sediments, such as the reduction of iron, are subordinated processes, most likely due to low concentrations of iron in the host rock limestone (Table 4, p. 71) and limited source of siliciclastic materials in this part of the YP. The elevated but still exceedingly low amounts of dissolved iron in the halocline as compared to the freshwater body (Fig. 18, p. 42) is due to limited iron solubility by the affinity to form iron sulfides in the presence of high amounts of sulfide.

5.1.3.2 Redoxcline biogeochemical processes

The redoxcline depth is characterized by a steep gradient of the redox potential with EH values decreasing from around +280 to around −100 mV in a narrow water layer from 35–36.8 m water depth (Fig. 2b, p. 7). The redoxcline coincides with a peak in turbidity, which is detectable both visually (Fig. 2b, p. 7) and geochemically (Fig. 16a and b, p. 38). Dissolved oxygen concentrations drop to undetectable levels at the top of the redoxcline, indicating that anaerobic biogeochemical processes prevail below (Fig. 39).

In the previous study by Stinnesbeck et al. (2017b), these conditions were tentatively attributed to a full heterotrophic redox zonation due to organic matter decomposition. Fine organic matter accumulates along the density contrast at the top of the halocline and heterotrophic microbial communities thrive from the aerobic and anaerobic decomposition of this organic matter. This is also indicated in the results of this study by minor nitrification from ~34–35 m water depth (Fig. 16b, p. 38), non-linearly decreasing dissolved oxygen contents from ~34–35 m and by slightly more acidic pH values above and in the uppermost part of the turbid layer.

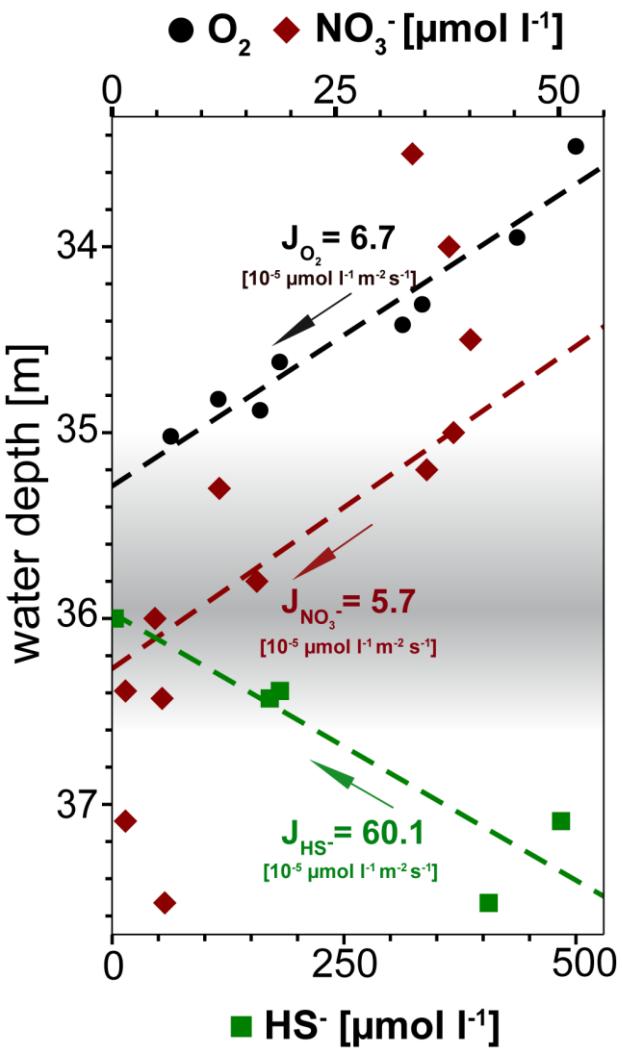

Fig. 39:Concentration profiles of dissolved O_2, NO_3^- and HS^- (calculated with PhreeqC) in water depths around the redoxcline. The fluxes J are given in 10^{-5} µmol m^{-2} s^{-1}. The linear fit of O_2 and HS^- is calculated for the range of plotted values, while for NO_3^- it is calculated only for the range from 34.4–36.6 m water depth. Only O_2 values above detection limit (6.3 µmol l^{-1}) from winch profile 2 were considered for the calculation (suppl. Table S1 in Ritter et al., 2019).

Nevertheless, the more detailed data presented here indicate the importance of planktonic chemolithoautotrophic processes in the pelagic redoxcline which are driven by the upward diffusion of reduced sulfur, carbon and nitrogen species released from the anaerobic degradation of organic material on the cenote floor. Pelagic redoxclines develop in density stratified marine (e.g Berg et al., 2015) as well as lake environments (e.g. Hartmann, 2018; Noguerola et al., 2015). In redoxclines below the photic zone the microbial community is dominated by chemolithoautotrophs, with a considerable amount of chemoautotrophic production and dark carbon fixation (e.g. Grote et al., 2008; Jørgensen et al., 1991; Jost et al., 2010; Noguerola et al., 2015). The development of pelagic redoxclines was also reported for deep density stratified cenotes of the YP (e.g. Socki et al., 2002; Stoessell et al., 1993; Torres-Talamente et al., 2011).

In the previous study by Stinnesbeck et al. (2017b), members of β-*proteobacteria Hydrogeophilaceae* and the *ε-proteobacteria* genus *Sulfurovum* were reported as dominant within the aqueous microbial community. Most members of these bacterial groups are chemolithotrophic or mixotrophic using reduced sulfur compounds or hydrogen as electron donors and oxygen or nitrogen-compounds as electron acceptors (Stinnesbeck et al., 2017b).

The white cloudy turbid layer at 35–36.8 m water depth could be the result of a dense accumulation of these microorganisms e.g. sulfur-oxidizing bacteria, analogous to that reported for Bundera sinkhole in Australia (Seymour et al., 2007). Elemental sulfur (S_8) particles or polysulfides were detected on the turbid layer filtrate and indicate sulfide oxidation in the turbid layer or redoxcline (Fig. 20, p.44); these particles are formed as intermediates in the microbial oxidation of sulfide (Findlay, 2016).

The oxidation of sulfide in the redoxcline is likely anaerobic, as sulfide vanishes at around 36 m while dissolved oxygen is already at undetectable levels in 35 m water depth and both concentration profiles are not overlapping (Fig. 39). Furthermore, the oxygen flux towards the redoxcline is around one magnitude lower than the flux of the reduced sulfur species HS^- indicating that sulfide oxidation via aerobic pathways is minor (Fig. 39). Thus, sulfide oxidation within the redoxcline must be predominantly via anaerobic pathways. As the downward flux of nitrate towards the redoxcline intersects with the upward flux of hydrogen sulfide (Fig. 39), assimilatory anaerobic sulfide oxidation could be obtained with nitrate as terminal electron acceptor producing zero-valent elemental sulfur and nitrogen under the consumption of protons (e.g. Bailey et al., 2009). The overall mass-balanced energy generating reaction for chemoautotrophic nitrate-driven anaerobic sulfide oxidation (ND-SO) is given in equation 3:

$$7HS^- + 2NO_3^- + CO_2 + 9H^+ \rightarrow 7S^0 + N_2 + CH_2O + 7H_2O \quad (3)$$

This overall reaction comprises a total transfer of 14 e^- and several interconnected biochemical processes that occur most likely within a balanced consortia of microbes with interdependent metabolisms. According to equation 3, ND-SO could account to one third of the HS^- oxidation considering the fluxes of HS^- and NO_3^- towards the redoxcline (Fig. 39). Furthermore, ND-SO is a proton-consuming process and sulfide oxidation to elemental sulfur is more proton-consuming than the full sulfide oxidation to sulfate (see also Visscher and Stolz, 2005). The abundance of elemental sulfur particles found in the turbid layer filtrate (Fig. 20, p.44) indicates that sulfide oxidation to zero-valent elemental sulfur is predominant. Full oxidation of sulfide to sulfate is

less likely as no increase of sulfate is observed in the redoxcline (Fig. 16c, p. 38). Maxima in pH are known to occur when sulfide is oxidized to elemental sulfur with nitrate as electron acceptor (Kamp et al. 2006). In consequence, the minimum of nitrate in the redoxcline and the slight alkaline pH shift, indicate that ND-SO is a relevant process in the redoxcline (Fig. 16b, p. 38 and c, Fig. 39). Thus, the proton consuming ND-SO could be the biogeochemical process in the redoxcline creating disequilibrium in the carbonate dissolution-precipitation reaction, favoring calcite precipitation. A similar mechanism was recently reported for the formation of stromatolites below the photic zone of the Arabian Sea. There, a collective effect of proton-consuming ND-SO and alkalinity-producing sulfate driven-oxidation of methane (SD-OM) leads to authigenic carbonate precipitation in microbial mats in the vicinity of CH_4-seeps (Himmler et al., 2018).

Anaerobic SD-OM (e.g. Bailey et al. 2009) is likely to occur in the redoxcline, as dissolved methane concentrations vanish at around the same depth as sulfide (~36.5 m) and $\delta^{13}C$-CH_4 values show a strong peak towards higher values at the same water depth (Fig. 19, p. 43).

Autotrophy also supports calcite precipitation by taking up carbon dioxide for the synthesis of biomass (Castanier et al., 1999; Kosamu and Obst, 2009). Chemolithoautotrophy in the redoxcline is indicated by the flux of DIC towards the redoxcline and by the peak of $\delta^{13}C$-HCO_3^- towards higher values in the redoxcline (Fig. 19, p. 43). This peak indicates inorganic carbon assimilation by microorganisms (dark-CO_2 uptake). Organisms usually prefer to metabolize ^{12}C (it takes less energy to break the ^{12}C bond instead of ^{13}C), which results in higher $\delta^{13}C$-HCO_3^- values in the remaining dissolved inorganic carbon. Hence, the peak towards more positive $\delta^{13}C$-HCO_3^- values identified in the redoxcline of cenote El Zapote at ~36 m water depth, may be attributed to microbial CO_2 assimilation or dark-CO_2 fixation.

5.1.4 Microbiology

In order to validate the proposed biogeochemical processes derived from the hydrogeochemical profiles of the water column at cenote El Zapote, water samples for microbiologic investigations were taken from above, within and below the redoxcline during the sampling campaign in 2018

(Leberecht et al., in prep.). The microbial diversity of the different sub-biotopes was determined via 16S rRNA amplicon sequencing. Additionally, the microbiology in the center of the redoxcline was studied on the metagenome (DNA) level to evaluate the relative abundance of taxa and the whole genetic potential of this specific community. Furthermore, this sample was analyzed on the metatranscriptome (mRNA) level in order to create a functional gene expression profile of the complex microbial community in the redoxcline. Both metadata sets combined allowed for the identification of microbial key players and the highest expressed genes critical for metabolic pathways in this specific environment.

On the transcriptome level, Leberecht et al. (in prep.) found that autotrophy or carbon fixation is dominantly conducted via the Calvin Cycle and that the sulfur and nitrogen cycles play the most important roles within the redoxcline. Regarding the sulfur-cycle, the dominant gene expressions in the redoxcline sample are related to oxidation of reduced sulfur compounds to zero-valent elemental sulfur. Regarding the nitrogen-cycle, the metabolic pathways of denitrification and oxidation of ammonium apparently dominate.

Hydrogenophilales are identified as the dominant taxon followed by Thaumarchaeota family Nitrosopumilaceae determined with metagenomics and metatransciptomic analyses. A taxonomic assignment of transcripts encoding key enzymes shows that the Hydrogenophilales dominate the sulfur cycle within the redoxcline. They also expressed all the genes for the reduction of nitrate to nitrogen and seem to fix carbon dioxide via the Calvin Cycle. In the Nitrogen cycle, the Thaumarchaeota seem to be key players as they predominantly express genes related to oxidation of ammonium to hydroxylamine and reduction of nitrite.

Furthermore, Leberecht et al. (in prep.) addresses the pressing question whether photosynthesis plays a role in the redoxcline, hence in Hells Bells formation. The genes relevant for the synthesis of bacteriochlorophyll, as well as for oxygenic and anoxygenic photosynthesis, show no or only negligible expressions in the redoxcline. Thus, light as an energy source does not seem to be available in the redoxcline at ~36 m water depth in cenote El Zapote.

In conclusion, the results of Leberecht et al. (in prep.) support the before proposed dominant biogeochemical processes in the redoxcline derived from the hydrogeochemical results (Fig. 40). The findings further substantiate that chemolithoautotrophy and proton consuming ND-SO are most likely the dominant biogeochemical processes within the redoxcline of cenote El Zapote.

5.1.5 Hypothesis on biologically-mediated authigenic calcite precipitation

Based on the indications of Hells Bells formation in the redoxcline and considering the biogeochemical processes discussed before, the following scenario of authigenic subaqueous calcite precipitation is proposed and illustrated in Figure 40. It summarizes the biogeochemical processes inducing calcite oversaturation favoring calcite precipitation in the turbid layer and the redoxcline of cenote El Zapote. Heterotrophic bacterial decomposition of organic matter in sediment of the debris mound releases CO_2 (HCO_3^-), nutrients (e.g. P_{ortho}) and reduced species of sulfur (S^{-II}) and nitrogen (NH_4^+). Due to the stagnant conditions in the cenote, these species are transported via diffusion, thereby allowing for the formation of a defined and stable redoxcline. Here, anaerobic chemolithoautotrophy, especially the proton consuming nitrate-driven sulfide oxidation (ND-SO), increase alkalinity, thus favoring calcite precipitation (Fig. 40). The required Ca^{2+} ions for calcite precipitation are constantly supplied to the redoxcline by upward diffusion from the Ca-enriched saline water body (Stinnesbeck et al., 2017b).

Previously, the growth of Hells Bells was attributed to microbial mediation (Stinnesbeck et al., 2017b). It was hypothesized by Stinnesbeck et al. (2017b) that autotrophy (ammonium oxidation) and denitrification are the main factors that trigger calcite precipitation at the surface of Hells Bells and that calcite precipitation could further be supported by the presence of negatively charged extracellular polymeric substances (EPS), leading to the accumulation of Ca^{2+} ions and to supersaturation of calcite within biofilms (e.g. Dupraz et al., 2009). However, the large size and form of the dog-tooth calcite crystals of Hells Bells rather resemble slow growing inorganic (authigenic) calcite crystals than biologically-mediated precipitates (Fig. 26, p. 57 and Fig. 27, p.58).

This hypothesis is supported by Bosak & Newman (2005) who investigated microbial kinetic controls on calcite morphology and found that microbially mediated calcite precipitated at low calcite supersaturation shows more anhedral crystal morphologies, compared to the more euhedral abiotic ones. Although the microbial activity in the redoxcline induces calcite oversaturation, the hypothesis presented in this study is compatible with an authigenic calcite precipitation of the Hells Bells from a biologically mediated water layer.

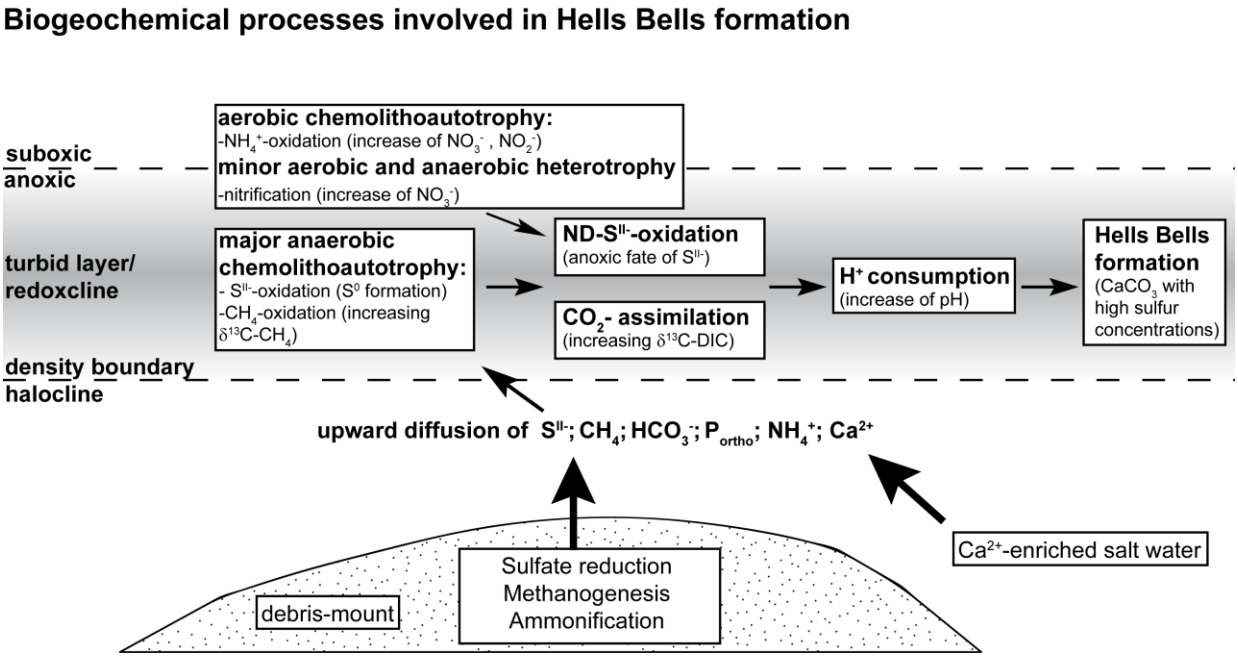

Fig. 40: Scheme of the biogeochemical processes involved in the sediment and redoxcline of the water column of the cenote El Zapote that lead to Hells Bells formation (updated from Ritter et al., 2019).

5.1.6 Rates of authigenic calcite precipitation in the pelagic redoxcline

In order to test the plausibility of the hypothesis on Hells Bells formation within the redoxcline, calcite precipitation rates of both biogeochemical processes, ND-SO and CO_2-assimilation are assessed. All used parameters and results are given in Table 6.

The overall chemical reaction of the carbonate balance is given in equation 4 and the partial reactions of equation 4 are given in equations 4a–d. Under equilibrium conditions, carbonate pre-

cipitation after equation 4 is acid producing because for each mole of precipitated calcite in equation 4 one proton is released to compensate for the abstracted carbonate ion (4b) due to proton shift in the partial reactions (4b–4d).

$$Ca^{2+} + 2HCO_3^- \leftrightarrow CaCO_3 + CO_2 + H_2O \quad (4)$$

$$Ca^{2+} + CO_3^{2-} \leftrightarrow CaCO_3 \quad (4a)$$

$$HCO_3^- \leftrightarrow CO_3^{2-} + H^+ \quad (4b)$$

$$HCO_3^- + H^+ \leftrightarrow H_2CO_3 \quad (4c)$$

$$H_2CO_3 \leftrightarrow CO_2 + H_2O \quad (4d)$$

Assuming that up to one third of the hydrogen sulfide flux towards the redoxcline (Fig. 39, p. 86) is oxidized by the proton consuming ND-SO after equation 3 (p. 87) and that the proton consumption of this process is compensated by both, the observed increase in pH values of 0.04 within the redoxcline (Fig. 16b, p. 38) and calcite precipitation after equation 4, allows for an estimation of the calcite precipitation rate $R_{ND\text{-}SO}$ derived from ND-SO within the redoxcline after equation 5.

$$R_{ND-SO} = \frac{1}{3} J_{HS^-} * \left(\frac{\alpha}{mHS^-} - \frac{\beta}{mHS^-} \right) \left[\frac{mol}{m^2\ s} \right] \quad (5)$$

With mHS^- = 7 (moles of HS^- in Eq. 3); α = 9 (moles of H^+ in Eq. 3); β = 0.91 (moles of H^+ consumed in pH increase of 0.04).

Equation 5 yields that 20 µmoles calcite m^{-2} d^{-1} or 0.73 g calcite m^{-2} a^{-1} could be precipitated within the redoxcline due to ND-SO. This adds up to a total calcite precipitation rate $R_{ND\text{-}SO}$ of 2.2–6.2 kg calcite a^{-1} in the whole redoxcline of the circular 60–100 m wide cenote El Zapote.

Additionally, the calcite precipitation rate in the redoxcline can be estimated considering the second biogeochemical process in the redoxcline that might lead to calcite precipitation, the CO_2-

assimilation or dark CO_2-fixation (Fig. 40). Chemolithoautotrophy or the CO_2-assimilation is already partly considered in the previous calculation based on ND-SO following equation 3 (p. 87). However, the entire CO_2-assimilation rate in the redoxcline can be approached by assuming that the upward flux of DIC ($J_{DIC(HCO3)}$) towards the redoxcline (calculated as HCO_3^- and given in Fig. 19, p. 43) is consumed by chemolithoautotrophy. Under equilibrium conditions and invariable pH, for each mole of abstracted or assimilated CO_2 one proton is consumed due to the carbonate balance (Eq. 4a–d) and this proton consumption is compensated by calcite precipitation (Eq. 4). The calcite precipitation rate $R_{CO2\text{-}assim.}$ derived from the CO_2-assimilation is then limited to the half of the HCO_3^- flux towards the redoxcline as given in equation (6).

$$R_{CO2-assim.} = \frac{1}{2} J_{DIC(HCO_3^-)} \quad (6)$$

Equation 6 yields a calcite precipitation rate $R_{CO2\text{-}assim.}$ of 110 µmoles calcite m^{-2} d^{-1}, which is 12–34 kg a^{-1} in the whole redoxcline. Such rates seem reasonable when compared to reported dark CO_2-fixation rates from 0.2–2.7 µmol CO_2 l^{-1} $d^{-1}$of deep marine pelagic redoxclines in the Black Sea (Jørgensen et al., 1991), the Baltic sea (Glaubitz et al., 2009; Jost et al., 2008) as well as for a deep karstic lake pelagic redoxcline (Noguerola et al., 2015) (Table 6). Applied to the redoxcline of cenote El Zapote, these rates would yield calcite precipitation rates from 11–420 kg calcite a^{-1} in the 0.5 m thick and 60–100 m wide redoxcline of the circular cenote El Zapote.

The summed up calcite precipitation rates of $R_{ND\text{-}SO}$ and $R_{CO2\text{-}assim.}$ in the redoxcline can be converted to calcite growth rates ranging from 0.27–1.46 µm a^{-1} m^{-2}, taking a calcite density of 2.7 g cm^{-3} into account. Calcite growth, however, is likely to be concentrated on a much smaller area, i.e. the crystal or substrate surfaces of Hells Bells hanging in the redoxcline, the cenote walls and the tree stem within the redoxcline (Fig. 7a, Fig. 8a and Fig. 12; p. 15, 19 and 25, respectively). This would result in a higher actual calcite growth rate, for example if the calcite growth is concentrated to 1 % of the area, this would result in actual growth rates of 27–146 µm a^{-1}.

Table 6: Results and parameters as well as reported values used for the estimations on calcite precipitation rates in the redoxcline of cenote El Zapote.

estimations on calcite precipitation and growth rates in the redoxcline of El Zapote:				
$R_{ND\text{-}SO}$ (Eq 5)	20	µmol m^{-2} d^{-1}	2.2–6.2	kg a^{-1} in the area of the redoxcline
$R_{CO2\text{-}assim.}$ (Eq 6)	110	µmol m^{-2} d^{-1}	12–34	kg a^{-1} in the area of the redoxcline
$R_{dark\text{-}CO2\ fixation}$	101–1150	µmol m^{-2} d^{-1}	31–420	kg a^{-1} in the area of the redoxcline
$\Sigma(R_{ND\text{-}SO} + R_{CO2\text{-}assim.})$	130	µmol m^{-2} d^{-1}	14.2–40.2	kg a^{-1} in the area of the redoxcline
growth rate	0.27–1.46	µm a^{-1}		
growth rate (on 1 % of the area)	27–146	µm a^{-1}		
net growth rates of Hells Bells	4–100	µm a^{-1}	reported here, in Stinnesbeck et al., 2017b and in Schorndorf et al, 2019	
Parameters used for estimations of calcite precipitation rates at El Zapote:				
HS^- flux	6	10^{-4} µmol m^{-2} s^-		
DIC(HCO_3^-) flux	2.5	10^{-3} µmol m^{-2} s^-		
diameter circular of El	60–100	m		
redoxcline thickness	0.5	m		
redoxcline volume	30–50	m^3		
calcite density	2.7	g cm^{-3}		
Reported dark CO_2-fixation rates of marine and freshwater redoxclines used for the estimations of :$R_{dark\text{-}CO2\ fixation}$:				
Jørgensen et al. (1991)	0.2	µmol CO_2 l^{-1} d^-	Black Sea	
Glaubitz et al. (2009)	0.5	µmol CO_2 l^{-1} d^-	Baltic Sea	
Jost et al. (2008)	1	µmol CO_2 l^{-1} d^-	Baltic Sea	
Noguerola et al. (2015)	2.7	µmol CO_2 l^{-1} d^-	karstic lake pelagic redoxcline	

These growth rates are close to the net growth rates of 4–100 µm a^{-1} for U-series dated Hells Bells specimen from cenote El Zapote (section 4.3.1.1, p. 65 and Schorndorf et al., 2019; Stinnesbeck et al., 2017b). The evaluation of calcite precipitation rates demonstrates the plausibility of Hells Bells formation by the biogeochemical mechanisms proposed in this study. However, the actual calcite growth rates must be significantly higher than the reported net growth rates, as these rates also comprise repeated phases of calcite dissolution (section 4.2.2, p. 60 and Stinnesbeck et al., 2017b). Eventually, the comparison of the estimated actual calcite precipitation rates in the redoxcline and the reported net growth rates is hindered by a lack of data of both, the actual area of calcite precipitation and the time and intensity of calcite dissolution.

5.2 Authigenic calcite formation in cenotes of the Yucatán Peninsula

The occurrence of Hells Bells speleothems is so far only reported for six deep stratified cenotes (cenotes Siete Bocas, Holbox, Maravilla, Tortugas, Kin-Ha and El Zapote) restricted to a small area west of Puerto Morelos on the North-Eastern YP (Fig. 5b, p.13) (Stinnesbeck et al., 2017b). This chapter aims to delimit the crucial factors for an authigenic calcite formation within redoxclines, hence Hells Bells formation, by comparison of deep stratified cenotes with and devoid of Hells Bells. Hydrologic and biogeochemical similarities of cenotes with Hells Bells are compared to the conditions of cenotes devoid of Hells Bells in order to identify the conditions required for the formation of subaqueous speleothems. The biogeochemistry of the water columns is intensively discussed in particular with regard to its regulation by stagnancy. Different stagnancy dependent stages of redoxclines are deviated and discussed on the basis of biogeochemistry and the related authigenic calcite precipitation. Finally, other cenotes showing potential for Hells Bells formation are extracted from literature using reported commonly measured water quality parameters.

5.2.1 Factors controlling Hells Bells formation

The results of different deep stratified cenotes with and without Hells Bells now allows for deriving essential factors for Hells Bells formation. First of all, there are a few apparent requirements to the morphology of a cenote in order to form Hells Bells. A cenote needs to be deep enough to reach the saltwater body and build up a halocline as density stratification seems to be essential to generate a redoxcline in which the microbial metabolism leads to calcite disequilibrium and calcite precipitation (section 5.1.2, p. 81). Furthermore, cenotes need to have a connection to the surface in order to allow organic matter to be introduced to the cenote to start the biochemical cycle with organic matter degradation in the sediments, which in turn fuels the chemolithoautotrophic processes in the redoxcline at the top of the halocline. Additionally, light seems to be a limiting factor to Hells Bells generation (Stinnesbeck et al., 2017b), which might be related to the

dominant metabolism of the microbes in the redoxcline, e.g. photoautotrophy vs. chemolithoautotrophy (section 5.1.4, p. 87). These factors already confine the number of possible cenotes considerably and indicate that Hells Bells formation is most likely restricted to lentic pit cenotes after the scheme suggested by Schmitter-Soto et al. (2002).

The one major characteristic that cenotes with Hells Bells have in common is a relatively low degree of advection of the water body, which results in stagnancy expressed in the thickness of the haloclines. If the fresh- and saltwater bodies are dominated by mixing or advective mass transport, then, a very thin halocline develops as transition zone between the two water masses (Fig. 41). The thickness of the halocline increases with decreasing advection within the fresh- and saltwater bodies until finally diffusion is the dominant transport process (Fig. 41).

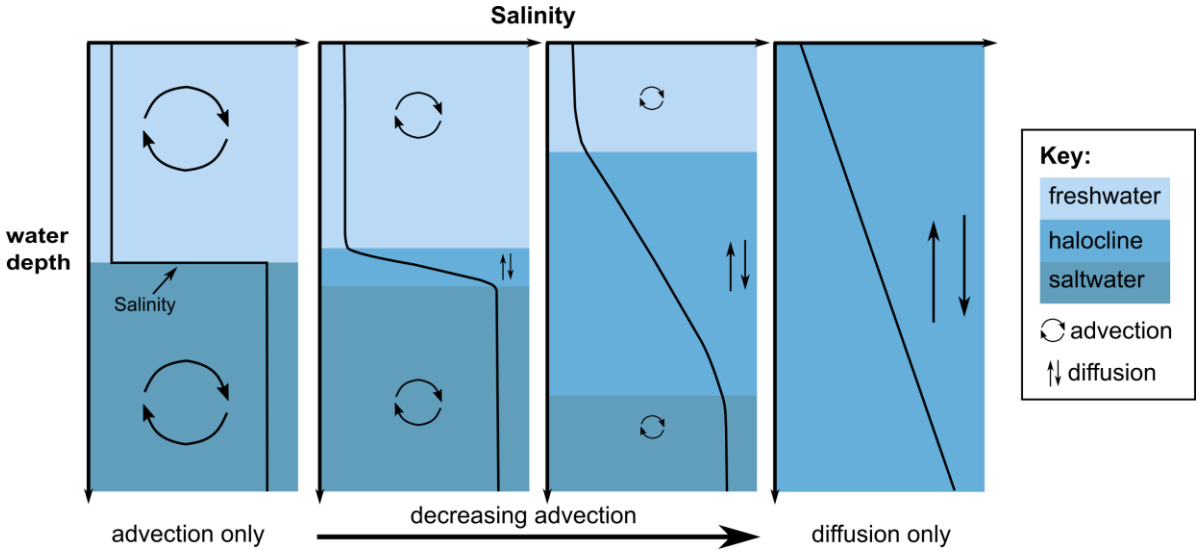

Fig. 41: Different schematic salinity patterns of density stratified fresh- and saltwater bodies showing different degrees of advection between the end-members stages of non-stagnant advection only and stagnant diffusion only water body.

The comparison of the vertical distribution of different hydrogeochemical parameters of the different deep stratified cenotes points towards advection of the water column as the main difference between cenotes with and without Hells Bells. While cenotes with Hells Bells all show stagnant water bodies with low degree of advection and thick haloclines (~10–19 m), cenote Angelita shows a higher degree of advection within the water body with a thin halocline (~4 m) (Table 1, p. 47). This indicates that the mass transport in cenote Angelita is dominantly via advection com-

pared to cenotes El Zapote, Maravilla and Tortugas, where mass transport is dominated by diffusion. This is supported by results of Stoessell (1995) who successfully modeled the thickness and shape of the halocline of cenote Angelita assuming two immiscible water bodies, which are both moving towards the coast with the same velocity.

This suggests that a stagnant water body with a low degree of advection is crucial regarding Hells Bells formation. Stagnancy as a key factor for Hells Bells formation implies that the degree of advection is also relevant with regard to the biogeochemistry of the water bodies of the cenotes, especially the redoxclines, where Hells Bells formation takes place according to the proposed biogeochemical mechanism of calcite precipitation (section 5.1.2, p. 81).

The degree as a measure of stagnancy impacts on the biogeochemistry of the deep-stratified cenotes twofold:

- decreased advection establishes an accumulation in the halocline of chemical species released from organic matter decay in the sediments of the debris mounds.
- the degree of advection basically regulates the supply of electron (e^-) donors/acceptors towards the redoxcline from above and below.

5.2.2 Regulation of redoxcline biogeochemistry by the degree of advection

5.2.2.1 Accumulation of byproducts from organic matter decay

The accumulation of chemical species attributed to organic matter decay in the sediments of the debris mounds is expressed in cenotes with Hells Bells by a peak of these species (e.g. HS^-, NH_4^+, HCO_3^-, P_{ortho}, Si) in the haloclines at ~40 m in both cenotes El Zapote and Tortugas (Fig. 22, p. 48 and Fig. 25, p. 55). Although the water body of cenote Maravilla was not sampled below 38 m, a negative peak of pH values together with slight increase of pH values from around 40 m water depth towards the cenote bottom indicates a similar accumulation of organic matter decay related chemical species Figure 21 (p. 46). Consequently, these chemical species show an upward flux towards the redoxclines and downward flux towards the cenote bottom (Fig. 25, p. 55) indicating an upper and a lower sink. The upper sink is the redoxcline and the lower sink may result from

advection of flowing water masses in conduits or zones of intensified hydraulic conductivity in a deeper cave system at around 60 m below the present sea level as already discussed in section 5.1.1 (p. 80). Smart et al. (2006) suggest that an extensive deep cave system may have developed during past glacial sea level low stands. Larger cavities below the cenote bottom seem likely regarding that the collapse of the karstic host rock formed the present-day El Zapote and Tortugas. The material from the collapse of the cenotes, the debris mounds, filled up deeper sections of the cenote and still leaving the recent large cavities of cenotes El Zapote and Tortugas. However, whether and to what extent the cavern room of the cenotes was formed prior to or after the collapse is unclear. Nevertheless, the coinciding water depth of ~40 m of maximum accumulation in all cenotes with Hells Bells (Fig. 25, p. 55) suggests a common lower sink for chemical species related to organic matter decay, which might be an extensive cave system at around 60 m below sea level.

Regarding Hells Bells formation, the accumulation of hydrogen carbonate (HCO_3^-) released from organic matter decay (section 5.1.3.1, p. 83) is most important, because it leads to an upwards flux of HCO_3^- from the halocline towards the redoxcline in cenotes with Hells Bells (Table 2, p. 54 and Fig. 25, p. 55). In cenote Angelita on the other hand, a downward flux of HCO_3^- from the redoxcline towards the halocline is observed due to lower concentrations of HCO_3^- in saltwater compared to the karstic freshwater due to a lack of accumulation in the less stagnant water body (Table 2, p. 54 and Fig. 25, p. 55). An upward flux of HCO_3^- is essential for Hells Bells formation in order to create oversaturation with respect to calcite within the redoxcline. Additionally, the upward flux of HCO_3^- may act as carbon source for the chemolithoautotropy in the redoxclines of cenotes with Hells Bells, and thus has large influence on the sort of microbial community that develops at the redoxcline.

5.2.2.2 Biochemical processes in cenotes with Hells Bells

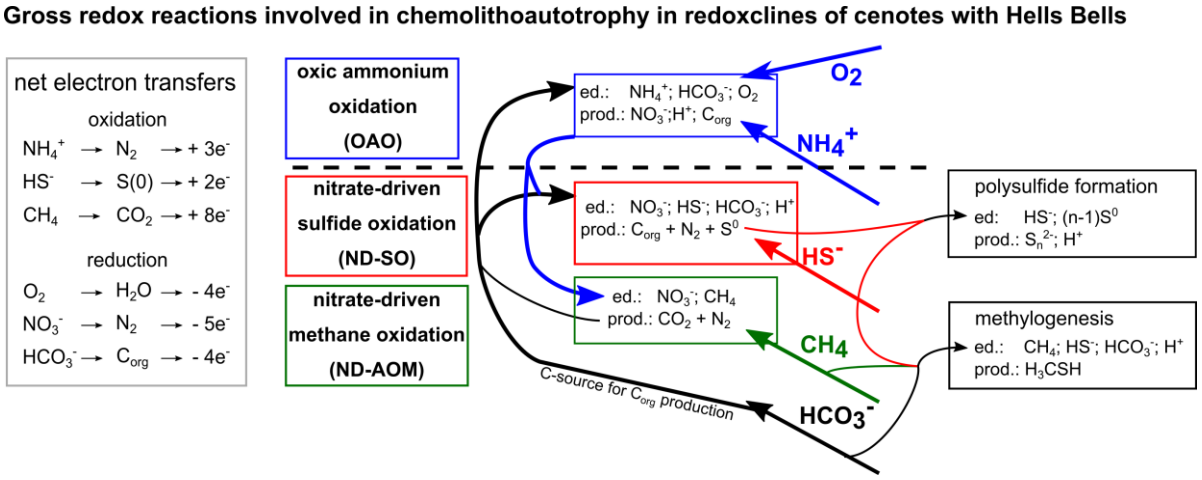

Fig. 42: Gross redox reactions involved in the biogeochemical processes within the redoxclines of cenotes with Hells Bells. The dashed line represents the top of the redoxcline.

The microbiome that develops at the redoxcline is largely determined by the supply of electron (e^-) acceptors/donors, which is regulated by the degree of advection in the water bodies. The decreased degree of advection in cenotes with Hells Bells determines the supply of e^- acceptors/donors towards the redoxclines. The fluxes from above and below the redoxclines (Table 2, p. 54) indicate that the redoxclines of cenotes with Hells Bells are rather limited by the available e^- acceptors oxygen and nitrate compared to e^- donors like sulfide, ammonium and methane, which most likely favors the development of the characteristic proton-consuming nitrate-driven anaerobic oxidation of sulfide (ND-SO) in redoxclines of cenotes with Hells Bells (section 5.1.3.2 , p. 84 and section 5.1.4, p. 87). However, estimations showed that ND-SO could only account for one third of the oxidation of the upward flux of hydrogen sulfide (HS^-) (section 5.1.6, p. 90). This imposes the need to further assess the biochemical processes involved in the oxidation of upwards diffusing reduced chemical species in the redoxclines of cenotes with Hells Bells. The gross redox reactions likely to be involved in the biochemical reactions at the redoxclines are comprised in Figure 42, while each aspect presented in Figure 42 is discussed in detail in the following.

Chemolithoautotropy

The overall dominant biochemical metabolic process in the redoxcline of cenotes with Hells Bells seems to be chemolithoautotropy, in which the microorganisms gain both, energy and carbon, from inorganic sources by energy-yielding redox reactions and uptake of carbon dioxide (as HCO_3^-), respectively. This is supported by the peak towards higher values of $\delta^{13}C\text{-}CO_2$ observed in the redoxclines of cenotes with Hells Bells due to preferential uptake of carbon with lower $\delta^{13}C$ by microorganisms, which results in higher $\delta^{13}C\text{-}CO_2$ values in the residue (Pohlman, 2011 and references therein) (Fig. 24, p. 51 and section 5.1.3.2 , p. 84). Dominance of chemolithautrophy in the redoxcline is further supported by the microbiology data of Leberecht et al. (in prep.), who found that carbon fixation is predominantly conducted via the Calvin Cycle (e.g. Alfreider et al., 2017 and section 5.1.4, p. 87). Another strong indication of this process, i.e. uptake of inorganic carbon as HCO_3^-, is the apparent sink of HCO_3^- ions at the redoxcline indicated by the flux of HCO_3^- ions towards the redoxclines in cenotes with Hells Bells (Fig. 24, p. 51 and Fig. 25, p. 55).

Regarding redox reactions related to chemolithoautotrophy processes, the oxidation state of the inorganic C-source (HCO_3^-) is reduced from C^{-IV} in hydrogen carbonate to C^0 in cell organic matter (C_{org}). Thus, hydrogen carbonate may act as electron acceptor in all chemolithoautotrophic redox reactions within the redoxcline of cenotes with Hells Bells (Fig. 42). The energy and electrons for reducing hydrogen carbonate to C_{org} in chemolithoautotrophy are generated by the oxidation of reduced species, e.g. sulfide, methane or ammonium, which are oxidized to chemical species of higher redox states, e.g. zero-valent sulfur, carbon dioxide and nitrate. These redox reactions are discussed in detail in the following.

Ammonium Oxidation

In cenotes with Hells Bells, Zapote, Tortugas and Maravilla, the upwards flux of ammonium (NH_4^+) fades in the redoxclines intersecting with the downward flux of dissolved oxygen only in cenote El Zapote (Fig. 24, p. 51 and Fig. 25, p. 55). Nitrate (NO_3^-) shows maximum concentrations at around the same water level where ammonium fades (Fig. 24, p. 51 and Fig. 25, p. 55). Nitrite

(NO_2^-) was determined around these water depths as well (Fig. 16c, p. 38 and Table A2). Furthermore, Leberecht et al. (in prep.) found only negligible gene expressions related to anaerobe ammonium oxidation (ANAMOX) indicating that this process is subordinate. This implies that ammonium is aerobically oxidized in the uppermost part of the redoxcline. Since chemolithoautotrophy via the Calvin Cycle is determined as the major metabolic carbon assimilating process for microbes in the redoxcline (Leberecht et al., in prep.), it seems likely that ammonium is fully oxidized to nitrate via oxic chemolithoautotrophic oxidation of ammonium (OAO) after the simplified equation (7):

$$NH_4^+ + CO_2 + O_2 \rightarrow NO_3^- + CH_2O + 2H^+ \qquad (7)$$

The OAO is an acid generating process, as for each mole of ammonium oxidized to nitrate, two moles of protons are released. This process might even be reflected in pH values of cenote El Zapote, where pH values show a small peak towards lower values at the same depth where dissolved oxygen and ammonium fluxes intersect (Fig. 24, p. 51). Regarding the fluxes given in Table 2 (p.54), OAO could account for 60, 12 and 1 % of the total ammonium depletion in cenotes El Zapote, Maravilla and Tortugas, respectively. This implies that the downward dissolved oxygen fluxes are insufficient to fully oxidize all NH_4^+ (N^{-III}) to NO_3^-(N^{+V}) indicating oxidation of ammonium to lesser oxidized species of nitrogen like N_2(N^0), N_2O(N^{+I}), NO_2^- (N^{+III}) plays a major role in the nitrogen cycle within the redoxclines of the cenotes. The degree of advection is reflected in the amount of ammonium that could be fully oxidized to nitrate, indicating an decreasing degree of advection in the studied cenotes in the order of El Zapote < Maravilla < Tortugas, following the order of halocline thicknesses of the cenotes (Table 1, p. 47).

Sulfide Oxidation

Sulfide diffusing upwards towards the redoxcline in cenote El Zapote intersects with the downward flux of nitrate, which is in water depths, where dissolved oxygen concentrations are significantly below the detection limit (<0.1 mg/l) (Fig. 39, Fig. 24a and Fig. 25a, p. 86, 51 and 55). The

process of the nitrate-driven sulfide oxidation to zero-valent elemental sulfur S_8 (ND-SO) was already discussed in detail for cenote El Zapote in section 5.1.3.2 (p. 84) and in Ritter et al. (2019).

This process seems also to be present in cenote Maravilla, where sulfide fluxes intersect with nitrate fluxes in the redoxcline. At the same depth, a white cloudy turbid layer of increased turbidity is present (Fig. 21b, p. 46 and Fig. 24b, p. 51), which presumably consists of zero-valent elemental sulfur (S_8^0) particles equivalent to the turbid layer of El Zapote described in section 4.1.1.4 (p. 44).

In cenote Tortugas, however, according to our technical divers, there is no visible turbid layer throughout the water column and turbidity values show only a minor increase within a narrow <0.2 m thick interval at the water depth, where sulfide, ammonium and methane fade (Fig. 24c, p. 51). Although sulfide clearly vanishes in the redoxcline, and sulfate concentrations show no increase at that depth, there is no obvious phase or chemical species to which sulfide is converted to. A conversion of the reduced sulfide (S^{-II}) to higher oxidized states above that of elemental sulfur (S_8^0) such as thiosulfate $S_2O_3^{2-}$ (S^{-II}) and SO_4^{2-} (S^{VI}) is unlikely considering that the redoxcline at cenote Tortugas reveals the highest reducing power of all studied cenotes indicated by the highest upward fluxes of reduced versus the lowest downward fluxes of oxidized chemical species (Table 2, p. 54). Therefore, it is likely that the reduced sulfur is converted into a dissolved sulfur species with a redox state between that of elemental sulfur (S_8^0) and sulfide (S^{-II}), which are polysulfides.

Schwarzenbach and Fischer (1960) showed that the solubility of elemental sulfur is increased due to the formation of polysulfides after equations 8 and 9.

$$nS^0 + S^{2-} \leftrightarrow S_{n+1}^{2-} \quad (8)$$

$$nS^0 + HS^- \leftrightarrow S_{n+1}^{2-} + H^+ \quad (9)$$

Polysulfides in the form of S_n^{2-} consist of linear sulfur chains containing at least one sulfur atom in a divalent oxidation state and one or more zero-valent sulfur atoms (Kamyshny et al., 2008). Their occurrence is limited to n=2–8 zero-valent sulfur atoms within the polysulfides, whereas

tetra (S_4^{2-}) and hexasulfides (S_5^{2-}) are the most abundant species (e.g. Kamyshny et al., 2006; Schwarzenbach and Fischer, 1960). Chen and Gupta (1973) stated that "When sulfur is formed in the presence of sulfide, polysulfides can be formed immediately" (Chen and Gupta, 1973, p. 199). Furthermore, their laboratory experiments demonstrated that polysulfides form as a reaction intermediate in the oxygenation of sulfide, whereas polysulfides contributed up to 9 and 14 % of the total sulfur in circumneutral pH and 1 mM sulfide solutions under atmospheric oxygen pressure (Chen and Gupta, 1973). Polysulfides are also important in natural samples, for example Li et al. (2008) found that in the redoxcline of the marine Cariaco Basin large fractions of the zero-valent sulfur occurs either colloidal or in the form of polysulfides. Additionally, polysulfides impact on biogeochemical cycling as they are observed as both substrates and products of microbial sulfur metabolism (Findlay, 2016).

Regarding the obvious absence of elemental sulfur particles at the redoxcline of cenote Tortugas this either indicates that elemental sulfur (S_8^0) that may be formed by chemolithoautotrophic sulfide oxidation, e.g. ND-SO, could be immediately converted to polysulfides or that the microbial oxidation of sulfide to zero-valent sulfur bound in dissolved polysulfides is predominant. Both processes would result in the observed absence of a turbid layer, which is most likely a consequence of the higher reducing power of cenote Tortugas compared to cenotes El Zapote and Maravilla, where elemental sulfur (S_8^0) particles can accumulate in the redoxcline to form a visible turbid layer. This is also consistent with the observation of cenotes with Hells Bells showing a decrease in turbidity with increasing reducing power in the order of El Zapote > Maravilla > Tortugas (Fig. 21, Fig. 24 and Table 2; p. 46, 51 and 54, respectively).

Methane Oxidation

Oxidation of methane in the redoxclines of cenotes with Hells Bells is clearly indicated by the fading of methane within the redoxcline and peaks of $\delta^{13}C\text{-}CH_4$ values towards higher values at the same water depth (Fig. 24, p. 49 and Fig. 25, p. 55). Previously, methane oxidation at the redoxcline of cenote El Zapote was tentatively attributed to sulfate-driven anaerobic oxidation of

methane (SD-AOM) (Ritter et al., 2019 and section 5.1.3.2 , p. 84). However, the recent results of microbiological investigations by Leberecht et al. (in prep.) showed no expressed genes in the microbiome of the redoxcline attributed to SD-AOM indicating that this process can be ruled out as a sink of methane at the redoxclines of cenotes with Hells Bells. In fact, Leberecht et al. (in prep.) found high expressions of genes that catalyze the oxidation of methane to methanol, while all other genes involved in the further oxidation of methanol to carbon dioxide were much lower or only marginally expressed. However, the genes related to the formate dehydrogenase, which catalyzes the final step of the oxidation of formate to carbon dioxide, were moderately expressed. Thus, the data of Leberecht et al. (in prep.) suggests that methane in cenotes with Hells Bells (or at least in cenote El Zapote) might not be fully oxidized to carbon dioxide and that SD-AOM is not a relevant process in methane oxidation.

Methanotrophs thrive from aerobic oxidation of methane with methane as their sole carbon source. Also, microbial anaerobic oxidation of methane coupled to nitrite (Ettwig et al., 2010) and nitrate reduction (ND-AOM) (e.g. Haroon et al., 2013) was shown to occur in natural environments after equation 10 (Caldwell et al., 2008).

$$CH_4 + 4NO_3^- \rightarrow CO_2 + 4NO_2^- + 2H_2O \qquad (10)$$

The CO_2 produced by full oxidation of methane to carbon dioxide could be metabolized by the methanotrophs and other chemolithoautotrophic microorganisms that thrive from oxidation of sulfide or ammonium, as already discussed above. The $\delta^{13}C\text{-}CO_2$ values released from the oxidation of methane are very low due to very low $\delta^{13}C\text{-}CH_4$ values. The $\delta^{13}C\text{-}CO_2$ values in the redoxclines show a peak towards higher values (Fig. 24 a, b and c, p. 51), which indicate that autotrophy in the redoxclines clearly outweighs the input of low $\delta^{13}C\text{-}CO_2$ of carbon dioxide produced by methane oxidation and that the carbon derived from oxidation of methane is metabolized to C_{org}.

Another interesting process in the oxidant limited-redoxclines of cenotes with Hells Bells could be the interaction of polysulfides with methane regarding the formation of organosulfides such as diemethyl sulfide (DMS) and methanethiol (Gun et al., 2000; Oduro et al., 2013). Formation

of methanethiol was suggested by Moran et al. (2008) who proposed that methylogenesis occurs in microbial anaerobic methane oxidation, where metabolically CH_4 oxidation provides the electrons for the energy-yielding reduction of CO_2 to a methyl group. The proposed proton-consuming reaction of this process is given in equation 11 (Moran et al., 2008).

$$CH_4 + \frac{1}{3}HCO_3^- + \frac{5}{3}H^+ + \frac{4}{3}HS^- \rightarrow \frac{4}{3}H_3CSH + H_2O \quad (11)$$

They further argued that conditions of low pH, high sulfide and inorganic carbon concentration would favor methylogenesis (Moran et al., 2008).

Manganese Oxidation

Elemental fluxes of manganese from the halocline towards the redoxclines in cenotes with Hells Bells intersect with downward fluxes of oxygen in cenotes with Hells Bells (Fig. 24, p. 51 and Fig. 25, p. 55) indicating manganese oxidation with oxygen to form Mn^{IV}-oxides after equation 12.

$$Mn^{2+} + \frac{1}{2}O_2 + H_2O \leftrightarrow MnO_2 + 2H^+ \quad (12)$$

The formed manganese particles could then be used as electron acceptor in all the oxidation processes of the upwards diffusing reduced chemical species discussed above. The formation of authigenic particles of "Mn-Fe-P" at pelagic redoxclines was observed in anoxic marine basins (Yakushev et al., 2009; Dellwig et al., 2010). Apparently, these particles are formed at the anoxic interface and subsequently sink down to be re-dissolved in lower more reducing water depths. This so called "Mn-Fe-P shuttle" likely affects phosphorous concentrations throughout the water column and thus also affects primary production. Such a process is likely to occur at the redoxclines in stratified stagnant cenotes as well, indicated by fluxes of dissolved manganese, iron and phosphorous towards the redoxclines (Fig. 25, p. 55 and Table A2). However, since concentrations of iron and manganese are very low in the water body of the cenotes, which is related to low contents of iron and manganese bearing minerals in the carbonate host rocks of the Yucatán Karst Aquifer, this process might be subordinate compared to other redox processes at redoxclines in cenotes with Hells Bells. Nevertheless, elevated manganese contents in different layers

of Hells Bells indicate variable manganese cycling in the cenote. Also, Mn-coatings on Hells Bells of shallower water depth indicate that manganese accumulation took place to some extent at some time in cenote El Zapote (section 4.2.1, p. 57).

5.2.2.3 Balancing redox processes in cenotes with Hells Bells

Balancing the transferred electrons ε of each electron (e^-) acceptor and donor allows for testing the plausibility of the proposed biochemical reactions at the redoxclines discussed and presented above (Fig. 42). This can be approached by calculating the e^- fluxes Je^- of each e^- acceptor and donor x by multiplying the transferred e^- of an electron acceptor/donor ε_x (given in Figure 42, p. 98and Table 7) with its respective ion flux J_x towards the redoxcline (J_x is given in Table 2, p. 54) after equation 13.

$$J\,e_x^- = J_x * \varepsilon_x \qquad (13)$$

The electrons e^- transferred (ε_x), which are considered for the calculation include the following assumptions (Table 7):

- ammonium (NH_4^+) is oxidized to nitrate (NO_3^-), which is reduced to di-nitrogen (N_2) gas
- hydrogen sulfide (HS^-) is oxidized to zero-valent sulfur (S^0), either in particulate form as elemental sulfur (S_8) or as dissolved polysulfides S_n^{2-}
- the whole flux of inorganic carbon (HCO_3^-) towards the redoxcline is reduced to organic matter (C_{org}) through chemolithoautotrophy
- methane (CH_4) is converted to CO_2, which is then converted to organic matter (C_{org}) in chemolithoautotrophy. This leaves a net conversion of methane (CH_4) to organic matter (C_{org})

The calculated e^- fluxes for each chemical species involved in the proposed biochemical redox reactions are given in Table 7. The calculations indicate that the proposed redox reactions comprised in Figure 42 (p. 98) and the accompanied e^- transfers are reasonable as a first approach considering that the ratios of the sum of all transferred e^- acceptors and e^- donors fall within a range of 0.42–1.57 for all cenotes with Hells Bells (Table 7). The e^- balance calculated for cenote

El Zapote shows the best results, which is valid considering the higher sample density at cenote El Zapote compared to cenotes Tortugas and Maravilla (Fig. 25, p. 55 and Table A2) and the strong dependency of the e^- balance on the calculated element fluxes of the respective elements towards the redoxclines.

The excess of e^- acceptors in cenotes El Zapote and Maravilla with values for the ratio of the sum of e^- acceptors to the sum of e^- donors of 0.88 and 0.42, respectively, indicate an overestimation of the flux of e^- acceptors towards the redoxcline (Table 7). This could be explained by an overestimation of the e^- flux derived from the HCO_3^- flux considering that calcite is permanently formed in the redoxclines, which consumes part of the HCO_3^- towards the redoxcline (section 5.1.2, p. 81). Accordingly, the e^- balance of cenotes El Zapote and Maravilla could be balanced considering that a portion of 14 and 63 % of the HCO_3^- flux is consumed by calcite precipitation in the redoxclines, respectively. This would correspond to precipitation rates of 3.3 and 38 mmol m^{-2} a^{-1} in the redoxclines of cenotes El Zapote and Maravilla, respectively.

The e^- balance of cenote Tortugas, however, reveals an excess in e^- donors (Table 7). This excess can be explained by taking the above described processes of methylation and polysulfide formation into account (Fig. 42). Both processes would reduce the fluxes of e^- donors towards the redoxcline and thus would compensate for the overestimation of e^- flux of donors given in Table 7. However, this cannot be quantified since these processes have not been documented so far to occur at the redoxcline of cenote Tortugas.

In conclusion, the results of the e^- balances demonstrate the plausibility of the discussed biochemical redox processes in the redoxclines of cenotes with Hells Bells, although details and relative abundances of each processes cannot be evaluated and may vary largely between the cenotes.

Table 7: Balances of electron (e^-) fluxes Je^- and e^- transfers of the proposed redox processes at the redoxcline of cenotes with Hells Bells. The calculation of the (e^-) fluxes is based in the fluxes J given in Table 2 (p. 54).

	e^- acceptors			e^- donors			e^- balance		
	$O_2 \rightarrow H_2O$	$\frac{1}{2} NO_3^- \rightarrow N_2$	$HCO_3^- \rightarrow C_{org}$	$HS^- \rightarrow S^0$	$NH_4^+ \rightarrow NO_{3-}$	$CH_4 \rightarrow C_{org}$			
e^- transfer	-4	-5	-4	2	8	4	$\mu eq.\ m^{-2}\ s^{-1}$		
	$J\ e^-$ in $\mu eq.\ m^{-2}\ s^{-1}$						Σe^- acc.	Σe^- don.	$(\Sigma e^-$ acc.)/ $(\Sigma e^-$ don.)
El Zapote 2018	3.65 E-04	1.51 E-04	3.10 E-03	1.58 E-03	1.24 E-03	3.73 E-04	**3.61 E-03**	**3.19 E-03**	**0.88**
Tortugas	2.55 E-05	4.83 E-04	5.71 E-03	2.79 E-03	4.38 E-03	5.96 E-03	**1.22 E-02**	**1.91 E-02**	**1.57**
Maravilla	2.91 E-05	3.33 E-04	7.74 E-03	2.49 E-03	4.73 E-04	2.82 E-04	**8.38 E-03**	**3.53 E-03**	**0.42**

5.2.2.4 Biochemical element cycling in cenotes with Hells Bells

In order to better understand the biochemical cycling in the cenotes with Hells Bells regarding its dependency of stagnancy and ultimately, its effects on calcite precipitation, it is beneficial to evaluate the element cycling with regard to its limitations and effects on the biochemical systems of the deep stratified cenotes. A schematic model comprising the element cycling within the interrelated pelagic and sedimentary processes of the redoxcline and halocline is shown in Figure 43. As a first approach, with regard to their biochemical inventory, the deep stratified cenotes are simple closed-systems with an upper and a lower source and sink, which are the cenote entrance at the surface and the basal connection to deeper aquifers below the cenote bottom, respectively. The initial biochemical energy-driving reaction is the heterotrophic decay of organic matter (C_{org}) in the sediments of the debris mounds and its decay products fuel the chemolithoautotrophic microbial community at the redoxcline above. This C_{org} is introduced into the cenote either from the outside via external sources such as leaves of trees and planktonic phototrophs (e.g. algae) from surface near water layers or via internal sources such as the planktonic chemolithoautotrophic microorganisms from the redoxcline (Fig. 43).

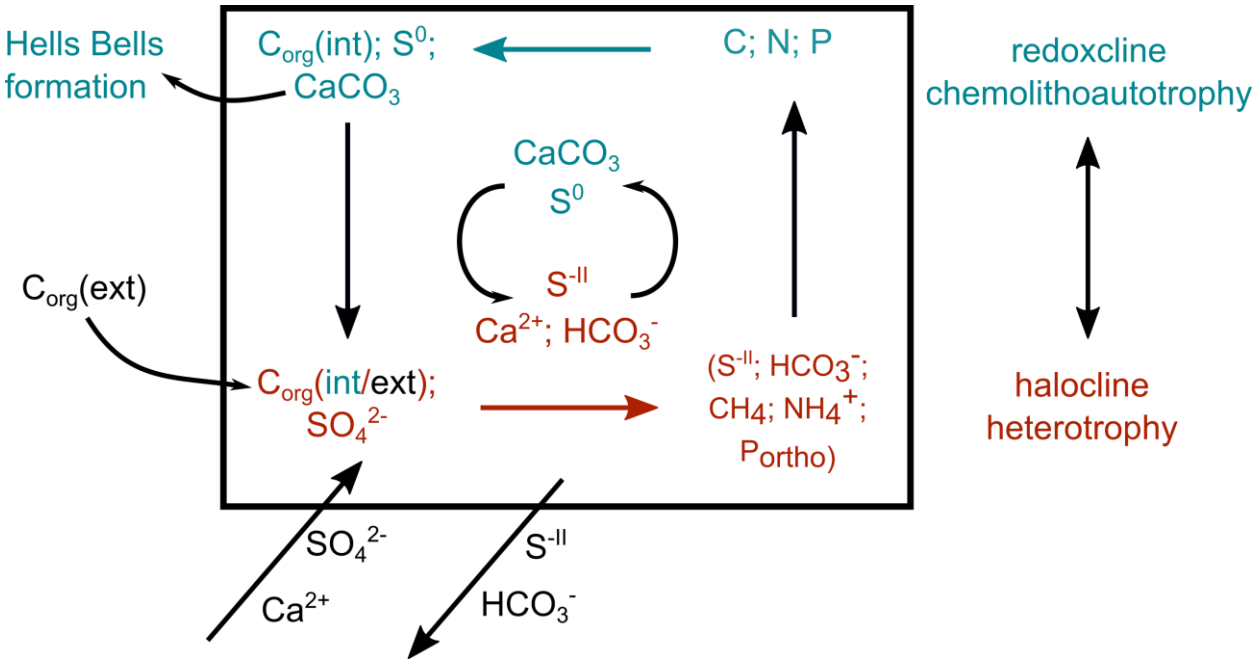

Fig. 43: Schematic model of the biochemical element cycling in the interrelated "self-sustaining" system of redoxcline chemolithoautotrophy – halocline heterotrophy. Internal and external organic matter is denoted as C_{org}(int.) and C_{org}(ext.), respectively.

The inventory of nitrogen and phosphorous compounds in the system of redoxcline autotrophy – halocline heterotrophy is thereby derived from external and internal sourced C_{org}, which is most likely completely recycled (Fig. 43). The carbon compounds are derived from both heterotrophic decay of internal and external C_{org}, as well as from inorganic carbon introduced by accompanied acid-buffering carbonate dissolution reactions in the calcite undersaturated sulfidic halocline. Carbon is either captured in the cell mass by chemolithoautotrophic microorganisms in the redoxcline, which is recycled as heterotrophic decay of internal C_{org} or temporarily or permanently stored via inorganic mineralization of calcite particles in the redoxcline or in Hells Bells carbonates, respectively (Fig. 43).

Sulfur compounds, however, are mainly derived from inorganic SO_4^{2-} from the saltwater body apart from the minor contributions of the sulfur content of organic matter considering a fairly constant C : N : P : S ratio of 100 : 8 : 2: 1 in global soils (Khan and Joergensen, 2019; Kirkby et al., 2011). The remainder of the sulfur, which is oxidized from sulfide to zero-valent sulfur at the redoxclines, either to elemental sulfur or to polysulfides, however, remains elusive. In the cenotes

El Zapote and Maravilla, where elemental sulfur particles are most likely formed in the redoxclines, zero-valent sulfur accumulates within the redoxclines in the form of elemental sulfur particles. These particles either sink down towards cenote bottom once they reached certain size and weight or they are used as electron acceptors for microbial oxidation processes in the lower part of the redoxcline or turbid layer. The latter seems more likely, as the technical divers reported no visible accumulation at the top of the sediments similar to the whitish overlay observed below the redoxcline in cenote Angelita (see YouTube video by Beloshin, 2013). This implies that sulfur has no sink above the redoxcline and is trapped below the halocline by constant recycling within the halocline, while its only sink is the flux of sulfide towards the cenote bottom (Fig. 43). Although a large fraction of the total zero-valent sulfur could be bound in polysulfides in the sulfidic haloclines of cenotes with Hells Bells (section 5.2.2.2, p. 98 and the sub-section "Sulfide Oxidation", p. 100), reduced sulfur compounds released by sulfate reducing organic matter decay in the sediments cannot accumulate infinitely within the halocline. This may be due to thermodynamic thresholds of the energy-generating sulfate reduction in heterotrophic organic matter decay or due to surpassing of toxic hydrogen sulfide levels. The abstraction of hydrogen sulfide due to the flux towards the cenote bottom is therefore apparently the only permanent sink for the reduced sulfur compounds in the cenotes with Hells Bells. Sulfate is not limiting the biochemical reactions, indicated by high concentrations within the halocline except in the upper parts of the halocline in cenote Tortugas (Fig. 23, p.49). Consequently, the advective depletion of reduced sulfur compounds below the cenotes could be the limiting factor for the biogeochemical system of redoxcline autotrophy – halocline heterotrophy in the extremely stagnant cenotes with Hells Bells. This also implies that the biochemical system of redoxcline chemolithoautotrophy – halocline heterotrophy could be self-sustaining once activated by a certain amount of introduced external C_{org}.

5.2.2.5 Biochemical processes in cenote Angelita without Hells Bells

In cenote Angelita, electron (e^-) acceptors and donors are roughly balanced in the redoxcline and oxidation of sulfide, ammonium and methane appears to be dominated by aerobic oxidation processes. Autotrophy might be an important metabolic process within the redoxcline, although no

significant increases of $\delta^{13}C\text{-}CO_2$ and $\delta^{13}C\text{-}CH_4$ values were detected in the redoxcline of cenote Angelita (Fig. 24, p. 51). This could solely be the result of the increased mass transfer and the accompanied faster isotope exchange in the water body of cenote Angelita. Ammonium and methane oxidation via aerobe microbial oxidation with oxygen and/or anaerobe microbial oxidation of methane with nitrate is supported by intersecting fluxes of ammonium and methane with dissolved oxygen and nitrate (Fig. 24, p. 51 and Fig. 25, p. 55).

Major aerobe sulfide oxidation in the redoxcline of cenote Angelita is supported by intersecting fluxes of dissolved oxygen and hydrogen sulfide at around 30 m water depth (Fig. 23, Fig. 24 and Fig. 25; p. 49, 51, and 55, respectively). Chemolithoautotrophic sulfur oxidizing bacteria (SOB) are able to generate energy from the oxidation of reduced sulfur compounds (Klatt and Polerecky, 2015). The energy yielding oxidation reactions can be performed to zero-valent sulfur (S^0) or sulfate (SO_4^{2-}) as possible end-products as shown in equations 14 and 15 (modified from Klatt and Polerecky, 2015).

$$HS^- + 0.5\,O_2 + H^+ \rightarrow S^0 + H_2O \quad (14)$$

$$HS^- + 2O_2 \rightarrow SO_4^{2-} + H^+ \quad (15)$$

According to the redox tower, the energy yield of sulfide oxidation to zero-valent sulfur (Eq. 14) is higher than the complete oxidation of sulfide to sulfate (Eq. 15) (Milazzo et al., 1978; Seager et al., 2012). It is most likely that both processes, namely the oxidation of hydrogen sulfide to zero-valent sulfur and sulfate occur simultaneously at cenote Angelita as indicated by an increase of SO_4^{2-}/Cl^- at the same depth (Fig. 23, p. 49), as well as by the thick white cloudy turbid layer (Fig. 7d, p. 15) formed at the top of the redoxcline (Fig. 21, p.46 and Fig. 24, p. 51) that strongly resembles the turbid layer of cenote Zapote, where abundant elemental sulfur (S_8) particles were found (section 4.1.1.4, p. 44). According to equations 14 and 15, stoichiometric ratios of hydrogen sulfide to dissolved oxygen of 0.5–2 are required to account for an oxidation of the total sulfide pool via aerobic sulfide oxidation. The stoichiometry of the obtained fluxes of dissolved oxygen and hydrogen sulfide towards the redoxcline in cenote Angelita is 0.7 (Table 2, p. 54) showing

that the total depletion of hydrogen sulfide could be due to aerobic sulfide oxidation after equations 14 and 15.

In order to evaluate the fractions of the total sulfide oxidized to S^0 and SO_4^{2-} within the redoxcline of cenote Angelita a generalized equation of both reactions (Eq. 14 and 15) is given in equation 16 (modified from Klatt and Polerecky, 2015).

$$HS^- + (2 - 1.5x)\, O_2 + x\, H^+ \rightarrow x\, S^0 + (1 - x)\, SO_4^{2-} x\, H_2O + (1 - x)\, H^+ \qquad (16)$$

Where x and (1-x) are the fractions of the total HS^- oxidized to S^0 and SO_4^{2-}, respectively ($0 \leq x \leq 1$).

Using the stoichiometry of the obtained fluxes of dissolved oxygen and hydrogen sulfide towards the redoxcline in cenote Angelita yields x = 0.87, indicating that 87 % of the hydrogen sulfide is oxidized to zero-valent sulfur and only 13 % of the sulfide is oxidized to sulfate.

Additionally, nitrate as oxidizing agent should also be taken into account and thus the fraction of zero-valent sulfur formed in the redoxcline of cenote Angelita can be estimated by balancing the transferred electrons (e^-) in the all likely redox reactions in the redoxcline of cenote Angelita. This is obtained by calculating the e^- fluxes of each e^--donor and e^--acceptor by multiplying the calculated ion fluxes J towards the redoxcline (Table 2, p. 54) with the amount of transferred electrons in the proposed redox processes (Table 8) after equation 13 (p. 105) as already specified in section 5.2.2.3 (p. 105). The electrons e^- transferred (ε_x), which are considered for the calculation, include the following assumptions (Table 8):

- ammonium (NH_4^+) is oxidized to nitrate (NO_3^-), which is reduced to di-nitrogen (N_2) gas
- hydrogen sulfide (HS^-) is either oxidized to zero-valent sulfur (S^0) or fully oxidized to sulfate (SO_4^{2-})
- methane (CH_4) is converted to carbon dioxide (CO_2), which is then converted to organic matter (C_{org}) in chemolithoautotrophy. This leaves a net conversion of methane (CH_4) to organic matter (C_{org})

As no electrical charge is generated in the redoxcline, the sum of all transferred electrons (ε_x) is zero, and thus, the flux of all e^- acceptors and e^- donors is zero. Assuming that the proposed redox processes and electron transfers occur at the redoxcline of cenote Angelita the fractions of sulfur oxidized to zero-valent elemental sulfur particles and the most oxidized sulfur species sulfate (SO_4^{2-}) can be estimated by solving equation 17 after the variable *x* and dividing the result of each fraction by their number of transferred e^-, which is given in Table 8.

$$e_{O2}^- + e_{NO3}^- + e_{NH4}^- + e_{CH4}^- + xe_S^- + (x-1)e_{SO4}^- = 0 \qquad (17)$$

Table 8: Balances of electron (e^-) fluxes *J*e^- and e^- transfers of the proposed redox processes at the redoxcline of cenote Angelita devoid of Hells Bells. The calculation of the (e^-) fluxes is based in the fluxes J given in Table 2 (p. 54).

	e^- acceptors		**e^- donors**			**e^- balance**		
	O_2 → H_2O	½ NO_3^- → N_2	HS^- → S^0	NH_4^+ → NO_3^-	CH_4 → C_{org}			
e^- transfer	-4	-5	2	8	4	**J e^- in µeq. m^{-2} s^{-1}**		
	J e^- in µeq. m^{-2} s^{-1}					**Σe^- acc.**	**Σe^- don.**	**(Σe^- acc.)/ Σe^- don.**
Angelita	4.18E-04	7.06E-04	2.99E-04	2.27E-04	6.37E-06	**1.12E-03**	**5.32E-04**	**0.47**

The calculation yields that 35 % of the hydrogen sulfide is oxidized zero-valent sulfur and 65 % of the sulfide is fully oxidized to sulfate, respectively, in the redoxcline of cenote Angelita. This result is in good agreement with the observation of a thick turbid layer at the redoxcline of cenote Angelita (Fig. 7d, p. 15) and slightly increasing SO_4^{2-}/Cl^- at the same water depth (Fig. 23, p.47).

The oxidation of a part of the sulfide to elemental sulfur particles implies that the sulfide oxidation in cenote Angelita could be a proton-consuming process depending on the amount of sulfide oxidized to elemental sulfur (Eq. 16), equivalent to the dominant ND-SO in the redoxcline of cenote El Zapote. Interestingly, there is a slight increase of pH at the water depth where the fluxes of dissolved oxygen and hydrogen sulfide intersect (Fig. 24, p. 51 and Table A2). However, there is no indication for calcite precipitation in the redoxcline of cenote Angelita, which is best exemplified by an undersaturation with respect to calcite throughout the water column (Fig. 24, p. 51). This is either due to a too low proton-consumption by the aerobe oxidation of sulfide to elemental

sulfur and low turnover rates of the S-cycle, or undersaturation with respect to calcite is due to a downward flux of hydrogen carbonate from the redoxcline to the halocline in cenote Angelita, or a combination of both, as these factors are interrelated by the superordinate degree of advection or stagnancy.

5.2.3 Extent of redoxcline biogeochemistry in deep stratified cenotes

As demonstrated above, the fluxes towards the redoxcline of deep stratified cenotes essentially determine the composition of the microbial community and the prevailing biogeochemical processes in the redoxclines. The fluxes, in turn, are strongly related to the degree of advection. In order to exemplify the interrelation of biogeochemistry, degree of advection or stagnancy and calcite precipitation within the redoxcline, the extent of different deep stratified cenotes of the YP at different biogeochemical stages is shown in Figure 44.

In less stagnant cenotes with high availability of oxidants indicated by $e^-_{acceptors} : e^-_{donors} > 1$ and by a minor organic matter decay-related accumulation of chemical species within the halocline, upwards diffusing sulfide is fully oxidized to sulfate in the redoxcline. Because this is an acidic reaction no calcite precipitation occurs. In cenotes with a decreased degree of advection and lower availability of oxidants indicated by $e^-_{acceptors} : e^-_{donors} \leq 1$, upwards diffusing sulfide is oxidized to sulfate and zero-valent sulfur while $SO_4^{2-} : S^0$ decreases with decreasing advection due to insufficient electron acceptors for a full oxidation of sulfide to SO_4^{2-}. Once $SO_4^{2-} : S^0 \leq 1$ is reached, sulfide oxidation is a proton-consuming reaction increasing the alkalinity within the redoxcline. Under such conditions, the potential of calcite precipitation is given, if the organic matter decay-related accumulation of chemical species in the halocline, i.e. hydrogen carbonate, is sufficient to generate an upward flux of hydrogen carbonate towards the redoxcline such as observed in cenotes El Zapote and Maravilla. The conditions for calcite precipitation may only be reached in conditions, where sulfide oxidation is predominantly anaerobe, as oxidation of sulfide to elemental sulfur

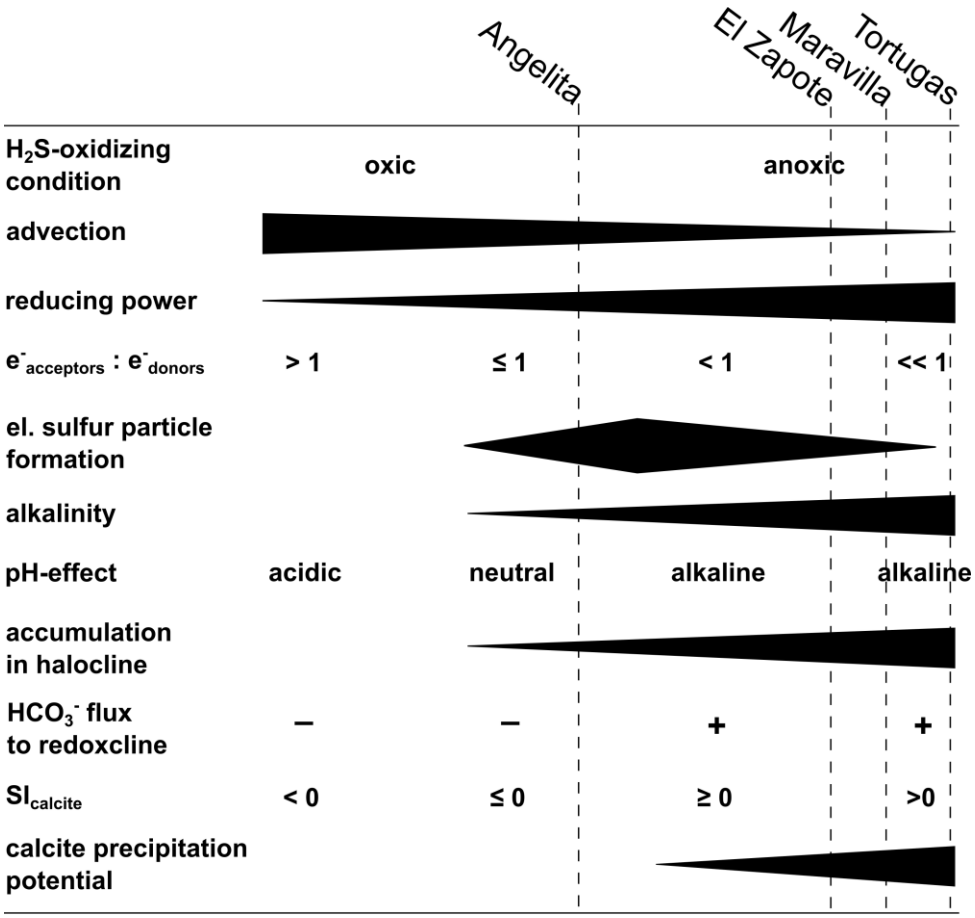

Fig. 44: Exemplary extent of stages of the redoxcline biogeochemistry in relation to the degree of advection and calcite precipitation potential of deep stratified cenotes of the Yucatán Peninsula determined from comparison of cenotes with and without Hells Bells. With decreased degree of advection and decreasing availability of oxidants, alkalinity and reducing power increases due to proton-consuming incomplete oxidation of reduced chemical species, e.g. HS^- to S^0 (section 5.2.2.3, p.105). The calcite precipitation potential increases with alkalinity and is at maximum, where sulfide is oxidized under anoxic conditions. Elemental sulfur (S_8) is only formed and stable within a certain range of oxidant to reductant relation and is not stable under conditions of very high reducing power (sections 5.2.2.2, p. 98 and 5.2.2.5, p. 109.

with nitrate (ND-SO) is by 28 % more proton consuming than the oxidation of sulfide to elemental sulfur with oxygen according to equations 3 (p.86) and 14 (p. 110), respectively. In highly stagnant cenotes such as cenote Tortugas, with high reducing power indicated by $e^-_{acceptors} : e^-_{donors} << 1$, elemental sulfur formation in the redoxcline might be limited by polysulfide formation resulting in a apparently clear redoxcline, which indicates that the formation or presence of a turbid layer is apparently not necessary for Hells Bells formation.

In conclusion, in order to generate calcite precipitating conditions within the redoxcline of deep stratified cenotes of the YP, a certain low degree of advection is required to overcome the following thresholds:

- the organic matter-related accumulation of hydrogen carbonate (HCO_3^-) in the halocline needs to be high enough to create an upwards diffusion towards the redoxcline
- the availability of oxidants needs to be low enough to create favorable conditions for chemolithoautotrophic proton-consuming microbial oxidation of upwards diffusing reduced chemical compounds (e.g. ND-SO) within the redoxcline.

As both processes occur simultaneously and are interrelated, it is impossible to determine which of both processes delimits calcite precipitation.

5.2.4 Other stagnant cenotes on the Yucatán Peninsula

Based on the afore discussed criteria for subaqueous calcite precipitation in deep stratified cenotes other deep stratified cenotes reported from the Yucatán Peninsula (YP) are reviewed with respect to their potential of forming Hells Bells in this chapter.

Hells Bells have so far been identified in only a few cenotes of a restricted area of the North-Eastern YP (Fig. 5, p.13 and Stinnesbeck et al., 2017b). On the other hand, the peninsula hosts many thousands of sinkholes (Bauer-Gottwein et al., 2011; Torres-Talamente et al., 2011). Thus, the questions arise if this phenomenon of calcite precipitation within the redoxcline, hence Hells Bells formation, is actually limited to cenotes of this area or if other so far unexplored and/or unrecognized deep stratified cenotes may reveal this phenomenon as well.

Therefore, the comparison of published hydrogeological data of deep stratified cenotes could offer valuable clues on the potential of Hells Bells formation at other sites. There is limited data available in literature on deep stratified pit cenotes of the YP, while most studies were conducted in the state of Quintana Roo in the North-Eastern part of the YP (Beddows et al., 2007; Kovacs et al., 2017b; Stoessell, 1995; Stoessell et al., 1993, 2002; Torres-Talamente et al., 2011) and only data of two deep stratified cenotes in the state of Yucatán in the North-Western part of the YP were found to be reported (Pedersen, 2007; Socki et al., 2002).

The hydrogeological characteristics derived from the available data of these cenotes are presented in Table 9 together with the cenotes studied in this work. The halocline thickness and the gradient

of the increase in electrical conductivity (grad EC) are promising parameters or proxies for the identification of the degree of advection within the water body of a cenote. Electrical conductivity measurement is a robust method and most likely to be reported in studies on water bodies of cenotes and therefore an easy to calculate and available parameter.

The reported deep stratified cenotes are ordered with increasing gradients of electrical conductivity in Table 9 alongside other important parameters such as halocline thickness, the water depth of the top of the halocline, the distance to the coast and whether the halocline is sulfidic or not. Table 9 is roughly separated into two groups of cenotes, where one is comprised of stagnant cenotes with grad EC values in the range of 2.5–6.5 mS cm^{-1} m^{-1} and halocline thicknesses of 10–40 m, while the other group is comprised of less stagnant or "convective" cenotes with grad EC values in the range of 13–50 mS cm^{-1} m^{-1} and halocline thicknesses of 1–5 m. Cenotes with Hells Bells all fall within the group of stagnant cenotes while cenote Angelita falls within the group of less stagnant or "convective" cenotes.

The latter group of "convective" cenotes are relatively close to the coast throughout and all of them are located in the area along the coast of the "Riviera Maya" between the cities Playa del Carmen and Tulum and just north of the Sian Ka´an Biosphere Reserve (Fig. 5, p.13). Therefore, this group of cenotes is by far not representative for deep stratified cenotes occurring on the YP and merely reflects a certain hydrogeological area of the YP. It is likely that the overrepresentation of this group is due to the fact that most of these cenotes are visitor cenotes close to the main road with good accessibility and infrastructure. It is highly unlikely that processes leading to calcite precipitation in the redoxclines of these cenotes occur due to a high degree of advection (section 5.2.2, p. 96).

Considering the factors controlling Hells Bells formation discussed before (section 5.2.1, p. 94), the cenotes Xcolac, Ucil, Big Calica and Calica Pit reveal characteristics similar to cenotes with

Hells Bells presented in this study (Table 9). Hells Bells formation or any indication for a precipitation of calcite within the redoxclines are not reported for these cenotes. However, pH logs are available for cenotes Xcolac, Ucil and Big Calica (Pedersen, 2007; Socki et al., 2002).

Table 9: Compilation of hydrologic characteristics of deep stratified cenotes reported for the Yucatán Peninsula with regard to stagnancy and Hells Bells formation. The cenotes are ordered with increasing gradient of electrical conductivity (grad EC), which indicates increasing degree of advection in the water body of the cenotes.

cenote	grad. EC mS cm^{-1} m^{-1}	Hells Bells	sulfidic	alkaline pH peak in redox-cline	top halo-cline m.b.w.l	halocline thickness m	distance to coast km	reference
Xcolac	~2.5	likely	yes	yes	~51	~40	~55	Socki et al. (2002)
Tortugas	2.7	yes	yes	yes	32.9	19.3	~19	this study
Big Calica	~5	likely	yes	yes	~12	~10	~5	Stoessel (2002)
Calica Pit	~5	likely	yes	yes	~12	~12	~3	Stoessel (2002)
7 Bocas	5.2	yes	yes	yes	29.5	> 6.5	~15	this study
Maravilla	5.5	yes	yes	yes	30.6	>12.8	~14	this study
Ucil	~6	likely	yes	yes	~68	> 12	~50	Socki et al. (2002)
Zapote	6.5	yes	yes	yes	36.7	10.3	~21	this study
The Pit	~13	no	yes	n.r.	~15	~5	~6	Kovacs et al. (2017b)
Ich Balam	~15	no	n.r.	n.r.	~16	~5	~7	Kovacs et al. (2017b)
Nohoch Hol	~15	no	yes	yes	~9	~6.5	~3	Torres-Talamente et al. (2011)
Litte Cal-	~21	no	yes	n.r.	~12	>2	~4	Stoessel (2002)
Angelita	27	no	yes	no	29.5	4	~11	this study
Angelita	~30	no	yes	no	~29	~2	~11	Stoessel et al. (1993)
Carwash	~28	no	n.r.	n.r.	~20	~2	~9	Kovacs et al. (2017b)
Cenote Eden	~40	no	n.r.	n.r.	~11	~1	~1.5	Beddows et al. (2007)
Cenote of the sun	~50	no	n.r.	n.r.	~17	~1	~4	Beddows et al. (2007)

m.b.w.l.: meters below water level; n.r.: not reported

Cenote Ucil shows no indications of a pH peak towards more alkaline values in the redoxcline, which might be due to its morphology that hinders organic material to enter the cenote (Socki et

al., 2002). Unfortunately, there is no hydrogeochemical data available for a further evaluation of cenote Ucil.

Cenotes Xcolac and Big Calica, however, are pit shaped cenotes similar to cenote Angelita allowing for organic matter to enter the cenote and accumulate at the cenote floor. Oxygen and EH profiles suggest a formation of a redoxcline at the top of the haloclines in these cenotes (Pedersen, 2007). Furthermore, they show pH patterns with depth that strongly resemble those found in cenotes with Hells Bells showing increasing pH at the redoxclines immediately below the oxygen depletion zone (Pedersen, 2007; Socki et al., 2002). Additionally, the reported saturation indices of calcite show a peak towards oversaturated values of SI values up to 0.5 in these zones. Pedersen (2007) attributed these pH excursions to increased sulfate reduction of organic matter accumulated at the top of the halocline. However, this conclusion lacks the basis of data as organic matter concentrations or accumulation were not determined. Furthermore, most likely because this was not within the scope of their study, alternative reasons for the uncommon observed pH excursions such as autotrophy and proton-consuming oxidation of sulfide to zero-valent sulfur were not discussed. Therefore, considering the mechanism of microbially-induced calcite precipitation in redoxclines of deep stratified cenotes presented in this work, it seems likely that this process might also occur in cenotes Big Calica and Xcolak. The latter might even bear more potential for this process to occur, as the top of the halocline is deep enough (~51m) to exclude photoautotrophy as dominant metabolism at the redoxcline, whereas photoautotrophy could be dominant at the redoxcline in cenote Big Calica, where the top of the halocline is found at only 12 m water depth (Table 9). The same applies for cenote Calica Pit, which is in vicinity of Big Calica and another cenote of the group of less stagnant or "convective" cenotes, Nohoch Hol (Table 9), which also shows a pH pattern similar to that of cenotes with Hells Bells with an pronounced peak towards alkaline pH values in the redoxcline (Torres-Talamente et al., 2011). The top of the halocline however, is already at 9 m water depth and the halocline with 6 m is not as thick as probably needed in order for an accumulation of inorganic carbon within the halocline. Unfortunately,

there is no complete hydrogeochemical data reported for Nochoch Hol in order to calculate calcite saturation or evaluate the accumulation within the halocline.

Nonetheless, the evaluation of reported data on deep stratified cenotes clearly suggests that the phenomenon of calcite precipitation in redoxclines of stagnant cenotes on the YP might be by far more prevalent than so far assumed. Considering the thousands of unexplored deep cenotes of the YP and its vast inaccessible areas, it is highly likely that the phenomenon of Hells Bells formation occurs also in other areas of the YP apart from the already known restricted area. Eventually, this brief literature review is also encouraging to encounter calcite precipitation or even subaqueous speleothem formation in already known and studied cenotes.

5.3 The role of the halocline elevation in Hells Bells formation

This chapter discusses a second major process, which is crucial for the formation of Hells Bells, a dynamic elevation of the halocline or the zone of subaqueous calcite precipitation.

Hells Bells at cenote El Zapote formed at least since ~120 ka BP up to modern times and occur in a relatively thick vertical zone of about 10 m from 28–38 m water (Schorndorf, 2018; Stinnesbeck et al., 2017b). This indicates that their underwater growth most likely occurred under environmental conditions similar to the ones described here, as modern sea levels were already reached at about 4.5 ka BP (Hengstum et al., 2010). Hells Bells are found in the depth zone reaching from ~28-38 m and subaqueous calcite precipitation occurs most likely only in the narrow 1–2 m thick redoxcline above the halocline (section 5.1.2, p. 81) due to biogeochemical processes (section 5.1.3, p. 83 and Fig. 40, p. 90). Therefore, growth of Hells Bells has to be a non-permanent episodic process, which majorly depends on the elevation of the zone of calcite precipitation, i.e. the halocline elevation in the cenote (Fig. 45). The depth of the halocline generally increases with increasing distance to the coast (Fig. 45a) (e.g. Bauer-Gottwein et al., 2011). The halocline depth position is a function of the hydrostatic pressure of the overlying freshwater layer, i.e. its thickness and the sea level. The halocline elevation varies on multiple timescales in response to droughts, recharge events and annual tidal fluctuations that are superimposed upon on a longer term sea level change. Extensive droughts occurred repeatedly in the Holocene (Hodell et al., 2001) and could have led to a prolonged elevation of the halocline, as the freshwater layer was thinner in consequence of lower precipitation (Evans et al., 2018). Also, extraordinary recharge events (e.g. hurricanes) must have an effect on the depth position of the halocline, though on much shorter timescales (Fig. 45b). Generally, during these events of enormous precipitation, the halocline is temporarily pushed downwards by the amount of the freshwater infiltrating into the Yucatán Karst Aquifer. However, it has been reported that the halocline can also be elevated as a response to precipitation events (Escolero et al., 2007).

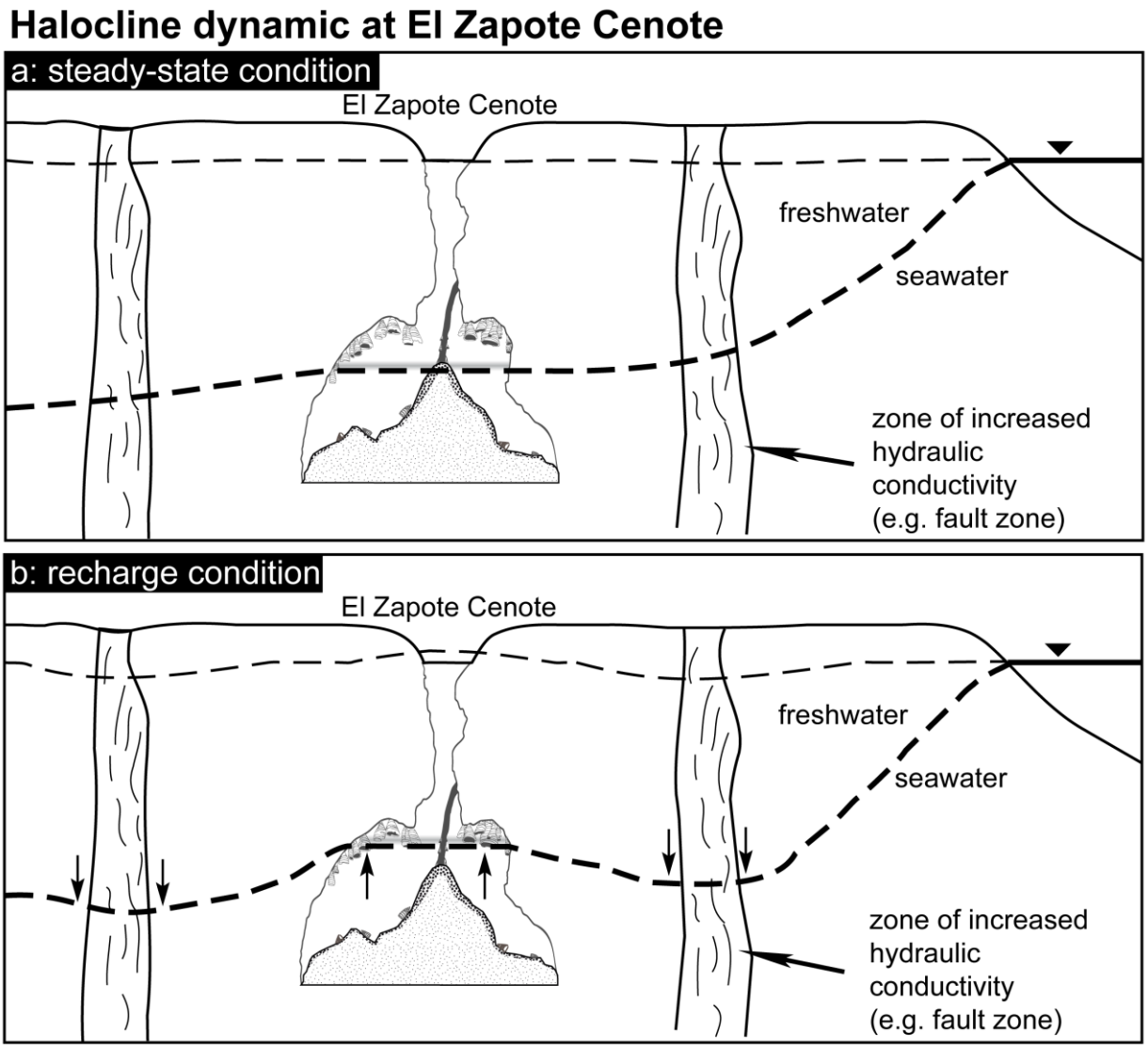

Fig. 45: Sketch of dynamic halocline elevation within the Yucatán Karst Aquifer. Halocline depth increases with increasing distance from the coast in a steady-state condition (a). Recharge events result in a lower halocline beneath areas of high vertical transmissivities and an elevated halocline in areas of low hydraulic transmissivity, e.g. cenote El Zapote (b). Modified from Ritter et. al (2019).

To date, only few studies present time series data on the dynamics of the Yucatán Karst Aquifer. They focus on coastal salt intrusion processes (Vera et al., 2012) and mixing processes of freshwater and saline water in caves and cenotes near the coast (Coutino et al., 2017; Kovacs et al., 2017b). However, there are no studies that report aquifer dynamics with regard to the halocline elevation and variation of the thickness of the freshwater lens. Recharge-driven halocline elevations were observed in in the preliminary results of the data loggers at cenotes El Zapote in response to recharge events (section 4.4, p. 75). However, the amplitudes of the observed halocline

elevations in these events were low (<10cm) and no heavy precipitation events occurred within the logging period (Fig. 38, p. 78).

Regional and local vertical and lateral hydraulic conductivities of both the epi- and the phreatic karst can result in spatially variable hydraulic pressure of the freshwater lens (Williams, 1983), thus leading to a lowered halocline beneath areas of higher, and an elevated halocline beneath areas of less vertical hydraulic conductivities. Cenote El Zapote is located in the Holbox fracture zone that in the area is characterized by N-S trending lineaments of increased permeability (Bauer-Gottwein et al., 2011, and references therein). Hurricanes that pass the area frequently (Farfán et al., 2014) could therefore lead to episodic elevation of the halocline (Fig. 45b). Hydraulic conductivities increase in karstic systems with time due to gradual karstification. Therefore, halocline elevations due to differences in hydraulic conductivities might have been prolonged in past Hells Bells growth phases, e.g. the past interglacial, due to generally lower hydraulic conductivities as compared to the present.

Both, a prolonged halocline elevation during droughts and short-term but frequent recharge-driven halocline elevations could result in the presence of Hells Bells in a zone of 28–38 m water depth. Age-dating of the lowermost "youngest" Hells Bells calcite of specimen from different water depth at cenote El Zapote show uniform ages of 100–200 a BP revealing no dependency on water depth (Schorndorf, 2018). This indicates that short-term halocline elevations might prevail at cenote El Zapote. Furthermore, repeated phases of precipitation and dissolution indicated by the alternating layers of dog-tooth calcite and microcrystalline calcite of Hells Bells thin sections suggest an episodic halocline elevation (section 4.2.2, p. 60 and Stinnesbeck et al., 2017b). During episodes of an elevated halocline, precipitation or dissolution of Hells Bells may occur in lower depths due to the concurrent elevation of the calcite precipitating redoxcline and the underlying sulfide-rich and carbonate undersaturated water.

A variable halocline depth position at cenote El Zapote is also supported by the positive correlation with water depth of Sr/Ca and a negative correlation of $\delta^{13}C$ of the Hells Bells calcite (Fig. 35,

p.73). Hells Bells formed in lower water depths show slightly higher contents of the trace elements Sr, Mg and Ba and slightly lower $\delta^{13}C$ values than Hells Bells formed in greater water depths (Fig. 35, p.73 and Table 5, p. 72). The higher incorporation of the trace elements Sr, Mg and Ba is either obtained by faster growth rates (Tesoriero and Pankow, 1996), or by elevated concentrations in the solution from which the calcite precipitated. The latter process is more likely, as the amount of saltwater increases in the turbid layer when the halocline is located at lower water depths. Lower $\delta^{13}C$ values support this assumption, as lowest $\delta^{13}C$-HCO_3^- values are detected in the halocline of the modern cenote El Zapote (Fig. 19, p. 43).

The increase in saltwater in the lowermost freshwater and the redoxcline could result from increased salinity of the freshwater body during droughts. Also, turbulences induced by halocline elevation as a reaction to recharge events were observed in cenotes of the YP (Kovacs et al., 2017b). Minor mixing of the water bodies would be sufficient to increase the concentrations of Sr, Mg, Ba and decrease $\delta^{13}C$-HCO_3^- in the turbid layer, as seen at El Zapote.

Following the model of an episodic halocline elevation, the question remains why Hells Bells are restricted to a zone of 28–38 m water depth. This range could solely depend on the hydraulic conditions, e.g. Hells Bells formation reflecting maximum and minimum elevations of the halocline as a result of droughts, recharge events and long-term sea level changes. The lower (38 m) level of Hells Bells formation may represent the stable environmental conditions in the modern El Zapote cave, influenced only by the thickness of the freshwater body and the mean sea level. Additionally, aquifer hydraulic characteristics impacting on the biogeochemistry and hence on calcite precipitation and Hells Bells growth could delimit this lower level to the water depth of ~38 m (section 5.2.2, p. 96). The upper range boundary, on the other hand, could well be given by the shape of the sinkhole and limnological conditions in the narrow cenote shaft reaching from 0–30 m water depth. In this latter unit the water body is mixing- rather than diffusion-dominated (Fig. 16, p. 38 and section 5.1.1, p. 80). A rise of the halocline to about 28 m water depth would therefore lead to an exposure to fast and convective oxygen supply from the mixed-in freshwater

body above, and consequently to severe changes of the biogeochemistry due to increased availability of oxidants, e.g. aerobic sulfide oxidation, which is an acid-producing reaction (Eq. 14, p. 110). Hells Bells formation would then stop as it is apparently tied to incomplete microbial oxidation of sulfide to zero-valent sulfur in the redoxcline, e.g. anaerobic ND-SO (section 5.2.3, p. 113). The occurrence of a zone of brown-colored manganese oxide coatings on Hells Bells and the cave wall at and above 30 m water depth, indicates that the redoxcline must temporarily have reached up to this level (Fig. 2c, d, p. 7). Manganese dissolved in the halocline and turbid layer was then oxidized to manganese oxide precipitates forming manganese coatings on the surfaces of Hells Bells calcites (Fig. 26b, p. 57).

5.4 Summary and synthesis on Hells Bells formation

This chapter aims to summarize and integrate the before presented detailed results and discussions on redoxcline biogeochemistry, its regulation by stagnancy or the degree of advection and the role of the halocline elevation in deep stratified cenotes of the Yucatán Peninsula (YP). First, a simple model is presented intending to illustrate Hells Bells growth as a combination of both authigenic calcite precipitation in the redoxcline and variable halocline elevations. Then, the characteristic morphological features of Hells Bells speleothems are discussed in the context of the hypotheses on authigenic calcite precipitation and dynamic halocline elevation. Finally, the regional hydrogeology is related to the distribution of the cenotes with Hells Bells on the North-Eastern YP based on the prerequisites for Hells Bells formation.

5.4.1 Conceptual model of net Hells Bells growth – interplay of authigenic calcite formation and episodic halocline elevation

The growth of Hells Bells is apparently the result of a combination of both, microbially induced authigenic calcite precipitation in the redoxcline and a permanent fixation or preservation of this calcite in elevated water levels due to a dynamic elevation of the halocline. If authigenic calcite would form in a static redoxcline regarding its elevation, the calcite formed would sink down to the cenote bottom once particles reach a certain size. Consequently, this would not result in permanent preservation of calcite in the form of Hells Bells, because calcite is undersaturated below the redoxcline (Fig. 17, p. 40 and Fig. 24, p. 51) and sinking calcite particles are likely to be re-dissolved (Fig. 43, p. 109). Therefore, considering the consistent hypothesis of authigenic calcite precipitation within the narrow zone of the redoxcline presented here, a variation of the halocline elevation and thus the zone of calcite precipitation is a necessity for a permanent fixation of the authigenic calcite formed in the redoxcline in the form of Hells Bells.

This relationship of calcite precipitation in the redoxcline and variable halocline depth level leading to Hells Bells growth in water depth levels above the mean minimum depth level of the halocline is exemplified with two simple models in Table 10. The models consider that the freshwater

is saturated with respect to calcite, and that the redoxcline precipitates and the halocline dissolves calcite. As a first approach, calcite precipitation and dissolution are considered to be equal with assumed rates of calcite precipitation and dissolution a rate of 10 mmol m^{-2} a^{-1}, which are derived from the estimations on calcite precipitation rates elaborated in section 5.1.6 (p. 90) (Table 10). Additionally, exact rates are insignificant for the purpose of the model. For each model, the halocline elevation was varied for a certain time interval of different duration, which depends on the respective simulated mechanism for the variation of the halocline elevation.

Model 1 represents a longer-term steady increases and decreases, respectively, of the halocline simulating droughts and wet periods of increased precipitation (t = 10 a in Table 10), discussed before in section 5.3 (p.121). The net calcite preserved at each depth level in Table 10 represents the sum of calcite that was either precipitated or dissolved in each time interval at the respective depth level. Model 2 is designed to reflect the observed periodic variation of the halocline depth level throughout one year due to annual tidal variations of ~0.4 m together with episodic short-term recharge-driven halocline elevation events (section 4.4, p. 75). The different time scales and estimated amplitudes of the proposed halocline elevation mechanisms are illustrated with respect to the Hells Bells growth in Figure 46.

A permanent fixation of calcite in water depths above the present-day halocline elevation is suggested by both models 1 and 2 indicated by positive net calcite values in water depth levels (cells) above the present-day halocline (Table 10). Model 2 shows that the net calcite precipitation throughout one year is only found in the mean halocline water depth levels and above (Table 10).

Both models show that a permanent preservation of calcite formed in the redoxcline is only possible with a variable halocline. Furthermore, the net calcite precipitation in the two models is only found within and above the mean halocline water depth level Table 10. This behavior is consistent with the observation that most Hells Bells appear in water depths of a certain range above the present-day halocline elevation (Fig. 46) and do not appear below certain water depths (not below ~38 m), which might reflect the long-term lowest position of the halocline.

Table 10: The net calcite precipitation or Hells Bells growth at each water depth level as a result of halocline depth level elevation changes due to steady increase and decrease of the halocline as a result of droughts and wet periods is simulated in Model 1. Periodic annual tidal sea level changes in combination with short-term episodic recharge-driven halocline elevations are simulated in Model 2.

input parameters:	calcite precipitation rate	10 mmol m^{-2} a^{-1}
	caclite dissolution rate	-10 mmol m^{-2} a^{-1}
	time interval model 1, t_s	10 a
	time intervals model 2, t_p; t_e	91; 10 d

Model 1		**steady increase (drought)**			**steady decrease (wet/freshwater build up)**					**net calcite [mmol]**
		t_s1	t_s2	t_s3	t_s4	t_s5	t_s6	t_s7		Σt_s
		mmol calcite per time interval t_s								
freshwater	calcite saturation	0	0	0	100	0	0	0		100
		0	0	100	-100	100	0	0		100
		0	100	-100	-100	-100	100	0		-100
redoxcline	calcite precipitatio	100	-100	-100	-100	-100	-100	100	present day	-300
halocline	calcite dissolution	-100	-100	-100	-100	-100	-100	-100	top halocline	-700

Model 2		**periodic variation (annual tidal)**				**net calcite [mmol]**		**episodic variation (recharge)**		**net calcite [mmol]**
		t_p1	t_p2	t_p3	t_p4	Σt_p		t_e		$\Sigma t_p + \Sigma t_e$
		mmol calcite per time interval t_p and t_e								
freshwater	calcite saturation	0.0	0.0	0.0	0.0	0.0		0.0		0.0
		0.0	0.0	2.5	0.0	2.5	+	0.3		2.8
redoxcline	calcite precipitatio	2.5	0.0	-2.5	2.5	2.5		-0.3	present day	2.2
		-2.5	2.5	-2.5	-2.5	-5.0		-0.3	top halocline	-5.3
halocline	calcite dissolution	-2.5	-2.5	-2.5	-2.5	-10.0		-0.3		-10.3

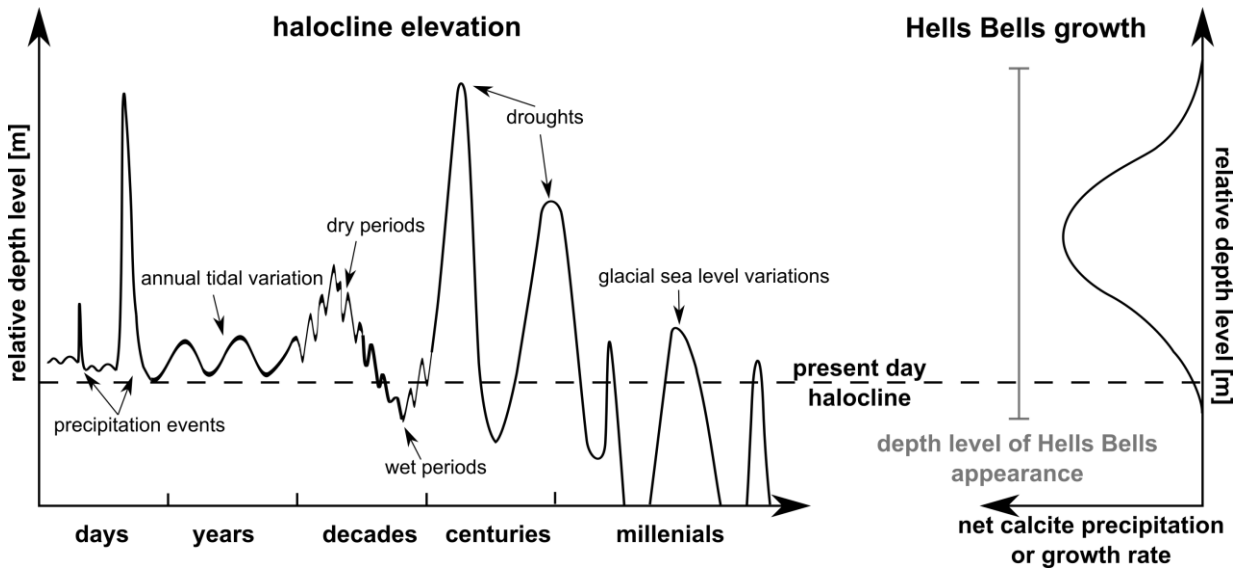

Fig. 46: Scheme of varying halocline elevation on different timescales due to the different indicated mechanisms (on the left). Hells Bells seem to grow faster in the center of the 10 m zone of Hells Bells appearance (on the right). This is visually indicated by the seize distribution with water depth of Hells Bells specimen and by measured net growth rates of Hells Bells from within and above the present-day redoxcline (section 4.3.1.1, p. 65, Schorndorf et al., 2019; and Stinnesbeck et al., 2017b).

The models are consistent with the observation of an increased Hells Bells growth and thus higher net growth rates in certain water depths within the 10 m thick zone of Hells Bells appearance (Fig. 46). This is indicated by the seize distribution of Hells Bells with water depth. In addition, measured net growth rates of Hells Bells above the present-day redoxcline are with 12–100 μm a^{-1} higher (Schorndorf et al., 2019; Stinnesbeck et al., 2017b) compared to lower net growth rate of Hells Bells from within the present-day redoxcline of 4–10 μm a^{-1} (section 4.3.1.1, p. 65). The observed alternations of petrographic phases 2 and 3 in the Hells Bells specimen "Long Bell" reflect phases of rather steady higher net growth indicated by massive spherulitic calcite (phase 2) and phases of rather unsteady lower net growth indicated by lamination due to frequent dissolution (phase 3) (section 4.2.3, p. 62). These alternating phases could result from the combination of a longer-term halocline elevation with short-term halocline elevations as simulated in Models 1 and 2, respectively. Furthermore, the results of Schorndorf et al. (in prep.) indicate that the lowermost parts of Hells Bells of different water depths reveal similar "young" ages and thus, short-term halocline elevation changes, as simulated in Model 2, are likely to be important Hells Bells formation.

Eventually, the model calculations in Table 10 show that Hells Bells formation inherently depends on a variation of the halocline elevation. Since all of the assumed mechanism for a halocline elevation reflected in Model 1 and 2 in Table 10 are relevant occurring processes, it is highly likely that Hells Bells growth represents a combination of long- and short-term variations of the halocline elevation as illustrated in Figure 46. However, in order to further evaluate these processes, more research is required, e.g. age-dating of Hells Bells specimens along their growth axis of different water depths and a longer period of logging the aquifer dynamics.

5.4.2 Shape of Hells Bells

The hypotheses of a dynamic halocline elevation and biogeochemically induced authigenic calcite precipitation in the redoxcline can be integrated to explain some of the morphological features of the Hells Bells. They grow downward and are conically divergent, with a strict horizontally

lower margin and a hollow interior (Fig. 1c, p. 5). Specimens also tend to be oriented towards the cenote center (Fig. 1a, p. 5 and Stinnesbeck et al., 2017b). The strictly horizontal downward growth is indicative for a precipitation from a defined layer within the water column (i.e. the redoxcline). In addition, an abrupt elevation of the redoxcline as a response to recharge events and a subsequent decelerated drop towards its original position serves to explain the downward growth of Hells Bells. This is indicated by the tendency towards downward orientation of the calcite crystal growth axis (Fig. 2e, p. 7). The fact that Hells Bells specimens growing on the inclined cave wall are always oriented towards the cenote center could result from a lateral gradient in the chemolithoautotrophic intensity. The energy and carbon sources used by the chemolithotrophic microbial community in the redoxcline are the released reduced carbon, sulfur and nitrogen species from anaerobic organic matter decay in the organic-rich sediments on the debris mound. Both, the morphology of the cenote and the diffusive mass transport, likely result in radial concentration gradients of upwards diffusing reduced species from sediment of the debris mound. These conditions limit the availability of reduced species in locations of the redoxcline distal to the debris mound, and vice versa. Consequently, the intensity of chemolithoautotrophy and hence calcite oversaturation is preferentially higher in the center proximal to the debris mound and decreases towards the cenote walls. This accounts for both the inclined bells as well as for horse-shoe like horizontal openings of Hells Bells, which always face towards the wall (Stinnesbeck et al., 2017b). Furthermore, the often observed hollow interior of Hells Bells could be due to preferential growth of the outer edges of Hells Bells, especially the parts facing towards the cenote center. Once such parts of Hells Bells grew slightly more, hence into deeper water depth, this will result in a higher net growth as these parts are likely to be reached more frequently by the narrow zone of calcite precipitation (redoxcline). Such a behavior may be observed in the "Long Bell" specimen, which is just opening or diverging in the lower part of the specimen (Fig. 11a4 and b2, p. 24). The conical shape and downward divergence of Hells Bells could be a simple continuation from the microscopic to the macroscopic level as the angles of the botryoidal and

spherulitc calcite phases observed in thin sections (Fig. 30c, e and f, p. 63) strongly resemble those of the large specimens of Hells Bells (Fig. 1, p. 5 and Fig. 2d, p. 7).

The potential influence of microorganisms forming a biofilm community on the surface of Hells Bells can also not be excluded. Stinnesbeck et al. (2017b) and the more recently measured data by Leberecht et al. (in prep.) showed that this community does not resemble the planktonically growing microbial biocenosis but forms a distinct community that seems to thrive catalyzing the reduction and oxidation of different nitrogen species. However, it is not known to date if, and to what extend the activity of these organisms contributes to the shape of the speleothems.

5.4.3 Distribution of cenotes with Hells Bells on the Yucatán Peninsula

Although cenotes revealing unique subaqueous speleothems Hells Bells are so far restricted to a limited area in the North-Eastern part of the YP, it is likely that this phenomenon appears elsewhere on the YP (section 5.2.4, p. 115). Taking the results and discussions presented in this study into account, the following apparent prerequisites for Hells Bells formation in cenotes of the YP appear likely:

- The cenote or sinkhole must be deep enough to reach the halocline in order to exhibit a density stratified water column (meromixis).
- A certain minimal distance to the coast is required for the cenote in order to develop a halocline deep enough to allow for prevalence of a non-phototrophic and rather chemeolithoautrohic microbial community.
- Sufficient input of organic material to the cenote bottom is required to create and maintain anoxia in the halocline with a release of reduced sulfur, carbon and nitrogen species.
- A meromictic stagnant water body indicated by a thick halocline is needed that allows for the formation of a redoxcline in which anaerobic chemolithoautotrophy prevails, as well as for accumulation of reduced chemical species in the halocline. Both combined lead to a narrow zone of calcite oversaturation in the water body.

- Special hydraulic conditions are needed, which allow the halocline to rise and fall in order to fixate and preserve the authigenic calcite formed in the redoxcline and ultimately form subaqueous speleothems.

Regarding these apparent prerequisites for Hells Bells formation, the local and regional karst hydrogeology seems to be the major determining factor as it controls the aquifer dynamics in response to recharge events and the degree of advection in the water body of stratified cenotes, which determines the redoxcline biogeochemistry and hence subaqueous calcite precipitation (section 5.2, p. 94). The North-Eastern part of the YP is characterized by the Holbox fracture zone consisting of North-East trending faults (Fig. 47). These faults reflect areas of increased permeability indicated by accumulation of cenotes along these zones (Bauer-Gottwein et al., 2011). The deep stratified cenotes investigated in this study are all located in some distance (15–30 km) west of such a fault lineament, which is in accordance to the derived prerequisites for Hells Bells formation. This leads to the conclusion that cenotes with Hells Bells might also occur in areas north and south of the so far known cenotes with Hells Bells (Fig. 47). This area is marked as potential Hells Bells zone in Figure 47. The cenotes Big Calica and Calica Pit, which were identified as possible deep stratified cenotes with Hells Bells fall within the lower end of this zone (Table 9, p.118 and section 5.2.4, p.115). Furthermore, another potential Hells Bells zone might occur west of Tulum and cenote Angelita in an area that reveals features similar to the area of cenotes with Hells Bells west of Puerto Morelos, which are a North-East trending fault and a certain distance to both, the fault and the coast (Fig. 47). The distance to the coast might be limiting the potential zone of Hells Bells towards the inland, as the depth of the halocline increases with increasing distance to the coast.

This would in turn reduce the probability of the occurrence of cenotes with a continuous stratified water body, because the required depth of such cenotes would increase as well. This behavior is indicated by the reported deep stratified cenotes along the Riviera Maya (Fig. 47) that are devoid of Hells Bells as listed in Table 9 (p.117).

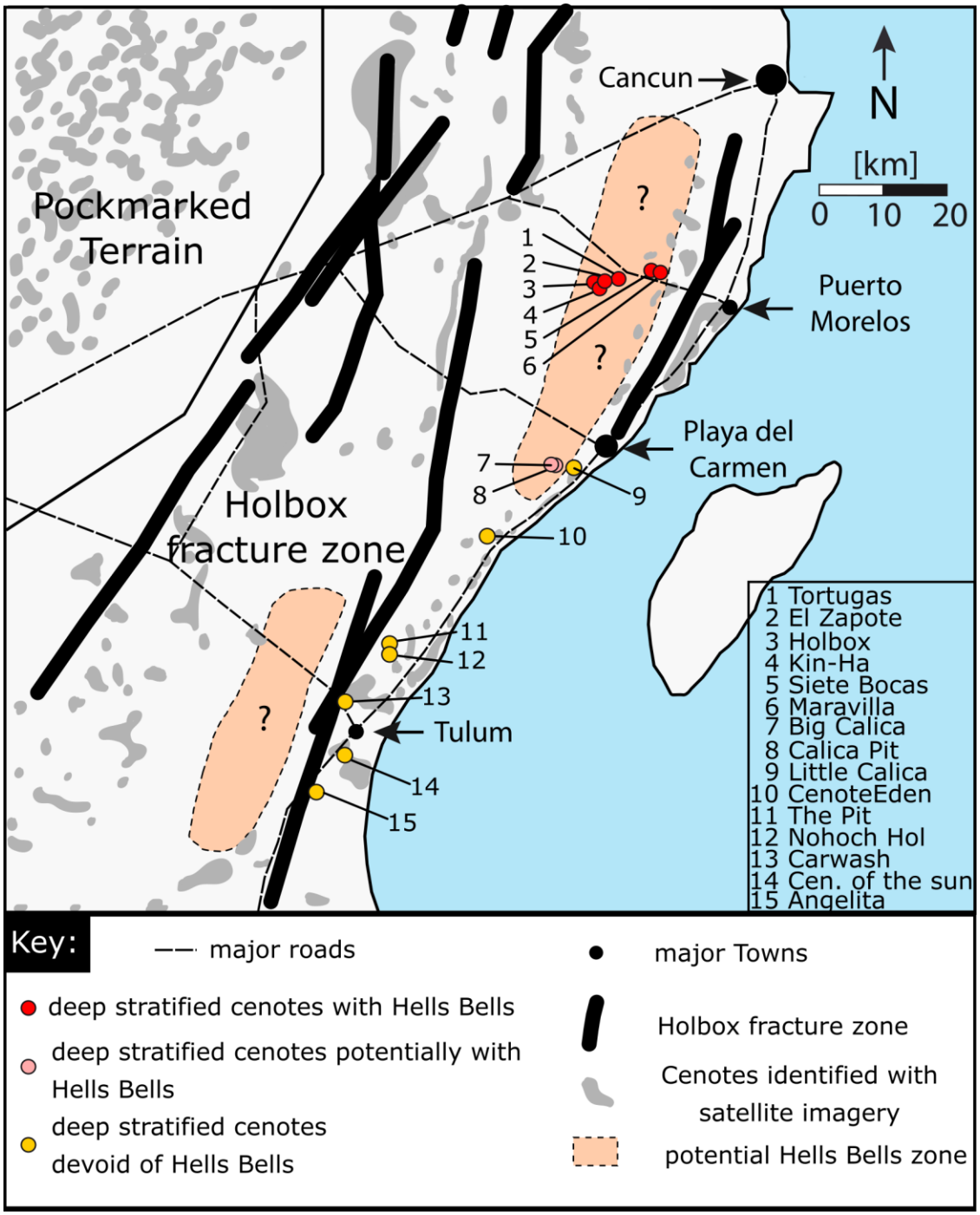

Fig. 47: Map of the North-Eastern YP with indicated areas of potential occurrence of deep stratified cenotes containing Hells Bells. The positions of the same deep stratified cenotes with and devoid of Hells Bells, as well as those with the potential of Hells Bells as listed in Table 9 (p.117) are delineated. Major tectonic structures and the distribution of cenotes identified via satellite images and the studied cenotes with and without Hells Bells presented in this study are denoted. (taken and modified from Klose , 2018, unpub.), cenote locations and fracture structures derived from preferential flow paths were taken from Bauer-Gottwein et al. (2011).

The deep stratified cenotes with Hells Bells are difficult to detect as they reveal very small water surfaces covered by vegetation that are not detectable with satellite imagery (e.g. cenotes El

Zapote, Maravilla, 7 Bocas) or even reveal no open water surface with only minor openings (locally also termed as “bocas”) to the surface often accommodating bat populations living under the cenote roof (e.g. cenotes Kin Ha and Holbox). Cenote Tortugas is the only cenote with Hells Bells showing a larger water surface (Fig. 7d, p.15). The difficulty to identify deep stratified cenotes together with the fact that large parts of the potential Hells Bells zones proposed in Figure 47 are not accessible via roads are likely to be the reasons for the so far small number of known cenotes with Hells Bells. This fact gets more explicit considering that the people exploring these cenotes, namely bold cave divers that need to carry a lot of equipment for their exploration, depend on at least rudimentary infrastructure.

In addition to the potential Hells Bells zones in the North-Eastern YP area illustrated in Figure 47, the so called pock-marked terrain in the North-Western YP associated to the “ring of cenotes” (Bauer-Gottwein et al., 2011) could also bear deep-stratified cenotes hosting subaqueous speleothems indicated by published data of cenote Xcolac, a stagnant deep stratified cenote located in the Tunkás municipality in the state of Yucatán (section 5.2.4, p. 115).

Lastly, discoverers of unknown deep stratified cenotes have to be able to recognize unique subaqueous speleothem structures and subsequently communicate their discovery to the diving and scientific communities.

5.5 Hells Bells – a novel geoarchive?

Along with the first publication on Hells Bells by Stinnesbeck et al. (2017b) and prior to a more comprehensive understanding of their formation developed in this thesis and presented in Ritter et al. (2019), Hells Bells speleothems were initially considered as potential geoarchives for the Yucatán Peninsula (YP). To date, speleothems most notably stalagmites are important archives for paleo environmental conditions in the area (e.g. Akers et al., 2016; Frappier et al., 2014; Medina-Elizalde et al., 2010; Moseley et al., 2013).

The use of Hells Bells as geoarchive is approached by Schorndorf et al. (in prep.) who mainly focus on detailed geochemical analyses and age-dating of several Hells Bells specimen. Age-dating of the lowermost parts of Hells Bells indicate that growth of Hells Bells is an ongoing process and the oldest measured dates of the root of "Big Bell" reach back to ~120 ka BP indicating that Hells Bells already grew during the last interglacial and outlasted the areal exposure during sea level low stands of the last glacial period (Schorndorf et al., 2019).

The Hells Bells specimen "Long Bell" or ZPT-7 in Stinnesbeck et al. (2017b) was investigated in detail with regard to its geochemistry and age-dating along the presumed growth axis by Schorndorf et al (in prep.), as well as with regard to its petrography by Tianxiao Sun (Sun, 2018, unpub.). The three distinct and distinguishable growth phases deviated from petrographic analyses are reflected in the geochemistry (sections 4.2.3, p. 62 and 4.3.1.2, p. 68). The specimen covers a period of ~12.5–1.4 ka BP, while the top 4–5 cm cover the period from ~12.5–8 ka and lowermost ~54 cm cover the period from ~8–1.4 ka BP showing rather continuous growth conditions with net growth rates of ~100 μm a^{-1} (Schorndorf et al., 2019). With regard to the potential of Hells Bells as a novel geoarchive for the YP, these results are very promising, and the following conclusions were drawn (Schorndorf et al., in prep.):

- Since Hells Bells grow underwater, Hells Bells growth records minimum relative sealevel elevations, assuming that the specimen "Long Bell" grew in range of water depth of 28–38 m suggested by the present-day zone of Hells Bells appearance.

- The build-up and the thickness of the freshwater layer of the Yucatán Karst Aquifer is recorded in Hells Bells calcites and can be reconstructed with the independent geochemical proxies Mg, Sr and Ba to Ca ratios and $d^{234}U_{initial}$ all reflecting variable seawater fractions within the freshwater body.
- Since a considerable amount of the carbon in Hells Bells calcites is derived from degradation of plantal material in the sediments on the debris mound (Ritter et al., 2019), thus, the observed shift of –5 ‰ of stable carbon isotopes of Hells Bells could indicate a climate and vegetational change from relatively cold and dry Late Pleistocene climate dominated by C4-plants towards a warmer more humid Early/Middle Holocene climate with increasing portions of C3-plants.

The findings of Schorndorf (2018, unpub.) correspond well with the results for the laminated Hells Bells specimens from different cenotes (section 4.3.1.1, p. 65). The small, ~6 cm long Hells Bells specimen TL4 from 35.8 m water depth and within the turbid layer of El Zapote seems to capture a similar time span as "Long Bell". The lamination indicates frequent phases of repeated dissolution, which is reflected in its low net growth rate of only 4–10 µm a^{-1} (Fig. 32, p. 66) compared to the 100 µm a^{-1} of "Long Bell" (Schorndorf et al., 2019). The limited geochemical results available for TL4 show the same trends observed in "Long Bell" regarding Mg, Sr and Ba to Ca ratios, $d^{234}U_{initial}$ and stable carbon and oxygen isotope values (Fig. 33, p.67 and Fig. 34, 69; Schorndorf, 2018, unpub.). This indicates that the environmental conditions in which Hells Bells grew are generally recorded in Hells Bells calcite.

Furthermore, the geochemical results of the laminated Hells Bells specimens of cenotes Maravilla and Tortugas also show similar trends regarding Sr and Ba to Ca ratios, $d^{234}U_{initial}$ and stable oxygen isotopes (Fig. 33, p. 67). Since these trends seem not restricted to a single cenote, these results support the suggested concept of Hells Bells recording variations of the Yucatán Karst Aquifer, especially with regard the thickness of the freshwater layer. However, the trends of S/Ca and stable carbon isotope values differ from each other (Fig. 33, p. 67). This indicates that these parameters

are rather cenote specific as their signal is most likely related to redox processes associated with the degradation of C_{org} ($\delta^{13}C$) and re-oxidation of reduced species (S/Ca).

The trends of increasing and decreasing growth rates in relation to water depth of the respective specimen indicated by the results of the laminated Hells Bells specimen (Fig. 32, p. 66) hint towards an interesting approach of deriving the development of the Yucatán Karst Aquifer. Hells Bells located at positions with less distance to the halocline, i.e. the redoxcline or zone of calcite precipitation, would reveal lower net growth rates compared to Hells Bells located at positions with more distance to the halocline. This is due to more frequent exposure to dissolution closer to the halocline as a result of episodic dynamic halocline elevation (section 5.4.1, p. 126). Thus, variations of the mean halocline elevation and its past development could be derived from growth rates analyses of Hells Bells specimen from different water depths.

In conclusion, the findings are encouraging and demand for further geochemical and age-dating investigations of Hells Bells specimens of known water depths in order to derive more precise estimations on minimum sea levels and the development of the Yucatán Karst Aquifer from Hells Bells calcites. Eventually, considering the potential of Hells Bells formation in cenotes all over the YP, as elucidated before, Hells Bells might complement to the present suite of geoarchives towards a better understanding of past environmental conditions in the region.

6. Conclusions

A biogeochemical mechanism for the subaqueous precipitation of calcite is elaborated in this study with regard to the underwater growth of Hells Bells. Calcite is most likely precipitated within the narrow 1–2 m thick redoxcline immediately above the halocline, indicated by increasing pH values and $SI_{calcite}$, as well as calcite particles found in the filtrate of this water layer. Chemolithoautotrophy and insufficient oxidation of sulfide to zero-valent sulfur via proton-consuming nitrate-driven microbial sulfide oxidation were identified as dominant processes within the redoxcline derived from hydrogeochemical profiles. This is supported by microbiological analyses by Leberecht et. al (in prep.). Both processes favor authigenic calcite precipitation within the redoxcline by increasing the pH of the surrounding water.

Investigations of other cenotes with and without Hells Bells allowed for deriving the controlling factors in subaqueous calcite precipitation in pelagic redoxclines deep stratified cenotes on the Yucatán Peninsula. Stagnancy is the most important factor for the formation of an "oxidant deficient" redoxcline in which biogeochemical conditions develop that are suitable for subaqueous calcite precipitation. Reviewing reported deep stratified cenotes from the YP in literature suggests the probability to also encounter the phenomenon of subaqueous calcite precipitation in pelagic redoxclines, thus Hells Bells formation, elsewhere on the Yucatán Peninsula. Since stagnancy in the water bodies of cenotes is closely related to hydrogeology, i.e. aquifer properties such as permeability, zones of possible occurrences of cenotes with Hells Bells could be derived on the basis of regional hydro- and structural geology.

In order to preserve the calcite formed in the narrow water layer of the redoxcline, a dynamic elevation of the halocline and thus the zone of calcite precipitation is postulated. Such halocline elevations may account for the observed Hells Bells growth over a vertical range of 10 m water depth. Preliminary results of aquifer monitoring at cenotes with Hells Bells support a dynamic halocline elevation driven by periodic annually sea level changes and gradual variations of the freshwater layer thickness related to variations of precipitation. Minor halocline elevations of <10

cm were observed at cenote El Zapote in response to several precipitation events demonstrating the general principle of a recharge-driven halocline elevation. Major precipitation events such as tropical storms and hurricanes, which could have greater impact on the aquifer dynamics, were not observed within the measurement period.

The characteristic morphology of Hells Bells is attributed to be the result of the interplay of calcite precipitation within the redoxcline driven by biogeochemical processes and a dynamic halocline elevation. However, since the morphology and structure of Hells Bells was not the focus of this study, more research effort is required focusing on the variability of Hells Bells morphologies and especially on small scale internal structures indicating direction and continuity of calcite growth with regard to the use of Hells Bells as a geoarchive.

Age-dating of several Hells Bells specimen from different cenotes and water depths indicate that Hells Bells growth is an ongoing process covering the whole period of the present interglacial from ~0.1–12.5 ka BP (Schorndorf et al., 2019). Surprisingly, Hells Bells already grew in previous interglacial phases ~90–120 ka BP outlasting aerial exposure during glacial sea level low stands. Eventually, Hells Bells bear great potential as a complementary geoarchive for reconstructing minimum sea levels, the development of the Yucatán Karst Aquifer and vegetation changes on the Yucatán Peninsula.

7. Bibliography

7.1 Published journal articles

Akers, P. D., Brook, G. A., Railsback, L. B., Liang, F., Iannone, G., Webster, J. W., Reeder, P. P., Cheng, H. and Edwards, R. L.: An extended and higher-resolution record of climate and land use from stalagmite MC01 from Macal Chasm, Belize, revealing connections between major dry events, overall climate variability, and Maya sociopolitical changes, Palaeogeogr. Palaeoclimatol. Palaeoecol., 459, 268–288, doi:10.1016/j.palaeo.2016.07.007, 2016.

Alfreider, A., Baumer, A., Bogensperger, T., Posch, T., Salcher, M. M. and Summerer, M.: CO2 assimilation strategies in stratified lakes: Diversity and distribution patterns of chemolithoautotrophs, Environ. Microbiol., 19(7), 2754–2768, doi:10.1111/1462-2920.13786, 2017.

Back, W., Hanshaw, B. B., Herman, J. S. and Van Driel, J. N.: Differential dissolution of a Pleistocene reef in the ground-water mixing zone of coastal Yucatan, Mexico, Geology, 14(February 1986), 137–140, 1986.

Bailey, J. V, Orphan, V. J., Joye, S. B. and Corsetti, F. A.: Chemotrophic Microbial Mats and Their Potential for Preservation in the Rock Record, Astrobiology, 9(9), 843–859, 2009.

Barton, H. A. and Northup, D. E.: Geomicrobiology in Cave Environments: Past, current and future Perspectives, J. Cave Karst Stud., 69(1), 163–178, 2007.

Bauer-Gottwein, P., Gondwe, B. R. N., Charvet, G., Marín, L. E., Rebolledo-Vieyra, M. and Merediz-Alonso, G.: Review: The Yucatán Peninsula karst aquifer, Mexico, Hydrogeol. J., (130), 507–524, doi:10.1007/s10040-010-0699-5, 2011.

Beddows, P. A., Smart, P. L., Whitaker, F. F. and Smith, S. L.: Density stratified groundwater circulation on the Caribbean Coast of Yucatan peninsula, Mexico, in Karst Waters Institute Special Publication 7: Hydrogeology and Biology of Post-Paleozoic Carbonate Aquifers, edited by J. B. Martin, C. M. Wicks, and I. D. Sasowsky, pp. 129–134, 2002.

Beddows, P. A., Smart, P. L., Whitaker, F. F. and Smith, S. L.: Decoupled fresh-saline groundwater circulation of a coastal carbonate aquifer: Spatial patterns of temperature and specific electrical conductivity, J. Hydrol., 346(1–2), 18–32, doi:10.1016/j.jhydrol.2007.08.013, 2007.

Berg, C., Vandieken, V., Thamdrup, B. and Ju, K.: Significance of archaeal nitrification in hypoxic waters of the Baltic Sea, ISME J., 9, 1319–1332, doi:10.1038/ismej.2014.218, 2015.

Bontognali, T. R. R., Angeli, I. M. D., Tisato, N., Vasconcelos, C., Bernasconi, S. M., Gonzales, E. R. G. and De Waele, J.: Mushroom Speleothems: Stromatolites That Formed in the Absence of Phototrophs, Fontiers Earth Sci., 4(Article 4), 1–8, doi:10.3389/feart.2016.00049, 2016.

Bosak, T. and Newman, D. K.: Microbial Kinetic Controls on Calcite Morphology in Supersaturated Solutions, J. Sediment. Res., 75(2), 190–199, doi:10.2110/jsr.2005.015, 2005.

Brankovits, D., Pohlman, J. W., Niemann, H., Leigh, M. B., Leewis, M. C., Becker, K. W., Iliffe, T. M., Alvarez, F., Lehmann, M. F. and Phillips, B.: Methane-and dissolved organic carbon-fueled microbial loop supports a tropical subterranean estuary ecosystem, Nat. Commun., 8(1), doi:10.1038/s41467-017-01776-x, 2017.

Caldwell, S. L., Laidler, J. R., Brewer, E. A., Eberly, J. O., Sandborgh, S. C. and Colwell, F. S.: Anaerobic oxidation of methane: Mechanisms, bioenergetics, and the ecology of associated microorganisms, Environ. Sci. Technol., 42(18), 6791–6799, doi:10.1021/es800120b, 2008.

Carrillo-Bastos, A., Islebe, G. A., Torrescano-Valle, N. and González, N. E.: Holocene vegetation and climate history of central Quintana Roo, Yucatán Península, Mexico, Rev. Palaeobot. Palynol., 160(3–4), 189–196, doi:10.1016/J.REVPALBO.2010.02.013, 2010.

Castanier, S., Métayer-Levrel, G. and Perthuisot, J.-P.: Ca-carbonates precipitation and limestone genesis – the microbiogeologist point of view, Sediment. Geol., 126, 9–23, 1999.

Chen, K. Y. and Gupta, S. K.: Formation of Polysulfides in aqueous solution, Environ. Lett., 4(3), 187–200, 1973.

Collins, S. V., Reinhardt, E. G., Rissolo, D., Chatters, J. C., Nava Blank, A. and Luna Erreguerena, P.: Reconstructing water level in Hoyo Negro, Quintana Roo, Mexico, implications for early Paleoamerican and faunal access, Quat. Sci. Rev., 124, 68–83, doi:10.1016/J.QUASCIREV.2015.06.024, 2015.

Coutino, A., Stastna, M., Kovacs, S. and Reinhardt, E.: Hurricanes Ingrid and Manuel (2013) and their impact on the salinity of the Meteoric Water Mass, Quintana Roo, Mexico, J. Hydrol., doi:10.1016/j.jhydrol.2017.04.022, 2017.

Curtis, J. H., Hodell, D. A. and Brenner, M.: Climate Variability on the Yucatan Peninsula (Mexico) during the Past 3500 Years, and Implications for Maya Cultural Evolution, Quat. Res., 46(1), 37–47, doi:10.1006/qres.1996.0042, 1996.

Dellwig, O., Leipe, T., März, C., Glockzin, M., Pollehne, F., Schnetger, B., Yakushev, E. V., Böttcher, M. E. and Brumsack, H. J.: A new particulate Mn-Fe-P-shuttle at the redoxcline of anoxic basins, Geochim. Cosmochim. Acta, doi:10.1016/j.gca.2010.09.017, 2010.

Dupraz, C., Reid, R. P., Braissant, O., Decho, A. W., Norman, R. S. and Visscher, P. T.: Processes of carbonate precipitation in modern microbial mats, Earth-Science Rev., 96(3), 141–162, doi:10.1016/j.earscirev.2008.10.005, 2009.

Escolero, O., Marin, L. E., Domínguez-Mariani, E. and Torres-Onofre, S.: Dynamic of the freshwater – saltwater interface in a karstic aquifer under extraordinary recharge action: the Merida Yucatan case study, Environ. Geol., 51, 719–723, doi:10.1007/s00254-006-0383-1, 2007.

Ettwig, K. F., Butler, M. K., Le Paslier, D., Pelletier, E., Mangenot, S., Kuypers, M. M. M., Schreiber, F., Dutilh, B. E., Zedelius, J., De Beer, D., Gloerich, J., Wessels, H. J. C. T., Van Alen, T., Luesken, F., Wu, M. L., Van De Pas-Schoonen, K. T., Op Den Camp, H. J. M., Janssen-Megens, E. M., Francoijs, K. J., Stunnenberg, H., Weissenbach, J., Jetten, M. S. M. and Strous, M.: Nitrite-driven anaerobic methane oxidation by oxygenic bacteria, Nature, 464(7288), 543–548, doi:10.1038/nature08883, 2010.

Evans, N. P., Bauska, T. K., Gázquez-sánchez, F., Brenner, M., Curtis, J. H. and Hodell, D. A.: Quantification of drought during the collapse of the classic Maya civilization, Science, 361(August), 498–501, 2018.

Farfán, L. M., D´Sa, E. J., Liu, K. and Rivera-Monroy, V.: Tropical Cyclone Impacts on Coastal Regions: the Case of the Yucatán and the Baja California Peninsulas, Mexico, Estuaries and Coasts, 37(February 2015), 1388–1402, doi:10.1007/s12237-014-9797-2, 2014.

Findlay, A. J.: Microbial impact on polysulfide dynamics in the environment, FEMS Microbiol. Lett., 363, 1–12, doi:10.1093/femsle/fnw103, 2016.

Frappier, A. B., Pyburn, J., Pinkey-Drobnis, A. D., Wang, X., Corbett, D. R. and Dahlin, B. H.: Two millennia of tropical cyclone-induced mud layers in a northern Yucatán stalagmite: Multiple overlapping climatic hazards during the Maya Terminal Classic "megadroughts," Geophys. Res. Lett., 41(14), 5148–5157, doi:10.1002/2014GL059882, 2014.

Glaubitz, S., Lueders, T., Abraham, W., Jost, G., Jürgens, K. and Labrenz, M.: 13C-isotope analyses reveal that chemolithoautotrophic Gamma - and Epsilonproteobacteria feed a microbial food web in a pelagic redoxcline of the central Baltic Sea, Environ. M, 11(2), 326–337, doi:10.1111/j.1462-2920.2008.01770.x, 2009.

Gondwe, B. R. N., Lerer, S., Stisen, S., Marín, L., Rebolledo-Vieyra, M., Merediz-Alonso, G. and Bauer-Gottwein, P.: Hydrogeology of the south-eastern Yucatan Peninsula: New insights from water level measurements, geochemistry, geophysics and remote sensing, J. Hydrol., 389(1–2), 1–17, doi:10.1016/j.jhydrol.2010.04.044, 2010.

Gradzinski, M., Chmiel, M. J. and Motyka, J.: Formation of calcite by chemolithoautotrophic bacteria - a new hypothesis on microcrystalline cave pisoids, Ann. Soc. Geol. Pol., 82, 361–369, 2012.

Grant, K. M., Rohling, E. J., Bar-Matthews, M., Ayalon, A., Medina-Elizalde, M., Ramsey, C. B., Satow, C. and Roberts, A. P.: Rapid coupling between ice volume and polar temperature over the past 150,000 years, Nature, 491(7426), 744–747, doi:10.1038/nature11593, 2012.

Grote, J., Labrenz, M., Herndl, G. J. and Ju, K.: Epsilonproteobacteria Represent the Major Portion of Chemoautotrophic Bacteria in Sulfidic Waters of Pelagic Redoxclines of the Baltic and Black Seas, Appl. Environ. Microbiol., 74(24), 7546–7551, doi:10.1128/AEM.01186-08, 2008.

Guido, A., Heindel, K., Birgel, D., Rosso, A., Mastandrea, A., San, R., Russo, F. and Peckmann, J.: Pendant bioconstructions cemented by microbial carbonate in submerged marine caves (Holocene, SE Sicily), Palaeogeogr. Palaeoclimatol. Palaeoecol., 388, 166–180, doi:10.1016/j.palaeo.2013.08.007, 2013.

Gulley, J. D., Martin, J. B. and Brown, A.: Organic carbon inputs, common ions and degassing: rethinking mixing dissolution in coastal eogenetic carbonate aquifers, Earth Surf. Process. Landforms, 41, 2098–2110, doi:10.1002/esp.3975, 2016.

Gun, J., Goifman, A., Shkrob, I., Kamyshny, A., Ginzburg, B., Hadas, O., Dor, I., Modestov, A. D. and Lev, O.: Formation of polysulfides in an oxygen rich freshwater lake and their role in the production of volatile sulfur compounds in aquatic systems, Environ. Sci. Technol., 34(22), 4741–4746, doi:10.1021/es991389x, 2000.

Harmon, R. S., Schwarcz, H. P. and Ford, D. C.: Late Pleistocene sea level history of Bermuda, Quat. Res., 9(2), 205–218, doi:10.1016/0033-5894(78)90068-6, 1978.

Haroon, M. F., Hu, S., Shi, Y., Imelfort, M., Keller, J., Hugenholtz, P., Yuan, Z. and Tyson, G. W.: Anaerobic oxidation of methane coupled to nitrate reduction in a novel archaeal lineage, Nature, 500(7464), 567–570, doi:10.1038/nature12375, 2013.

Hartmann, J. F.: Methane dynamics in Lakes, PhD Thesis, Heidelberg University, Germany, pp. 211, doi.org/10.11588/heidok.00026307, 2018.

Hengstum, P. J. Van, Reinhardt, E. G., Beddows, P. A. and Gabriel, J. J.: Linkages between Holocene paleoclimate and paleohydrogeology preserved in a Yucatan underwater cave, Quat. Sci. Rev., 29(19–20), 2788–2798, doi:10.1016/j.quascirev.2010.06.034, 2010.

Hildebrand, A. R., Pilkington, M., Connors, M., Ortiz-Aleman, C. and Chavez, R. E.: Size and structure of the Chicxulub crater revealed by horizontal gravity gradients and cenotes, Nature, 376(6539), 415–417, doi:10.1038/376415a0, 1995.

Himmler, T., Smrzka, D., Zwicker, J., Kasten, S., Shapiro, R. S. and Bohrmann, G.: Stromatolites below the photic zone in the northern Arabian Sea formed by calcifying chemotrophic microbial mats, Geology, (4), 2–5, 2018.

Hodell, D. A., Curtis, J. H. and Brenner, M.: Possible role of climate in the collapse of Classic Maya civilization, Nature, 375(6530), 391–394, doi:10.1038/375391a0, 1995.

Hodell, D. A., Brenner, M., Curtis, J. H. and Guilderson, T.: Solar Forcing of Drought Frequency in the Maya Lowlands, Science, 292(5520), 1367–1371, 2001.

Holmes, A. J., Tujula, N. A., Holley, M., Contos, A., James, J. M., Rogers, P. and Gillings, M. R.: Phylogenetic structure of unusual aquatic microbial formations in Nullarbor caves, Australia, Environ. Microbiol., 3(4), 256–264, 2001.

Huang, Y. and Fairchild, I. J.: Partitioning of Sr2+ and Mg2+ into calcite under karst-analogue experimental conditions, Geochim. Cosmochim. Acta, 65(1), 47–62, doi:10.1016/S0016-7037(00)00513-5, 2001.

Islebe, G. A., Hooghiemstra, H., Brenner, M., Curtis, J. H. and Hodell, D. A.: A Holocene vegetation history from lowland Guatemala, The Holocene, 6(3), 265–271, doi:10.1177/095968369600600302, 1996.

Jones, D. S., Lyon, E. H. and Macalady, J. L.: Geomicrobilogy of biovermiculations from the Frasassi cave system, Italy, J. Cave Karst Stud., 70(2), 78–93, 2008.

Jones, D. S., Albrecht, H. L., Dawson, K. S., Schaperdoth, I., Freeman, K. H., Pi, Y., Pearson, A. and Macalady, J. L.: Community genomic analysis of an extremely acidophilic sulfur-oxidizing biofilm, ISME J., 6, 158–170, doi:10.1038/ismej.2011.75, 2012.

Jørgensen, B. B., Fossing, H., Wirsent, C. and Jannasch, H.: Sulfide oxidation in the anoxic Black Sea chemocline, Deep Sea Res., 38, 1083–1103, doi:10.1016/S0198-0149(10)80025-1, 1991.

Kamyshny, A., Ekeltchik, I., Gun, J. and Lev, O.: Method for the determination of inorganic polysulfide distribution in aquatic systems, Anal. Chem., 78(8), 2631–2639, doi:10.1021/ac051854a, 2006.

Jost, G., Zubkov, M. V., Yakushev, E., Labrenz, M. and Jürgens, K.: High abundance and dark CO2 fixation of chemolithoautotrophic prokaryotes in anoxic waters of the Baltic Sea, Limnol. Oceanogr., 53(1), 14–22, 2008.

Jost, G., Martens-habbena, W., Pollehne, F., Schnetger, B. and Labrenz, M.: Anaerobic sulfur oxidation in the absence of nitrate dominates microbial chemoautotrophy beneath the pelagic chemocline of the eastern Gotland Basin, Baltic Sea, FEMS Microbiol. Ecol., 71, 226–236, doi:10.1111/j.1574-6941.2009.00798.x, 2010.

Kamp, A., Stief, P., Schulz-vogt, H. N. and Icrobiol, A. P. P. L. E. N. M.: Anaerobic Sulfide Oxidation with Nitrate by a Freshwater Beggiatoa Enrichment Culture, Appl. Env. Microbiol., 72(7), 4755–4760, doi:10.1128/AEM.00163-06, 2006.

Kamyshny, A., Zilberbrand, M., Ekeltchik, I., Voitsekovski, T., Gun, J. and Lev, O.: Speciation of polysulfides and zerovalent sulfur in sulfide-rich water wells in Southern and Central Israel, Aquat. Geochemistry, 14(2), 171–192, doi:10.1007/s10498-008-9031-6, 2008.

Kennett, D. J., Breitenbach, S. F. M., Aquino, V. V., Asmerom, Y., Awe, J., Baldini, J. U. L., Bartlein, P., Culleton, B. J., Ebert, C., Jazwa, C., Macri, M. J., Marwan, N., Polyak, V., Prufer, K. M., Ridley, H. E., Sodemann, H., Winterhalder, B. and Haug, G. H.: Development and Disintegration of Maya Political Systems in Response to Climate Change, Science, 338(6108), 788–791, doi:10.1126/science.1226299, 2012.

Keppler, F., Laukenmann, S., Rinne, J., Heuwinkel, H., Greule, M., Whiticar, M. and Lelieveld, J.: Measurements of 13C/12C Methane from Anaerobic Digesters: Comparison of Optical Spectrometry with Continuous-Flow Isotope Ratio Mass Spectrometry, Environ. Sci. Technol., 44, 5067–5073, 2010.

Khan, K. S. and Joergensen, R. G.: Stoichiometry of the soil microbial biomass in response to amendments with varying C/N/P/S ratios, Biol. Fertil. Soils, 265–274, doi:10.1007/s00374-019-01346-x, 2019.

Kirkby, C. A., Kirkegaard, J. A., Richardson, A. E., Wade, L. J., Blanchard, C. and Batten, G.: Stable soil organic matter: A comparison of C:N:P:S ratios in Australian and other world soils, Geoderma, doi:10.1016/j.geoderma.2011.04.010, 2011.

Klatt, J. M. and Polerecky, L.: Assessment of the stoichiometry and efficiency of CO 2 fixation coupled to reduced sulfur oxidation, Front. Microbiol., 6(Article 484), 1–19, doi:10.3389/fmicb.2015.00484, 2015.

Kosamu, I. B. M. and Obst, M.: The influence of picocyanobacterial photosynthesis on calcite precipitation, Int. J. Environ. Sci. Technol., 6(4), 557–562, 2009.

Kovacs, S. E., Reinhardt, E. G., Chatters, J. C., Rissolo, D., Schwarcz, H. P., Collins, S. V, Kim, S., Blank, N. A. and Erreguerena, P. L.: Calcite raft geochemistry as a hydrological proxy for Holocene aquifer conditions in Hoyo Negro and Ich Balam (Sac Actun Cave System), Quintana Roo, Mexico, Quat. Sci. Rev., 175, 97–111, doi:10.1016/j.quascirev.2017.09.006, 2017a.

Kovacs, S. E., Reinhardt, E. G., Stastna, M., Coutino, A., Werner, C., Collins, S. V., Devos, F. and Le Maillot, C.: Hurricane Ingrid and Tropical Storm Hanna's effects on the salinity of the coastal aquifer, Quintana Roo, Mexico, J. Hydrol., 551, 703–714, doi:10.1016/j.jhydrol.2017.02.024, 2017b.

Laukenmann, S., Polag, D., Heuwinkel, H., Greule, M., Gronauer, A., Lelieveld, J. and Keppler, F.: Identification of methanogenic pathways in anaerobic digesters using stable carbon isotopes, Eng. Life Sci., 10(6), 509–514, 2010.

Lefticariu, M., Perry, E. C., Ward, W. C. and Lefticariu, L.: Post-Chicxulub depositional and diagenetic history of the northwestern Yucatan Peninsula, Mexico, Sediment. Geol., 183, 51–69, doi:10.1016/j.sedgeo.2005.09.008, 2006.

Li, X., Taylor, G. T., Astor, Y. and Scranton, M. I.: Relationship of sulfur speciation to hydrographic conditions and chemoautotrophic production in the Cariaco Basin, Mar. Chem., 112(1–2), 53–64, doi:10.1016/j.marchem.2008.06.002, 2008.

Macalady, J. L., Jones, D. S. and Lyon, E. H.: Extremely acidic, pendulous cave wall biofilms from the Frasassi cave system, Italy, Environ. Microbiol., 9(6), 1402–1414, doi:10.1111/j.1462-2920.2007.01256.x, 2007.

Macintyre, I. G.: Extensive submarine lithification in a cave in the Belize Barrier Reef Platform, J. Sediment. Petrol., 54(1), 221–235, 1984.

Medina-Elizalde, M., Burns, S. J., Lea, D. W., Asmerom, Y., von Gunten, L., Polyak, V., Vuille, M. and Karmalkar, A.: High resolution stalagmite climate record from the Yucatán Peninsula spanning the Maya terminal classic period, Earth Planet. Sci. Lett., 298(1–2), 255–262, doi:10.1016/j.epsl.2010.08.016, 2010.

Medina-Elizalde, M., Polanco-Martínez, J. M., Lases-Hernández, F., Bradley, R. and Burns, S.: Testing the "tropical storm" hypothesis of Yucatan Peninsula climate variability during the Maya Terminal Classic Period, Quat. Res., 86(2), 111–119, doi:10.1016/j.yqres.2016.05.006, 2016.

Melim, L. A., Shinglman, K. M., Boston, P. J., Northup, D. E., Spilde, M. N. and Queen, M. J.: Evidence for Microbial Involvement in Pool Finger Precipitation, Hidden Cave, New Mexico, Geomicrobiology Journal, 18(February 2014), 311–239, doi:10.1080/01490450152467813, 2001.

Milazzo, C. G., Caroli, S. and Sharma, V. K.: Tables of Standard Electrode Potentials, Wiley, Chichester, UK., 1978.

Mook, W. G.: Environmental isotopes in the hydrological cycle, edited by W. G. Mook, UNESCO/IAEA, IHP-V Technical Documents in Hydrology No. 39, Vol. 1, Paris., 2000.

Moore, Y. H., Stoessell, R. K. and Easley, D. H.: Fresh-Water/Sea-Water relationship within a Ground-Water flow system northeastern coast of the Yucatan, Ground Water, 30(3), 343–350, 1992.

Moran, J. J., Beal, E. J., Vrentas, J. M., Orphan, V. J., Freeman, K. H. and House, C. H.: Methyl sulfides as intermediates in the anaerobic oxidation of methane, Environ. Microbiol., 10(1), 162–173, doi:10.1111/j.1462-2920.2007.01441.x, 2008.

Moseley, G. E., Smart, P. L., Richards, D. A. and Hoffmann, D. L.: Speleothem constraints on marine isotope stage (MIS) 5 relative sea levels, Yucatan Peninsula, Mexico, J. Quat. Sci., 28(3), 293–300, doi:10.1002/jqs.2613, 2013.

Mylroie, J. E. and Carew, J. L.: The flank margin model for dissolution cave development in carbonate platforms, Earth Surf. Process. Landforms, 15, 413–424, 1990.

Noguerola, I., Picazo, A., Llir, M., Camacho, A. and Borrego, C. M.: Diversity of freshwater Epsilonproteobacteria and dark inorganic carbon fixation in the sulphidic redoxcline of a meromictic karstic lake, FEMS Microbiol. Ecol., 91(July), 1–15, doi:10.1093/femsec/fiv086, 2015.

Obert, J. C., Scholz, D., Lippold, J., Felis, T., Jochum, K. P. and Andreae, M. O.: Chemical separation and MC-ICPMS analysis of U, Th, Pa and Ra isotope ratios of carbonates, J. Anal. At. Spectrom., 33(8), 1372–1383, doi:10.1039/c7ja00431a, 2018.

Oduro, H., Kamyshny, A., Zerkle, A. L., Li, Y. and Farquhar, J.: Quadruple sulfur isotope constraints on the origin and cycling of volatile organic sulfur compounds in a stratified sulfidic lake, Geochim. Cosmochim. Acta, doi:10.1016/j.gca.2013.06.039, 2013.

Parkhurst, B. D. L. and Appelo, C. a J.: User's Guide to PHREEQC (version 2) – a Computer Program for Speciation, and Inverse Geochemical Calculations, Exch. Organ. Behav. Teach. J., D(Version 2), 326, doi: Rep.99-4259, 1999.

Paul, D., Skrzypek, G. and Forizs, I.: Normalization of measured stable isotopic compositions to isotope reference scales – a review, Rapid Commun. mass Spectrom., 21, 3006–3014, doi:10.1002/rcm.3185, 2007.

Pedersen, B.: Water Geochemistry and Geomicrobiology of Two Sulfidic Cenotes, Yucatan Peninsula, Mexico, PhD thesis, Northern Illinois University, pp. 149, 2007.

Perry, E., Marin, L., McClain, J. and Velazquez, G.: Ring of Cenotes (sinkholes), northwest Yucatan, Mexico: its hydrogeologic characteristics and possible association with the Chicxulub impact crater, Geology, 23(1), 17–20, doi:10.1130/0091-7613(1995)023<0017:ROCSNY>2.3.CO;2, 1995.

Perry, E., Velazquez-Oliman, G. and Marin, L.: The hydrogeochemistry of the karst aquifer system of the northern yucatan peninsula, Mexico, Int. Geol. Rev., 44(3), 191–221, doi:10.2747/0020-6814.44.3.191, 2002.

Perry, E., Paytan, A., Pedersen, B. and Velazquez-Oliman, G.: Groundwater geochemistry of the Yucatan Peninsula, Mexico: Constraints on stratigraphy and hydrogeology, J. Hydrol., 367(1–2), 27–40, doi:10.1016/j.jhydrol.2008.12.026, 2009.

Pohlman, J. W.: The biogeochemistry of anchialine caves: progress and possibilities, Hydrobiologia, 33–51, doi:10.1007/s10750-011-0624-5, 2011.

Queen, M. J. and Melim, L. A.: Biothems: biologically influenced speleothems in caves of the Guadalupe Mountains, New Mexico, USA, in Caves and Karst of Southeastern New Mexico, New Mexico Geological Society Guidebook, 57th Field Conference., edited by W. Raatz, L. Land, and P. J. Boston, pp. 167–174., 2006.

Rimstidt, J. D., Balog, A. and Webb, J.: Distribution of trace elements between carbonate minerals and aqueous solutions, Geochim. Cosmochim. Acta, 62(11), 1851–1863, doi:10.1016/s0016-7037(98)00125-2, 1998.

Ritter, S. M., Isenbeck-Schröter, M., Scholz, C., Keppler, F., Gescher, J., Klose, L., Schorndorf, N., Avilés Olguín, J., González-González, A. and Stinnesbeck, W.: Subaqueous speleothems (Hells Bells) formed by the interplay of pelagic redoxcline biogeochemistry and specific hydraulic conditions in the El Zapote sinkhole, Yucatán Peninsula, Mexico, Biogeosciences, 16(11), 2285–2305, doi:10.5194/bg-2018-520, 2019a.

Schmitter-Soto, J. J., Comín, F. A., Escibar-Briones, E., Herrera- Silveira, J., Alcocer, J., Suárez-Morales, E., Elías-Gutiérrez, M., Díaz-Arce, V., Marín, L. E. and Steinich, B.: Hydrogeochemical and biological characteristics of cenotes in the Yucatan Peninsula (SE Mexico), Hydrobiologia, 467, 215–228, 2002.

Schorndorf, N., Ritter, S. M., Frank, N., Klose, L. and Stinnesbeck, W.: Hells Bells – underwater speleothems: A novel paleohydrological archive for the Yucatán Peninsula, Mexico, in Goldschmidt Abstracts, p. 3015., 2019.

Schwarzenbach, G. and Fischer, A.: Die Acidität der Sulfane und die Zusammensetzung wässeriger Polysulfidlösungen, Helv. Chim. Acta, 43(5), 1365–1390, doi:10.1002/hlca.19600430521, 1960.

Seager, S., Schrenk, M. and Bains, W.: An Astrophysical View of Earth-Based Metabolic Biosignature Gases An Astrophysical View of Earth-Based Metabolic Biosignature Gases, Astrobiology, 12(September 2012), 61–82, doi:10.1089/ast.2010.0489, 2012.

Seymour, J. R., Humphreys, W. F. and Mitchell, J. G.: Stratification of the microbial community inhabiting an anchialine sinkhole, Aquat. Microb. Ecol., 50, 11–24, doi:10.3354/ame01153, 2007.

Smart, P. L., Beddows, P. A., Coke, J., Doerr, S., Smith, S. and Whitaker, F. F.: Perspectives on karst geomorphology, hydrology, and geochemistry – a tribute volume to Derek C Ford and William B White, edited by R. S. Harmon and C. M. Wicks, Geological Society of America, Boulder, CO., 2006.

Socki, R. A., Perry, E. C. and Romanek, C. S.: Stable isotope systematics of two cenotes from the northern Yucatan Peninsula, Mexico, Limnol. Oceanogr., 47(6), 1808–1818, doi:10.4319/lo.2002.47.6.1808, 2002.

Stinnesbeck, S. R., Frey, E., Avilés Olguín, J., Stinnesbeck, W., Zell, P., Mallison, H., González González, A., Núñez, E. A., Velázquez Morlet, A., Terrazas Mata, A., Benavente Sanvicente, M., Hering, F. and Rojas Sandoval, C.: Xibalbaonyx oviceps, a new megalonychid ground sloth (Folivora, Xenarthra) from the Late Pleistocene of the Yucatán Peninsula, Mexico, and its paleobiogeographic significance, PalZ, 91, 245–271, doi:10.1007/s12542-017-0349-5, 2017a.

Stinnesbeck, W., Frey, E., Zell, P., Avilés, J., Hering, F., Frank, N., Arps, J., Geenen, A., Gescher, J., Isenbeck-Schröter, M., Ritter, S., Stinnesbeck, S., Núñez, E. A., Dahne, V. F., González, A. G. and Deininger, M.: Hells Bells –

unique speleothems from the Yucatán Peninsula, Mexico, generated under highly specific subaquatic conditions, Palaeogeogr. Palaeoclimatol. Palaeoecol., 489, 209–229, doi:10.1016/j.palaeo.2017.10.012, 2017b.

Stoessell, R. K.: Dampening of Transverse Dispersion in the Halocline in Karst Limestone in the Northeastern Yucatan Peninsula, Groundwater, 33(3), 366–371, doi:10.1111/j.1745-6584.1995.tb00291.x, 1995.

Stoessell, R. K., Moore, Y. H. and Coke, J. G.: The Occurrence and Effect of Sulfate Reduction and Sulfide Oxidation on Coastal Limestone Dissolution in Yucatan Cenotes, Groundwater, 31(4), 566–575, 1993.

Stoessell, R. K., Coke, J. G. and Easley, D. H.: Localized Thermal Anomalies in Haloclines of Coastal Yucatan Sinkholes, Groundwater, 40(4), 416–424, 2002.

Tesoriero, A. and Pankow, J.: Solid solution partitioning of Sr 2+, Ba 2+, and Cd 2+ to calcite, Geochim. Cosmochim. Acta, 60(6), 1053–1063, 1996.

Torres-Talamente, O., Alcocer, J., Beddows, P. A., Escobar-Briones, E. G. and Lugo, A.: The key role of the chemolimnion in meromictic cenotes of the Yucatan Peninsula, Mexico, Hydrobiologia, 677(Anchialine Ecosystems), 107–127, doi:10.1007/s10750-011-0746-9, 2011.

Tredici, S. M., Buccolieri, A., Tanini, L., Manno, D., Alifano, P., Maurizio, S., Buccolieri, A., Tanini, L., Manno, D. and Alifano, P.: Calcite-forming Bacillus licheniformis Thriving on Underwater Speleothems of a Hydrothermal Cave Calcite-forming Bacillus licheniformis Thriving on Underwater Speleothems of a Hydrotermal cave, Geomicrobiol. J., 1–14, doi:10.1080/01490451.2018.1476626, 2018.

Tuccimei, P., Soligo, M., Ginés, J., Ginés, A., Fornós, J., Kramers, J. and Villa, I. M.: Constraining Holocene sea levels using U-Th ages of phreatic overgrowths on speleothems from coastal caves in Mallorca (Western Mediterranean), Earth Surf. Process. Landforms, 35(7), 782–790, doi:10.1002/esp.1955, 2010.

Vera, I., Mario-Tapia, I. and Enriquez, C.: Effects of drought and subtidal sea-level variability on salt intrusion in a coastal karst aquifer, Mar. Freshw. Res., 63(6), 485–493, doi:10.1071/MF11270, 2012.

Vesica, P. L., Tuccimei, P., Turi, B., Fornós, J. J., Ginés, A. and Ginés, J.: Late Pleistocene Paleoclimates and sea-level change in the Mediterranean as inferred from stable isotope and U-series studies of overgrowths on speleothems, Mallorca, Spain, Quat. Sci. Rev., 19(9), 865–879, doi:10.1016/S0277-3791(99)00026-8, 2000.

Villasuso, M. J. and Méndez Ramos, R.: A conceptual model of the Aquifer of the Yucatán Peninsula, in Population, Development, and Environment on the Yucatan Peninsula, edited by W. Lutz, L. Prieto, and W. Sanderson, pp. 120–139, Vienna., 2000.

Visscher, P. T. and Stolz, J. F.: Microbial mats as bioreactors: populations, processes, and products, Palaeogeogr. Palaeoclimatol. Palaeoecol., 219, 87–100, doi:10.1016/B978-0-444-52019-7.50009-7, 2005.

Weidie, A. E.: Geology of the Yucatán Plattform, in Geology and Hydrogeology of the Yucatán and Quartenary Geology of Northeastern Yucatán Peninsula, edited by W. C. Ward, A. E. Weidie, and W. Back, pp. 1–19, New Orleans Geological Society Publication., 1985.

Weiss, R. F.: Carbon Dioxide in Water and Seawater: The Solubility of a Non-Ideal Gas, Mar. Chem., 2, 203–215, 1974.

Whiticar, M. J.: Carbon and hydrogen isotope systematics of bacterial formation and oxidation of methane, Chem. Geol., 161, 191–314, 1999.

Wiesenburg, D. A. and Guinasso, N. L.: Equilibrium solubilities of methane, carbon monoxide, and hydrogen in water and sea water, J. Chem. Eng. Data, 24(4), 356–360, doi:10.1021/je60083a006, 1979.

Williams, P. W.: The role of the subcutaneous zone in karst hyrology, J. Hydrol., 61, 45–67, 1983.

7.2 Publications in preparation

Leberecht, K., Ritter, S. M., Isenbeck-Schröter, M., Klose, L., Stinnesbeck, W., Gescher, J.: Microbially promoted growth of subaqueous calcite formations called Hells Bells in an oxidant-deficient pelagic redoxcline, in preparation.

Schorndorf, N., Ritter, S. M., Frank, N., Warken, Sophie and Stinnesbeck, W.: U-series dating of subaqueous speleothems (Hells Bells) from the Yucatán Peninsula in Mexico and their usability as a paleohydrological archive, in preparation.

7.3 Videos and online Links

Beloshin, A.: Cenote Angelita: "Underwater River," YouTube. [online] Available from: https://www.youtube.com/watch?v=iHBvKDOfWiI (Accessed 28 September 2019)

Gasse, A.: Extracción campana cenote el Zapote, YouTube [online] Available from: https://www.youtube.com/watch?v=oPeO3oNXiQ8&t=13s (Accessed 24 September 2019)

QRSS: Quintana Roo Speleological Survey, [online] Available from: http://caves.org/project/qrss/qrss.htm (Accessed 23 November 2018), 2018.

Ritter, S.: Hells Bells - Under water speleothems from the Yucatán Peninsula, Copernicus Publications., 2018. Available from: https://doi.org/10.5446/39353

Ritter, S.: "Unravelling the formation of Hells Bells: underwater speleothems from the Yucatán Peninsula [Data]", Available from: https://doi.org/10.11588/data/TMYLWS

Stoessel, R.K, unpublished hydrogeochemical data of cenote Angelita, Quintana Roo, Mexico, Sampling of 1992 and 1993. Available from: http://www.ronstoessell.org/Publications%20and%20Data/Yucatan_Data.pdf (Accessed 12 November 2018)

7.4 Unpublished Theses

Klose, L.: Hydrogeologischer und hydrogeochemischer Vergleich unterschiedlicher Cenoten auf der Yucatán Halbinsel, Mexiko, Heidelberg University., pp. 120, 2018.

Schorndorf, N.: Uranium series dating, stable isotopes and geochemistry of "Hells Bells" Speleothems from the Yucatán Peninsula, Heidelberg University., pp. 79, 2018.

Sun, T.: Petrography of Hells Bells - unique underwater speleothems of El Zapote cenote, Yucatán peninsula, Mexico, Heidelberg University., pp. 42, 2018.

8. Appendix

8.1 Supplementary Tables

Tables A1, A2, A3, A4, A5 and A6 are accessible online from https://doi.org/10.11588/data/TMYLWS

8.2 Correction of water depth

The following calculations were conducted by Lukas Klose as part of his Master thesis (Klose, 2018). The multiparameter water sonde EXO-1 (Xylem Analytics, Norway) has an integrated pressure sensor, which calculated the water depth according to Pascal's law (equation A1) and calculates water density from measured salinity. Before each measurement the sonde was calibrated to ambient atmospheric pressure. The sampled cenotes show a strong vertical increase of salinity <1‰ to ~35‰. The differences in temperature within the water column are in a range of 1-2 °C. Due to the increase of salinity the density of the water also increases vertically within the water column. Since Pascal's law is applicable to calculate the hydrostatic pressure of fluids with constant salinity the sonde underestimates the water depth with increasing sampling depth.

$$p(h) = \rho\, g\, h + p(0) \quad \text{(A1)}$$

Hydrostatic pressure:	$p(h)$	$[kg\ m^{-1}\ s^{-2}]$	
Density of water:	ρ	$[kg\ m^{-3}]$	
Acceleration of gravity:	g	$[m\ s^{-2}]$	
Water column:	h	[m]	
Atmospheric pressure:	$p(0)$	$[kg\ m^{-1}\ s^{-2}]$	

Therefore, a numeric approach to correct the water depth of logged in-situ parameters and samples was applied a. The vertical profiles are divided into n parcels, each defined by two consecutive measurements. The density of the water at every measured point of the water column was calculated depending on salinity and temperature. These calculations were carried out according to the Tenth report of the Joint Panel on Oceanographic Tables and Standards (UNESCO, 1981) (see appendix for further information). The density of the water within each parcel is assumed to be constant. Water depth of the first parcel (n=1) was calculated according equation A2.

$$h_1 = \frac{p(h)_1 - p(0)_1}{\rho_1\, g_1} \quad \text{(A2)}$$

Water column at parcel 1:	h_1	[m]
Hydrostatic pressure at parcel 1:	$p(h)_1$	$[kg\ m^{-1}\ s^{-2}]$
Ambient atmospheric pressure:	$p(0)_1$	$[kg\ m^{-1}\ s^{-2}]$
Density of the water at parcel 1:	ρ_1	$[kg\ m^{-3}]$
Acceleration of gravity:	g	$[m\ s^{-2}]$

Water depth of parcels 2 to parcel n was calculated according to equations A3:

$$h_n = \frac{(p(h)_n - p(h)_{n-1}) - p(0)}{\rho_n\, g} + h_{n-1} \quad \text{(A3)}$$

Water column at parcel n,			
Between	$(p(h)_n - p(h)_{n-1}$:	h_n	[m]
hydrostatic pressure			
at parcel n:	$p(h)_n$	$[kg\ m^{-1}\ s^{-2}]$	
hydrostatic pressure			
at parcel n-1:	$p(h)_{n-1}$	$[kg\ m^{-1}\ s^{-2}]$	
ambient atmospheric pressure:	$p(0)$	$[kg\ m^{-1}\ s^{-2}]$	

density of water
at parcel n: ρ_n $[kg\ m^{-3}]$
Acceleration of gravity: g $[m\ s^{-2}]$
Water column at parcel n-1: h_{n-1} [m]

Water density for each parcel was calculated according to the Tenth report of the Joint Panel on Oceanographic Tables and Standards (UNESCO, 1981). Units of coefficients are results of equations A4–8. Values for salinity and temperature were logged by the multiparameter water sonde EXO-1 (Xylem Analytics, Norway).

Equation A4 describes the density of water ρ_{t_n} at measuring point n of the profile depending on temperature.

$$\rho_{t_n} = a_0 + a_1 T_n + a_2 {T_n}^2 + a_3 {T_n}^3 + a_4 {T_n}^4 + a_5 {T_n}^5 \quad \text{(A4)}$$

Density of water depending on temperature: ρ_{t_n} $[kg\ m^{-3}]$
Temperature at measuring point n. T_n [°C]
coefficients: a_0: $999.842594\ kg\ m^{-3}$
a_1: 6.793953×10^{-2}
a_2: -9.095290×10^{-3}
a_3: 1.001685×10^{-4}
a_4: -1.120083×10^{-6}
a_5: 6.536332×10^{-9}

Equation A5 describes the density of the water depending on salinity and temperature at measuring point n.

$$\rho_{s_n} = \rho_{t_n} + B * S_n + C * {S_n}^{\frac{3}{2}} + D * {S_n}^2 \quad \text{(A5)}$$

Density of water depending on S and T: ρ_{s_n} $[kg\ m^{-3}]$
Density of water depending on T: ρ_{t_n} $[kg\ m^{-3}]$
Salinity: S_n [‰]

Where B, C and D are temperature depending coefficients described in equations A3 to A5

$$B = b_0 + b_1 T_n + b_2 {T_n}^2 + b_3 {T_n}^3 + b_4 {T_n}^4 \quad \text{(A6)}$$

Temperature at measuring point n: T_n [°C]
b_0: 8.2449×10^{-1}
b_1: -4.0899×10^{-3}
b_2: 7.6438×10^{-5}
b_3: -8.2467×10^{-7}
b_4: 5.3875×10^{-9}

$$C = c_0 + c_1 T + c_2 {T_n}^2 \quad \text{(A7)}$$

Temperature at measuring point n: T_n [°C]
c_0: -5.7246×10^{-3}
c_1: 1.0227×10^{-4}
c_2: -1.6546×10^{-6}

$$D = 4.8314 \times 10^{-4} \quad \text{(A8)}$$

Reference:

Unesco/ICES/SCOR/IAPSO Joint Panel on Oceanographic Tables and Standards, (1981), Tenth report of the Joint Panel on Oceanographic Tables and Standards, UNESCO technical papers in marine science- No. 36, http://unesdoc.unesco.org/images/0004/000461/046148eb.pdf

Acknowledgements

I am very grateful to my wife and my parents who always supported and encouraged me in pursuing my academic studies.

I am very thankful to my mentor Prof. Dr. Margot Isenbeck-Schröter for providing me the opportunity to be part of her exceptional research group for such a long time now. Thank you, for your continuous guidance and for always giving me the freedom in going after new research topics.

I would like to thank Prof. Dr. Wolfgang Stinnesbeck for offering me to cooperate and work on this exciting topic in Mexico. Thank you for the uncomplicated collaboration and supporting us in many sampling campaigns in Mexico.

I am very grateful to all active and former members of the research group Hydrogeochemistry and Hydrogeology for their energetic assistance in broad areas of my research/life ranging from extensive sampling campaigns, various excellent laboratory analyses and profound technical discussions to recreative lunch-time breaks, occasional bike repairs and sporting events. Every one of you has his or her particular share in this PhD thesis. Thank you.